

Tailored Carbon Nanodots

Shining light on their synthesis and applications



Francesca Arcudi



UNIVERSITÀ DEGLI STUDI DI TRIESTE

**XXIX CICLO DEL DOTTORATO DI RICERCA IN SCIENZE E
TECNOLOGIE CHIMICHE E FARMACEUTICHE**

**TAILORED CARBON NANODOTS:
SHINING LIGHT ON THEIR SYNTHESIS
AND APPLICATIONS**

Settore scientifico-disciplinare: **CHIM/06**

Ph.D. Candidate:

Ms. **FRANCESCA ARCUDI**

Advisor:

Prof. **MAURIZIO PRATO**

Ph.D. Program Director:

Prof. **MAURO STENER**

ANNO ACCADEMICO 2015/2016

“Knowledge is limited, whereas imagination embraces the entire world, stimulating progress, giving birth to evolution.”

Albert Einstein – Cosmic Religion: With Other Options and
Aphorisms, 1931

Acknowledgements

I wish to express my sincere appreciation to those who have contributed to this thesis and sustained me during this amazing journey.

Above any others, I am extremely grateful to my enthusiastic supervisor *Prof. Maurizio Prato*. My Ph.D. has been a fantastic experience and I thank you wholeheartedly. I remain amazed that despite your busy and crazy schedule, you were able to patiently guide me constantly throughout my Ph.D. research studies. I'm proud and honored to have started a new exciting research line with you! You gave me the freedom I needed to grow as a research scientist and your kind advices have been priceless. Thanks for believing in me and for encouraging my research. I have been extremely lucky to have a supervisor who cared so much about my work, and who responded to my questions and queries so promptly. I could not have imagined having a better supervisor and you have been a formidable mentor for me. Throughout these years beside you I learned more than I was expecting from a Ph.D. It was a real privilege for me to share your exceptional and immense scientific knowledge, but also your extraordinary human qualities.

I wish to thank all the members of the Prato lab. Thanks to the nanodots people: *Ms. Jennifer Gomez*, *Mr. Michele Cacioppo*, and especially *Mr. Francesco Rigodanza*.

A particular acknowledgement goes to *Dr. Luka Đorđević*. I'm indebted for our fruitful scientific exchange that helped me at various stages of my research.

A special thanks goes to *Prof. Luisa De Cola* for the fantastic period spent in her research laboratories in Strasbourg. Thanks for your advices and support.

Actually, this thesis is the result of diverse exciting projects, and I would like to thank all the other people I had the opportunity to work with (in an order based on the thesis chapters): *Prof. Giuseppe Gigli and Dr. Fabrizio Mariano* (CNR NANOTEC, Lecce, Italy); *Dr. Blanca Arnaiz* (CicBiomagune, San Sebastian, Spain); *Ms. Serena Carrara* (Institut de Science et d'Ingénierie Supramoléculaires, Université de Strasbourg, France); *Prof. Dirk Guldi, Dr. Volker Strauss and Dr. Alejandro Cadranel* (Friedrich-Alexander-Universität Erlangen-Nürnberg, Germany); *Prof. Francesca D'Anna, Dr. Carla Rizzo and Prof. Nadka Tz. Dintcheva* (University of Palermo, Italy); *Prof. Alessandro Moretta, Prof. Simona Sivori and Dr. Simona Carlomagno* (University of Genova, Italy); *Prof. Roberto Purrello and Dr. Alessandro D'Urso* (University of Catania, Italy).

This thesis is also the result of many experiences, and the one in Strasbourg was the most special. I have very fond memories of my time there and a heartfelt thanks goes to *Matteo, Cristina, Matilde and Youssef*. Most importantly, I struck up an irreplaceable friendship with you *Serena*. Thank you for being my French sister and for becoming a fantastic friend.

Thanks to my dear friend in Trieste, *Valentina*. Your friendship has made my stay here special.

A big “Thank you!” also goes out to my super and closer friends: *Federica, Gabriele, Carla, Gloria, Vittoria, Marta, Rosanna, Cristina, Manuela*. Thanks for your unconditional friendship throughout these years. Many of us are not still living in our Palermo...but when we are together it's as if no time has passed for us!

Words cannot express the feelings I have for my family for their constant support, patience, understanding, encouragement and endless love. *Papà e mamma* you are the best parents anybody could have and I would not be here if it not for you. *Sara e Mimi* you were more than a sister and a brother for me, you brought me up. I was really missing you and the fantastic babies in these years. The hardest thing of my Ph.D. was to be so far away from all of you, but you were always close to my heart.

And 'only to' *Luka* this time, for sticking by my side as a constant source of love, strength and inspiration. You are the most brilliant and marvelous person I have ever met. Without you I would not have come this far, because of you and with you I can image to go much further away.

Table of Contents

Abbreviations	I
Abstract.....	VI
Riassunto.....	IX
1 Carbon Nanoallotropes: Who is next?.....	1
1.1 Classification, fundamental properties and applications of nanocarbons.....	3
1.1.1 Carbon-based dots.....	6
1.2 Overview of the dissertation	9
1.3 References.....	12
2 Nitrogen-Doped Carbon Nanodots	17
2.1 Introduction.....	18
2.1.1 Synthetic methods.....	18
2.1.2 Photophysical properties.....	27
2.1.3 Aim of the project	30
2.2 Preparation of NCNDs	32
2.2.1 Synthesis	32
2.2.2 Morphological and structural characterization	33
2.2.3 Photophysical characterization	43
2.2.4 Towards applications	47
2.3 Conclusions and perspectives	50
2.4 Experimental section	52
2.4.1 Materials	52
2.4.2 Apparatus and characterization.....	53
2.4.3 Synthesis of NCNDs.....	57
2.4.4 Supporting figures.....	58
2.5 References.....	68
3 Carbon Nanodots in Electrochemiluminescence	76

Table of Contents

3.1	Introduction.....	77
3.1.1	ECL: fundamentals and mechanisms.....	77
3.1.2	Luminophores.....	81
3.1.3	Co-reactants.....	89
3.1.4	Ru(bpy) ₃ ²⁺ /TPA as ECL model system.....	90
3.1.5	Analytical applications.....	93
3.1.6	Aim of the project.....	95
3.2	NCNDs as ECL co-reactant.....	97
3.2.1	NCNDs/Ru(bpy) ₃ ²⁺ system.....	98
3.2.2	mNCNDs/Ru(bpy) ₃ ²⁺ system.....	103
3.2.3	Epinephrine sensing.....	108
3.3	NCNDs-based hybrids as ECL platforms.....	111
3.3.1	Syntheses.....	113
3.3.2	Structural, morphological and photophysical characterization.....	113
3.3.3	Electrochemical characterization.....	120
3.3.4	Electrochemiluminescence.....	123
3.3.5	Self-enhanced and multi-label ECL platforms.....	127
3.4	Conclusions and perspectives.....	130
3.5	Experimental section.....	133
3.5.1	Materials.....	133
3.5.2	Apparatus and characterization.....	134
3.5.3	Syntheses of the hybrids.....	140
3.5.4	Synthesis of mNCNDs.....	141
3.6	References.....	142
4	Carbon Nanodots-based Hybrid Materials.....	161
4.1	Introduction.....	162
4.1.1	Photofunctional nanocarbon-based hybrids.....	162
4.1.2	Supramolecular gel.....	173
4.1.3	Aim of the project.....	176

4.2	NCNDs with porphyrin antennas: covalent and non-covalent electron donor-acceptor hybrids.....	178
4.2.1	Porphyrin/NCNDs supramolecular ensemble.....	178
4.2.2	Porphyrin-NCNDs covalently linked system.....	182
4.3	NCNDs/Ionogels	190
4.3.1	Gelation tests.....	191
4.3.2	Rheological properties	194
4.3.3	Self-healing properties	196
4.3.4	Kinetic of gel formation.....	199
4.3.5	Fluorescence properties	200
4.3.6	Morphological investigation	202
4.3.7	Aggregation studies	203
4.3.8	Anti-radical activity	205
4.4	Conclusions and perspectives	208
4.5	Experimental section	210
4.5.1	Materials	210
4.5.2	Apparatus and characterization.....	210
4.5.3	Synthesis of TCPP	214
4.5.4	Synthesis of TPP-COOCH ₃	215
4.5.5	Synthesis of TPP-COOH	216
4.5.6	Synthesis of TPP-CONH-NCNDs	217
4.5.7	Preparation of gels and T _{gel} determination.....	218
4.5.8	Supporting figures.....	219
4.6	References.....	229
5	Rationally Designed Carbon Nanodots.....	242
5.1	Introduction.....	244
5.1.1	Multicolored emission	244
5.1.2	Tunable electrochemistry.....	256
5.1.3	Optical activity.....	258
5.1.4	Aim of the project	262
5.2	White-light-emitting CNDs	264

Table of Contents

5.2.1	Design and synthesis.....	264
5.2.2	Photophysical characterization	270
5.2.3	Morphological and structural characterization	274
5.3	BODIPY-based CNDs.....	280
5.3.1	Design and synthesis.....	280
5.3.2	Photophysical characterization	283
5.3.3	Morphological and structural characterization	286
5.3.4	BCNDs effects on human natural killer cells	290
5.4	Chiral CNDs	298
5.4.1	Design and synthesis.....	298
5.4.2	Morphological and structural characterization	299
5.4.3	Photophysical and chiro-optical properties.....	301
5.4.4	Induced chiral supramolecular assemblies.....	304
5.5	Customizing energy-level in CNDs.....	308
5.5.1	Design and synthesis.....	308
5.5.2	Morphological, structural and electrochemical characterization	309
5.5.3	Photophysical characterization	313
5.6	Conclusions and perspectives	316
5.7	Experimental section	318
5.7.1	Materials	318
5.7.2	Apparatus and characterization.....	318
5.7.3	Synthesis of WCNDs	321
5.7.4	Synthesis of NDI•CNDs	322
5.7.5	Synthesis of cNDI•CNDs.....	323
5.7.6	Synthesis of BODIPY-COOH	324
5.7.7	Synthesis of BCNDs	325
5.7.8	Synthesis of (—)- and (+)-CNDs.....	325
5.7.9	Synthesis of qCNDs.....	326
5.7.10	Chiral supramolecular assembly	327
5.7.11	Supporting figures.....	327
5.8	References.....	334

Table of Contents

6	Experimental techniques.....	354
6.1	Absorption spectroscopy	354
6.2	Fluorescence spectroscopy	355
6.3	Luminescence quantum yield	357
6.4	Lifetime measurement	360
6.5	X-ray photoelectron spectroscopy	362
6.6	Atomic force microscopy	363
6.7	Electrochemistry	365
6.7.1	Cyclic voltammetry.....	365
6.7.2	Potentiostatic techniques.....	366
6.8	References.....	368
	Curriculum Vitae.....	370
	Publications	370

Abbreviations

1-D	Mono-dimensional
2-D	Bi-dimensional
3-D	Tri-dimensional
A	electrode surface (cm^2)
Å	Angstrom
a.u.	arbitrary units
AFM	Atomic Force Microscopy
APDEA	<i>N</i> -(3-Amino-Propyl)Diethanolamine
Arg	Arginine
AuNPs	Gold Nanoparticles
BDAE	<i>N</i> -Butyldiethanolamine
Br ₂ NDA	2,6-Dibromonaphthalene-1,4:5,8-Tetracarboxylic Dianhydride
c	speed of light (2.99×10^8 m/s)
CD	Circular Dichroism
CE	Counter Electrode
CIE	Commission Internationale d'Eclairage
CL	Chemiluminescence
cNDIs	Core-substituted Naphthalene Diimides
CNDs	Carbon Nanodots
CQDs	Carbon Quantum Dots
CR	Charge Recombination
CS	Charge Separation

Abbreviations

CV	Cyclic Voltammetry
<i>D</i>	Diffusion coefficient (cm ² /s)
<i>d</i>	Deuterated
DBAE	2-(Dibutylamino)Ethanol
DBM	Dibenzoylmethide
Dend	Dendrimer
DFT	Density Functional Theory
DMF	Dimethylformamide
DMSO	Dimethylsulfoxide
DNA	Deoxyribonucleic Acid
DOS	Dicationic Organic Salt
DOSY	Diffusion-Ordered Spectroscopy
<i>e.g.</i>	<i>exempli gratia</i> (latin) – for example
ECL	Electrochemiluminescence
EDA	Ethylenediamine
EL	Electroluminescence
EMCCD	Electron Multiplying Charge Coupled Device
EP	Epinephrine
ESI	Electrospray Ionization
ESIPT	Excited-State Intramolecular Proton Transfer
eV	electronvolt (1eV = 1.602 × 10 ⁻¹⁹ J)
exc	Excitation
FL	Fluorescence
FRET	Föster Resonance Energy Transfer
FWHM	Full Width at Half Maximum

Abbreviations

GC	Glassy Carbon
GQDs	Graphene Quantum Dots
<i>h</i>	Plank constant (6.63×10^{-34} J·s)
HMBC	Heteronuclear Multiple Bond Correlation
HOMO	Highest Occupied Molecular Orbital
HSQC	Heteronuclear Single Quantum Coherence
<i>i.e.</i>	<i>id est</i> (latin) – that is to say
ICP-MS	Inductively Coupled Plasma Mass Spectrometry
IL	Ionic Liquid
IR	Infrared
ITO	Indium Tin Oxide
K	Kelvin degree
k	kilo (10^3)
LED	Light-Emitting Diode
LLCT	Ligand-to-Ligand Charge Transfer
LOD	Limit of Detection
LOQ	Limit of Quantification
LUMO	Lower Unoccupied Molecular Orbital
m	mass
M	Molar
MeOH	Methanol
MLCT	Metal-to-Ligand Charge Transfer
mNCNDs	methylated-NCNDs
mol	mole
MTT	3-(4,5-dimethylthiazol-2-yl)-2,5-diphenyltetrazolium bromide

Abbreviations

MWCNT	Multi-Walled Carbon Nanotube
NAD	Nicotinamide Adenine Dinucleotide
NDAs	Naphthalene Dianhydrides
NDIs	Naphthalene Diimides
nm	nanometer
NMP	<i>N</i> -Methyl-2-pyrrolidone
NMR	Nuclear Magnetic Resonance
NP	Nanoparticle
OLED	Organic Light-Emitting Diode
OMS	Ordered Mesoporous Silica
PBI	Perylene Bisimide
PBS	Phosphate Buffered Saline
PEDOT:PSS	Poly(3,4-ethylenedioxythiophene): Polystyrene sulfonate
PEG	Polyethylene glycol
PEI	Polyethyleneimine
PL	Photoluminescence
PMMA	Poly(methyl methacrylate)
PMT	Photomultiplier Tube
poly-TPD	Poly- <i>[N,N'</i> -bis(3-methylphenyl)- <i>N,N'</i> -diphenylbenzidine]
psi	pound-force per square inch
Pt	Platinum
PVK	Poly(<i>N</i> -vinylcarbazole)
QDs	Quantum Dots
QRE	Quasi-Reference Electrode

Abbreviations

RGB	red, green, blue
Ru(bpy) ₃ ²⁺	Ruthenium(II)tris(2,2'-bipyridyl)
s	second
SAM	Self-Assembled Monolayer
SCE	Saturated Calomel Electrode
SEC	Size Exclusion Chromatography
SWCNT	Single-Walled Carbon Nanotube
T	Temperature
TBAPF ₆	Tetra-butylammonium hexafluorophosphate
TBET	Through bond energy transfer
TCPP	Tetrakis(4-carboxyphenyl)porphyrin
TCSPC	Time-Correlated Single-Photon Counting
TEM	Transmission Electron Microscopy
TPP	Tetraphenylporphyrin
TPA	Tripropylamine
TTA	Triplet-Triplet Annihilation
WCNDs	White-light-emitting Carbon Nanodots
WE	Working Electrode
WOLED	White Organic Light-Emitting Diode
XPS	X-ray Photoelectron Spectroscopy
λ	Wavelength
τ	Lifetime
Φ (QY)	Quantum Yield

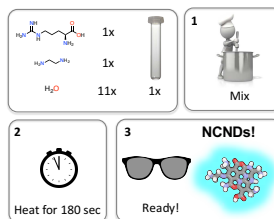
Abstract

The great developments made in nanotechnology have enabled a variety of nanomaterials to join the carbon party and the newcomers carbon nanodots (CNDs) represent an ever-expanding research field. Defined as carbon nanoparticles with size below 10 nm, CNDs possess intriguing properties and hold great promises as new-generation luminescent materials. Additionally, owing to their inexpensive and safe nature, facile surface modification, high solubility and resistance to photobleaching, they are expected to have a huge impact in a plethora of applications.

In the first part of *Chapter 1*, a brief classification of the nanocarbons, in terms of their dimensionality and the hybridization state of the carbon atoms, is provided. The second part, focuses on carbon-based dots in an attempt to shed light on the huge inconsistencies in literature about their classification, providing a general guideline in identifying properly the various dots.

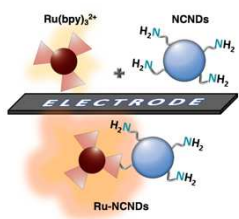


Chapter 2 describes our efforts directed to a simple, scalable, reliable and cost-effective synthetic process for producing high-quality nanodots. A bottom-up approach to nitrogen-doped CNDs (NCNDs), by employing arginine and ethylenediamine as precursors, is presented. By using a microwave reactor, an accurate control of the parameters, that affect the nanodots growth, such as reaction time, temperature and power, was accomplished. NCNDs were



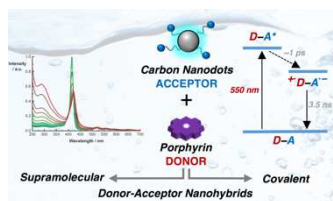
obtained within a few minutes heating and were characterized through spectroscopic, morphological and structural analyses. They display among the smallest size and the highest fluorescence quantum yields reported so far. Moreover, they can be easily post-functionalized. Finally, preliminary investigation on their cytotoxicity, cell uptake and imaging capability, and on their employment for LED fabrication, suggested their potentialities for various applications.

In *Chapter 3*, the use of CNDs in electrochemiluminescence (ECL) is discussed. In the first part, it has been shown that our NCNDs can act as powerful alternative to the conventional co-reactant species for ECL generation. Additionally, their employment towards sensitive biosensing platform for the detection of interesting bioanalytes has



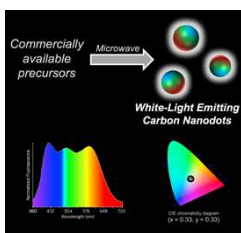
been shown. In the second part, the use of NCNDs in covalently-linked systems with ECL labels has been reported, for the first time. A deep spectroscopic and electrochemical investigation demonstrated that all the redox centers retains their properties in the hybrids, substantiating their use in ECL. Finally, it was probed that our NCNDs-based hybrids exhibit self-enhanced ECL and can be used as platform for signal amplification.

Chapter 4 focuses on the use of CNDs for the design of novel hybrid systems. The first part deals with photofunctional donor-acceptor hybrids. Due to their intriguing photophysical properties, porphyrins have been explored for the first time with CNDs: both covalent and supramolecular ensembles have been studied, in which the electron donating properties of porphyrins were combined with the electron



accepting features of our NCNDs. An extensive photophysical characterization has been performed and suggested the formation of a charge separated transfer complex between nanodots and porphyrins. In the second part, the first example of CNDs-based ionogels and their comprehensive characterization is reported. It has been observed that NCNDs induce gel formation for no gelating systems and module the properties of pure gels. For instance, the NCNDs exert a positive influence on the rheological response of the gel phases. Finally, interesting features such as the ability to self-repair after disruption and antiradical activity have been demonstrated.

Chapter 5 presents a rational synthetic design for mastering CNDs properties, showing the pivotal importance of a proficient choice of the precursors. By using properly designed functional units, the desired properties have been induced from the molecular to the nanoscale level in a controlled fashion. One-pot, bottom-up, cost-



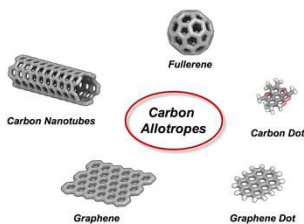
effective and time-saving synthetic methods, built on commercially available or easy-to-synthesize organic building blocks, were employed. In the first part, CNDs with customized emission have been approached. Green, red and finally white-emitting CNDs were synthesized. In the second part, it is

demonstrated that the introduction of properly designed ‘dopants’ impart chiro-optical or tunable redox properties to CNDs.

Riassunto

Per merito dei progressi raggiunti nell'ambito delle nanotecnologie, svariate nanostrutture sono entrate a far parte della famiglia dei nanomateriali a base di carbonio, ed i nuovi arrivati “carbon nanodots” (CNDs) rappresentano un ambito di ricerca in costante espansione. Definiti come nanoparticelle di carbonio aventi dimensioni inferiori a 10 nm, i CNDs godono di interessanti proprietà e sono dei promettenti materiali luminescenti di nuova generazione. Inoltre, data la loro poco costosa e innocua natura, la semplice modificazione della loro superficie, l'elevata solubilità e resistenza a fenomeni di “photobleaching”, sembrano essere destinati ad avere un grande impatto nell'ambito di una pletera di applicazioni.

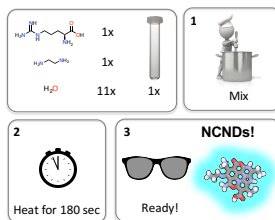
Nella prima parte del *Capitolo 1* viene fornita una breve classificazione dei nanomateriali di carbonio in termini della loro dimensionalità e dello stato di ibridizzazione degli atomi di carbonio. La seconda parte è incentrata sui “dots” a base di carbonio, nel tentativo di fare luce sulle notevoli inconsistenze in letteratura riguardo la loro classificazione, suggerendo una generale linea guida per la loro appropriata identificazione.



dimensionalità e dello stato di ibridizzazione degli atomi di carbonio. La seconda parte è incentrata sui “dots” a base di carbonio, nel tentativo di fare luce sulle notevoli inconsistenze in letteratura riguardo la loro

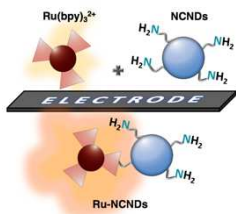
Il *Capitolo 2* mostra gli sforzi volti allo sviluppo di un processo semplice, scalabile, riproducibile per la produzione di “high-quality nanodots”. Viene presentato un approccio sintetico “bottom-up” di CNDs dopati con azoto (NCNDs), utilizzando arginina ed etilendiammina come precursori. Un accurato controllo dei parametri che influenzano la crescita dei nanodots, come il tempo, la

temperatura e la potenza impiegati nella reazione, è stato raggiunto mediante l'impiego di un reattore a microonde. Sono stati preparati NCNDs in pochi minuti di riscaldamento e sono stati ampiamente caratterizzati mediante analisi



spettroscopiche, morfologiche e strutturali. Quest'ultimi possiedono tra le più piccole dimensioni e le più alte rese quantiche di fluorescenza fino ad ora riportate. Inoltre, essi possono essere facilmente funzionalizzati. Infine, sono stati condotti degli studi preliminari sulla loro citotossicità, “uptake” cellulare e capacità di “imaging”, nonché sul loro impiego per la realizzazione di “LED”, che ne suggeriscono elevate potenzialità per varie applicazioni.

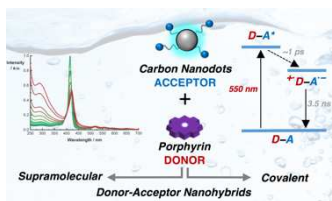
Nel *Capitolo 3*, viene affrontato l'impiego dei CNDs in elettrochemiluminescenza (ECL). Nella prima parte viene dimostrato



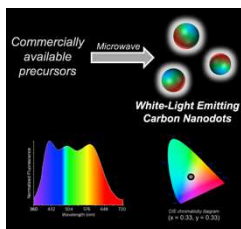
che i NCNDs rappresentano una valida alternativa ai co-reattanti convenzionalmente utilizzati per la generazione di luce per via elettrochimica. È stato inoltre riportato il loro impiego in biosensori con elevata sensibilità per la rivelazione di interessanti bioanaliti. Nella

seconda parte, è riportato per la prima volta l'uso di NCNDs in sistemi covalenti con luminofori per ECL. Un dettagliato studio fotofisico ed elettrochimico dei sistemi ha dimostrato che la totalità dei centri redox negli ibridi presenta le stesse proprietà della singola molecola, incoraggiando pertanto il loro uso in ECL. È stato infine dimostrato che gli ibridi mostrano un effetto di auto-accrescimento dell'emissione per via elettrochimica e possono essere impiegati come piattaforme per l'amplificazione della luminescenza.

Il *Capitolo 4* è incentrato sull'impiego dei CNDs per il “design” di sistemi ibridi innovativi. La prima parte riguarda sistemi ibridi foto-funzionali donatore-accettore. Considerate le interessanti proprietà fotofisiche delle porfirine, ne è stato esplorato il loro impiego con i CNDs per la prima volta. Sono stati studiati sistemi donatore-accettore basati su porfirine e NCNDs sia covalenti che supramolecolari. Sono pertanto state condotte delle approfondite caratterizzazioni fotofisiche, che hanno suggerito la formazione di complessi a trasferimento di carica tra porfirine e NCNDs. Nella seconda parte è riportato il primo esempio di ionogel ibridi con CNDs e la loro completa caratterizzazione. È stato osservato che i NCNDs inducono la formazione di gel supramolecolari per sistemi che non sono in grado di gelificare, e riescono, inoltre, a modulare le proprietà dei gel puri. In particolare, i NCNDs esercitano un effetto positivo sulla risposta reologica delle fasi gel. Infine, i gel ibridi hanno mostrato la capacità di riformarsi dopo rottura meccanica ed inoltre una eccellente attività antiradicalica.



Nel *Capitolo 5* è presentato un approccio sintetico razionale per la modulazione delle proprietà dei CNDs, mostrando la decisiva importanza di una appropriata scelta dei precursori. Sono state indotte le desiderate proprietà dal livello molecolare alla nano-scala in modo controllato, mediante l'impiego di unità funzionali opportunamente ingegnerizzate. Sono stati impiegati metodi di sintesi “one-pot”, “bottom-up”, efficaci e poco dispendiosi sia dal punto di vista dei costi che dei tempi, ed incentrati sull'impiego di “building blocks” organici



commercialmente disponibili o di facile sintesi. Nella prima parte sono stati sintetizzati CNDs aventi specifiche emissioni di fluorescenza, ovvero verde, rossa e infine bianca. Nella seconda parte, è stato dimostrato che l'impiego di opportuni dopanti impartisce proprietà chiro-ottiche ai CNDs e ne consente la modulazione delle caratteristiche redox.

1 Carbon Nanoallotropes: Who is next?

Serendipitous discoveries have marked human and scientific evolution, but “change favors only the prepared minds” as Pasteur said.¹

Twenty years ago “prepared minds” were Robert F. Curl, Harold W. Kroto and Richard E. Smalley, who shared the 1996 Nobel Prize in Chemistry for the discovery of fullerene.² This discovery has set in motion a new world-wide research boom that is still growing.

Apart from fullerene, the popularity of carbon nanostructures is greatly due to carbon nanotubes (CNTs) and graphene.^{3,4} The great developments made in nanotechnology and in advanced material synthetic methods have enabled other members to join the carbon nanomaterial party. As for the beginning of this new era in carbon nanoscience, serendipity has played an important role for the newcomers carbon-based dots. After their accidental finding during the purification of carbon nanotubes in 2004,⁵ such small carbon nanoparticles have promptly attracted the interest of alert and curious scientists. They possess even more intriguing properties compared to other carbon nanomaterials and, with their fascinating photoluminescence, are attracting considerable attention as new-generation luminescent materials.

In the following sections, a classification of the nanocarbons in terms of their dimensionality and the hybridization state of the carbon atoms is suggested. Apart from carbon-based dots, in this section we refer in particular to fullerene, carbon nanotubes, graphene (**Figure 1.1**), leaving out other nanocarbons, whose discoveries are sometimes considered as less relevant. In any case, a profound discussion on the preparation, properties and potential applications of all of these

nanocarbons is beyond the scope of this chapter and in general of this dissertation. On the contrary, in this chapter a particular focus on the carbon based-dots, which include graphene or carbon quantum dots (GQDs or CQDs) and carbon nanodots (CNDs), is provided.

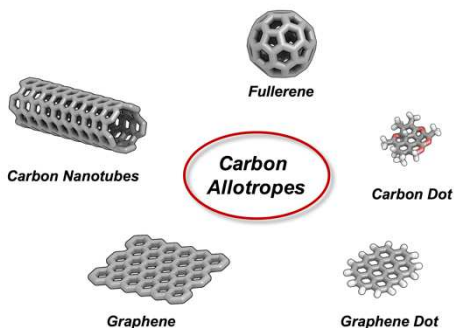


Figure 1.1 Carbon allotropes overview.

1.1 Classification, fundamental properties and applications of nanocarbons

A possible and convenient approach to carbon allotropes classification is based on their dimensionality: they can be cataloged as 0-D, 1-D or 2-D nanostructures. While fullerenes and carbon-based dots (GQDs, CQDs and CNDs) can be considered as representative examples of 0-D allotropes, carbon nanotubes and graphene are classified as 1-D and 2-D nanostructures, respectively.

All of these carbon allotropes can be regarded as members of the same groups of nanostructures, consisting mainly of sp^2 carbon atoms, except for CQDs and CNDs that contain a mixture of sp^3 and sp^2 carbon atoms in various ratios. However, GQDs usually display sp^3 carbons at the edge and sp^2 carbons in the core. Moreover, although all the fullerene carbon atoms are sp^2 -hybridized, as the arrangement of carbon atoms is not planar but rather pyramidalized, a “pseudo”- sp^3 -bonding component must be present and C_{60} (the most abundant fullerene) and other larger fullerenes can be viewed as a carbon nanoallotrope with hybridization between sp^2 and sp^3 .

The nanostructures primarily made up of sp^2 carbon atoms that are densely packed in a hexagonal honeycomb crystal lattice (although they may also contain some sp^3 carbon atoms at defect sites or edges) are defined as graphenic nanostructures. They are based on the ability of carbon to form three identical covalent bonds with other carbon atoms using sp^2 orbitals, generating a 2-D lattice.

The simplest and most representative member of this group is graphene, a two-dimensional, one atom thick sheet of sp^2 -hybridized carbon arranged in a hexagonal lattice, with dimension usually in excess of 500 nm. GQDs usually consist of a few stacked graphene monolayers based on their graphenic nanosheet precursors and, from a theoretical perspective, graphene can be regarded as the building material for other nanocarbons. For example, a properly cut piece of

a graphene sheet could, in principle, be wrapped up into 0-D fullerene, rolled into 1-D nanotubes or stacked into 3-D graphite.⁶

This common sp^2 structure means that they have some similar properties in terms of electrical conductivity, mechanical strength and chemical reactivity, although obvious differences due to their different sizes and shapes should be taken in account.

Typically, sp^2 -carbon allotropes are only (and slightly in most of the case) dispersible in organic solvents, with fullerenes and GQDs being the only nanostructures that can be defined as soluble in specific organic solvents with opposite trends. GQDs display a good solubility in polar solvents, whereas fullerenes are essentially insoluble, preferring, for instance, aromatic hydrocarbons solvents such as toluene or *o*-dichlorobenzene.

Likewise to GQDs, CNDs and CQDs are hydrophilic, generally due to the presence of oxygenated groups. This common property, that makes all these carbon-based dots water soluble, is undoubtedly one of their most appealing features and is closely related to their good biocompatibility and low toxicity.

Besides dimensionality effects, each carbon nanoallotrope shows unique physicochemical properties that are discussed in the following paragraphs. It is worth pointing out that we do not seek to comprehensively discuss them, but we do highlight only some of their key features.

The major interest in graphene and CNTs rely on their outstanding mechanical and electronic properties and, especially, the ability to transfer them to composite materials on a macroscopic scale, generating advanced hybrid systems. Indeed, they are the strongest known materials. The Young's modulus of graphene was found to be ~ 1.0 TPa,⁷ and similar measurements have shown that carbon nanotubes are also very strong.⁸⁻¹⁰

These impressive mechanical properties together with other unique characteristics, such as their flexibility, chemical inertness, and electrical conductivity, have been explored for several technological applications. The high electrical conductivity of graphene monolayers and their capacity to carry large currents at room temperature are their most well-known and extensively studied properties.⁶ The conducting properties of CNTs are determined by the way in which the graphene monolayer is rolled up to form the cylinder, which means that CNTs can be metals or semiconductors, and the electrical characteristics of carbon nanotubes are strongly governed by the diameter and chirality of the nanotubes.¹¹

Carbon nanotubes and graphene also have interesting optical properties. CNTs have absorptions accompanied by sharp electronic transitions at energies of 0.98–0.99 eV, corresponding to electromagnetic waves from the far-ultraviolet (~200 nm) to the far-infrared (~200 μm) regions of the spectrum. For this reason, CNTs were regarded as “practical black bodies”.¹² Interestingly, graphene exhibits electrochromic behavior, *i.e.* its absorption and emission of light are controllable by electrical stimulation.¹³

Fullerene lacks many of the fundamental properties of other carbon nanostructures such as conductivity and mechanical strength. However, its structural morphology makes, for instance, C₆₀ a very useful radical scavenger.^{14,15} Due to its spherical shape and electron-deficient character, C₆₀ reacts easily with all kinds of free radicals. More so, another fundamental property of C₆₀ is its ability to act as an electron acceptor in donor–acceptor units of energy conversion systems, due to its high electron affinity and low reorganization energy.^{16,17}

Regarding the newcomers, it is undoubtedly that the most interesting property of carbon-based dots is their photoluminescence.¹⁸ This fact together with their size, solubility (not dispersibility) in water and

their low toxicity makes them potentially useful in a wide range of applications.¹⁹ However, the research is in its early stages, and although there is still a long way to go for practical applications, for sure there is a large room for researchers.

1.1.1 Carbon-based dots

The term "dot" (or "nanodots") is referred to object in the nanometer scale, possessing properties diverse from molecules and bulk materials. On the other hand, the term "quantum dot" is mostly referred to semiconductor nanoparticles (QDs) with quantum confinement to zero dimensions.²⁰ The excitons are confined in the spatial dimensions with quantized energy states and there is a carrier confinement by the reduced dimensions.

In the first publication dealing with carbon-based dots the term "carbon quantum dots" was used,²¹ without proving the necessary requirements for "quantum dots". There are huge inconsistencies on the named used to classified the type of carbon-based dots used in many of the articles published until now. Therefore, we here report a brief discussion on what we believe can be considered a rational and generally accepted classification of carbon-based dots, that represented our reference in identifying properly the type of dots presented in this dissertation.

In the case of defect-free QDs, the photoluminescence is entirely governed by quantum confinement effects, originated from HOMO-LUMO transition and there are not interstates within the bandgap. This result in size-dependence photoluminescence and excitation-independent emission regardless their compositions and/or synthetic methods. On the other hand, the synthetic methods play a pivotal role for the carbon counterpart, because the surface chemistry impart crucial effects. Indeed, the photoluminescence of CQDs and GQDs is believed to arise not only from the quantization effects of the core,

but also from surface effects, due to the presence of functional groups and/or defects. The bandgap transitions arise from conjugated π -domains, which resemble large aromatic systems with extended π -conjugation of specific electronic energy bandgap for emissions. However, in the case of CNDs, the presence of different surface trap states, which act as photoluminescence emitter centers, is considered the major contribution to their photoluminescence.

As common properties, and in contrast to QDs, carbon-based dots display broad absorption bands as well as broad and excitation-dependent photoluminescence emission.

While all the carbon-based dots are composed by carbon, oxygen and hydrogen atoms, the three class of dots present substantial differences in terms of structure and shape.

GQDs can be considered as small fragments of graphene and this results in a discoidal shape with size typically under 20 nm. On the contrary, CQDs and CNDs are quasi-spherical nanoparticle with a mixture of sp^3 and sp^2 carbon atoms (mainly sp^2 in the case of CQDs) with size below 10 nm, and while the former usually show a crystalline structure, the latter are composed by an amorphous core.

It is worth mentioning that, due to their benign composition, carbon-based dots should be considered as a no-toxic alternative to the heavy metal-based QDs. Nevertheless, their hydrophilicity and (sometimes) ease of synthesis provide outstanding advantages respect the inorganic counterpart. Their luminescent and electronic properties deserve further investigations and systematic efforts. Nonetheless, the improvement of their (usually low) luminescence performance is an urgent task for adequately replacing other emitters. Moreover, emissions at longer wavelengths, respect to the ones of the current nanodots (mostly emitting in the blue region), need to be achieved.

It should be highlighted that, although the research in this field can be considered at early stages, they have already shown an enormous

potential in many fields, from biological to optoelectronic and energy related applications. In particular, their employment as new type of biocompatible carbon-based nanomaterials in biomedical applications have been the most studied so far, but also optoelectronic and energy devices are rapidly rising and described in recent reviews.^{19,22–29}

Concluding, in little over decade of carbon-based dots impressive advances have been made. Undoubtedly, further developments are needed and the plethora of potential applications compels further investigations, and joint efforts of the scientific community are required. They possess fascinating properties when compared to their ‘carbon cousins’, they have heralded a new chapter in carbon nanosciences and don’t seem to play a subordinate role. Many wonder if they will replace the famous semiconductor quantum dots. We could envisage that it’s a quite long-term perspective, but we believe that their unique properties will make it possible. Time will give the answers, but it’s our belief that the future of these nanocarbon newcomers will be bright.

1.2 Overview of the dissertation

The research activity of this doctoral thesis was directed towards designing and preparing tailored CNDs for various applications (**Figure 1.2**). The work has been divided into four main chapters, as presented below.

Chapter 2 showcases our efforts towards a simple, scalable, reliable and cost-effective synthetic procedures for preparing high-quality CNDs, without the need of sophisticated equipment and/or additional surface passivation. In order to enhance the CNDs optical properties, nitrogen has been used as dopant. In particular, a bottom-up approach to nitrogen-doped CNDs (NCNDs) is presented. Heteroatoms have been inherited from precursors and, by using molecules containing primary amines (specifically arginine and ethylenediamine) a simultaneous nitrogen doping and surface passivation during the synthetic process has been achieved. The increasingly popular microwave-assisted hydrothermal synthesis has been chosen as synthetic route, which would avoid multi-step synthesis and provide benefits from features such as faster rates, milder conditions, and low energy consumption. More so, by using a MW reactor an accurate control of the parameters, that affect the nanodots growth, such as reaction time, temperature and power, was accomplished. NCNDs were obtained within few minutes of heating and were characterized through spectroscopic, morphological and structural analyses. They can be easily post-functionalized and preliminary studies on their cytotoxicity, cell uptake and imaging capability, as well as LEDs fabrications, suggested their potentialities for various applications.

Chapter 3 deals with the largely unexplored application of CNDs in electrochemiluminescence (ECL). In the first part, NCNDs has been studied as co-reactant to promote ECL. Their high potential as alternative to the conventional co-reactant species has been

demonstrated and a mechanism has been proposed. Moreover, their employment towards sensitive biosensing platform for the detection of interesting bioanalytes has been showed. In the second part, the first NCNDs-based covalently-linked systems with ECL labels have been reported and studied in deep through different techniques. Notably, optical and electrochemical studies demonstrated that all the redox centers are ECL actives, in close contact with the electrode and able to diffuse towards it. Furthermore, the use of the NCNDs-based hybrids as platforms for self-enhancing ECL and signal amplification has been shown.

Chapter 4 is dedicated to novel CNDs-based hybrid systems. In the first section, the role of CNDs in photofunctional ensembles has been investigated. In this context, beside extensive studies on their ‘carbon cousins’, the use of CNDs is still in its infancy. In particular, the electron donating properties of porphyrins has been combined with the electron accepting features of CNDs, for the first time. The formation of a charge transfer complex between nanodots and porphyrins, both in covalent and in supramolecular systems, has been probed by photophysical studies. In the last part, the first example of CNDs-based ionogels and their comprehensive characterization has been reported. NCNDs induce gel formation for non-gelating systems and modulate the properties of pure gels, for instance, exerting a positive influence on the rheological response of the gel phases. Moreover, their ability to self-repair after disruption has been showed, which is an important feature for future applications. Finally, it has been demonstrated that the dissolution of the NCNDs in the gel matrix enhances their antiradical activity.

Chapter 5 is dedicated to the engineering of CNDs with tailored properties. A rational synthetic design, by using properly designed functional units, has been proposed. Conscious that realizing real-world applications require time- and cost-effective procedures, a cost-

efficiency parameter has been used to guide the design of the synthetic procedures and the choice of the molecular precursors. To this aim, the desired nanodots were produced in only one synthetic step through a quick and controlled microwave heating of commercially available, or easy-to-synthesize, organic building blocks. In the first two sections, CNDs with customized emission have been approached. CNDs with emission from blue-white, to pure white and further to red-white have been described, resulting in tunable white emission, which could find applications according to requirements. Moreover green-emitting CNDs have shown positive effect on natural killer cells maturation process and activation, suggesting their high potential in bio-related applications. Then, the preparation of inherently chiral CNDs has been presented, together with their use as template for the induction of preferential chirality to porphyrin aggregates. Finally, it has been demonstrated that the use of properly designed dopants enables the preparation of CNDs with tunable redox properties.



Figure 1.2 Schematic representation of the work presented in this doctoral dissertation: design and preparation of tailored carbon nanodots for various applications. (Adapted from a design of Freepik).

1.3 References

- (1) *Louis Pasteur, in a Lecture, University of Lille (7 December 1854); Reported in Houston Peterson, A Treasury of the World's Great Speeches; 1954.*
- (2) Kroto, H. W.; Heath, J. R.; O'Brien, S. C.; Curl, R. F.; Smalley, R. E. C60: Buckminsterfullerene. *Nature* **1985**, *318*, 162–163.
- (3) Iijima, S. Helical Microtubules of Graphitic Carbon. *Nature* **1991**, *354*, 56–58.
- (4) Novoselov, K. S. Electric Field Effect in Atomically Thin Carbon Films. *Science* **2004**, *306*, 666–669.
- (5) X. Xu, R. Ray, Y. Gu, H.J. Ploehn, L. Gearheart, K. Raker, W. A. Scrivens. Electrophoretic Analysis and Purification of Fluorescent Single-Walled Carbon Nanotube Fragments. *J. Am. Chem. Soc.* **2004**, *126*, 12736–12737.
- (6) Geim, A. K.; Novoselov, K. S. The Rise of Graphene. *Nat. Mater.* **2007**, *6*, 183–191.
- (7) Eda, G.; Lin, Y.-Y.; Mattevi, C.; Yamaguchi, H.; Chen, H.-A.; Chen, I.-S.; Chen, C.-W.; Chhowalla, M. Blue Photoluminescence from Chemically Derived Graphene Oxide. *Adv. Mater.* **2010**, *22*, 505–509.
- (8) Yu, M. Strength and Breaking Mechanism of Multiwalled Carbon Nanotubes Under Tensile Load. *Science* **2000**, *287*, 637–640.
- (9) Wong, E. W. Nanobeam Mechanics: Elasticity, Strength, and Toughness of Nanorods and Nanotubes. *Science* **1997**, *277*, 1971–1975.
- (10) Treacy, M. M. J.; Ebbesen, T. W.; Gibson, J. M. Exceptionally High Young's Modulus Observed for Individual Carbon Nanotubes. *Nature* **1996**, *381*, 678–680.
- (11) Belin, T.; Epron, F. Characterization Methods of Carbon

- Nanotubes: A Review. *Mater. Sci. Eng. B* **2005**, *119*, 105–118.
- (12) Mizuno, K.; Ishii, J.; Kishida, H.; Hayamizu, Y.; Yasuda, S.; Futaba, D. N.; Yumura, M.; Hata, K. A Black Body Absorber from Vertically Aligned Single-Walled Carbon Nanotubes. *Proc. Natl. Acad. Sci.* **2009**, *106*, 6044–6047.
- (13) Kürüm, U.; Ekiz, O. Ö.; Yaglioglu, H. G.; Elmali, A.; Ürel, M.; Güner, H.; Mızrak, A. K.; Ortaç, B.; Dâna, A. Electrochemically Tunable Ultrafast Optical Response of Graphene Oxide. *Appl. Phys. Lett.* **2011**, *98*, 141103.
- (14) Dugan, L. L.; Lovett, E. G.; Quick, K. L.; Lotharius, J.; Lin, T. T.; O'Malley, K. L. Fullerene-Based Antioxidants and Neurodegenerative Disorders. *Parkinsonism Relat. Disord.* **2001**, *7*, 243–246.
- (15) Gharbi, N.; Pressac, M.; Hadchouel, M.; Szwarc, H.; Wilson, S. R.; Moussa, F. [60]Fullerene Is a Powerful Antioxidant in Vivo with No Acute or Subacute Toxicity. *Nano Lett.* **2005**, *5*, 2578–2585.
- (16) Imahori, H.; Mori, Y.; Matano, Y. Nanostructured Artificial Photosynthesis. *J. Photochem. Photobiol. C Photochem. Rev.* **2003**, *4*, 51–83.
- (17) D'Souza, F.; Deviprasad, G. R.; Zandler, M. E.; Hoang, V. T.; Klykov, A.; VanStipdonk, M.; Perera, A.; El-Khouly, M. E.; Fujitsuka, M.; Ito, O. Spectroscopic, Electrochemical, and Photochemical Studies of Self-Assembled via Axial Coordination Zinc Porphyrin–Fulleropyrrolidine Dyads. *J. Phys. Chem. A* **2002**, *106*, 3243–3252.
- (18) Baker, S. N.; Baker, G. A. Luminescent Carbon Nanodots: Emergent Nanolights. *Angew. Chem. Int. Ed.* **2010**, *49*, 6726–6744.
- (19) Lim, S. Y.; Shen, W.; Gao, Z. Carbon Quantum Dots and Their Applications. *Chem. Soc. Rev.* **2015**, *44*, 362–381.
- (20) Schoenlein, R. W.; Fujimoto, J. G.; Eesley, G. L.; Capehart,
-

- T. W. Femtosecond Studies of Image-Potential Dynamics in Metals. *Phys. Rev. Lett.* **1988**, *61*, 2596–2599.
- (21) Sun, Y.-P.; Zhou, B.; Lin, Y.; Wang, W.; Fernando, K. A. S.; Pathak, P.; Mezziani, M. J.; Harruff, B. A.; Wang, X.; Wang, H.; *et al.* Quantum-Sized Carbon Dots for Bright and Colorful Photoluminescence. *J. Am. Chem. Soc.* **2006**, *128*, 7756–7757.
- (22) Li, X.; Rui, M.; Song, J.; Shen, Z.; Zeng, H. Carbon and Graphene Quantum Dots for Optoelectronic and Energy Devices: A Review. *Adv. Funct. Mater.* **2015**, *25*, 4929–4947.
- (23) Hola, K.; Zhang, Y.; Wang, Y.; Giannelis, E. P.; Zboril, R.; Rogach, A. L. Carbon dots—Emerging Light Emitters for Bioimaging, Cancer Therapy and Optoelectronics. *Nano Today* **2014**, *9*, 590–603.
- (24) Shen, J.; Zhu, Y.; Yang, X.; Li, C. Graphene Quantum Dots: Emergent Nanolights for Bioimaging, Sensors, Catalysis and Photovoltaic Devices. *Chem. Commun.* **2012**, *48*, 3686–3699.
- (25) Li, H.; Kang, Z.; Liu, Y.; Lee, S.-T. Carbon Nanodots: Synthesis, Properties and Applications. *J. Mater. Chem.* **2012**, *22*, 24230–24253.
- (26) Luo, P. G.; Sahu, S.; Yang, S.-T.; Sonkar, S. K.; Wang, J.; Wang, H.; LeCroy, G. E.; Cao, L.; Sun, Y.-P. Carbon “quantum” dots for Optical Bioimaging. *J. Mater. Chem. B* **2013**, *1*, 2116–2127.
- (27) Roy, P.; Chen, P.-C.; Periasamy, A. P.; Chen, Y.-N.; Chang, H.-T. Photoluminescent Carbon Nanodots: Synthesis, Physicochemical Properties and Analytical Applications. *Mater. Today* **2015**, *18*, 447–458.
- (28) Zheng, X. T.; Ananthanarayanan, A.; Luo, K. Q.; Chen, P. Glowing Graphene Quantum Dots and Carbon Dots: Properties, Syntheses, and Biological Applications. *Small* **2015**, *11*, 1620–1636.
- (29) Zhao, A.; Chen, Z.; Zhao, C.; Gao, N.; Ren, J.; Qu, X. Recent
-

Advances in Bioapplications of C-Dots. *Carbon* **2015**, *85*, 309–327.

2 Nitrogen-Doped Carbon Nanodots

In this chapter a brief overview of the most common synthetic methodologies focusing on the two main approaches (top-down and bottom-up) for CNDs is presented. Then, a discussion on their optical properties, as well as the most common post-synthetic treatments aimed at the photoluminescence enhancement, is provided.

Finally, the preparation and characterization of highly fluorescent nitrogen-doped CNDs (NCNDs) through a facile bottom-up approach is reported. Moreover, preliminary experiments, in order to reveal their potential applications, are reported.

The structural characterization of NCNDs through NMR spectroscopy has been carried out by *Dr. Luka Dorđević* (University of Trieste, Italy). *Ms. Jennifer Gomez* and *Dr. Blanca Arnaiz* (University of Trieste, Italy and CIC biomaGUNE, San Sebastián, Spain) performed cytotoxicity and confocal microscopy imaging experiments. The project on NCNDs-LEDs has been done thanks to a collaboration with *Prof. Giuseppe Gigli* (CNR NANOTEC, Lecce, Italy), with the aid of *Dr. Fabrizio Mariano*.

Part of the work presented in this chapter has been published as “Synthesis, Separation, and Characterization of Small and Highly Fluorescent Nitrogen-Doped Carbon NanoDots” in *Angewandte Chemie Int. Ed.* **2016**, *128*, 2147-2152 and has been used for the preparation of the manuscript “Carbon NanoDots as New Nanocarriers for the Imagin-Guided-Delivery of Poorly Water-Soluble Antineoplastic Drugs”.

2.1 Introduction

2.1.1 Synthetic methods

Over the past few years a variety of synthetic methods for CNDs have been explored. They can be generally classified into two main categories, namely, top-down and bottom-up synthetic approaches. While the former route involves the breaking down of larger carbon structures, in the latter CNDs are formed from small molecular precursors (**Figure 2.1**).

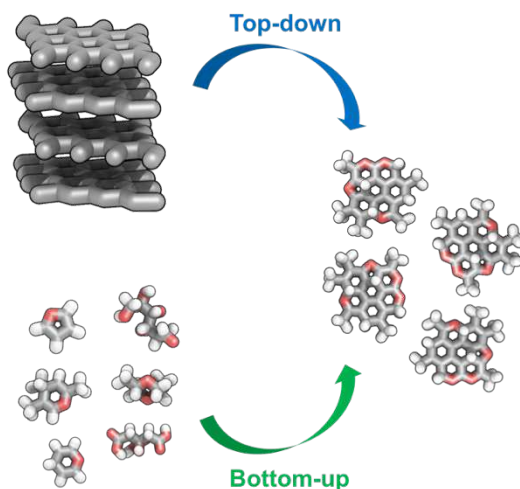


Figure 2.1 Schematic representation of top-down and bottom-up syntheses of CNDs.

Top-down methods mainly consist of arc discharge, laser ablation and electrochemical methods, using starting materials such as graphite powder or multi-walled carbon nanotubes (MWCNTs) (**Figure 2.2**).

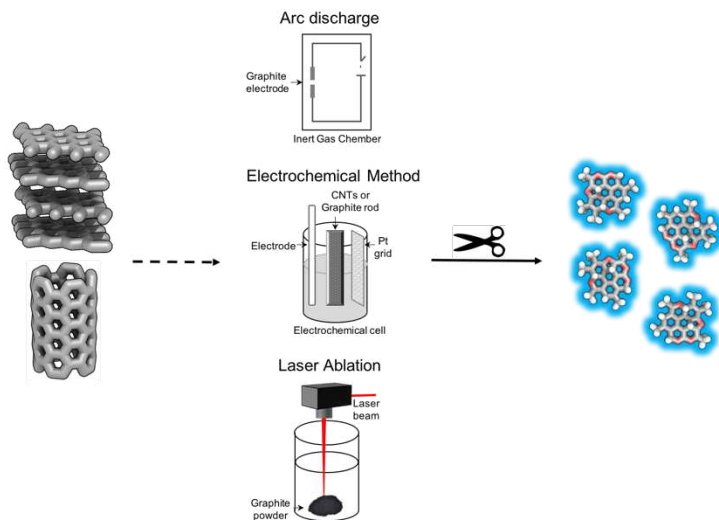


Figure 2.2 Common synthetic procedures for CNDs production using top-down approaches.

They have played an important role especially at the beginning, marking most of the pioneering works of CNDs.

In 2004, CNDs were discovered as fluorescent single-walled carbon nanotubes (SWCNTs) fragments, during the electrophoretic purification of SWCNTs derived from arc-discharge.¹ Arc-discharged soot was oxidized with nitric acid and then extract with basic water. During the purification of the as-obtained suspension through gel electrophoresis, it was observed the surprising presence of three class of materials, *i.e.* long nanotubes, a slow-moving dark band of nanotubes and fast-moving fluorescent band (**Figure 2.3a**). This fluorescent material was found to be a mixture of nanoparticles composed by carbon, hydrogen, oxygen and nitrogen atoms and was separated into three fractions having different emission colors under UV light (**Figure 2.3b**).

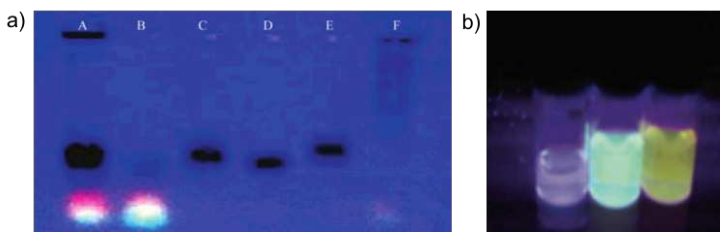


Figure 2.3 a) Electrophoretic profile in 1% agarose gel under 365 nm UV light: (A) crude SWCNTs suspension; (B) fluorescent carbon; (C) short tubular carbon; (D) and (E) further separation of (C); (F) cut SWCNTs; b) picture of different fractions of fluorescent carbon under 365 nm UV light.¹

This was the research that found the existence of dots and since then, these fluorescent nanoparticles have grabbed the attention of many researchers.

Few years later, the first electrochemical preparation of blue luminescent carbon nanocrystals was reported.² Luminescent spherical-shaped materials were obtained through the electrochemical cleavage of MWCNTs grown on a carbon paper, in a degassed acetonitrile solution containing tetrabutylammonium perchlorate as a supporting electrolyte and by applying cycling potentials ranging from -2.0 to 2.0 V.

Later on, the use of low-cost and readily available graphite as a carbon source was reported.³⁻⁶ Interestingly, it was found that different carbon nanomaterials, including fluorescent carbon nanoparticles, can be formed using an ionic liquid-assisted electrochemical exfoliation of graphite (**Figure 2.4a**). The exfoliation mechanism involves the interplay of the anionic intercalation in the graphite planes from the ionic liquids (ILs) and the anodic oxidation of water. Hydroxy and oxygen radicals, as well BF_4^- play the role of intercalators in the graphitic planes. Tuning of the ILs/water ratio affects the exfoliation mechanism changing the shape and size

distribution of the exfoliated products. High ILs content facilitates the intercalation process by BF_4^- , which leads to the expansion of graphene anode and its oxidative cleavage in nanoribbons. While by increasing the water/ILs ratio, a large concentration of hydroxy and oxygen radicals oxidize the graphite anode that is dissolved as fluorescent carbon nanoparticles. As shown in **Figure 2.4b**, upon dipping a graphite rod into the ionic liquid mixture and applying a voltage for 240 minutes, the carbon nanomaterial is dissolved and the rod expanded. When the expanded graphite rod is dip into DMF a strong blue fluorescence coming from the dots present in solution can be seen.³

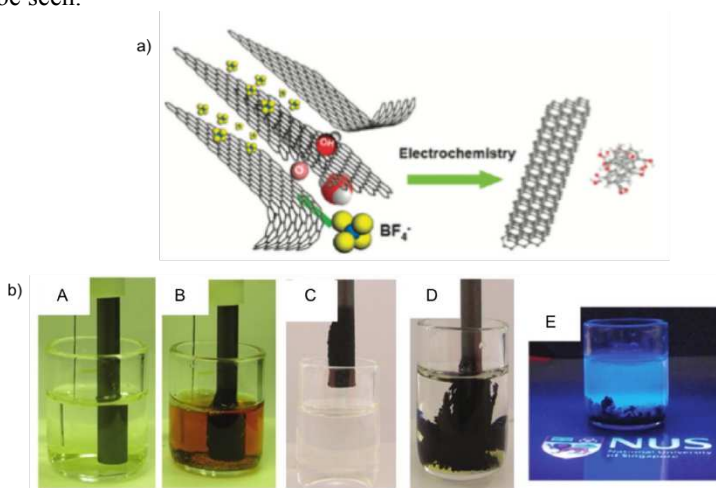


Figure 2.4 a) Illustration of the exfoliation process showing the attack of the graphite edge planes by hydroxy and oxygen radicals, which facilitate the intercalation of BF_4^- anion. The dissolution of hydroxylated carbon nanoparticles gives rise to the fluorescent carbon nanoparticles. Oxidative cleavage of the expanded graphite produces graphene nanoribbons; b) graphite rod exfoliated in IL- $\text{BF}_4^-/\text{water}$ (40:60 v/v) mixture solution: (A,B) color change of the electrolyte solution with the corrosion of the graphite rod; (C) the expanded graphite rod is immersed into DMF; (D) the

expanded portion of the anodic graphite rod is exfoliated in DMF; (E) the supernatant solution emits blue fluorescence upon irradiation with 254 nm UV light.³

It was in the first report of Sun *et al.*, describing for the first time the laser ablation of a carbon source as possible production route, that these small and fluorescent nanoparticles were named as they are currently known.⁷ The ablation of a mixture of graphite powder and cement with a Q-switched Nd:YAG laser, in the presence of water vapor and with argon as carrier gas, resulted in the formation of dots. However, they showed luminescence emission with quantum yields between 4-10% only upon post-synthetic surface passivation with diamine-terminated oligomeric poly(ethylene glycol).

Nevertheless, the above-described top-down methods are usually limited by the need of severe synthetic conditions, complex processes and expensive starting materials.

In this context, bottom-up syntheses provide more accessible and cost-effective processes by applying external energy as heating and microwave or template-assisted synthesis, through the possible use of facile experimental set-up and inexpensive starting materials.

Heating treatments can be generally classified in hydrothermal and solvothermal carbonization. They led to processes of condensation, polymerization and aromatization that result in the formation of larger structures.

Hydrothermal synthesis implies the use of an aqueous medium over 100 °C and 0.1 MPa. It provides low toxicological impact of materials and processes, and has been widely used for the synthesis of various carbon materials in the last century.^{8,9}

The use of hydrothermal conditions results in increased or changed solubility of the reagents, improves their physical and chemical interactions and facilitates the final formation of the carbonaceous structures. The hydrothermal process at high temperatures (between

300 and 800 °C) is a well-established production method for materials with high carbon content, such as carbon nanotubes or graphitic carbon materials. Instead, when the carbonization is performed at low temperatures (below 300 °C), the resulting materials present typically various surface functional groups and C-H-O structures. This latter process has been recently widely explored for CNDs synthesis and usually the formation of CNDs soluble in aqueous media is accomplished.

A variety of small organic molecules were used to prepare nanodots. Considerable research efforts have been focused on preparing CNDs from inexpensive and biocompatible starting materials, such as citric acid, ascorbic acid and saccharides (**Figure 2.5**).^{10–15} Moreover, conversion of biodegradable waste into value-added products is an essential topic in the field of green chemistry and has recently grabbed the attention of many researchers in the CNDs framework. Some examples include the hydrothermal treatments of orange, strawberry or banana juices or coffee grounds,^{16–19} which usually results in the formation of blue emissive CNDs (**Figure 2.5**).

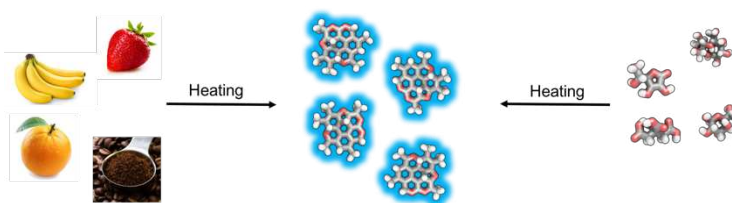


Figure 2.5 Common starting materials for CNDs production using bottom-up approaches.

The reaction media could impart different properties on the final CNDs. In a representative example, the carbonization of citric acid at 300 °C for 3 hours resulted in oil- or water-soluble CNDs depending on the reaction solvent and capping agent. While the use of

octadecene and 1-hexadecylamine as non-coordinating solvents and surface passivation agents resulted in CNDs soluble in common non-polar solvent with QY of 53%, water soluble CNDs with QY of 17% were produced using glycerin and polyethylene glycol (PEG₁₅₀₀).²⁰

Hard or soft-templating effects have shown powerful capability for CNDs with narrow size distribution and for avoiding aggregation phenomena. Uniform and controlled pore sizes make mesoporous silica an ideal host for growing nanoparticles with narrow size distribution. Water soluble CNDs showing blue luminescence (QY 23%) and narrowly size distribution (1.5-2.5 nm) were prepared by using an impregnation method with mesoporous silica spheres as hard-template and citric acid as precursor.²¹ However the preparation of mesoporous silica with highly ordered pores is usually hard and it was reported that the simultaneous presence of micelles of the copolymer Pluronic P123 and carbon precursors in the pores allows a better size control of the final CNDs (**Figure 2.6a**).²²

Alternatively, surfactant-modified silica nanospheres were used as carriers, providing anchors for the polymerization of the carbon precursors (resols) in solution, and also preventing the aggregation of the CNDs during pyrolysis (**Figure 2.6b**).²³

Microwave methods have been emerged as powerful synthetic routes for CNDs and have been widely used.^{12,14,24-27} Microwave heating can address problems of conventional heating process for the preparation of nanomaterials, such as the heating inhomogeneity, which usually results in broadened size distributions especially in large-scale reactions. In such context, microwave technique has become an increasingly popular method for the synthesis of nanomaterials, since the first report of microwave-assisted synthesis in 1986.²⁸ Microwaves are a form of electromagnetic energy with frequencies in the range of 300 MHz to 300 GHz. Materials, be they solvents or reagents, can absorb microwave energy and convert it to heat.

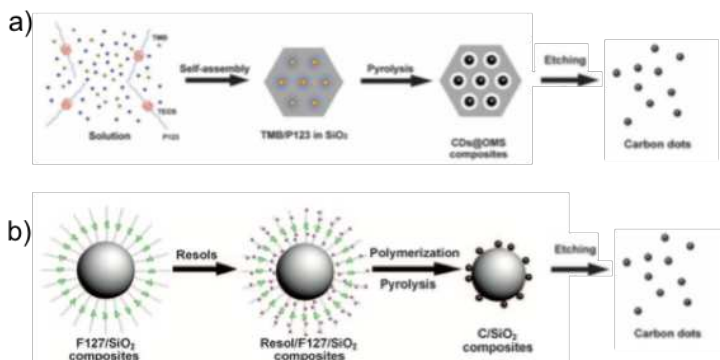


Figure 2.6 Processing diagram of a) the soft-hard template approach toward CNDs using 1,3,5-trimethylbenzene (TMB) as carbon source, pluronic P123 as soft template and ordered mesoporous silica (OMS) as hard template; b) the synthesis of CNDs using polymer/F127/silica composites as carriers for resols.^{22,23}

Interactions between materials and microwaves are based on two specific mechanisms: dipole interactions and ionic conduction. Dipole interactions occur with polar molecules. The polar ends of a molecule tend to re-orient themselves and oscillate in step with the oscillating electrical field of the microwaves. Heat is generated by molecular collision and friction. Generally, more polar is a molecule, more effectively it is coupled with the microwave field. Ionic conduction is only minimally different from dipole interaction. Ions in solution do not have a dipole moment. They are charged species distributed in solution and can couple with the oscillating electrical field of microwaves. The concentration of ions in solution often significantly affects the efficiency of microwave heating of an ionic solution. Because of its high energy efficiency, microwave irradiation offers a clean, cheap, and convenient method of heating, which often results in a higher yield and shorter reaction time. Moreover, it can lead to important advancement in large-scale production of high-quality nanomaterials, since provide scaled-up processes with a

uniform nucleation environment.

The role of water as a solvent in microwave-assisted organic syntheses has risen dramatically because of the interest in ecofriendly processes in Green Chemistry. As a result, microwave-assisted hydrothermal method has become a very important production process for CNDs, since it combines both the advantages of hydrothermal and microwave techniques. Many parameters may affect the growth of the CNDs. The final CNDs dimensions, as well as their optical properties strongly depend on the microwave power and heating time. For example, in a facile and economical synthesis, different amounts of PEG₂₀₀ and saccharides were added to distilled water to form a transparent solution. The solution was then heated in a 500 W microwave oven for several minutes and, with increasing reaction time, the solution changed from colorless to yellow (sample A in **Figure 2.7**), and finally to dark brown (sample B in **Figure 2.7**), which implied the formation of CNDs. The size of these CNDs was tuned to 2.75 ± 0.45 (sample A) and 3.65 ± 0.6 nm (sample B) by employing heating times of 5 or 10 minutes, respectively.¹⁴

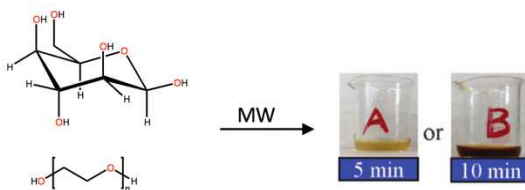


Figure 2.7 Microwave-assisted synthesis by employing heating times of 5 or 10 minutes (A or B on the right, respectively).

However, most of the CNDs microwave syntheses are carried out exploiting domestic microwave ovens and are poorly reproducible. Indeed, with a domestic microwave system, the reactions are hard to

control since it is very difficult to accurately measure the temperature and the microwave power.

2.1.2 Photophysical properties

A discussion about the possible origin of CNDs photoluminescence was included in *Chapter 1*. Therefore, this section gives mostly a supplementary overview functional to the introduction of the fundamental approaches for photoluminescence enhancement.

CNDs typically show strong optical absorption in the UV region, with a tail extending to the visible range. Most have an absorption band around 260–320 nm, and the positions of UV absorption peaks of CNDs prepared by different methods and/or precursors are quite different.

From a fundamental and an application viewpoint, photoluminescence is one of the most fascinating features of CNDs. The majority of the CNDs synthesized so far exhibit blue PL emission and one unique property is the excitation wavelength-dependence of the emission wavelength and intensity (**Figure 2.8**).

Generally, CNDs have quantum yields around 10% and higher values are needed in order to rival their semiconductor counterparts and extend their application in many areas.

Doping and surface passivation are the most common methods to improve the functionality of CNDs.

Surface passivation consists in the introduction of a thin insulating layer on the bare CNDs surface. Usually, polymeric materials are used, such as polymeric PEG. Passivation by the organic moieties renders the surface state sites more stable facilitating a more effective radiative recombination.^{29,30}

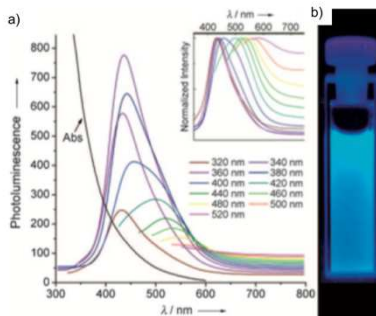


Figure 2.8 a) UV-Vis absorption and photoluminescence emission spectra (recorded for progressively longer excitation wavelengths from 320 to 520 nm in 20 nm increments) of CNDs in water. In the inset, the emission spectral intensities are normalized; b) photograph obtained under excitation at 365 nm.²³

Sun *et al.* first reported the use of diamine-terminated oligomeric poly (ethylene glycol) $\text{H}_2\text{NCH}_2(\text{CH}_2\text{CH}_2\text{O})_n\text{-CH}_2\text{CH}_2\text{CH}_2\text{NH}_2$ (average $n \sim 35$, PEG_{1500N}) to increase the emission QYs of CNDs produced via laser ablation from 4% to more than 10%, as a result of surface energy traps stabilization upon passivation.⁷ Moreover, QYs around 55% can be achieved through a more rigorous control of the surface passivation step, as well as the purification process, or doping with inorganic salts, such as ZnO or ZnS, before their surface passivation.^{31,32} On the other hand, the treatment with nitric acid of commercially activated carbon source (coal, wood, and wood activated carbon),³³ or saccharide dehydration with concentrated sulfuric acid,³⁴ followed by further passivation with amine-terminated compounds that led to low-cost production of CNDs with QY of around 10%.

More convenient strategies based on the simultaneous synthesis and surface modification were reported.^{35,36} Passivated CNDs were produced via laser ablation of graphite powders and the use of PEG_{200N} as reaction medium, instead of water, results in a luminescent

emission (QY 5%) otherwise not visible (**Figure 2.9a**).³⁵ Alternatively, the use of citric acid (CA) as carbon source and hyperbranched polyethyleneimine (PEI) as surface passivation agent, through hydrothermal route, results in passivated CNDs with QY of 24% (**Figure 2.9b**).³⁶

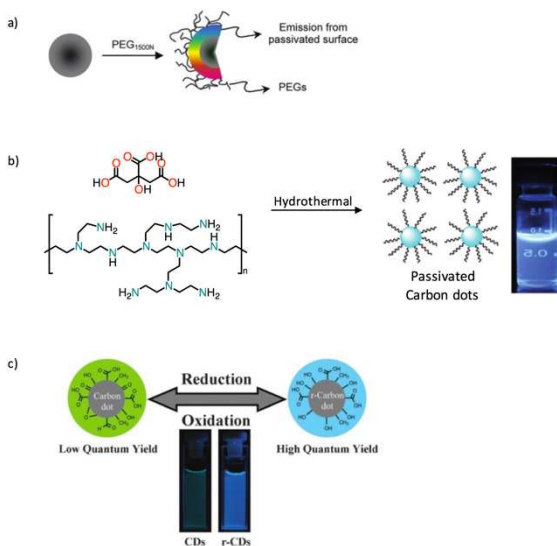


Figure 2.9 Passivated CNDs using a) poly(ethylene glycol) (PEG_{200N}) as reaction medium³⁵ and b) hyperbranched polyethyleneimine (PEI) as precursors;³⁶ c) CNDs with improved optical performance through the chemical reduction by NaBH₄.³⁷

Although surface passivation is considered the most applicable and efficient method for CNDs with improved optical performance, it was reported that the chemical reduction by NaBH₄ could enhance the fluorescence emission.^{37,38} CNDs produced by hydrothermal method and then reduced, have a decreased carbonyl groups content and an increased sp³-type defective sites number that favors the QY enhancement to 40% (**Figure 2.9c**).³⁷ Moreover, it was demonstrated

that doping could enhance the CNDs optical properties and nitrogen is the typical dopant used. Using bottom-up approaches, heteroatoms can be inherited from precursors during synthesis avoiding further modifications steps, and thus offering a particularly promising strategy.

Nitrogen-doped CNDs (NCNDs) with QY around 14% were synthesized in a single-step reaction under mild conditions (heating at 70 °C overnight) with 2-azidoimidazole as starting material.³⁹ On the other hand, molecules containing primary amines allow simultaneous nitrogen doping and surface passivation during the synthetic process. For instance, in the case of CNDs prepared through a solvothermal treatment of CCl₄, the fluorescence was enhanced from 10% up to 36% by nitrogen doping using different diamines instead of glycol.⁴⁰ In this context, amino acids are ideal carbon and nitrogen sources for CNDs owing to their low cost and abundance.⁴¹ However, the nitrogen doping effect on the CNDs fluorescence could not be easily generalized. While, high nitrogen content led to higher emission in some cases,⁴¹ it was also observed that the different nitrogen types might have different influence on their fluorescence property. For instance, it was reported that quantum yields correlate with the ratio of pyrrolic and pyridinic nitrogen atoms, suggesting that the protonation of amino groups prevents electron transfer in the excited state improving the fluorescence recovery from local emissive states.⁴⁰

2.1.3 Aim of the project

The aim of this project is to develop a simple bottom-up method for high-quality CNDs without the need of sophisticated equipment and/or additional surface passivation.

To this end, we investigated the use of arginine and ethylenediamine as carbon and nitrogen sources. Amino acids are ideal carbon and

nitrogen sources for CNDs owing to their low cost and abundance. Moreover, molecules containing primary amines allow simultaneous nitrogen doping and surface passivation during the synthetic process. Due to the outstanding advantages discussed in the introduction, we used the microwave-assisted synthetic approach. Aiming at a high reproducibility, we employed a MW reactor under controlled conditions.

Finally, preliminary results on their cytotoxicity, cell uptake and imaging capability, as well as their employment for LEDs fabrication are reported, in order to shed light on their potential applications.

2.2 Preparation of NCNDs

2.2.1 Synthesis

Nitrogen-doped carbon nanodots (NCNDs) were prepared via MW-assisted hydrothermal synthesis by using Arginine (Arg) and ethylenediamine (EDA) as carbon and nitrogen sources (**Figure 2.10**).

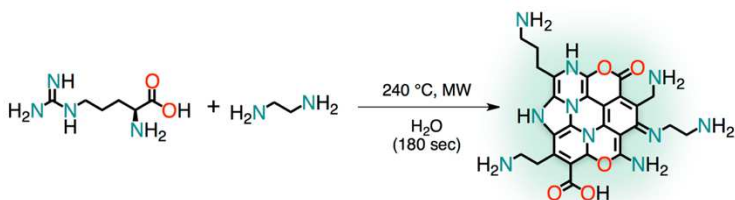


Figure 2.10 Reaction scheme for NCNDs. NCNDs are drawn as a tentative representation of a structural unit.

The MW parameters were optimized to obtain the desired properties of the final material, in terms of optical performance. Appropriate viscosity and temperature control are needed for a uniform carbonization process that leads to the formation of NCNDs. Fluorescent NCNDs were obtained at 240 °C, 377 psi, 200 W with a MW heating time of 180 seconds using water as reaction medium (see experimental section for details).

The heterogeneous solution underwent thermal carbonization of the precursors and led to nucleation. Finally, the nuclei grew by diffusion of other molecules towards the surface of the nanoparticles. In the process of microwave heating, the solution changed color from transparent to dark brown as a result of the formation of NCNDs (**Figure 2.11**).

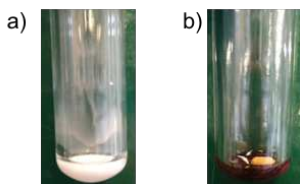


Figure 2.11 Photographs of the vials a) before and b) after the heating process.

Large carbon nanoparticles were removed by filtration and the yellow solution was dialyzed against Milli-Q water. The obtained NCNDs (26% yield based on weight) exhibited a high solubility in water (up to 80 mg/mL) and also in common polar organic solvents.

Alternatively, the crude mixture of NCNDs produced after MW treatment was separated by means of low pressure size exclusion chromatography using a column packed with Sephadex LH-20 and operating at a pressure of 150 psi. According to their elution time, we collected three fractions, named NCNDs1 (19% yield based on weight), NCNDs2 (10% yield based on weight) and NCNDs3 (11% yield based on weight).

2.2.2 Morphological and structural characterization

Atomic force microscopy (AFM) confirmed the round shape and showed that NCNDs have a rather homogeneous size distribution. AFM images, height profiles and size distributions of the three fractions NCNDs1, NCNDs2 and NCNDs3 are reported in **Figure 2.12**. By statistical analysis of the height of about one hundred nanoparticles, we determined an average size of 2.47 ± 0.84 (FWHM: 1.977). Average sizes of 2.65 ± 0.48 (FWHM: 1.141), 2.04 ± 0.57 (FWHM: 1.345), 1.24 ± 0.43 (FWHM: 1.013) were determined for NCNDs1, NCNDs2 and NCNDs3, respectively. These are among the smaller CNDs ever reported.^{42,43}

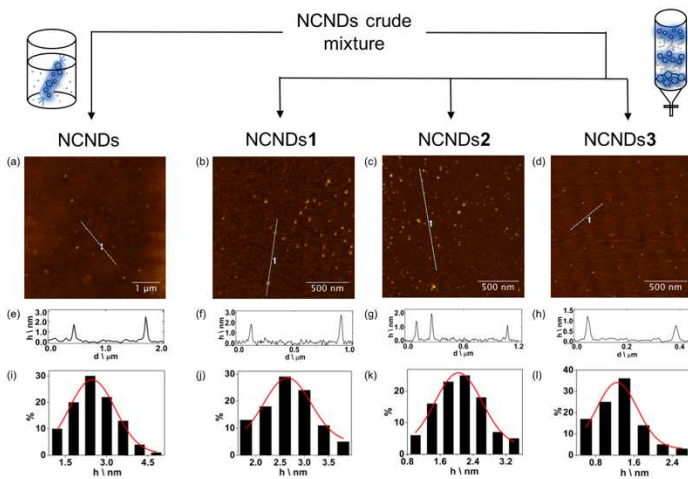


Figure 2.12 a-d) Tapping mode AFM images of NCNDs ($5.0 \times 5.0 \mu\text{m}$) and NCNDs1-3 ($1.7 \times 1.7 \mu\text{m}$) on a mica substrate; e-h) height profiles of NCNDs and NCNDs1-3; i-l) size histograms of NCNDs and NCNDs1-3 with curves fit to the data using a Gaussian model.

In order to gain unprecedented structural information, we report extensive NMR studies on carbon nanodots.

For this purpose, we prepared ^{13}C -enriched NCNDs (N^{13}CNDs) for ^{13}C -NMR investigations, starting with fully ^{13}C -enriched Arg and EDA. First of all, the contribution of each component was evaluated, using separated and combined ^{13}C -Arg and ^{13}C -EDA (**Figures 2.13, S2.2, S2.5**). **Figure 2.13-top** shows the ^{13}C -NMR spectrum of NCNDs produced using only ^{13}C -enriched Arg. It is clear that the aromatic core and the aliphatic, as well as the carbonyl regions, mainly originate from Arg. While EDA mostly contributes to the typical region of aliphatic carbon atoms connected to heteroatoms, signals arising from EDA were also found in the aromatic core of N^{13}CNDs .

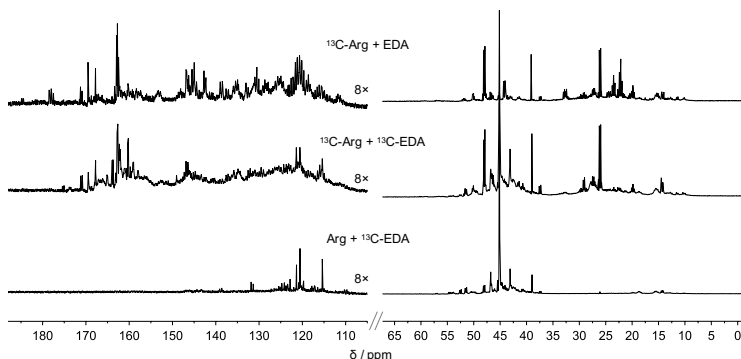


Figure 2.13 ^{13}C -NMR spectra of N^{13}CNDs prepared starting from ^{13}C -Arg and EDA (top), ^{13}C -Arg and ^{13}C -EDA (middle), and Arg and ^{13}C -EDA (bottom). The intensity of the aromatic region was increased 8.0 times to facilitate the visualization.

A tentative interpretation of a representative structural unit of NCNDs is reported in **Figure 2.14**, with a very general peak assignment. Typically, ^{13}C -NMR spectra of N^{13}CNDs consist of an aliphatic region (**Figure 2.14**, C_a), with carbon atoms connected to heteroatoms (**Figure 2.14**, C_b) or to an aromatic core (**Figure 2.14**, C_c) and an aromatic region (**Figure 2.14** C_{d-h}).

Additional bidimensional experiments (^1H - ^{13}C) revealed numerous H-C correlations both by direct (HSQC, **Figure 2.15** H_a - C_a H_b - C_b H_c - C_c , **Figures S2.6**, **S2.7**) or through multiple-bond correlations (HMBC, **Figure 2.16** H_a - C_b - C_c H_c - C_d - C_e , **Figures S2.8**, **S2.9**). Remarkably, protons that lie in the aliphatic region and close to heteroatoms were found to correlate with the aromatic sp^2 -carbon core (**Figure 2.14**, red lines). Analogous data was obtained from ^{13}C - ^{13}C one bond correlation (INADEQUATE, **Figure 2.17** C_a - C_c C_c - C_d C_f - C_g - C_h **Figures S2.10**, **S2.11**). Additionally, Diffusion-Ordered Spectroscopy (DOSY, **Figure 2.18**) was performed through ^1H - ^{13}C

multiple-bond correlation in order to unambiguously assign the signals to macromolecular species.

^{15}N -NMR preliminary experiments were also performed, but they were not as informative as the ^{13}C -NMR spectra (**Figure S2.12**).

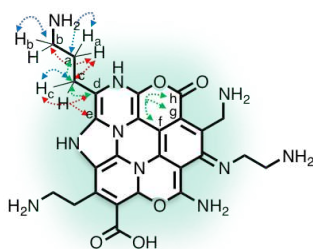


Figure 2.14 Representative structural correlations found in NMR experiments of N^{13}CNDs reported in dashed arrows (HSQC blue lines, HMBC red lines, and INADEQUATE green lines).

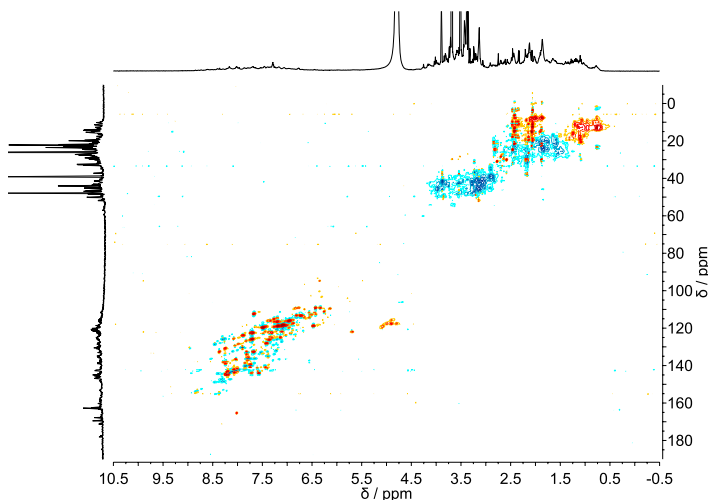


Figure 2.15 HSQC spectra of N^{13}CNDs prepared starting from ^{13}C -Arg and EDA (scan t1 increment = 16, t1 increments = 256, one-bond J_{1xh} = 146.0 Hz).

2 Nitrogen-Doped Carbon Nanodots

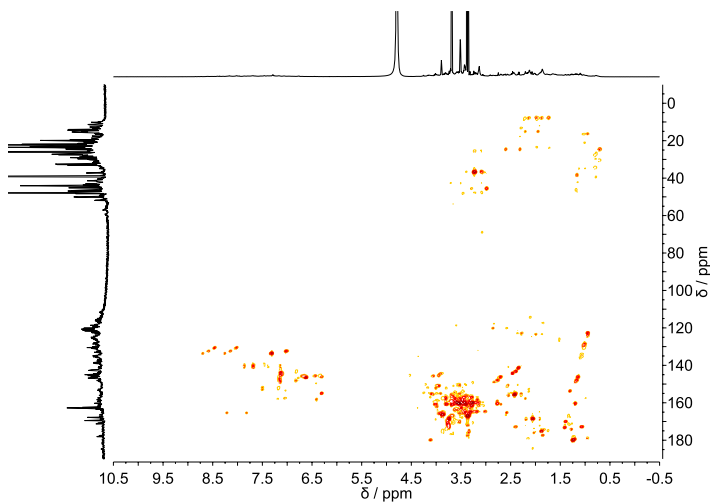


Figure 2.16 HMBC spectra of N^{13}CNDs prepared starting from ^{13}C -Arg and EDA (scan t_1 increment = 16, t_1 increments = 400, one-bond $J_{\text{NCH}} = 8.0$ Hz).

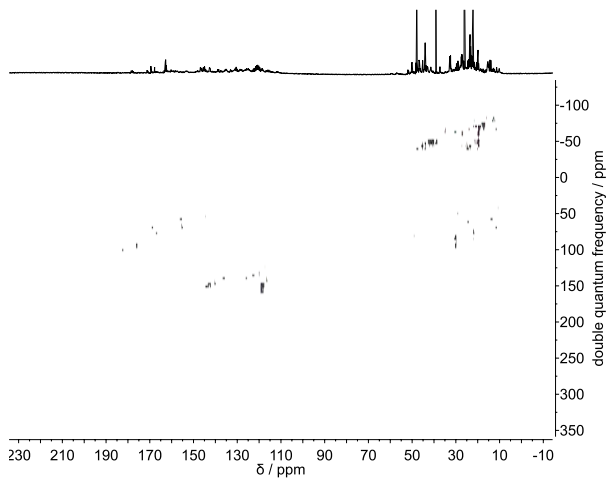


Figure 2.17 INADEQUATE spectra of N^{13}CNDs prepared starting from ^{13}C -Arg and EDA (scans = 256, $J = 55$ Hz).

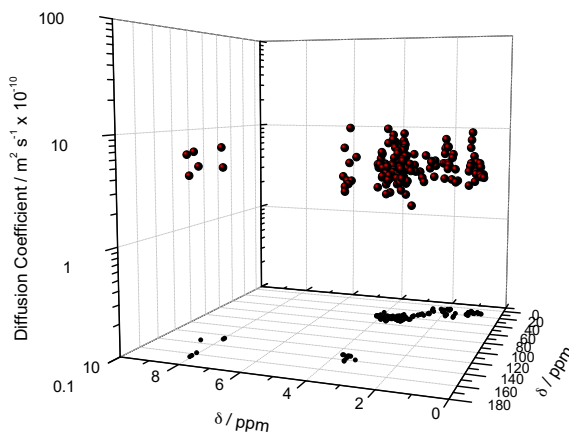


Figure 2.18 3D-DOSY spectra of $N^{13}CNDs$ prepared starting from ^{13}C -Arg and EDA.

The structure and composition of the NCNDs, as well as the separated NCNDs1-3, were determined by FT-IR spectroscopy and X-ray photoelectron spectroscopy (XPS).

The FT-IR spectrum (**Figure 2.19**) show that NCNDs have many oxygenated functional groups on their surface such as carboxylic acid, epoxy, alkoxy, hydroxyl and carbonyl groups. Absorptions at 1194 and 1111 cm^{-1} can be attributed to C-O-C bond, while absorptions at 1350 and 1318 cm^{-1} confirm the presence of C-O bonds. Moreover, the absorption peaks at 1655 , 1704 and 1767 cm^{-1} are indicative of C=O bonds, whereas the broad peak centered at 3299 cm^{-1} revealed O-H/N-H bonding. In addition, C-N (1492 and 1437 cm^{-1}) and C=N (1557 cm^{-1}) functional groups can be identified, while peaks at 2932 and 2862 cm^{-1} are related to the C-H bond stretching vibrations.

The separated NCNDs1, NCNDs2 and NCNDs3 have similar IR spectra, suggesting a similar functional group distribution (**Figure 2.20**).

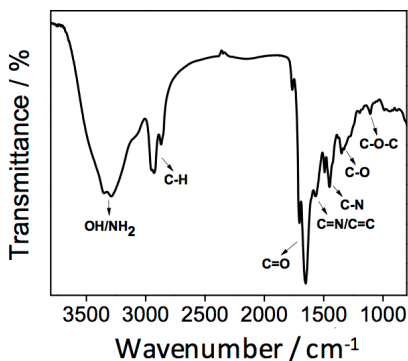


Figure 2.19 FT-IR spectrum of NCNDs.

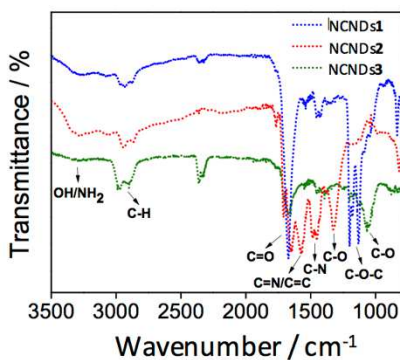


Figure 2.20 FT-IR spectra of NCNDs1-3.

To further confirm the functional groups present on the surface of NCNDs, XPS characterization was carried out.

From the full-scan XPS spectra of all the nanodots (**Figures 2.21, S2.13**) C, N, O are detected. **Figure 2.21** show the survey of NCNDs with peaks at 286.8 eV (C1s), 400.33 eV (N1s), and 532.34 eV (O1s). To determine the C and N configurations in the nanodots, C1s and N1s spectra were analyzed (**Figures 2.22, 2.23**). The C1s spectrum of NCNDs can be deconvoluted into five surface components

corresponding to sp^2 (C=C) at 284.5 eV, sp^3 (C-C, and C-H) at 285.5 eV, C-O/C-N at 286.2 eV, C=O/C=N at 288.3 eV, as well as COOH at 290.5 eV (**Figure 2.22a**). The N1s spectrum of NCNDs can be deconvoluted into four peaks centered at 398.3, 399.6, 400.5, 401.9 eV corresponding to C=N, NH_2 , C-N-C and $N-C_3$ respectively (**Figure 2.22b**).⁴⁴⁻⁴⁶

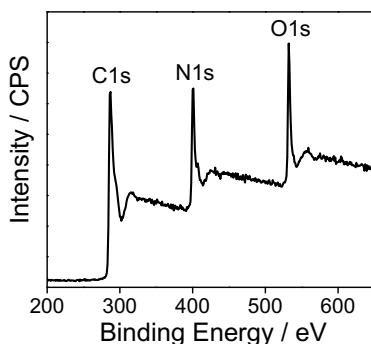


Figure 2.21 XPS survey of NCNDs.

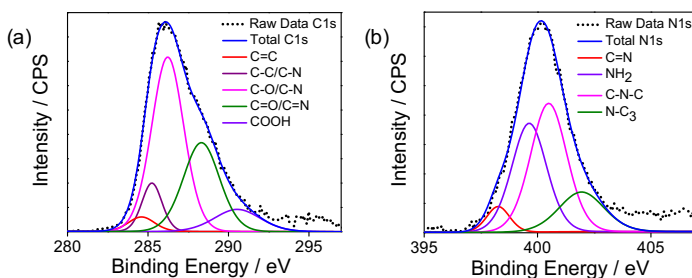


Figure 2.22 Deconvoluted a) C1s and b) N1s spectra of NCNDs.

The XPS data for NCNDs1-3 are showed in **Figure 2.23**, and along with that of NCNDs are collected in **Table 2.1**. The results show that all the NCNDs contain similar multiple oxygen and nitrogen

functional groups on particle surface but with different contents, a result which is consistent with the FT-IR measurements.

The surface components of NCNDs, as determined by XPS, are in good agreement with the FT-IR and NMR results. The presence of primary amino groups was confirmed by a positive Kaiser test. From this highly sensitive colorimetric test, it was possible to estimate a value of 1350 $\mu\text{mol/g}$ of amino groups: their presence makes NCNDs prompt to the easy insertion of further functional groups and/or interesting molecules/ions through standard organic chemistry protocols.

Table 2.1 Percentages of C, N, and O atoms in NCNDs and NCNDs1–3, as determined by XPS measurements.

Entry	NCNDs	NCNDs1	NCNDs2	NCNDs3
C%	68.0	65.9	68.7	63.9
C=C	3.4	21.7	4.1	15.8
C-C	8.7	25.1	25.6	6.4
C-O C-N	50.1	28.2	53.0	56.2
C=O C=N	28.7	24.9	14.7	21.6
COOH	9.1		2.5	
N%	16.1	11.1	9.0	7.0
C=N	5.4		10.6	
NH ₂	35.0	40.6	20.4	17.8
C-N-C	43.1	46.7	57.1	70.7
N-C3	16.5	12.7	11.9	11.4
O%	15.9	23.0	22.3	29.0

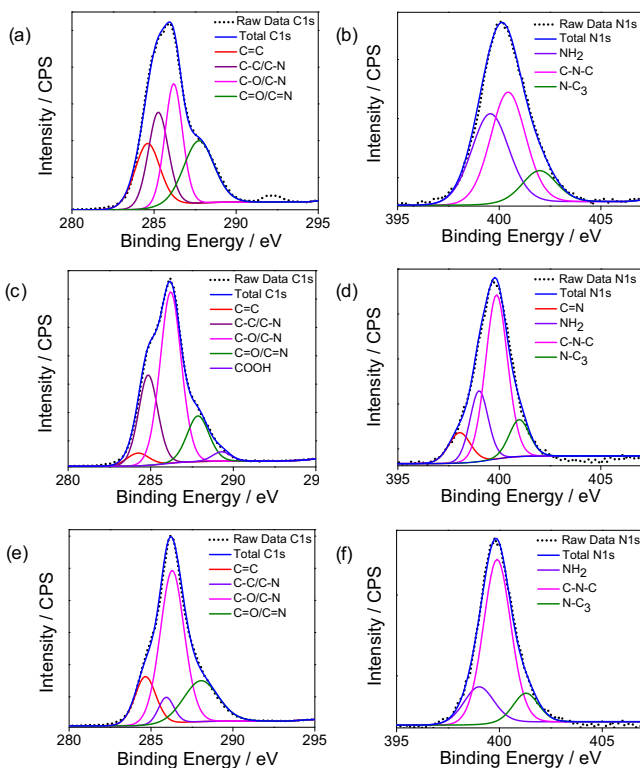


Figure 2.23 a,b) Deconvoluted C1s and N1s spectra of NCNDs1; c,d) deconvoluted C1s and N1s spectra of NCNDs2; e,f) deconvoluted C1s and N1s spectra of NCNDs3.

The cyclic voltammogram of NCNDs shows two irreversible peaks corresponding to the oxidation (+1.14 V vs SCE) and reduction (-2.52 V vs SCE) of amines (**Figure 2.24**). The high current in oxidation and the steep slope of the peak are remarkable, demonstrating the easy way to oxidize a high quantity of amino groups on the surface.

The functional groups located at the surface of NCNDs act as a “passivation” layer, which improves their hydrophilicity and stability in aqueous systems as well as their efficient photoluminescence

properties.⁴⁷ The aqueous solutions (0.5 mg/mL) of NCNDs appeared yellow in daylight and remained stable for several weeks, with no change in their spectral features.

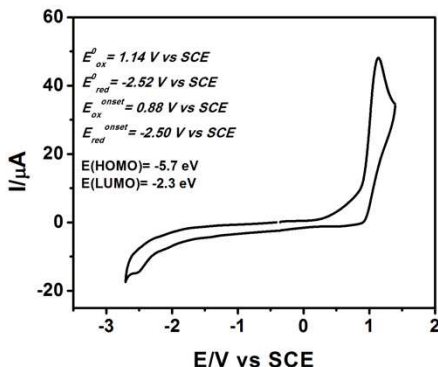


Figure 2.24 CV of NCNDs 1 mg/mL in DMF using TBAPF₆ as supporting electrolyte on GC. Scan rate 100 mV/s.

2.2.3 Photophysical characterization

Upon excitation under a 365 nm UV lamp, NCNDs emit with strong blue luminescence, while the UV-Vis spectrum of ap-NCNDs show an absorption band at 286 nm, ascribed to the $\pi-\pi^*$ transition of the conjugated C=C units from the carbon core (**Figure 2.25a**).^{7,43}

Spectrally broad FL emission, with excitation wavelength dependence, is a common phenomenon observed in CNDs.^{47,48} CNDs produce multi-fluorescence colors under different excitation wavelengths and this behavior may arise not only from particles of different size, but also from a distribution of different emissive domains on each carbon dots. This property implies that the emission of CNDs can be tuned by changing the excitation wavelength since the emission arises from different surface emissive traps. The luminescence properties of the NCNDs have been explored. A broad

emission peak at 356 nm is observed when the sample is excited at the optimal excitation wavelength (300 nm, **Figure 2.25b**). The fluorescence peaks shift from 356 nm to 474 nm when the excitation wavelength changes from 300 to 420 nm and the fluorescence intensity decreases as the peak red shifts.

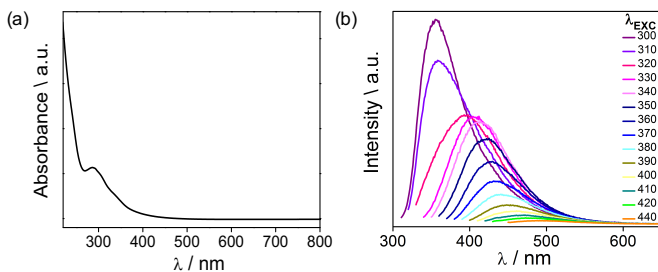


Figure 2.25 a) UV-Vis absorption spectrum of NCNDs in water; b) FL spectra of NCNDs in water (298 K) at different excitation wavelengths.

The many kinds of functional groups presented on the surface of NCNDs have different surface states energy levels, which results in a series of emissive traps that dominate the emission at different excitation wavelengths and explain the excitation wavelength dependent phenomenon of NCNDs. The fluorescence quantum yield (FLQY) was found to be 17%, using a reported procedure and quinine sulphate as the reference (see experimental section for details).^{49,50}

As expected, size and functional groups affect the optical properties. **Figure 2.26** shows NCNDs1-3 UV-Vis absorption spectra. NCNDs1 have an absorption peak located at 315 nm, while NCNDs2 have two peaks at 285 and 315 nm and NCNDs3 have three peaks at 253, 278, and 328 nm. These peaks are most probably related to the electron transitions from π (or n) to π^* of C=C and C=O.^{7,43} Typically, as the particles become smaller, the luminescence energies are blue shifted to higher energies.⁵¹ However, the FL mechanism of CNDs is affected

also by zigzag edge sites and defects effect. Hence, size-independent FL could be also observed because the surface state emission can play a predominant role in the FL properties.⁵² NCNDs1-2 show a clear excitation-dependent emission spectra, whereas NCNDs3 exhibit an almost excitation-independent behavior. Each sample has its optimal emission for a characteristic excitation wavelength, revealing the presence of different energy levels corresponding to the maximum transition probability (**Figure 2.26**). The surface of NCNDs significantly affects the FL properties since it determines the trapping of excitons under excitation.

Therefore, the radiative recombination of surface-trapped excitons leads to FL with the corresponding energy. NCNDs1, NCNDs2 and NCNDs3 exhibited their most intense emission at 380 nm (excitation at 320 nm), 357 nm (excitation at 300 nm), 421 nm (excitation at 340 nm), respectively.

The FLQYs of NCNDs1, NCNDs2 and NCNDs3 were 7%, 31% and 46%. To the best of our knowledge, the latter is among the highest FLQY values so far reported for CNDs.⁵³ **Figure 2.27** clearly shows the increased emitted blue luminescence from NCNDs1 to NCNDs3 upon excitation under a 365 nm UV lamp.

As reported in **Table 2.1**, NCNDs1-3 have similar functional groups and nitrogen content. The QYs increase with the reduced amount of amine groups, with NCNDs3 having the highest degree of surface oxidation, resulting in more surface defects, which can trap more excitons leading to higher FL quantum yield.⁵⁴

2 Nitrogen-Doped Carbon Nanodots

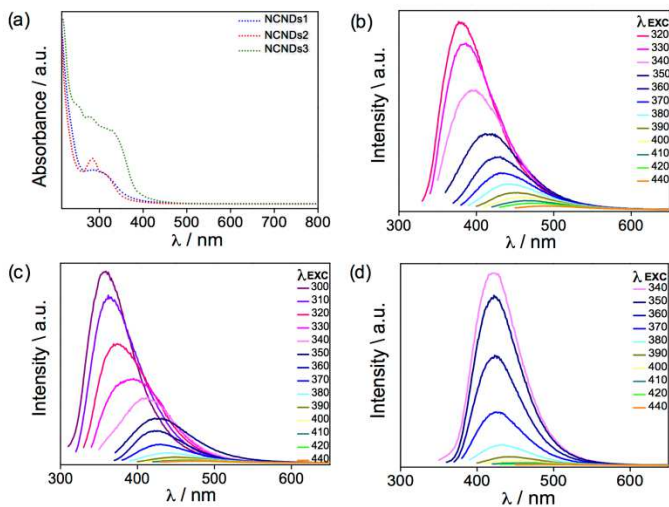


Figure 2.26 a) UV-Vis absorption spectra of NCND1–3 in water; b–d) FL spectra of NCND1–3 in water (298 K) at different excitation wavelengths.

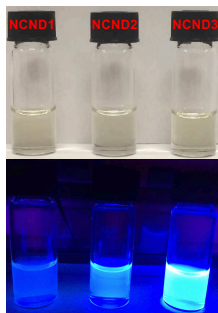


Figure 2.27 Photographs of NCND1, NCND2, and NCND3 in daylight (top) and under UV light (365 nm) illumination (bottom).

2.2.4 Towards applications

Due to their excellent PL properties, our CNDs are an attractive candidate for biological applications and light-emitting diodes (LEDs) fabrication.

In order to evaluate their application for biological purposes, the cell viability and bioimaging capability of our NCNDs was investigated. The cell viability of NCNDs was determined by the 3-(4,5-dimethylthiazol-2-yl)-2,5-diphenyltetrazolium bromide (MTT) colorimetric assay.⁵⁵ It was observed that the viability of several cell lines varies between 80-100% after 72 h of incubation with NCNDs at concentrations 1 $\mu\text{g/mL}$ to 1 mg/mL (**Figure S2.14**). These results suggested that NCNDs exhibited low cytotoxicity and can be used in high concentration for imaging or other biomedical applications. NCNDs were then introduced into C33-A cells to show their bioimaging capabilities through confocal microscopy imaging experiments (**Figure 2.28**). The luminescent spots indicated the internalization of our NCNDs following 24 h of incubation.

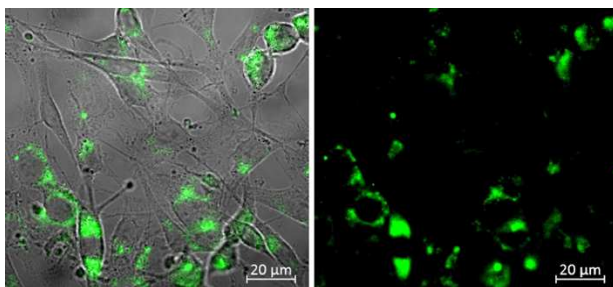


Figure 2.28 Confocal fluorescence images of C33-A cells after incubation with 300 $\mu\text{g/mL}$ NCNDs. Left: merged picture of the fluorescent bright field. Right: fluorescent image.

Finally, preliminary results on the use of our NCNDs for the fabrication of LEDs are reported. The architecture of the vapor-deposited device is shown in **Figure 2.29a**. The employed materials were chosen in order to match the energy levels for a better charges and excitons confinement.

In order to increase the anode work-function and reduce the hole-injection barrier, the Indium Tin Oxide (ITO) surface was previously treated with oxygen-plasma. On top the ITO electrode, the hole injection film consists of 40 nm of poly(3,4-ethylenedioxythiophene):polystyrene sulfonate (PEDOT:PSS). In order to enhance the holes transport a 30 nm layer of poly-*[N,N'*-bis(3-methylphenyl)-*N,N'*-diphenylbenzidine] (poly-TPD) was spin-coated on top of PEDOT:PSS, followed by a 10 nm thick film of poly(9-vinylcarbazole) (PVK). The thickness of the spin-coated NCNDs film was 30 nm. Then the n-doped layer consisted of 30 nm of 4,7-diphenyl 1,10-phenanthroline (BPhen) doped with cesium atoms using a suitable dispenser from SAES Getters. A 10 nm thick neat film of pure BPhen after the emissive layer was also included as blocking layers. The structure was closed with a cathode of 130 nm thick silver (Ag). The last two organic layers and the metal films were thermally evaporated in a Kurt J. Lesker cluster tool at a base pressure around 10^{-7} mbar. Bilayer-structured hole-transport interlayers of poly-TPD/PVK take advantage of the deep highest-occupied molecular-orbital energy level of PVK to realize efficient hole injection into the dot layers and the relatively high hole mobility of poly-TPD to achieve lower turn-on voltage.

The fabricated LEDs was then characterized by electro-optical measurements. The normalized electroluminescence spectra, biased at various voltages, is shown in **Figure S2.15**. Red emission from the double-layer PLEDs was probably from the interface between HTL and EML, and in particular probably from an exciplex associating

with poly-TPD and defects of NCNDs. This red emission, added to the blue one of the NCNDs, results in a white light with Commission Internationale d'Éclairage (CIE) coordinates of (0.28, 0.31) at 10 V, as shown in **Figure 2.29c**. **Figure 2.29b** shows the luminance and the current density flowing in the devices as a function of the applied voltage. The devices were turned on at about 9.4 V and exhibited a maximum brightness of 100 cd/m^2 at 13 V, which is among the highest values reported so far.^{56,57}

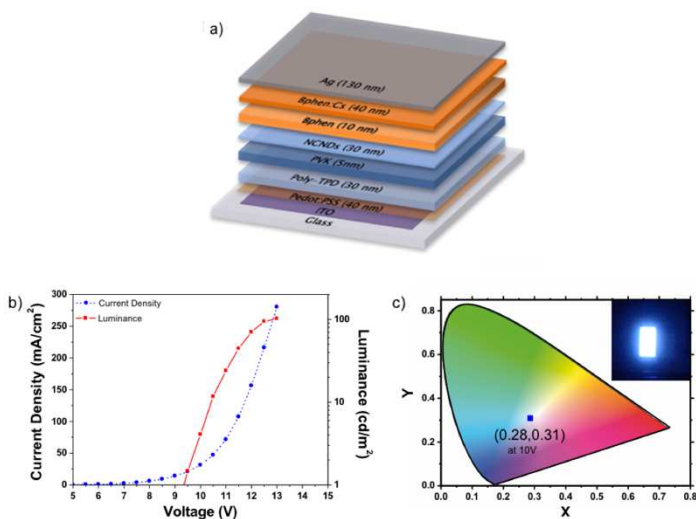


Figure 2.29 a) NCNDs-LED device structure; b) current density and brightness of NCNDs-LED; c) CIE (1931) coordinates and photographs of the LED operating at 10 V as applied voltage.

2.3 Conclusions and perspectives

In this chapter we have described a straightforward, simple and controllable method to prepare NCNDs under microwave irradiation. Using this approach, NCNDs could be obtained within three minutes without the need of sophisticated equipment or additional surface passivation and by using commercially available compounds. We have reported a general method for the separation of NCNDs with different size and properties by low-pressure size exclusion chromatography. These NCNDs are narrowly distributed in size, and their abundant surface traps and functional groups endowed them with tunable fluorescent emission, bright luminescence (quantum yield as high as 0.46), and excellent solubility in water and in common polar organic solvents. We demonstrated that a profound NMR study could be an important tool to fill the gap of a real structural understanding of this new nanomaterial. The mono and bidimensional NMR studies have provided an unprecedented level of detail and insight in CNDs structure and should give other scientist the direction to perform work in this new field. Additionally, we have shown that the fluorescence strongly depends on the surface states of the NCNDs because their optical properties are affected by the competition among different emission centers and traps.

We have demonstrated that our NCNDs show low cytotoxicity also at high concentrations. An efficient cell uptake was observed, together with their cellular imaging capability. Accordingly, current efforts in our laboratory are directed towards their use for biological purpose, such as drug delivery systems.

Finally, preliminary experiments that may do serve the purpose of a proof of concept, showed that our nanomaterials could be a potential candidate for LEDs fabrication, but further studies and improvements of the device architecture are needed and are currently underway in our laboratory.

In summary, a convenient route to size- and surface-controllable NCNDs have been demonstrated. Their superior optical properties, coupled with their low cost and ease of labeling, should enable their use in numerous applications.

2.4 Experimental section

2.4.1 Materials

L-Arginine (Fluorochem; $\geq 98\%$), L-Arginine- $^{13}\text{C}_6$ $^{15}\text{N}_4$ (Sigma-Aldrich, 99 atom % ^{15}N , 99 atom % ^{13}C), ethylenediamine (Sigma-Aldrich, $\geq 99.5\%$) and ethylenediamine- $^{13}\text{C}_2$ (Sigma-Aldrich, 99 atom % ^{13}C), Sephadex LH20 (Sigma-Aldrich) were used without further purifications.

Kaiser test kit was purchased from Sigma-Aldrich.

Dialysis tubes with molecular weight cutoff 0.5-1 KDa were bought from Spectrum Labs.

Ultrapure fresh water obtained from a Millipore water purification system ($>18\text{M}\Omega$ Milli-Q, Millipore) was used in all experiments.

D_2O was purchased from Sigma-Aldrich.

All cell lines were purchased from ATCC-LGC and cultured in DMEM or RPMI-1640 media from Sigma Aldrich completed with 2 nM L-glutamine, 100 ug/mL penicillin, 100 ug/mL streptomycin and 10% heat-inactivated fetal bovine serum from Gibco[®]. The PBS buffer was purchased in Sigma Aldrich in tablets and prepared following manufacturer procedures, corresponding to 10 mM phosphate buffer containing 137 mM NaCl and 2.7 mM KCl at pH 7.4. Cell Proliferation kit I was purchased from Roche and was used to quantify relative cell viability, 3(4,5-Dimethylthiazol-2-yl)-2,5-diphenyltetrazolium bromide, MTT.

PVK (average molecular weight 25,000-50,000 g/mol⁻¹), Bphen (molecular weight 332.4 g/mol), chlorobenzene (anhydrous, 99.8%, molecular weight 112.56 g/mol), *N,N*-dimethylformamide (anhydrous, 99.8%, molecular weight 73.09 g/mol) and *m*-xylene (anhydrous, $\geq 99\%$, molecular weight 106.17 g/mol) were purchased from Sigma Aldrich. Poly-TPD (average molecular weight 100,000-150,000 g/mol) was purchased from Solaris Chem Inc.. Patterned

ITO-glass substrates (sheet resistance, 12 Ω /sq) were purchased from Visiontek Systems Ltd.. All materials were used as received.

2.4.2 Apparatus and characterization

The microwave synthesis was performed on a CEM Discover-SP.

NMR experiments were carried out with a Varian Inova 500 MHz and 125 MHz (^1H and ^{13}C) in D_2O (around 25 mg of sample in 0.6 mL). ^{15}N -NMR was acquired on a Bruker 300 MHz. Bidimensional spectra were acquired using HSQCAD, gHMBCAD, and INADEQUATE sequences in the VnmrJ 3.2 software package. 3D-DOSY experiment was carried out using Varian Inova NMR spectrometer equipped with Performa II-Z gradient coils with Absolute Value – gradient compensated stimulated Echo gHMBC. Diffusion gradient length = 1.4 ms, diffusion delay = 100.0 ms and from 0 to 25 m^2/s . The 3D-DOSY process gave each signal region labelled with its diffusion coefficient and the corresponding information (^1H ppm, ^{13}C ppm and diffusion coefficient) was plotted in 3D graph with Origin.

UV-Vis spectra were recorded at room temperature on a PerkinElmer Lambda 35 UV-Vis spectrophotometer. Fluorescence spectra were recorded on a Varian Cary Eclipse Fluorescence Spectrophotometer. All the spectra were recorded at room temperature using 10 mm path-length cuvettes.

Fourier-transform infrared spectroscopy was performed by the attenuated total reflection (ATR) method on a GladiATR (Pike Technologies) equipped with a germanium crystal plate.

Atomic force microscopy (AFM) images were obtained with a Nanoscope IIIa, VEECO Instruments. As a general procedure to perform AFM analyses, tapping mode with a HQ:NSC19/ALBS probe (80kHz; 0.6 N/m) (MikroMasch) from drop cast of samples in an aqueous solution (concentration of few mg/mL) on a mica

substrate was performed. The obtained AFM-images were analyzed in Gwyddion 2.35.

X-ray photoemission spectroscopy (XPS) spectra of the samples were measured on a Thermo Scientific K-Alpha XPS system (Thermo Fisher Scientific, UK). For each analysis, about 0.5 mg of material were deposited on a copper thin film, which was then fixed on an XPS sample holder using a double side adhesive conductive carbon tap (SPI supplies). Spectra were collected using a monochromatized Al-K α radiation (1486.6 eV). The surface normal emitted photoelectron was analyzed in a double-focusing hemispherical analyzer and recorded on a multi-channel detector. All the spectra were acquired in the constant analyzer energy mode. The Thermo Scientific Advantage software (Thermo Fisher Scientific) was used for digital acquisition and data processing.

The electrochemical characterization has been carried out in DMF/tetra-butylammonium hexafluorophosphate (TBAPF₆) 0.1M. Oxygen was removed by purging the DMF solution with high-purity Argon. A typical three-electrode cell was employed, which was composed of a glassy carbon working electrode (3 mm diameter, 66-EE047 Cypress Systems), a platinum wire as counter, and a silver wire as quasi-reference (QRE) electrode. A CHI750C Electrochemical Workstation (CH Instruments, Inc., Austin, TX, USA) was used. The potential of the reference electrode was calibrated after each measurement using Ferrocene/Ferrocenium (Fc/Fc⁺) redox couple as the internal standard. The formal potential of Fc/Fc⁺ is 0.464V for DMF against the KCl saturated calomel electrode (SCE). The GC electrodes were stored in ethanol, and before experiments were polished with a 0.05 μm diamond suspension (Metadi Supreme Diamond Suspension, Buehler) and ultrasonically rinsed with deionized water for 15 minutes and ethanol for 15 minutes. The electrodes were electrochemically activated in the background

solution by means of several voltammetric cycles at 0.5 V/s between the anodic and cathodic solvent/electrolyte discharges. The measurements were carried out at a scan rate of 0.1 V/s.

The quantum yield measurements were performed with quinine sulphate in 0.10 M H₂SO₄ (literature quantum yield 0.54 at 360 nm) as the standard.⁵⁰

Cell viability assay: cell viability of adherent human cell lines was measured with the colorimetric MTT assay. 4×10^3 PC3 (prostate cancer), 4×10^3 A-549 (small cell lung carcinoma), 2.5×10^3 C33-A (cervix carcinoma), 2.5×10^3 HeLa (cervix carcinoma), 4×10^3 MDA-MB-231 (breast adenocarcinoma), 10×10^3 MCF-7 (breast adenocarcinoma) cells were seeded in 200 μ L media per well in 96-well plates and cultured for 24 h at 37 °C and 5%CO₂. Then, they were incubated for 72 h with CNDs-PTX at the concentrations of 1 μ g/mL, 10 μ g/mL, 25 μ g/mL, 50 μ g/mL, 150 μ g/mL, 300 μ g/mL, 450 μ g/mL, 600 μ g/mL, 750 μ g/mL, 900 μ g/mL, 1 mg/mL in 100 μ L media at 37 °C and 5%CO₂ in a humidified atmosphere. Cells were washed twice with 100 μ L incomplete media and incubated for 30-60 min at 37 °C and 5%CO₂ with 100 μ L media containing MTT at the dilution of 1:20. The formazan crystals produced by the mitochondrial processing of MTT were dissolved in 100 μ L DMSO. Absorbance of MTT product was detected in a micro plate reader (Genios Pro, TECAN) at 550 nm. Data are expressed as a percentage of absorbance of treated cells related to the untreated control cells and represented as means of quadruplicates \pm SD.

Confocal microscopy: 2×10^4 C33-A cells per well were seeded in a 8-well chamber slide (Millicell EZslide, Millipore) and cultured for 1 day. Supernatants were replaced by 200 μ L media alone or media containing 300 μ g/ml of CNDs, then incubated for 24 h at 37 °C and 5 %CO₂. Cells were washed twice with sterile PBS prior to fixation

with sterile PBS containing 4% paraformaldehyde for 15min at room temperature. Wells were disassembled, cells were washed twice with PBS and, the slide was mounted with 1 drop mounting media (DAKO) and a 1.5 coverslip (24×60mm). The mounted slides were let to harden overnight at 4°C. Images were taken in a confocal microscope (lsm 500 meta, Zeiss) with laser 488 nm, 505 LP filter and 20X magnification objective with differential interference contrast for transmitted light.

Device fabrication and characterization: before the plasma oxygen, ITO substrates have been cleaned in acetone and isopropyl alcohol for 10 min in an ultrasonic bath. A PEDOT:PSS solution (Heraeus - Clevios P VP Al 4083, filtered through a 0.45 μm Millipore Millex-HV hydrophilic polyvinylidene fluoride filter) was spin-coated onto the ITO-coated glass substrates at 3.000 r.p.m. for 60 s and baked at 145 °C for 15 min. The PEDOT:PSS-coated substrates were transferred into a nitrogen filled glove box. Poly-TPD (in chlorobenzene, 16 mg/mL), PVK (in m-xylene, 3 mg/mL), NCNDs (in DMF, 9 mg/mL), were deposited layer by layer by spin coating at 2,000 r.p.m. for 45 s. The poly-TPD, PVK and NCNDs layers were baked at 110°C for 20 min, 170°C for 30 min and at 120°C for 10 min, respectively, before the deposition of the subsequent layer. Ag electrodes were deposited through a shadow mask. The device area was 15 mm² as defined by the overlapping area of the ITO and Ag electrodes.

The electroluminescence from the devices was characterized under vacuum with an NIST calibrated Optronics OL770 spectrometer, coupled through an optical fiber to an OL610 telescope unit for the luminance measurements, and a Keithley 2420 current–voltage source-meter.

2.4.3 Synthesis of NCNDs

NCNDs were obtained via microwave irradiation of an aqueous solution of Arginine (Arg) and ethylenediamine (EDA) (1:1 mol). Typically, Arg (87.0 mg), EDA (33.0 μ L) and Milli-Q water (100.0 μ L) were heated at 240 $^{\circ}$ C, 377 psi and 200 W for 180 seconds.

In the process of microwave heating, the solution changes color from transparent to brown as a result of formation of NCNDs.

The solution was diluted with water and was filtered through a 0.1 μ m microporous membrane separating a deep yellow solution that was dialyzed against pure water through a dialysis membrane for 2 days. The aqueous solution of NCNDs was lyophilized giving a brownish solid (NCNDs: 23.0 mg).

Alternatively, the water was removed under reduced pressure, the crude mixture dissolved in methanol (1.0 mL) and separated by SEC. It was used a column packed with Sephadex LH-20 eluting with MeOH 2 mL/min operating at a pressure of 150 psi. As a result, were obtained three fractions named NCNDs1, NCNDs2 and NCNDs3 according to their elution time. Finally, the methanol was removed under reduced pressure obtaining three oils that were dissolved in water and lyophilized giving brownish solids (NCNDs1: 17.0 mg, NCNDs2: 8.7 mg, NCNDs3: 10.0 mg).

By following the same experimental procedures, the N^{13} CNDs and 15 NCNDs were prepared from the 13 C-enriched and 15 N-enriched precursors (L-Arginine- 13 C $_6$ 15 N $_4$ and ethylenediamine- 13 C $_2$).

2.4.4 Supporting figures

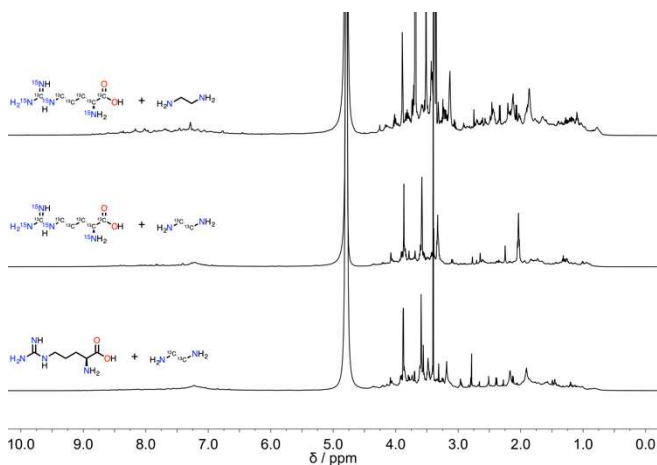


Figure S2.1 ^1H -NMR spectra of N^{13}CNDs obtained from starting from ^{13}C -Arg and EDA (top), ^{13}C -Arg and ^{13}C -EDA (middle) and Arg and ^{13}C -EDA (bottom).

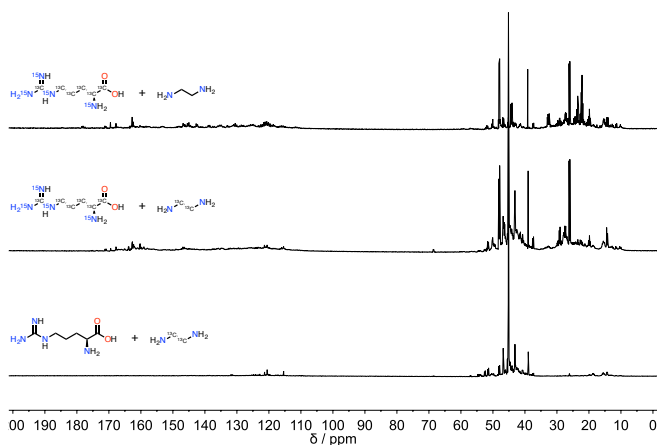


Figure S2.2 ^{13}C -NMR spectra of N^{13}CNDs obtained from starting from ^{13}C -Arg and EDA (top), ^{13}C -Arg and ^{13}C -EDA (middle) and Arg and ^{13}C -EDA (bottom).

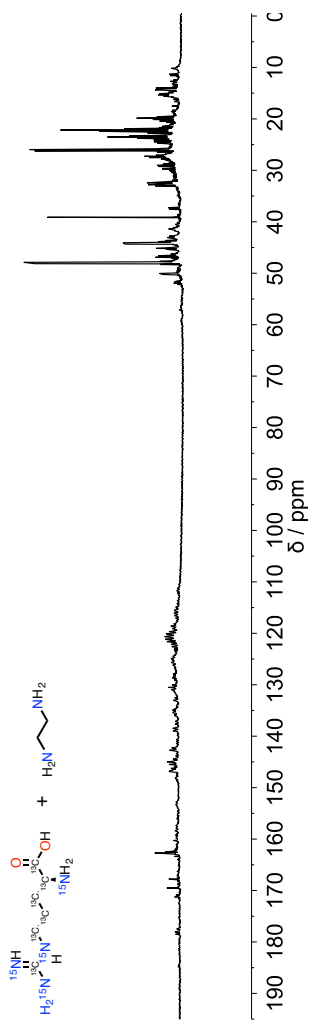


Figure S2.3 ^{13}C -NMR spectra of N ^{13}C NDs prepared starting from ^{13}C -Arg and EDA (nt = 5500, d1 = 5 s, 32768 complex points).

2 Nitrogen-Doped Carbon Nanodots

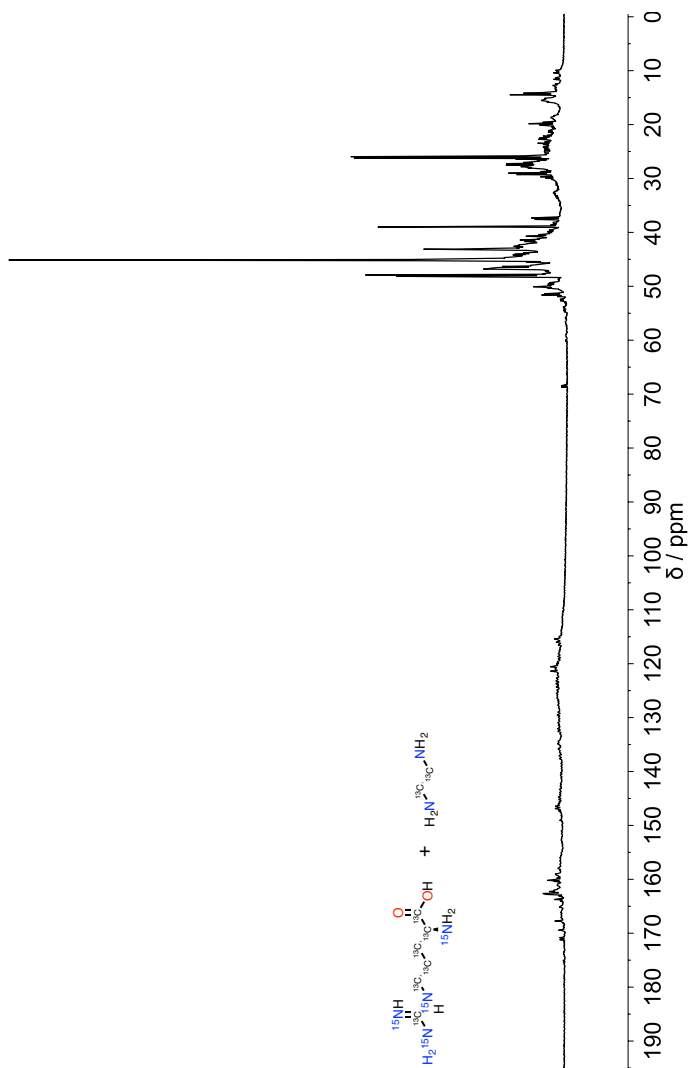


Figure S2.4 ^{13}C -NMR spectra of N 13 CNDs prepared starting from ^{13}C -Arg and ^{13}C -EDA (nt = 6900, d1 = 5 s, 32768 complex points).

2 Nitrogen-Doped Carbon Nanodots

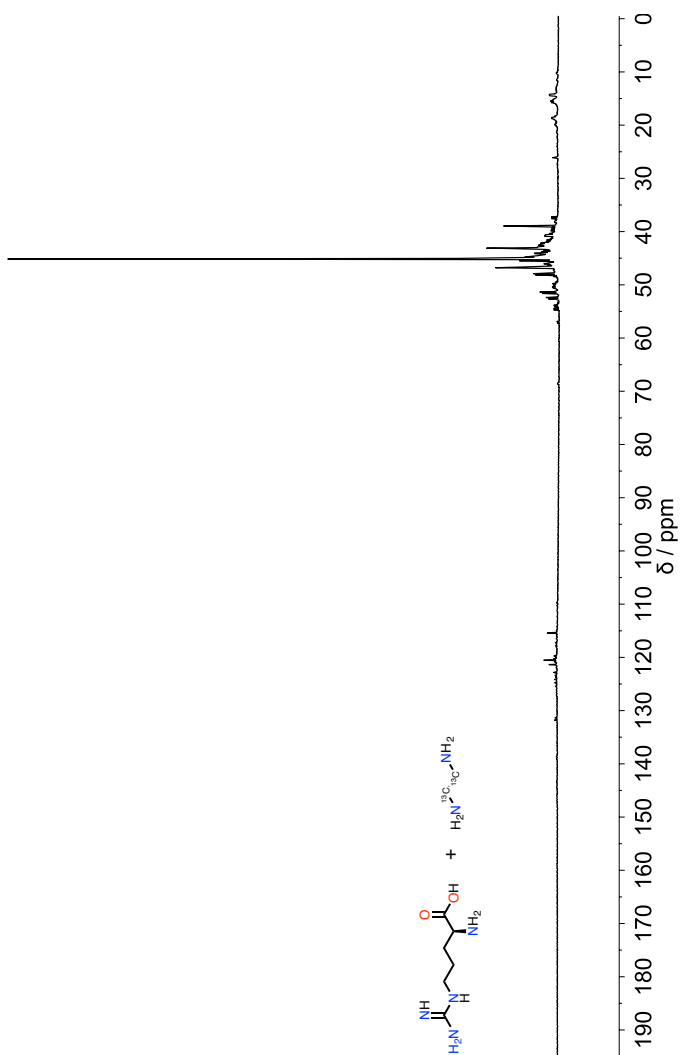


Figure S2.5 ^{13}C -NMR spectra of N^{13}CNDs prepared starting from Arg and ^{13}C -EDA (nt = 5312, d1 = 5 s, 32768 complex points).

2 Nitrogen-Doped Carbon Nanodots

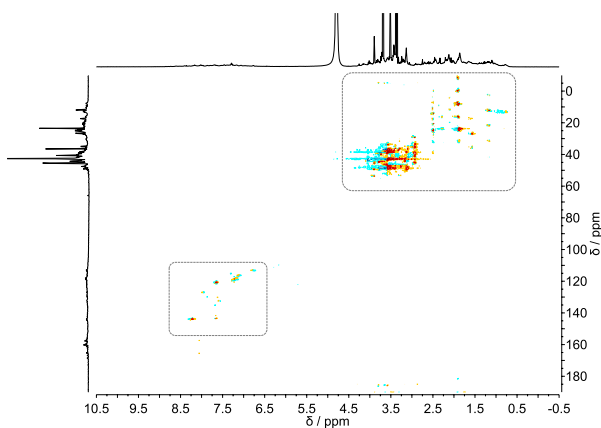


Figure S2.6 HSQC spectra of N^{13}CNDs prepared starting from ^{13}C -Arg and ^{13}C -EDA (scan t1 increment = 16, t1 increments = 400, one-bond $J_{1\text{H}}$ = 146.0 Hz). Regions corresponding to aliphatic H that correlate with aliphatic C and aromatic H with aromatic C have been highlighted

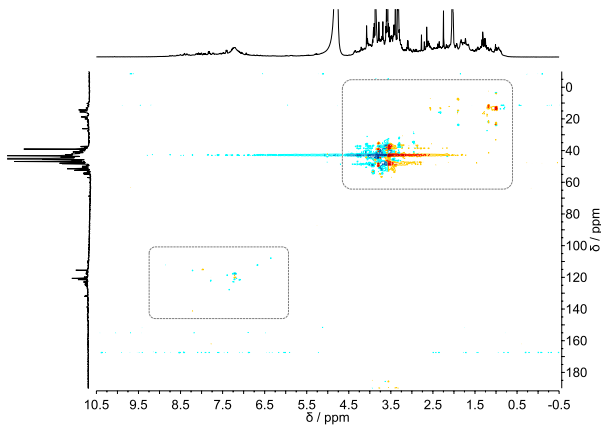


Figure S2.7 HSQC spectra of N^{13}CNDs prepared starting from Arg and ^{13}C -EDA (scan t1 increment = 16, t1 increments = 256, one-bond $J_{1\text{H}}$ = 146.0 Hz). Regions corresponding to aliphatic H that correlate with aliphatic C and aromatic H with aromatic C have been highlighted.

2 Nitrogen-Doped Carbon Nanodots

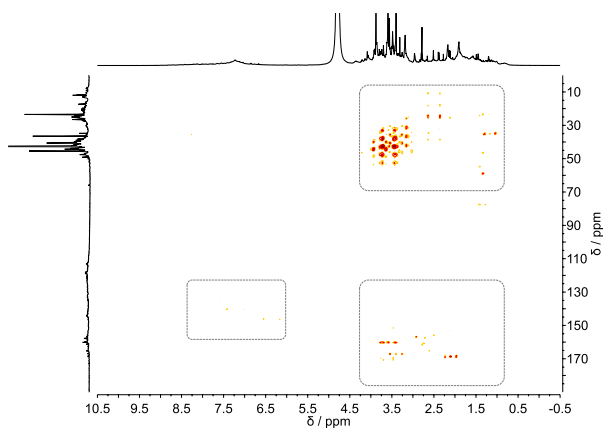


Figure S2.8 HMBC spectra of N^{13}CNDs prepared starting from ^{13}C -Arg and ^{13}C -EDA (scan t1 increment = 32, t1 increments = 400, multiple bond $J_{\text{nxh}} = 8.0$ Hz). Regions corresponding to aliphatic H-C, aliphatic H-aromatic C and aromatic H-C have been highlighted.

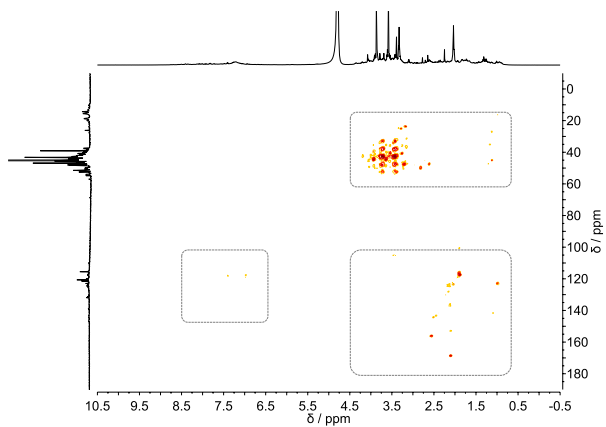


Figure S2.9 HMBC spectra of N^{13}CNDs prepared starting from Arg and ^{13}C -EDA (scan t1 increment = 16, t1 increments = 400, multiple bond $J_{\text{nxh}} = 8.0$ Hz). Regions corresponding to aliphatic H-C, aliphatic H-aromatic C and aromatic H-C have been highlighted.

2 Nitrogen-Doped Carbon Nanodots

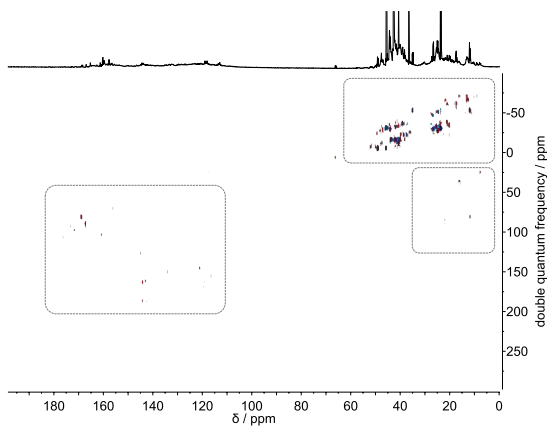


Figure S2.10 INADEQUATE spectra of $N^{13}CNDs$ prepared starting from ^{13}C -Arg and ^{13}C -EDA (scans = 128, J = 55 Hz). Regions corresponding to direct aliphatic C-C, aliphatic C-aromatic C and aromatic C-C have been highlighted.

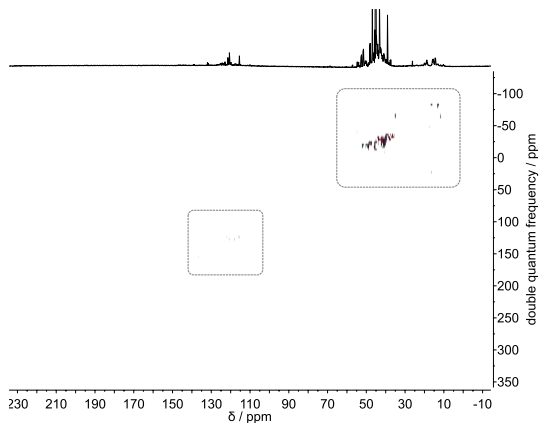


Figure S2.11 INADEQUATE spectra of $N^{13}CNDs$ prepared starting from Arg and ^{13}C -EDA (scans = 256, J = 55 Hz). Regions corresponding to direct aliphatic C-C and aromatic C-C have been highlighted.

2 Nitrogen-Doped Carbon Nanodots

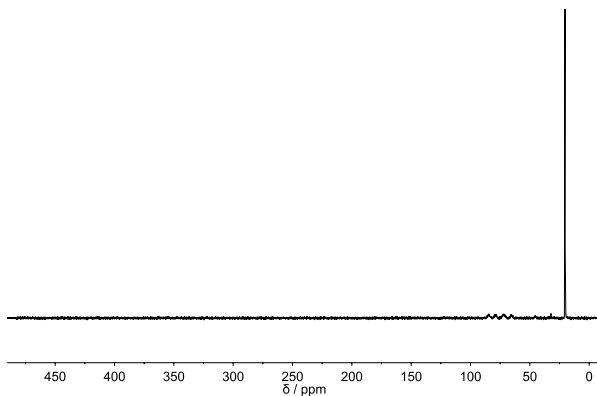


Figure S2.12 ^{15}N -NMR spectra of ^{15}N NCNDs prepared starting from ^{15}N -Arg and EDA (coupled, scans = 13306, relaxation delay = 15 s).

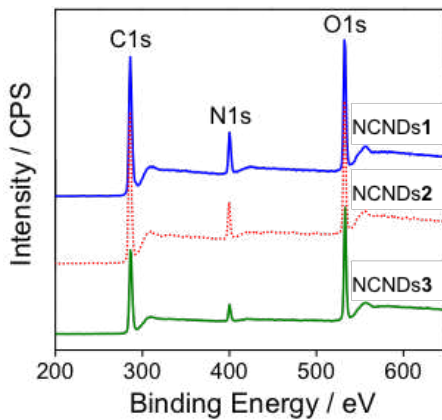


Figure S2.13 XPS survey of NCNDs1-3.

2 Nitrogen-Doped Carbon Nanodots

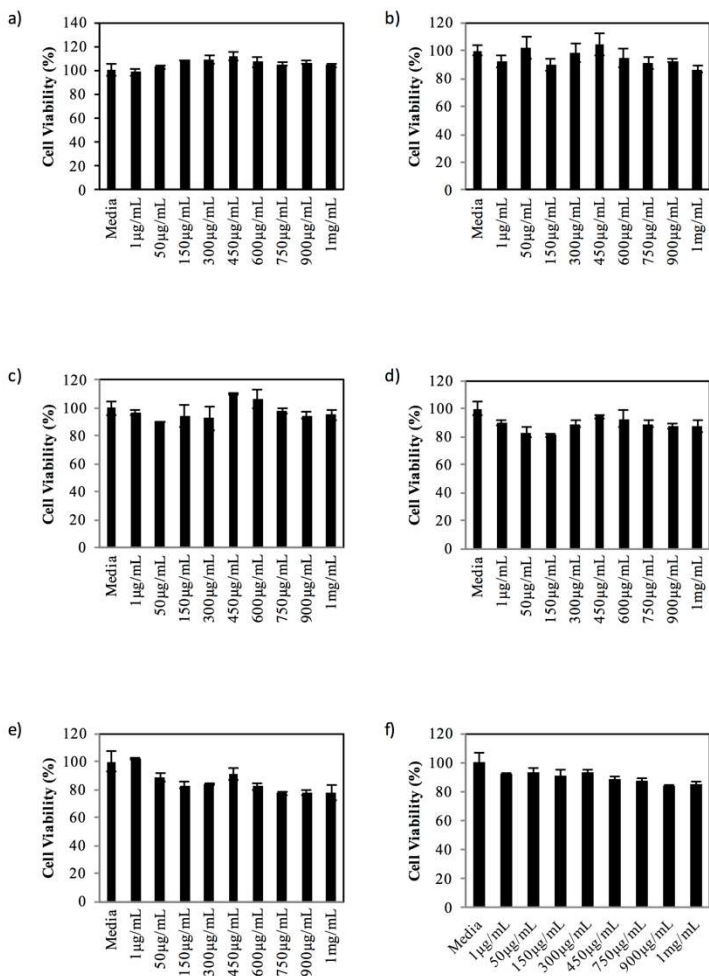


Figure S2.14 Cell viability assays of NCNDs at different concentrations (1 µg/mL to 1 mg/mL) with different cell lines at 72 h of incubation, 37 °C and 5 %CO₂. a) C33-A; b) MCF-7; c) MDA-MB-231; d) A-549; e) PC-3; f) HeLa cancer cell line.

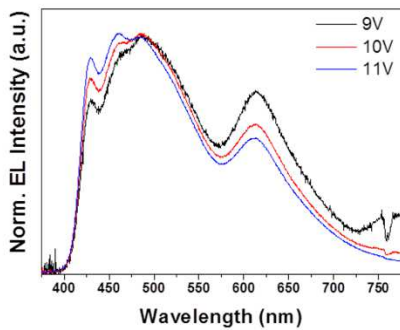


Figure S2.15 EL spectra of the NCNDs-based device at different bias voltage.

2.5 References

- (1) X. Xu, R. Ray, Y. Gu, H.J. Ploehn, L. Gearheart, K. Raker, W. A. Scrivens. Electrophoretic Analysis and Purification of Fluorescent Single-Walled Carbon Nanotube Fragments. *J. Am. Chem. Soc.* **2004**, *126*, 12736–12737.
- (2) Zhou, J.; Booker, C.; Li, R.; Zhou, X.; Sham, T.-K.; Sun, X.; Ding, Z. An Electrochemical Avenue to Blue Luminescent Nanocrystals from Multiwalled Carbon Nanotubes (MWCNTs). *J. Am. Chem. Soc.* **2007**, *129*, 744–745.
- (3) Lu, J.; Yang, J.; Wang, J.; Lim, A.; Wang, S.; Loh, K. P. One-Pot Synthesis of Fluorescent Carbon Nanoribbons, Nanoparticles, and Graphene by the Exfoliation of Graphite in Ionic Liquids. *ACS Nano* **2009**, *3*, 2367–2375.
- (4) Li, H.; He, X.; Kang, Z.; Huang, H.; Liu, Y.; Liu, J.; Lian, S.; Tsang, C. H. A.; Yang, X.; Lee, S.-T. Water-Soluble Fluorescent Carbon Quantum Dots and Photocatalyst Design. *Angew. Chem. Int. Ed.* **2010**, *49*, 4430–4434.
- (5) Zheng, L.; Chi, Y.; Dong, Y.; Lin, J.; Wang, B. Electrochemiluminescence of Water-Soluble Carbon Nanocrystals Released Electrochemically from Graphite. *J. Am. Chem. Soc.* **2009**, *131*, 4564–4565.
- (6) Zhao, Q.-L.; Zhang, Z.-L.; Huang, B.-H.; Peng, J.; Zhang, M.; Pang, D.-W. Facile Preparation of Low Cytotoxicity Fluorescent Carbon Nanocrystals by Electrooxidation of Graphite. *Chem. Commun.* **2008**, *281*, 5116–5118.
- (7) Sun, Y.-P.; Zhou, B.; Lin, Y.; Wang, W.; Fernando, K. A. S.; Pathak, P.; Mezziani, M. J.; Harruff, B. A.; Wang, X.; Wang, H.; *et al.* Quantum-Sized Carbon Dots for Bright and Colorful Photoluminescence. *J. Am. Chem. Soc.* **2006**, *128*, 7756–7757.
- (8) Rabenau, A. Role of Hydrothermal Synthesis in Preparative Chemistry. *Angew. Chem. Int. Ed.* **1985**, *24*, 1026–1040.

- (9) Hu, B.; Wang, K.; Wu, L.; Yu, S. H.; Antonietti, M.; Titirici, M. M. Engineering Carbon Materials from the Hydrothermal Carbonization Process of Biomass. *Adv. Mater.* **2010**, *22*, 813–828.
- (10) Chandra, S.; Das, P.; Bag, S.; Laha, D.; Pramanik, P. Synthesis, Functionalization and Bioimaging Applications of Highly Fluorescent Carbon Nanoparticles. *Nanoscale* **2011**, *3*, 1533–1540.
- (11) Yang, Z.-C.; Wang, M.; Yong, A. M.; Wong, S. Y.; Zhang, X.-H.; Tan, H.; Chang, A. Y.; Li, X.; Wang, J. Intrinsically Fluorescent Carbon Dots with Tunable Emission Derived from Hydrothermal Treatment of Glucose in the Presence of Monopotassium Phosphate. *Chem. Commun.* **2011**, *47*, 11615–11617.
- (12) Zhai, X.; Zhang, P.; Liu, C.; Bai, T.; Li, W.; Dai, L.; Liu, W. Highly Luminescent Carbon Nanodots by Microwave-Assisted Pyrolysis. *Chem. Commun.* **2012**, *48*, 7955–7957.
- (13) Zhang, B.; Liu, C.; Liu, Y. A Novel One-Step Approach to Synthesize Fluorescent Carbon Nanoparticles. *Eur. J. Inorg. Chem.* **2010**, *2010*, 4411–4414.
- (14) Zhu, H.; Wang, X.; Li, Y.; Wang, Z.; Yang, F.; Yang, X. Microwave Synthesis of Fluorescent Carbon Nanoparticles with Electrochemiluminescence Properties. *Chem. Commun.* **2009**, 5118–5120.
- (15) Zhu, S.; Meng, Q.; Wang, L.; Zhang, J.; Song, Y.; Jin, H.; Zhang, K.; Sun, H.; Wang, H.; Yang, B. Highly Photoluminescent Carbon Dots for Multicolor Patterning, Sensors, and Bioimaging. *Angew. Chem. Int. Ed.* **2013**, *52*, 3953–3957.
- (16) Sahu, S.; Behera, B.; Maiti, T. K.; Mohapatra, S. Simple One-Step Synthesis of Highly Luminescent Carbon Dots from Orange Juice: Application as Excellent Bio-Imaging Agents. *Chem. Commun.* **2012**, *48*, 8835–8837.

- (17) De, B.; Karak, N. A Green and Facile Approach for the Synthesis of Water Soluble Fluorescent Carbon Dots from Banana Juice. *RSC Adv.* **2013**, *3*, 8286–8290.
- (18) Huang, H.; Lv, J.-J.; Zhou, D.-L.; Bao, N.; Xu, Y.; Wang, A.-J.; Feng, J.-J. One-Pot Green Synthesis of Nitrogen-Doped Carbon Nanoparticles as Fluorescent Probes for Mercury Ions. *RSC Adv.* **2013**, *3*, 21691–21696.
- (19) Hsu, P.-C.; Shih, Z.-Y.; Lee, C.-H.; Chang, H.-T. Synthesis and Analytical Applications of Photoluminescent Carbon Nanodots. *Green Chem.* **2012**, *14*, 917–920.
- (20) Wang, F.; Pang, S.; Wang, L.; Li, Q.; Kreiter, M.; Liu, C. Y. One-Step Synthesis of Highly Luminescent Carbon Dots in Noncoordinating Solvents. *Chem. Mater.* **2010**, *22*, 4528–4530.
- (21) Zong, J.; Zhu, Y.; Yang, X.; Shen, J.; Li, C. Synthesis of Photoluminescent Carbogenic Dots Using Mesoporous Silica Spheres as Nanoreactors. *Chem. Commun.* **2011**, *47*, 764–766.
- (22) Yang, Y.; Wu, D.; Han, S.; Hu, P.; Liu, R. Bottom-up Fabrication of Photoluminescent Carbon Dots with Uniform Morphology via a Soft-Hard Template Approach. *Chem. Commun.* **2013**, *49*, 4920–4922.
- (23) Liu, R.; Wu, D.; Liu, S.; Koynov, K.; Knoll, W.; Li, Q. An Aqueous Route to Multicolor Photoluminescent Carbon Dots Using Silica Spheres as Carriers. *Angew. Chemie* **2009**, *121*, 4668–4671.
- (24) Jaiswal, A.; Ghosh, S. S.; Chattopadhyay, A. One Step Synthesis of C-Dots by Microwave Mediated Caramelization of Poly(ethylene Glycol). *Chem. Commun.* **2012**, *48*, 407–409.
- (25) Jiang, J.; He, Y.; Li, S.; Cui, H. Amino Acids as the Source for Producing Carbon Nanodots: Microwave Assisted One-Step Synthesis, Intrinsic Photoluminescence Property and

- Intense Chemiluminescence Enhancement. *Chem. Commun.* **2012**, *48*, 9634–9636.
- (26) Liu, C.; Zhang, P.; Tian, F.; Li, W.; Li, F.; Liu, W. One-Step Synthesis of Surface Passivated Carbon Nanodots by Microwave Assisted Pyrolysis for Enhanced Multicolor Photoluminescence and Bioimaging. *J. Mater. Chem.* **2011**, *21*, 13163–13167.
- (27) Wang, J.; Cheng, C.; Huang, Y.; Zheng, B.; Yuan, H.; Bo, L.; Zheng, M.-W.; Yang, S.-Y.; Guo, Y.; Xiao, D. A Facile Large-Scale Microwave Synthesis of Highly Fluorescent Carbon Dots from Benzenediol Isomers. *J. Mater. Chem. C* **2014**, *2*, 5028–5035.
- (28) Gedye, R.; Smith, F.; Westaway, K.; Ali, H.; Baldisera, L.; Laberge, L.; Rousell, J. The Use of Microwave Ovens for Rapid Organic Synthesis. *Tetrahedron Lett.* **1986**, *27*, 279–282.
- (29) Cao, L.; Meziani, M. J.; Sahu, S.; Sun, Y.-P. Photoluminescence Properties of Graphene versus Other Carbon Nanomaterials. *Acc. Chem. Res.* **2013**, *46*, 171–180.
- (30) Wilson, W. L.; Szajowski, P. F.; Brus, L. E. Quantum Confinement in Size-Selected, Surface-Oxidized Silicon Nanocrystals. *Science* **1993**, *262*, 1242–1244.
- (31) Wang, X.; Cao, L.; Yang, S.-T.; Lu, F.; Meziani, M. J.; Tian, L.; Sun, K. W.; Bloodgood, M. A.; Sun, Y.-P. Bandgap-Like Strong Fluorescence in Functionalized Carbon Nanoparticles. *Angew. Chem. Int. Ed.* **2010**, *49*, 5310–5314.
- (32) Sun, Y.-P.; Wang, X.; Lu, F.; Cao, L.; Meziani, M. J.; Luo, P. G.; Gu, L.; Veca, L. M. Doped Carbon Nanoparticles as a New Platform for Highly Photoluminescent Dots. *J. Phys. Chem. C* **2008**, *112*, 18295–18298.
- (33) Qiao, Z.-A.; Wang, Y.; Gao, Y.; Li, H.; Dai, T.; Liu, Y.; Huo, Q. Commercially Activated Carbon as the Source for Producing Multicolor Photoluminescent Carbon Dots by
-

- Chemical Oxidation. *Chem. Commun.* **2010**, *46*, 8812–8814.
- (34) Peng, H.; Travas-Sejdic, J. Simple Aqueous Solution Route to Luminescent Carbogenic Dots from Carbohydrates. *Chem. Mater.* **2009**, *21*, 5563–5565.
- (35) Hu, S.-L.; Niu, K.-Y.; Sun, J.; Yang, J.; Zhao, N.-Q.; Du, X.-W.; Vollath, D.; Szabó, D. V.; Schlabach, S.; Yu, S. J.; *et al.* One-Step Synthesis of Fluorescent Carbon Nanoparticles by Laser Irradiation. *J. Mater. Chem.* **2009**, *19*, 484–488.
- (36) Wang, C.; Xu, Z.; Zhang, C. Polyethyleneimine-Functionalized Fluorescent Carbon Dots: Water Stability, pH Sensing, and Cellular Imaging. *ChemNanoMat* **2015**, *1*, 122–127.
- (37) Shen, R.; Song, K.; Liu, H.; Li, Y.; Liu, H. Dramatic Fluorescence Enhancement of Bare Carbon Dots through Facile Reduction Chemistry. *ChemPhysChem* **2012**, *13*, 3549–3555.
- (38) Zheng, H.; Wang, Q.; Long, Y.; Zhang, H.; Huang, X.; Zhu, R. Enhancing the Luminescence of Carbon Dots with a Reduction Pathway. *Chem. Commun.* **2011**, *47*, 10650–10652.
- (39) Chen, X.; Jin, Q.; Wu, L.; Tung, C.; Tang, X. Synthesis and Unique Photoluminescence Properties of Nitrogen-Rich Quantum Dots and Their Applications. *Angew. Chemie* **2014**, *126*, 12750–12755.
- (40) Qian, Z.; Ma, J.; Shan, X.; Feng, H.; Shao, L.; Chen, J. Highly Luminescent N-Doped Carbon Quantum Dots as an Effective Multifunctional Fluorescence Sensing Platform. *Chem. - A Eur. J.* **2014**, *20*, 2254–2263.
- (41) Xu, Y.; Wu, M.; Liu, Y.; Feng, X.-Z.; Yin, X.-B.; He, X.-W.; Zhang, Y.-K. Nitrogen-Doped Carbon Dots: A Facile and General Preparation Method, Photoluminescence Investigation, and Imaging Applications. *Chem. - A Eur. J.* **2013**, *19*, 2276–2283.
-

- (42) Yang, Z.; Li, Z.; Xu, M.; Ma, Y.; Zhang, J.; Su, Y.; Gao, F.; Wei, H.; Zhang, L. Controllable Synthesis of Fluorescent Carbon Dots and Their Detection Application as Nanoprobes. *Nano-Micro Lett.* **2013**, *5*, 247–259.
- (43) Roy, P.; Chen, P.-C.; Periasamy, A. P.; Chen, Y.-N.; Chang, H.-T. Photoluminescent Carbon Nanodots: Synthesis, Physicochemical Properties and Analytical Applications. *Mater. Today* **2015**, *18*, 447–458.
- (44) Sandeep Kumar, G.; Roy, R.; Sen, D.; Ghorai, U. K.; Thapa, R.; Mazumder, N.; Saha, S.; Chattopadhyay, K. K. Amino-Functionalized Graphene Quantum Dots: Origin of Tunable Heterogeneous Photoluminescence. *Nanoscale* **2014**, *6*, 3384–3391.
- (45) Moon, J.; An, J.; Sim, U.; Cho, S.-P.; Kang, J. H.; Chung, C.; Seo, J.-H.; Lee, J.; Nam, K. T.; Hong, B. H. One-Step Synthesis of N-Doped Graphene Quantum Sheets from Monolayer Graphene by Nitrogen Plasma. *Adv. Mater.* **2014**, *26*, 3501–3505.
- (46) Yang, Y.; Cui, J.; Zheng, M.; Hu, C.; Tan, S.; Xiao, Y.; Yang, Q.; Liu, Y. One-Step Synthesis of Amino-Functionalized Fluorescent Carbon Nanoparticles by Hydrothermal Carbonization of Chitosan. *Chem. Commun.* **2012**, *48*, 380–382.
- (47) Baker, S. N.; Baker, G. A. Luminescent Carbon Nanodots: Emergent Nanolights. *Angew. Chem. Int. Ed.* **2010**, *49*, 6726–6744.
- (48) Strauss, V.; Margraf, J. T.; Dolle, C.; Butz, B.; Nacken, T. J.; Walter, J.; Bauer, W.; Peukert, W.; Spiecker, E.; Clark, T.; *et al.* Carbon Nanodots: Toward a Comprehensive Understanding of Their Photoluminescence. *J. Am. Chem. Soc.* **2014**, *136*, 17308–17316.
- (49) Lakowicz, J. R. *Principles of Fluorescence Spectroscopy*; Lakowicz, J. R., Ed.; Springer US: Boston, MA, 2006.

- (50) Würth, C.; Grabolle, M.; Pauli, J.; Spieles, M.; Resch-Genger, U. Relative and Absolute Determination of Fluorescence Quantum Yields of Transparent Samples. *Nat. Protoc.* **2013**, *8*, 1535–1550.
- (51) Ye, R.; Xiang, C.; Lin, J.; Peng, Z.; Huang, K.; Yan, Z.; Cook, N. P.; Samuel, E. L. G.; Hwang, C.-C.; Ruan, G.; *et al.* Coal as an Abundant Source of Graphene Quantum Dots. *Nat. Commun.* **2013**, *4*, 2943–2948.
- (52) Tang, L.; Ji, R.; Li, X.; Bai, G.; Liu, C. P.; Hao, J.; Lin, J.; Jiang, H.; Teng, K. S.; Yang, Z.; *et al.* Deep Ultraviolet to near-Infrared Emission and Photoresponse in Layered N-Doped Graphene Quantum Dots. *ACS Nano* **2014**, *8*, 6312–6320.
- (53) Lim, S. Y.; Shen, W.; Gao, Z. Carbon Quantum Dots and Their Applications. *Chem. Soc. Rev.* **2015**, *44*, 362–381.
- (54) Zhu, S.; Zhang, J.; Liu, X.; Li, B.; Wang, X.; Tang, S.; Meng, Q.; Li, Y.; Shi, C.; Hu, R.; *et al.* Graphene Quantum Dots with Controllable Surface Oxidation, Tunable Fluorescence and up-Conversion Emission. *RSC Adv.* **2012**, *2*, 2717–2720.
- (55) Mosmann, T. Rapid Colorimetric Assay for Cellular Growth and Survival: Application to Proliferation and Cytotoxicity Assays. *J. Immunol. Methods* **1983**, *65*, 55–63.
- (56) Zhang, X.; Zhang, Y.; Wang, Y.; Kalytchuk, S.; Kershaw, S. V.; Wang, Y.; Wang, P.; Zhang, T.; Zhao, Y.; Zhang, H.; *et al.* Color-Switchable Electroluminescence of Carbon Dot Light-Emitting Diodes. *ACS Nano* **2013**, *7*, 11234–11241.
- (57) Li, X.; Rui, M.; Song, J.; Shen, Z.; Zeng, H. Carbon and Graphene Quantum Dots for Optoelectronic and Energy Devices: A Review. *Adv. Funct. Mater.* **2015**, *25*, 4929–4947.

2 Nitrogen-Doped Carbon Nanodots

3 Carbon Nanodots in Electrochemiluminescence

In this chapter the use of nitrogen-doped carbon nanodots (NCNDs) in electrochemiluminescence (ECL) technology is discussed. The chapter is divided into three main sections. Firstly, a general overview on ECL is presented. Then, the use of NCNDs as alternative and powerful co-reactant species for ECL generation is shown. Moreover, their potentiality in biosensing platforms is demonstrated. Finally, novel covalent systems based on NCNDs and ECL probes are presented, together with their extensive characterization and evaluation as self-enhanced and multi-label ECL platforms.

The work presented in this chapter has been accomplished during an Erasmus period spent in the research group of *Prof. Luisa De Cola* (Institut de Science et d'Ingénierie Supramoléculaires, Université de Strasbourg, France), with the aid of *Ms. Serena Carrara*.

Part of the work discussed in this chapter has been published as “Amine-Rich Nitrogen-Doped Carbon NanoDots as Platform for Self-Enhancing Electrochemiluminescence” in *Angewandte Chemie Int. Ed.* **2017**, *56*, 4757-4761.

3.1 Introduction

3.1.1 ECL: fundamentals and mechanisms

Electrochemiluminescence (ECL) is a redox-induced light emission in which high-energy species, generated at the electrodes, undergo a high-energy electron transfer reaction forming an excited state that emits light.¹

The excited state can be produced through the reaction of radicals generated from the same (usually) chemical species (emitter) in the so-called *annihilation* mechanism or from two different precursors (emitter and co-reactant) via *co-reactant* ECL.^{1,2}

The *annihilation* mechanism, illustrated in **Figure 3.1**, involves an electron-transfer reaction between an oxidized and a reduced species generated at an electrode by alternate pulsing of the potential.^{3,4}

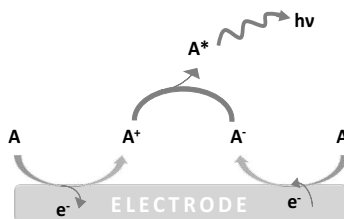
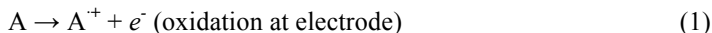


Figure 3.1 Schematic diagram describing the electron transfer reactions responsible for emission during *annihilation* ECL.

Upon the application of a potential rapidly changing from highly reductive to highly oxidative values (or viceversa), an emitter A is both oxidized and reduced to $A^{\bullet+}$ and $A^{\bullet-}$, respectively, according to equations 1 and 2.

The as-generated species react in the Nernst diffusion layer, according to equation 3, in close proximity to the electrode surface, forming an

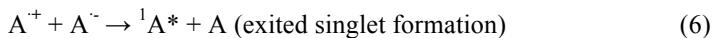
excited state A^* , which produces light emission upon relaxation to the ground state (equation 4).



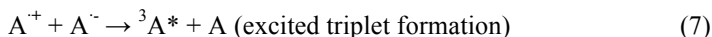
The annihilation step may occur also between radical cation and anion formed from different species. The system has an energy correlated to the redox potentials for the reaction 1 and 2, that is the enthalpy of annihilation and can be calculated from equation 5:³

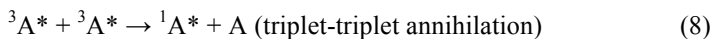
$$-\Delta H_{\text{ann}} = E_p(A/A^+) - E_p(A/A^-) - 0.16 \quad (5)$$

where $-\Delta H_{\text{ann}}$ (eV) is the enthalpy for ion annihilation, E_p is the peak potential for electrochemical oxidation or reduction, 0.16 is the entropy approximation term ($T\Delta S$) at 25°C (0.10 eV) with an additional resulting from the difference between the reversible peak potentials of the redox reaction (0.057 eV). Depending on the available energy of the annihilation reaction, the excited state is generated in the lowest excited singlet state $^1A^*$ or in the triplet excited state $^3A^*$. In the first case, the system is called *energy-sufficient system* and the reaction follow the S(Singlet)-route (equation 6):



Whereas, when the triplet excited state $^3A^*$ is produced (equation 7), it can be transformed to $^1A^*$ by triplet-triplet annihilation (TTA) (equation 8). This is called *energy-deficient system* and the reaction follows the T(Triplet)-route:





Both the redox and photophysical properties of the species involved in the generation of the emitting excited state need to satisfy some requirements. Their oxidation and reduction reactions must undergo within a potential range accessible in the employed solvent, and the produced radical ions must be sufficiently long-lived to diffuse and react with one another through a high-energy electron transfer reaction. Moreover, high photoluminescence efficiency is required. Finally, an adequate energy must be provided for the formation of the excited states. From the following equation (equation 9), an energy between 3.1 to 1.8 eV for visible range emission (~400-700 nm) can be calculated:

$$E_s = h\nu = hc/\lambda \text{ (excited triplet formation)} \quad (9)$$

where h is the Plank constant ($6.63 \cdot 10^{-34}$ J·s), ν is frequency (Hz), c is speed of light ($2.99 \cdot 10^8$ m/s) and λ is wavelength of the emission (m). Therefore, a wide potential window (from ~3.3 to 2 V) needs to be used to generate sufficiently stable radical cations and anions during *annihilation* ECL. As a result, rigorously purified and deoxygenated non-aqueous solvents are required, because the available potential range in water is too narrow to generate the required energetic precursors. For instance, *annihilation* ECL is mainly performed in inert atmosphere and non-aqueous media, such as acetonitrile, dimethyl-sulfoxide or methylene-chloride.⁴

Although *annihilation* ECL is frequently used in light-emitting electrochemical cells (LECs),⁵ the latter requirements of non-aqueous solution and inert atmosphere are noteworthy limitations, which can be overcome using the *co-reactant* pathway.

In *co-reactant* ECL, the formation of radicals in aqueous solutions, and the subsequent generation of ECL, is attainable without potential cycling and at less extreme potentials compared to common organic

solvents, opening up a wide range of bioanalytical applications. In contrast to *annihilation* mechanism, *co-reactant* ECL involves two precursors: a luminophore (emitter) and a reagent called co-reactant, during a single potential step or scan.^{2,3}

Depending on the polarity of the applied potential, both the emitter and the co-reactant are first oxidized or reduced at the electrode surface. The as-formed co-reactant radicals undergo a fast chemical degradation producing powerful oxidized or reduced species, which react with the oxidized or reduced luminophore, producing its excited state that emits light. Thus, depending on the nature of the co-reactant, “oxidative-reduction” or “reductive-oxidation” mechanisms are possible. In the former case, the luminophore is oxidized at the electrode surface and then reduced by the co-reactant intermediate. In the latter, after the luminophore reduction, a strong oxidizing co-reactant radical react with the luminophore.

Considering the one potential step generation, *co-reactant* ECL shows several advantages over *annihilation* ECL. First, there is no need for wide potential windows, consequently solvents with a narrow potential window and aqueous solutions can be also used. Furthermore, there is no need of rigorously purified and deoxygenated solvents because the oxygen and water quenching is less efficient. Accordingly, reactions can be carried out in air. Finally, fluorophores with reversible electrochemical oxidation or reduction can also be used.

To summarize, as ECL is a method of producing light at an electrode, it represents an ideal marriage between electrochemical and spectroscopic methods. Electrochemistry provides very convenient ways to ignite a chemiluminescence (CL) reaction through the generation of a pair of high-energy reactants, thus leading to electrogenerated chemiluminescence. Comparing with the CL, where light emission is initiated by mixing the necessary reagents and can

be controlled by manipulation of the fluid flow, the light emission in ECL is initiated and controlled by application of electrode potential. Therefore, ECL exhibits the great advantage that the process takes place *in situ* (at the electrode surface) and at will (upon the application of the electrochemical pulse).

Moreover, despite ECL being typically confined at the electrode surface, the generation of excited species through an electrochemical stimulus, rather than via light excitation, generally displays improved signal to noise ratios with respect to photoluminescence. As a consequence, light scattering and background fluorescence in ECL are minimized.

Taking advantage of a relatively low-cost instrumentation, the analytical applications of ECL have been widely developed over the last 20 years. To date, ECL systems are commercialized, *i.e.* by Roche Diagnostics Corp. and by MesoScale Diagnostic for a variety of assays, with a particular emphasis on immunoassay for the detection of many important biological molecules and macromolecules, such as DNA,^{6,7} cancer biomarker proteins,⁸ cytochromes,⁹ cocaine,¹⁰ toxins or hormones.¹¹

3.1.2 Luminophores

A chemical species to be an efficient ECL emitter has to fulfil various electrochemical and photophysical requirements, along with other criteria depending on the envisaged application. For instance, in ECL-based biological assays, accessible binding sites for bioconjugation, together with good solubility and intense and stable ECL signal, are crucial.

In the past several years, numerous organic and inorganic compounds have been shown to be capable of producing ECL. ECL-emitting species are usually classified into three categories: (*i*) inorganic systems, which mainly cover organometallic complexes; (*ii*) organic

systems, which mainly cover polycyclic aromatic hydrocarbons and (iii) nanomaterial systems.

3.1.2.1 Inorganic systems

Transition metal complexes and, in particular, ruthenium and iridium complexes, play a privileged role among the ECL-emitting inorganic systems. Indeed, they combine a rich and highly stable redox behavior, with long-lived, highly luminescent excited states. However, limited water solubility together with the, usually, difficult introduction of binding sites without affecting their photophysical/electrochemical properties, restrict the possible candidates.

Ruthenium polypyridine complexes are the most successfully used ECL luminophores with broad applications, because of great luminescence efficiency, reversible electrochemical behavior, chemical stability and versatility.¹²⁻¹⁵ In particular, Ruthenium(II) tris(2,2'-bipyridyl) ($\text{Ru}(\text{bpy})_3^{2+}$)-based ECL has been developed into a mature, highly sensitive bioanalytical technology widely employed in basic research laboratories, pharmaceutical industry, clinical settings, and homeland security.¹⁶⁻²⁵ For ECL immunoassay, it serves as a protein labeling reagent, which, upon electrochemical oxidation generates luminescence through its metal-to-ligand charge-transfer (MLCT) excited state. It is practically the only luminophore employed so far in the ECL commercial applications. Ru^{2+} is a d^6 system with electron configuration $[\text{Kr}]4d^6$. In $\text{Ru}(\text{bpy})_3^{2+}$, the metal is surrounded by three bidentate polypyridine ligands that are usually colorless molecules with σ -donor orbitals localized on the nitrogen atoms and π -donor and π^* -acceptor orbitals delocalized mainly on the aromatic rings.¹² $\text{Ru}(\text{bpy})_3^{2+}$ with an ECL efficiency of $\Phi_{\text{ECL}} = 0.05$ produces an emitting charge-transfer triplet with an efficiency that

approaches unity and is comparable with photoluminescence data of $\Phi_{\text{PL}} = 0.05$.²⁶

Many attempts have been made in designing or modifying the ligands of ruthenium complexes to improve molecular recognition ability. For example, ruthenium complexes containing crown ether moieties covalently bonded to bipyridyl or phenanthroline ligands have been used for metal-cation sensing.²⁷⁻²⁹ Ruthenium complexes with dipyrido[3,2-a:2',3'-c]phenazine (dppz) ligand ($[\text{Ru}(\text{bpy})_2\text{dppz}]^{2+}$) are popular “light-switch” molecules. They have been found to intercalate into DNA with high affinity ($K_a = 10^6 \text{ M}^{-1}$), due to the extended aromatic structure, and display an intense photoluminescence otherwise not visible. Their ECL emission increases about 1000 times when they intercalate into the nucleic acid structure (**Figure 3.2**). This switch behavior is usually ascribed to the shield of the phenazine nitrogens from the solvent upon intercalation, which results in a luminescent excited state, and holds great promise for DNA-related biosensors.³⁰

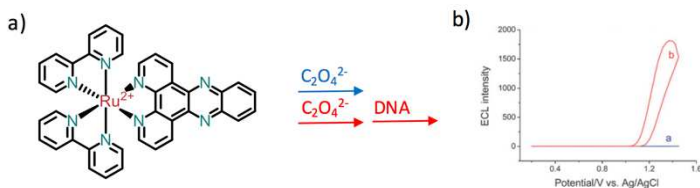


Figure 3.2 a) Scheme of ECL switch based on $[\text{Ru}(\text{bpy})_2\text{dppz}]^{2+}$ and DNA; b) ECL intensities in 5 mM pH 5.5 oxalate solution containing 0.1 mM $[\text{Ru}(\text{bpy})_2\text{dppz}]^{2+}$ (curve a) and 0.1 mM $[\text{Ru}(\text{bpy})_2\text{dppz}]^{2+}$ + 0.16 mM DNA (curve b).³⁰

In order to increase sensitivity, a variety of multi-metallic ruthenium complexes have been designed and studied.³¹⁻³⁵ The presence of multiple redox centers increases the number of charge recombination

events, enhancing the ECL signal. However, the accessibility of the redox centers to the electrode surface and to the co-reactant species must be preserved. De Cola *et al.* reported large dendritic complexes [Ru2-Dend]⁴⁺, [Ru4-Dend]⁸⁺, and [Ru8-Dend]¹⁶⁺ containing two, four, and eight Ru(bpy)₃²⁺ units, respectively, bound to a modified progesterone molecule.³¹ In phosphate buffer solutions no variations of the intensity integrals were observed, because slower diffusion plays an important role in limiting the ECL intensity enhancement. However, in heterogeneous assays where the transport of the ECL ruthenium active species to the electrode surface does not occur by diffusion, the limitations due to the small diffusion coefficients of the large complexes are overcome. As a result, upon increasing the number of ruthenium units bound to the dendritic structure that labels a biological molecule (*i.e.* antigen, antibody), the ECL signal of the immunoassays can increase linearly with the number of the active ruthenium centers, although for large systems, such as [Ru8-Dend]¹⁶⁺, an intense background signal due to nonspecific binding led to lower ECL sensitivity.

Most of the ruthenium complexes emit in the region between 600 and 650 nm and it is very difficult to tune the color of ruthenium complexes due to the limited ligand-field splitting energies of central metal ions. Recently, a new series of acrylate-containing ruthenium (tris)bipyridine-based complexes with photoluminescence emission maxima ranging from 640 to 700 nm have been reported.³⁶ The large red shift in the photoluminescence emission (**Figure 3.3**) probably arises from a decrease in their ligand-based lowest unoccupied molecular orbital (LUMO) value and the resulting lower energy triplet metal-to-ligand charge-transfer excited state transitions. Consequently, an ECL emission maxima for these compounds ranging from 680 to 722 nm was observed, which is the lowest-energy

emission reported so far in light-emitting electrochemical cells (LECs) based on tris-chelated ruthenium complexes.

In this context, iridium (III) complexes, containing in particular cyclometalated moieties, represent a promising alternative for color tuning due to higher ligand-field splitting energies of the trivalent iridium ion. Blue-shifted ECL emission can be accomplished by stabilizing the highest occupied molecular orbital (HOMO) via anchoring electron-withdrawing substituents on the cyclometalated ligands.³⁷⁻⁴¹ For instance, introducing fluorine or methylsulfone electron-withdrawing substituents, blue- or green-emitting iridium complexes have been reported (**Figure 3.4**).^{38,39}

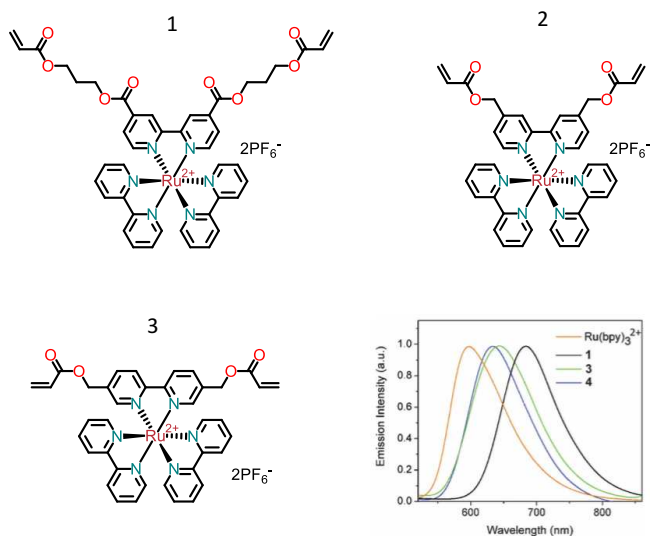


Figure 3.3 Acrylate-containing Ru(bpy)₃²⁺-based coordination complexes (1-3) and their normalized photoluminescence spectra obtained from thin solid films together with Ru(bpy)₃²⁺ 2PF₆⁻ (excitation wavelength at 450 nm).³⁶

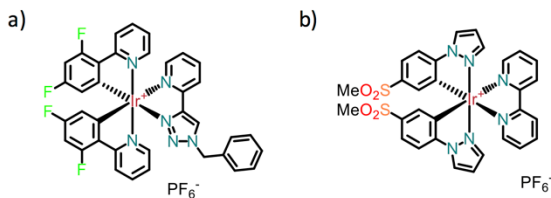


Figure 3.4 a) Blue-emitting iridium(III) complex; b) green-emitting iridium(III) complex.

Most iridium(III) complexes have low solubility in aqueous solutions limiting their application in bioanalysis. However, some iridium(III) complexes emerged as promising alternatives to traditional ruthenium(II) complexes for ECL detection in the aqueous medium. For instance, a water-soluble iridium(III) diimine complex with appended sugar showed an ECL signal much higher than that of Ru(bpy)₃²⁺.⁴²

3.1.2.2 Nanomaterial systems

Since the ECL phenomenon of silicon nanocrystals was first reported in 2002,⁴³ a series of miscellaneous nanomaterials with various compositions, sizes and shapes, such as nanoparticles and nanotubes prepared from metals, semiconductor, carbon or polymeric species, have also been used as ECL emitters in the recent years.⁴⁴⁻⁵⁴ Among them, quantum dots (QDs) are particularly attractive and various ECL investigations have been reported.^{43,55-59} They show remarkable properties, such as high fluorescence quantum yields, stability against photobleaching, and size-controlled luminescence properties.

However, apart from some examples, low solubility and low stability of the oxidized and reduced species usually limit their applications. ECL of water soluble CdTe QDs has been recently reported. Stable and intense ECL was obtained from mercaptopropionic acid-capped

CdTe QDs at about 1.2 V vs. Ag/AgCl in phosphate buffer (pH 9.3). The ECL emission involved the generation of superoxide ions at the ITO electrode surface, which then injected an electron into CdTe QDs to form CdTe anion species. Then, the collisions between the CdTe anion species and the oxidation products led to the formation of species in an excited state that emitted light at around 580 nm (**Figure 3.5**).⁵⁷

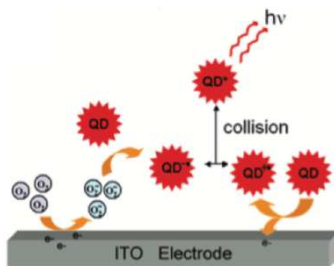


Figure 3.5 Anodic ECL mechanism of QDs.⁵⁷

Despite that many nanomaterials-based luminophores have been developed, they generally have certain disadvantages, such as uneven size distribution and great changes of luminescent properties after interaction with other substances. Instead, the combination of traditional light-emitting reagents with nanomaterials by using the latter as ECL labels carriers, is a very promising way to develop new efficient luminophores.^{60,61}

Great efforts have been made to produce strong ECL signal improving the ECL sensitivity through the use of multiple ECL labels loaded on metal nanoparticles, carbon nanotubes, micro-sized polystyrene microspheres and silica nanoparticles.^{8,62-76}

However, most studies report on the use of nanomaterials with sizes between 100 and 7 nm for the development of hybrid systems resulting in typically low diffusion coefficients. This yields lower

ECL efficiencies in solution,⁷⁷ and the immobilization of the ECL probe on a solid electrode surface can become a crucial strategy to overcome diffusion limitations.⁷⁸

Moreover, in order to generate the ECL signal, the redox centers must be in very close contact with the electrode surface and they must be able to diffuse towards it. It has been reported that the encapsulation of ruthenium or iridium complexes in silica nanoparticles is an efficient strategy to protect them from water and oxygen quenching. However, only a fraction (*c.a.* 65%) of the ruthenium complexes inside the nanoparticle is electrochemically active. Their larger size does not promote an ECL enhancement in solution and the hindered contact with the electrode surface limits the electrons tunneling (**Figure 3.6a**).⁷⁶

Additionally, possible quenching phenomena in hybrid systems should affect the optical properties of the redox centers. For example, it was reported the quenching effect of gold nanoparticles (AuNPs) on the photoluminescence and ECL of ruthenium complexes in ruthenium-functionalized nanoparticles (**Figure 3.6b**).⁷⁵

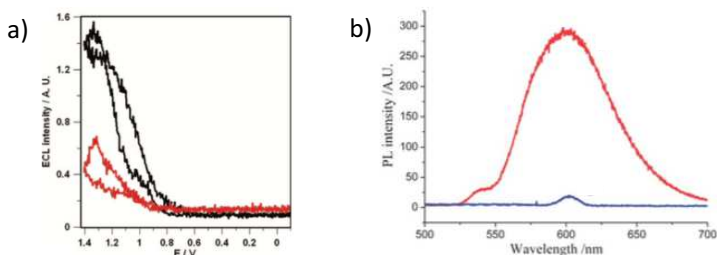


Figure 3.6 a) ECL/E profiles of a $\text{Ru}(\text{bpy})_3^{2+}$ (black line) and $\text{Ru}(\text{bpy})_3^{2+}$ covalently doped silica nanoparticles (red line) solution having the same ruthenium absorption ($2 \cdot 10^{-5}$ M);⁷⁶ b) photoluminescence spectra of $\text{Ru}(\text{bpy})_2(\text{NH}_2\text{-phen})^{2+}$ (red line) and AuNPs synthesized with $\text{Ru}(\text{bpy})_2(\text{NH}_2\text{-phen})^{2+}$ (blue line).⁷⁵

3.1.3 Co-reactants

Co-reactant species have to obey to some stringent requirements, such as matching redox potentials, fast charge transfer kinetics and rapid degradation routes to produce a high-energy radicals capable to initiate the ECL process. Moreover, good solubility and high chemical stability are two crucial conditions.²

A typical co-reactant used for reductive-oxidation ECL is peroxydisulfate, which, upon reduction, forms a strong oxidant intermediate $\text{SO}_4^{\cdot-}$,^{79,80} while oxalate is a classical oxidative-reduction co-reactant, which loses CO_2 , producing $\text{CO}_2^{\cdot-}$ as strongly reducing agent.^{14,81,82}

Currently, alkyl amines have become the most representative class of oxidative-reduction co-reactants. Upon deprotonation, they form strongly reducing radical species. Among them, tripropylamine (TPA) is the most widespread one,^{83,84} and provides the optimum ECL signal when used in combination with $\text{Ru}(\text{bpy})_3^{2+}$, so that the system $\text{Ru}(\text{bpy})_3^{2+}/\text{TPA}$ is widely used in commercial ECL application.^{2,3} TPA has several disadvantages, being toxic, corrosive, volatile and scarcely soluble. Moreover it needs to be used in high concentrations (usually up to 100 mM) to obtain good sensitivity, eventually resulting in interferences with target biochemical analytes.⁸⁵

However, only a few co-reactants are more efficient than TPA. In some reports 2-(dibutylamino)ethanol (DBAE),⁸⁶ and *N*-butyldiethanolamine (BDAE) as co-reactants are used.⁸⁷ More recently, *N*-(3-amino-propyl) diethanolamine (APDEA) has been explored as a potential co-reactant for enhancing $\text{Ru}(\text{bpy})_3^{2+}$ ECL. For instance, APDEA is more efficient than tripropylamine at gold (Au) and platinum (Pt) electrodes although it has primary amino groups besides tertiary amines. The ECL intensities of the $\text{Ru}(\text{bpy})_3^{2+}/\text{APDEA}$ system are approximately 10 and 36 times stronger than that

of $\text{Ru}(\text{bpy})_3^{2+}/\text{TPA}$ system and about 1.6 and 1.14 times stronger than that of $\text{Ru}(\text{bpy})_3^{2+}/\text{BDAE}$ system at Au and Pt electrodes, respectively.⁸⁸

Among the amine-based co-reactants, β -nicotinamide adenine dinucleotide reduced salt (NADH) is worth to be mentioned.⁸⁹ It was found that NADH oxidizes to NADH^+ , which deprotonates forming highly reducing species NAD \cdot . On the other hand, β -nicotinamide adenine dinucleotide (NAD^+) has an aromatic structure and does not undergo electrochemiluminescent reaction. For this reason, ECL is used for the detection of NADH, especially in enzymatic systems where NADH is produced from NAD^+ .^{90,91}

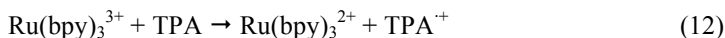
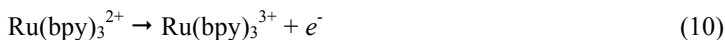
Recently, suitably designed fluorophores with groups acting as co-reactant have attracted a lot of attention. When an emitter and its co-reactant group exist in the same molecular unit through covalently linking, it is possible to observe a newly developed ECL reaction pattern named self-enhanced ECL. In this systems the electron transfer between the luminophore and the co-reactant group occurs intramolecularly, showing several advantages when compared to the intermolecular ECL reaction. They include shorter electronic transmission distance, improved luminous stability, simpler operation, decreased measurement error, and use of less reagent. Moreover, the intramolecular self-enhanced ECL reaction could obviously reduce the loss of energy caused by the relaxation effect in the intermolecular reaction when the co-reactants diffuse to the electrode surface, resulting in a noteworthy luminous efficiency enhancing.⁹²⁻¹⁰²

3.1.4 $\text{Ru}(\text{bpy})_3^{2+}/\text{TPA}$ as ECL model system

$\text{Ru}(\text{bpy})_3^{2+}/\text{TPA}$ system exhibits high ECL efficiency and represent the most common luminophore/ co-reactant couple, which forms the basis of commercial immunoassays and DNA analyses,^{3,103} and can

be considered as an ECL standard. The general mechanism is illustrated in **Figure 3.7** and can be represented by the following reactions:^{83,104}

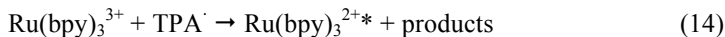
Oxidation step:



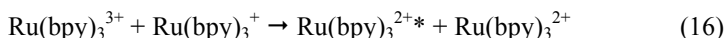
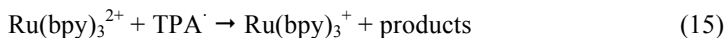
Deprotonation:



Excited state formation 1 (direct oxidation):



Excited state formation 2:



Light emission:

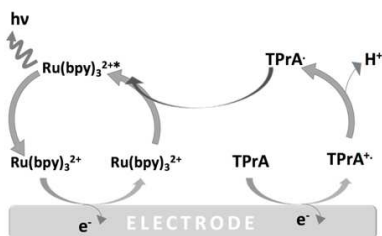
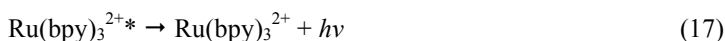


Figure 3.7 Schematic diagram describing the electron transfer reactions responsible for emission during a *co-reactant* ECL reaction involving $\text{Ru}(\text{bpy})_3^{2+}$ and TPA.

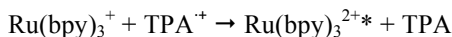
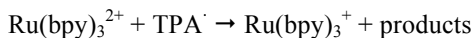
During the anodic scan, both $\text{Ru}(\text{bpy})_3^{2+}$ and TPA are oxidized (equations 10-11). The oxidation of TPA generates a strongly reducing species and shows a broad wave due to the preceding of the acid-base equilibrium ($\text{p}K_a$ of ~ 10.4).¹⁰⁵

TPA can be oxidized by direct reaction at the electrode surface (equation 11) as well as via “catalytic route” where electrogenerated $\text{Ru}(\text{bpy})_3^{3+}$ reacts with TPA (equation 12). The relative contribution of the two routes depends on a variety of factors, such as the relative concentrations of $\text{Ru}(\text{bpy})_3^{2+}$ and TPA.¹⁰⁴

When the $\text{Ru}(\text{bpy})_3^{2+}$ concentration is relatively high, the co-reactant oxidation mainly proceeds via the catalytic pathway. Instead, direct oxidation plays an important role in the ECL process particularly in dilute $\text{Ru}(\text{bpy})_3^{2+}$ solutions (less than approximately micromolar) and concentrated TPA.¹⁰⁴ The direct oxidation of TPA produces a short-lived intermediate radical cation species, which undergo a fast deprotonation forming a strong reducing free radical (equation 13) able to reduce $\text{Ru}(\text{bpy})_3^{3+}$ to the excited state $\text{Ru}(\text{bpy})_3^{2+*}$ (equation 14), that finally emits light (equation 17).

For high concentration of TPA, the ECL profile shows two peaks.^{77,104}

The previous discussed mechanism explains only the peak at higher potential, which corresponds to the direct oxidation of $\text{Ru}(\text{bpy})_3^{2+}$. Miao and Bard shed light on the peak at lower potential through the oxidation of $\text{Ru}(\text{bpy})_3^{2+}$ by TPA radical cation. Indeed, they reported the possibility to produce the ruthenium excited state without the direct oxidation of $\text{Ru}(\text{bpy})_3^{2+}$, in a mechanism that involves reactive radical cation of TPA, according to the following reactions:⁷⁷



To summarize, the excited state of $\text{Ru}(\text{bpy})_3^{2+}$ may be produced via three different routes: (i) $\text{Ru}(\text{bpy})_3^{3+}$ reduction by TPA; (ii)

$\text{Ru}(\text{bpy})_3^{3+}$ and $\text{Ru}(\text{bpy})_3^+$ annihilation reaction; (iii) $\text{Ru}(\text{bpy})_3^+$ oxidation by TPA^+ radical cation. The ECL intensity of the first and second waves are proportional to the concentration of both $\text{Ru}(\text{bpy})_3^{2+}$ and TPA in a large dynamic range,^{77,83,104,105} with detection limits of 0.5 pM for $\text{Ru}(\text{bpy})_3^{2+}$,¹⁰⁶ and 10 nM for TPA.⁸⁹

3.1.5 Analytical applications

Over the past two decades, ECL developed rapidly and has emerged as a very powerful analytical technique, since the ECL intensity is proportional to the concentration of the ECL luminophore or to the concentration of the co-reactant. In the presence of high and constant concentrations of co-reactant, ECL intensity linearly depends on the concentration of ECL emitter, in a wide dynamic range. Alternatively, in the presence of constant emitter concentration, ECL signal depends on co-reactant concentration.

ECL can be easily integrated in analytical systems such as capillary electrophoresis (CE), high performance liquid chromatography (HPLC) and flow injection analysis (FIA).

ECL-based separation/detection methods offer a number of advantages when compared to other commonly used techniques, including UV-Vis or fluorescent detection, such as powerful resolving ability, good selectivity, high sensitivity and easy sample preparation without the need of sample pre-treatment.¹⁰⁷ The analytes should act as ECL co-reactants, and, consequently, lot of efforts have been made to introduce appropriate groups to initially less or non-ECL sensitive analytes such as amino acids and fatty acids.^{108,109}

Amino acids such as proline, valine and leucine can be successfully detected in CE-ECL system with detection limit in the μM - nM concentration range.¹⁰⁸ Moreover, CE-ELC was successfully used to investigate drug-protein binding and three basic drugs, such as

pridinol, procyclidine and trihexyphenidyl, were successfully separated by CE with end-column Ru(bpy)₃²⁺ ECL detection.¹¹⁰ In HPLC-ECL systems, besides pre- and post- column methods,^{111,112} the immobilization of Ru(bpy)₃²⁺ on a solid electrode surface can provide several advantages, such as reducing the consumption of expensive reagents, simplifying experimental design, and creating a regenerable detector based on the Ru(bpy)₃²⁺ recycled on the electrode surface during the ECL reaction. For example, a simple method based on reverse-phase HPLC with Ru(bpy)₃²⁺-modified single Pt wire as ECL detector for the determination of metoclopramide, itopride and sulphiride was developed. This method allowed the simultaneous detection of these antiemetic drugs in human serum, offering short analysis times, low baseline and background noise levels.¹¹³

One of the most important applications of ECL is its use in diagnostic assays.^{5,114} ECL assays are performed either in solution phase or in solid phase. Solid phase is usually used for biomolecules with poor or no co-reactant ability, which are linked to the ECL labels and then immobilized onto a solid substrate (like screen printed electrode, micro-sized polystyrene beads or magnetic beads). The ECL signal is proportional to the concentration of the analyte in the presence of the ECL co-reactant.

Conventional antigen-antibody reactions and ECL have also been combined in a technology commonly used for commercially available ECL immunoassay purchased by Roche Diagnostics.¹¹⁵ The sample is combined with a reagent containing the biotinylated-capture antibody and a ruthenium-labelled secondary antibody. During the incubation step, the antibodies capture the target molecules and the biotinylated moiety is then attached to the streptavidin coated magnetic particles. The samples are then drawn into the ECL measuring cell along with a buffer containing TPA. A magnet located

under the electrode immobilized the microparticles at the electrode surface and all the unbound reagents are washed out from the cell. The magnet is then removed and a potential is applied to the electrode initiating the ECL process.

3.1.6 Aim of the project

The aim of this project rely on the use of carbon nanodots in ECL technology. It is actually one of their less explored application field, which hold great promise for bioanalytical purpose.

In this context, there is an extended research devoted on alternative co-reactant species since the co-reactant pathway plays a dominant role in the current ECL field.

In particular, oxidative-reduction co-reactants for $\text{Ru}(\text{bpy})_3^{2+}$ ECL are of great interest to extend ECL applications and improve ECL efficiencies.

We envisage that carbon nanodots can be an ideal candidate for this role, but their use as co-reactants is still at the initial stages.^{116,117} However, apart from a recent study in which benzylic alcohol moieties were identified as co-reactant sites,¹¹⁶ the identification of the functional group responsible of their co-reactant behavior is difficult, though fundamental.

The NCNDs presented in *Chapter 2* show abundant amino groups on their surface. Since they are the most efficient and used co-reactant units in combination with $\text{Ru}(\text{bpy})_3^{2+}$, the first part of this project focuses on NCNDs bearing primary and tertiary alkyl amine groups on the surface as co-reactant for $\text{Ru}(\text{bpy})_3^{2+}$ ECL generation. Their facile and low cost synthesis, good solubility in water and biocompatibility, make our NCNDs a promising alternative to the toxic TPA. Moreover, in an attempt to evaluate the possible use of this novel ECL system NCNDs/ $\text{Ru}(\text{bpy})_3^{2+}$ as biosensing platform,

the detection of epinephrine, important neurotransmitter studied for diagnosis of neurological disorders, is discussed.

The second part of this project builds on the active research field of ECL systems functionalized with nanomaterials for ECL signal enhancement. A variety of nanomaterials and in particular nanoparticles (NPs), such as gold or silicon NPs, have been investigated with transition metal complexes as emitters in the framework of ECL hybrid systems. However, carbon nanodots-based hybrid ECL system has not so far been explored. For this purpose, we investigated the use of carbon nanodots as carrier for ECL labels.

Our NCNDs presents outstanding advantages over other nanoparticles. Their easily functionalizable surface, without the need of additional treatments after the synthesis, and their small size, together with all the above mentioned appealing characteristics, make NCNDs a particularly valuable carrier for ECL active species.

We prepared NCND-based nanohybrids bearing multiple ruthenium or iridium complexes as ECL labels. An extensive study was devoted to their redox and photophysical properties in order to evaluate the NCNDs effect on the ECL active units. Indeed, as previously discussed, the major concern about nanomaterial-based hybrid systems is associated to the proximity of the redox centers to the electrode surface, their ability to diffuse to it and the occurrence of quenching phenomena influencing their optical and electrochemical properties.

To conclude, the novel systems were evaluated for self-enhanced ECL, which is, as discussed in the introduction, a promising ECL reaction pattern with enhanced luminous efficiency. Additionally, we investigated the immobilization of these hybrids on the electrode surface for signal intensity enhancement due to the presence of a plurality of signal-generating units on each NCNDs.

3.2 NCNDs as ECL co-reactant

In this section, the primary amino groups on the NCNDs (synthesis and characterization are described in *Chapter 2*) were investigated as oxidative-reduction co-reactants for $\text{Ru}(\text{bpy})_3^{2+}$ ECL generation. Moreover, since generally the ECL intensity increases using amines as co-reactant in the order primary < secondary < tertiary,⁸⁹ we converted the primary groups of NCNDs to tertiary amines. The synthesis, characterization and co-reactant behavior of the methylated-NCNDs (mNCNDs) is discussed (**Figure 3.8**). As a proof of concept of the potentiality of the $\text{Ru}(\text{bpy})_3^{2+}/(\text{m})\text{NCNDs}$ system as biosensing platform, the detection of a bioanalyte (epinephrine) is reported.

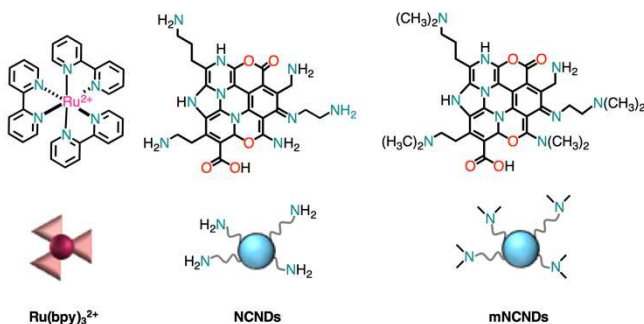


Figure 3.8 Systems studied in this section. Tris(2,2'-bipyridine)ruthenium(II) ($\text{Ru}(\text{bpy})_3^{2+}$) on the left, nitrogen-doped carbon nanodots (NCNDs) in the middle and methylated-NCNDs (mNCNDs) on the right.

3.2.1 NCNDs/Ru(bpy)₃²⁺ system

To be active as ECL co-reactants, the amino functional groups should have a hydrogen atom attached to the α -carbon, in order to produce a strongly reducing intermediate, which supplies chemical energy to generate the luminophore emissive excited state.¹¹⁸

As discussed in *Chapter 2*, the abundant presence of primary amino groups on NCNDs was confirmed by a strongly positive Kaiser test. In addition, the reported 2D-NMR studies of NCNDs demonstrated the presence of $-\text{CH}_2\text{NH}_2$ groups. Also, the high current and steep slope of the oxidation peak (+1.14 V vs SCE) in the cyclic voltammogram (CV) of NCNDs suggested that a high number of amino groups on the NCNDs surface can be easily oxidized. Additionally, the process was found to be a mono-electron oxidation, by using ferrocene as reference.¹¹⁹

To gain further information on the amino groups present on the NCNDs surface we have measured the CV of a variety of amine derivatives (**Figure 3.9**): aromatic, aliphatic, primary, secondary and tertiary, in the same solvent and at the same concentration. Oxidation potentials E_{ox} are listed in **Table 3.1**. Among the amines investigated, the cyclic voltammogram of NCNDs shows significative similarities with those of phenethylamine and benzylamine (**Figure 3.9a**, brown and green lines).

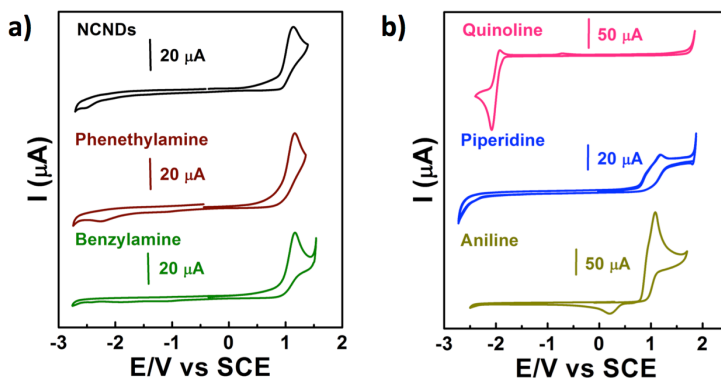


Figure 3.9 CVs of a) NCNDs (black line), phenethylamine (brown line), benzylamine (green line), b) quinolone (pink line), piperidine (blue line), 1 mg/mL aniline (dark yellow line) (concentration of 1mg/mL for all), in DMF using TBAPF₆ as supporting electrolyte on GC. Scan rate 100 mV/s.

Table 3.1 Electrochemical data of NCNDs and different amines: E_{ox} (V) vs SCE, 0.1 M TBAPF₆/DMF. GC working electrode, 298 K, $v=0.1$ V/s.

	E_{ox} (V)
NCNDs	+1.15
Phenethylamine	+1.15
Benzylamine	+1.16
Piperidine	+1.20
Aniline	+1.08

These results suggest that the NCNDs amino groups may have a hydrogen atom attached to the α -carbon. Therefore, these amino

groups should be capable of forming reductive or oxidative species during a unidirectional voltammetric scan.³

Finally, it was also determined the diffusion coefficient of NCNDs (**Figure 3.10**) observing that the process is diffusion controlled. For this purpose, cyclic voltammetric experiments at different scan rate from 0.05 to 1 V/s were performed and the Randles–Sevcik equation was applied (see experimental section). It was determined a value of $5.4 \cdot 10^{-6} \text{ cm}^2/\text{s}$.

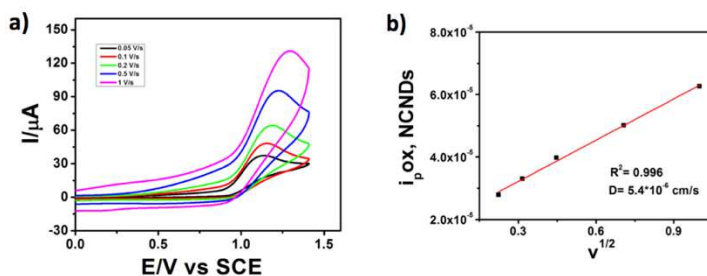


Figure 3.10 a) CVs of NCNDs 1 mg/mL, in DMF using TBAPF₆ as supporting electrolyte on GC. Scan rate from 0.05 V/s to 1 V/s, potential referred to SCE at room temperature using platinum as counter electrode; b) i_p vs $v^{1/2}$.

Since Ru(bpy)₃²⁺ and NCNDs have almost the same HOMO values (-6.1 and -5.7 eV respectively), both species can be oxidized at the electrode surface upon applying a positive voltage. Thus, the Ru(bpy)₃²⁺ ECL signal of a 0.1 mM Ru(bpy)₃²⁺ solution in PBS (pH = 7.4) was recorded upon addition of NCNDs (0.1 mg/mL) at a glassy carbon electrode (during a cyclic voltammetry between +0.5 V and +1.4 V) and compared to the one recorded without NCNDs (**Figure 3.11**, bottom part).

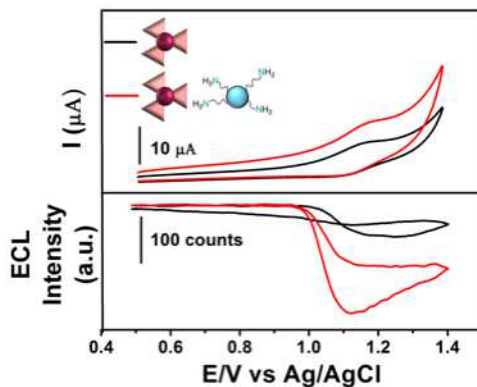


Figure 3.11 CV (upper part) and ECL (bottom part) potential curves of 0.1 mM $Ru(bpy)_3^{2+}$ (black lines) and $Ru(bpy)_3^{2+}/NCNDs$ system (red lines) in PBS (pH = 7.4) on GC electrode. Scan rate 0.05 V/s.

$Ru(bpy)_3^{2+}$ background ECL emission in aqueous solutions can be attributed to a light-emitting reduction of $Ru(bpy)_3^{3+}$ by OH^- ions (chemiluminescence) or other reducing agents, rather than the annihilation reaction.¹²⁰⁻¹²³ The presence of NCNDs (**Figure 3.11**, bottom part, red line) results in a four-time intensity enhancement of the $Ru(bpy)_3^{2+}$ ECL signal rising at +1.0 V and peaking at +1.1 V (**Figure 3.11**, bottom part, black line).

This result confirms the NCND co-reactant behavior during the oxidation process, which can be further corroborated by the higher ECL signal of $Ru(bpy)_3^{2+}$ upon increasing the concentration of NCNDs from 0.002 to 0.1 mg/mL (**Figure 3.12**).

In order to prove the efficiency of our system over time, several cycles were performed, scanning between +1.1 V and -0.9 V, at a rate of 0.05 V/s. In contrast to TPA, the ECL response with NCNDs is relatively constant for more than 15 cycles (**Figure 3.13**), revealing their great electrochemical stability, the abundant presence of available amino

groups for further ECL cycles and their consequent eligibility for biosensing platforms.

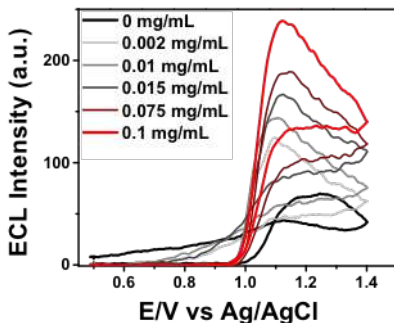


Figure 3.12 ECL intensity during a scan potential of 0.1 mM PBS solution of $\text{Ru}(\text{bpy})_3^{2+}$ upon addition of different concentrations of NCNDs.

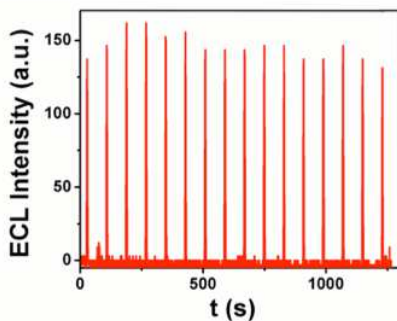


Figure 3.13 ECL responses of $\text{Ru}(\text{bpy})_3^{2+}/\text{NCNDs}$ system in PBS solution obtained during a continuous potential scan between +1.1 V and -0.9 V. 16 cycles under scan rate 0.05 V/s.

CV measurements were performed to shed light on the co-reactant mechanism. The CV of a 0.1 mM PBS (pH = 7.4) solution of $\text{Ru}(\text{bpy})_3^{2+}$ shows the typical reversible oxidation peak at +1.1 V vs

Ag/AgCl (**Figure 3.11**, upper part, black line). However, upon addition of 0.1 mg/mL NCNDs (**Figure 3.11**, upper part, red line) the intensity of the oxidation peak of $\text{Ru}(\text{bpy})_3^{2+}$ became higher, while the reduction peak becomes lower. This behavior is commonly observed in the system $\text{Ru}(\text{bpy})_3^{2+}/\text{TPA}$ and suggests a NCND catalytic effect on the $\text{Ru}(\text{bpy})_3^{2+}$ oxidation.⁷⁷

Therefore, the following mechanism can be proposed (**Figure 3.14**). Upon oxidation, the amino groups of NCNDs become a unstable reductive intermediate able to form the excited-state $\text{Ru}(\text{bpy})_3^{2+*}$ through highly energetic electron transfer. The latter emits light and produces $\text{Ru}(\text{bpy})_3^{2+}$, which in turn can be re-oxidized for a new cycle.

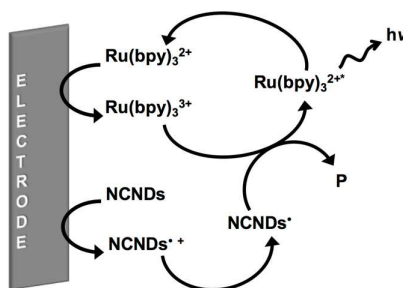


Figure 3.14 Proposed ECL mechanism for $\text{Ru}(\text{bpy})_3^{2+}/\text{NCNDs}$ system.

3.2.2 mNCNDs/ $\text{Ru}(\text{bpy})_3^{2+}$ system

The primary groups of NCNDs were converted to tertiary amines through a one-pot Eschweiler-Clarke methylation reaction (see experimental section for details). The completion of the reaction was checked with the Kaiser test (**Figure 3.15** and experimental section for details), and the methylated NCNDs, denoted as mNCNDs, were fully characterized.

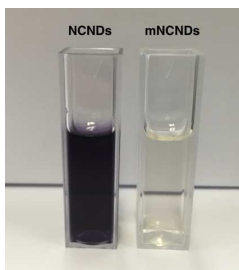


Figure 3.15 Photographs of colorimetric Kaiser Test of NCNDs (left) and mNCNDs (right).

The changes observed in their photophysical properties are consistent with the NCNDs surface modification (**Figure 3.16**). While the UV-Vis absorption spectrum did not show significant differences compared to the one of NCNDs (reported in *Chapter 2*), mNCNDs showed the typical excitation wavelength-dependent FL with an optimal emission at an excitation wavelength (330 nm) different compared to NCNDs, and a FLQYs of around 8%.

As discussed in *Chapter 2*, the surface of NCNDs significantly affects the FL properties because it determines the trapping of excitons under excitation. Therefore, the different FL features observed for mNCNDs compared to NCNDs (reported in *Chapter 2*) can be explained with the surface modification induced by the methylation reaction.

The CV of mNCNDs exhibits a new peak at +0.80 V vs SCE, which shows strong similarity with the one observed in the CV of TPA (at +0.87 V vs SCE) (**Figure 3.17**) and can be, therefore, associated to the formation of tertiary amines on the surface of mNCNDs.

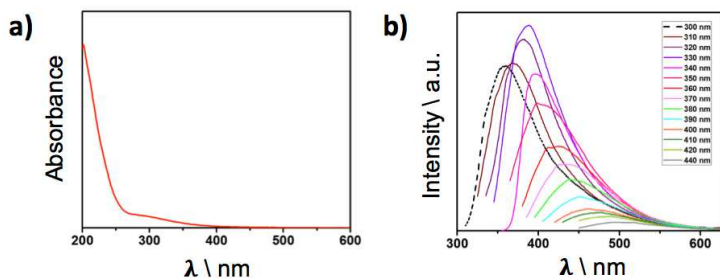


Figure 3.16 a) UV-Vis absorption spectrum of mNCNDs in water; b) FL spectra of mNCNDs in water (298 K) at different excitation wavelengths.

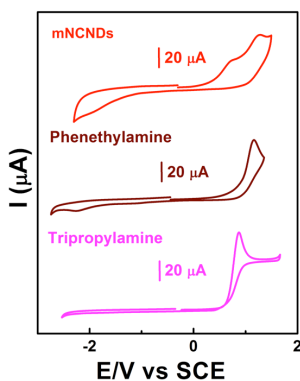


Figure 3.17 Cyclic Voltammetry of mNCNDs (red line), phenethylamine (brown line), tripropylamine (pink line) (concentration of 1mg/mL for all), in DMF using TBAPF₆ as supporting electrolyte on GC. Scan rate 100 mV/s.

It was also estimated the diffusion coefficient of mNCNDs performing cyclic voltammetric experiments at different scan rates (from 0.05 to 1 V/s) and applying the Randles–Sevcik equation (**Figure 3.18**), and values of $1 \cdot 10^{-6}$ and $9 \cdot 10^{-7}$ cm^2/s were determined.

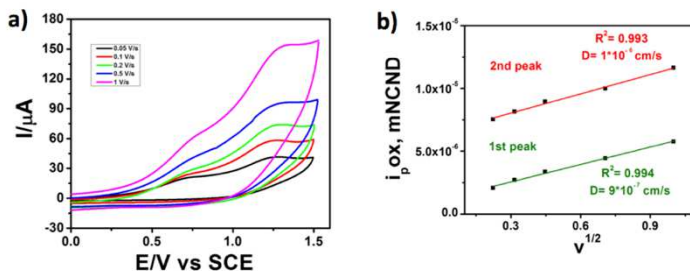


Figure 3.18 a) CVs of NCNDs 1 mg/mL in DMF using TBAPF₆ as supporting electrolyte on GC. Scan rate from 0.05 V/s to 1 V/s, potential referred to SCE at room temperature using platinum as counter electrode; b) i_p vs $v^{1/2}$.

ECL experiments of solutions at the same optical density of Ru(bpy)₃²⁺, reveal that the ECL activity is ten times higher for mNCNDs with respect to NCNDs (**Figure 3.19**, green and red lines). Thus, tertiary amines on the mNCNDs surface provide an enhanced ECL activity with respect to primary amines, as usually observed with all the alkyl amines commonly used as oxidative-reductive co-reactants.^{83,105}

Moreover, a comparison with the widely used TPA clearly demonstrated the potential of NCNDs as alternative co-reactant species. Impressively, a small amount of mNCNDs (0.1 mg/mL, corresponding to concentration around 0.13 mM in amines) gave the same Ru(bpy)₃²⁺ ECL intensity recorded using a TPA 20 mM solution (2.86 mg/mL), which corresponds to an improvement of *c.a.* 150 times (**Figure 3.19**, green and black lines) despite of the slower diffusion coefficient of the mNCNDs vs TPA ($5 \cdot 10^{-6}$ cm²/s).¹²⁴

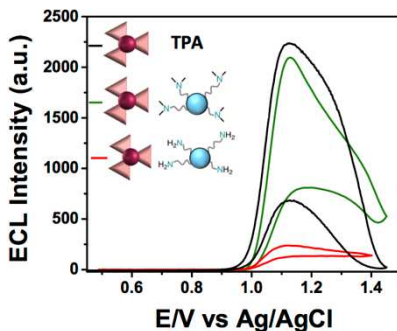


Figure 3.19 ECL emission of $\text{Ru}(\text{bpy})_3^{2+}$ in PBS solution enhanced by NCNDs 0.1 mg/mL (red line), mNCNDs 0.1 mg/mL (green line) and TPA 20 mM (black line).

Additionally, as in the case of NCNDs, higher ECL signals for $\text{Ru}(\text{bpy})_3^{2+}$ were observed upon increasing the concentration of mNCNDs (**Figure 3.20**).

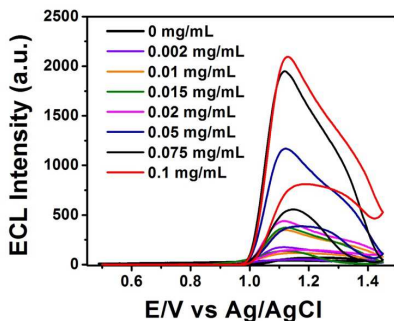


Figure 3.20 ECL intensity during a scan potential of $\text{Ru}(\text{bpy})_3^{2+}$ 0.1 mM PBS solution upon addition of different concentration of mNCNDs.

Moreover, constant ECL response for the system were obtained for over 20 cycles (**Figure 3.21**).

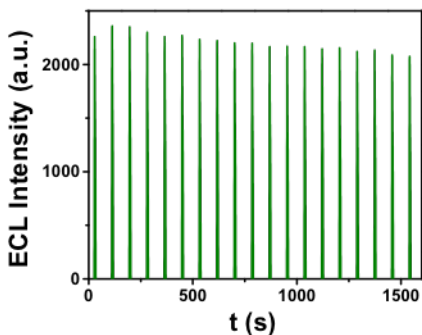


Figure 3.21 ECL responses of Ru(bpy)₃²⁺/mNCNDs system in PBS solution obtained during a continuous potential scan between +1.1 V and -0.9 V. 20 cycles under scan rate 0.05 V/s.

3.2.3 Epinephrine sensing

The Ru(bpy)₃²⁺/(m)NCNDs system was evaluated for bioanalytical applications. It is reported a simple methodology to detect epinephrine (EP), also known as adrenaline, an important catecholamine neurotransmitter in the mammalian central nervous systems involved in Parkinson's disease. Its quantification is relevant for the diagnosis of nerve diseases and a variety of analytical methods have been employed for this purpose, such as capillary electrophoresis,¹²⁵ fluorimetry,¹²⁶ electrochemistry and ECL.¹²⁷⁻¹²⁹

EP is a catecholamine that forms an ortho-benzoquinone derivative by electro-oxidation (at around +0.2 V vs SCE), resulting in the quenching of the Ru(bpy)₃²⁺ luminescence due to an electron transfer from the excited state of the metal complex to the quinone derivative.¹²⁹

The EP detection experiments were performed in a PBS solution at pH = 7.4 by means of chronoamperometry coupled with PMT tube. The measurements were performed with NCNDs 0.1 mg/mL and varying the concentration of EP from 0.5 to 15 μM. A linear

dependence of I_0/I on the concentration ($R^2=0.993$) was found (**Figure 3.22a**). The limit of detection (LOD) and quantification (LOQ) have been determined from the standard deviation of the response and the slope (see experimental section for details). The values obtained are respectively LOD 0.2 μM and LOQ 0.6 μM ($S/N = 3$). The resulting LOD for an ECL sensor in solution compared to other methodologies reported (capillary electrophoresis and fluorimetry)^{125,126} is lower because the system suffers of the slow diffusion towards the electrode surface, which is a crucial point in the formation of an excited state. However, the performance of the system studied is competitive compared to other systems already reported using nanoparticles, such as other CNDs,^{116,117} since the amino groups on the surface of our NCNDs are powerful co-reactant species. For instance, Long *et al.* reported the determination of dopamine with oxygen-doped CNDs with a LOD of 0.3 μM .¹¹⁶

The use of mNCNDs as co-reactant (0.1 mg/mL), decreasing the minimum concentration of EP to 0.05 μM , was also evaluated. The linear dependence is shown in **Figure 3.22b** ($R^2 = 0.994$). By using mNCNDs, the LOD and LOQ (30 nM and 110 nM, respectively, with $S/N = 3$) decreased by a factor 10, when compared to NCNDs. This result is ten times higher than the ones reported for different CNDs,^{116,130} and competitive with the one obtained for the detection of bisphenol with nitrogen-doped CNDs,¹¹⁷ reaching the same limit of all the other techniques discussed above.¹²⁵⁻¹²⁹

We believe that the outstanding result obtained by using mNCNDs is related to the presence of tertiary amines, which are among the best functional groups for enhancing the $\text{Ru}(\text{bpy})_3^{2+}$ luminescence, resulting in a detection of lower concentration of analytes.

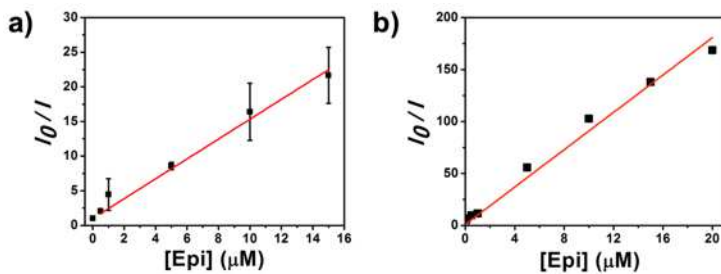


Figure 3.22 Linear fitting of I_0/I versus the concentration of EP when a) NCNDs and b) mNCNDs are employed as co-reactant with a concentration of 0.1 mg/mL. (For b the error bars are of the same size of the square symbols).

3.3 NCNDs-based hybrids as ECL platforms

In this section, we report the first carbon nanodots covalently-linked systems with transition metal complexes for ECL applications.

The preparation, as well as the structural and morphological characterizations, of a ruthenium or iridium complex-NCNDs (Ru-NCNDs or Ir-NCNDs) nanohybrids are discussed. For analytical purpose it is imperative that the multiple redox groups in the hybrids are molecularly and functionally identical, and therefore their photophysical behaviors in solutions were evaluated. Moreover, electrochemical studies were performed to shed light on the mobility of the hybrids towards the electrode through the determination of their diffusion coefficients. Finally, the ECL properties in solution of these nanohybrids were studied.

To conclude, considering the NCNDs co-reactant behavior discussed in the previous section, we investigated if they can act not only as innocent ECL carriers, but also as co-reactant in the ECL process, aiming to a self-enhanced ECL system. Additionally, we immobilized our systems on an electrode surface in order to evaluate our NCNDs as platform for more signal-generating units and consequent signal amplification.

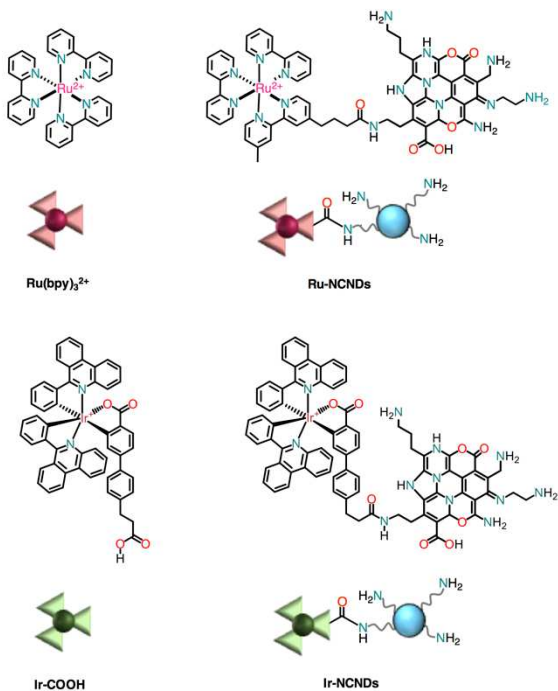


Figure 3.23 Systems studied in this section. Tris(2,2-bipyridine)ruthenium(II) ($\text{Ru}(\text{bpy})_3^{2+}$) and covalently linked ruthenium-NCND nanoconjugate on the top (left to right). Ir(6-phenylphenanthridine)₂ 2-(carboxyethyl-phenyl)pyridine-2-carboxylic acid (Ir-COOH) and covalently linked iridium-NCND nanoconjugate on the bottom (left to right).

3.3.1 Syntheses

The ruthenium-NCND nanohybrid (denoted as Ru-NCNDs) was prepared through a condensation reaction of the NHS-ester activated ruthenium bipyridine derivative (bis-(2,2'-bipyridyl)(4-carboxypropyl, 4'-methyl-2,2'-bipyridine) ruthenium(II) chloride (Ru-COOSu) and the amines of NCNDs in a PBS solution, for 16 hours. The hybrid material was obtained as an orange solid after size exclusion chromatography (details in the experimental section). On the other hand, the iridium-NCND nanohybrid (denoted as Ir-NCNDs) was prepared through a carbodiimide condensation reaction of the carboxy moiety on the iridium complex (Ir(6-phenylphenanthridine)₂-2-(carboxyethyl-phenyl)pyridine-2-carboxylic acid, Ir-COOH) and the amines of NCNDs in DMF, for 16 hours. The hybrid material was obtained as an orange solid after size exclusion chromatography (details in the experimental section).

3.3.2 Structural, morphological and photophysical characterization

The structures of the Ru-NCND and Ir-NCND hybrids were studied through FT-IR spectroscopy. Especially, it was confirmed the successful formations of the nanoconjugates through the amide linkage. The spectra of the hybrids (**Figures 3.24, 3.25**) show the typical peaks of NCNDs (discussed in *Chapter 2*) and the metal complexes.

In the case of the ruthenium-based system, three peaks corresponding to the vibrations of the NHS-ester bonds at 1814, 1783, and 1736 cm^{-1} , observed for Ru-COOSu, disappeared in the hybrid spectrum, while two characteristic vibrations of amide I (at 1653 cm^{-1}) and amide II (1547 cm^{-1}) were observed. Similarly, in the Ir-NCNDs spectrum, new peaks related to the amide bond formation can be detected (at

1630 and 1555 cm^{-1}), together with the disappearance of the C=O stretching mode of the carboxylic acid at 1722 cm^{-1} .

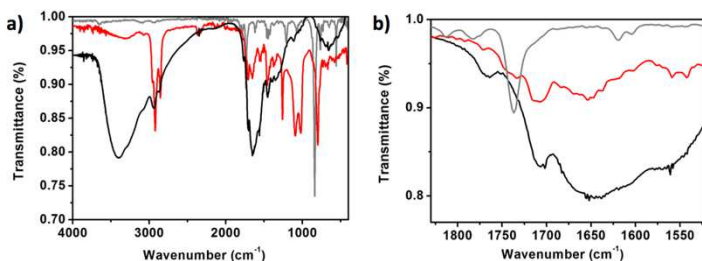


Figure 3.24 a) FT-IR spectra of NCNDs (black line), Ru-COOSu (grey line) and Ru-NCNDs (red line); b) zoom of the spectra in the region 1900-1400 cm^{-1} .

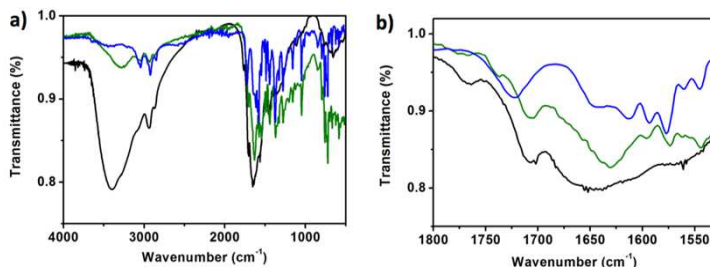


Figure 3.25 a) FT-IR spectra of NCNDs (black line), Ir-COOH (blue line) and Ir-NCNDs (green line); b) zoom of the spectra in the region 1900-1200 cm^{-1} .

Transmission electron microscopy (TEM) was employed to probe the morphological features of the nanoconjugate. TEM images show that the quasi-spherical shape of NCNDs is retained, while the average size increases in the hybrid system (**Figure 3.26**). Average size of around 4.5 ± 0.4 nm (FWHM: 0.798) and 3.9 ± 0.3 nm (FWHM: 0.570) were estimated for Ru-NCNDs and Ir-NCNDs, respectively.

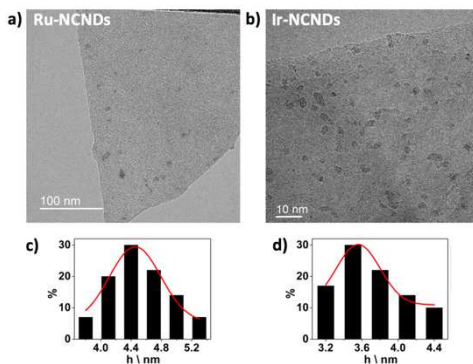


Figure 3.26 Representative TEM images of a) Ru-NCNDs and b) Ir-NCNDs hybrid drop-casted on a lacy carbon grid; size histograms of c) Ru-NCNDs and d) Ir-NCNDs hybrid with curve fit to the data using a Gaussian model.

ICP-MS measurements revealed the presence of about three ruthenium and two iridium complexes for each dot (details in experimental section), in accordance with the hybrids sizes estimated from TEM.

Fluorescence anisotropy measurements were used to further demonstrate the increased size of the hybrids in comparison to the NCNDs alone (**Figure 3.27**). This technique is commonly used for rotational time measurements associated to the emission transition moment that lies along the fluorophore structure.^{131,132} The rotational time depends on the viscosity of the solvent and on the size of the fluorophore. The bigger the fluorophore, the longer is the rotational time necessary to get a depolarized emission. As expected, the rotational time of the anisotropic emission of NCNDs increases, from 1.45 ns for the free NCNDs to 2.3 ns for Ru-NCND nanohybrid and to 2.2 ns for the Ir-NCND nanohybrid.

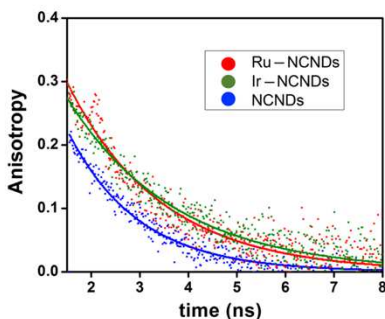


Figure 3.27 Anisotropy of Ru-NCNDs (red dots), Ir-NCNDs (green dots) and NCNDs (blue dots) in ethylene glycol (298 K).

For the sake of utilization in practical bioanalytical settings, both photophysical and ECL measurements were performed in a buffer solution (ProCell[®]) specially designed for commercial immunoassay system. ProCell[®] solution was provided by Roche and consists in a PBS solution enriched of TPA and different surfactants with a confidential specific chemical composition.

The absorption and fluorescence spectra of the Ru-NCNDs and Ir-NCNDs nanohybrids, together with the metal complexes and NCNDs as reference, are reported in **Figures 3.28, 3.29**. The absorption spectra of both hybrid systems, revealed the main features of the two references, at the same concentration of metal complex units, with a slight shift of the metal to ligand charge transfer, ¹MLCT, band at lower energy for the Ru-NCNDs conjugate.

The UV-Vis absorption spectrum of Ru-NCNDs exhibited the expected features of most ruthenium-based metal complexes.^{12,133,134} They are characterized by intense transitions at high energy (200 - 350 nm) and weaker bands in the visible region (400 - 500 nm). In particular, the band at 285 nm is assigned to bipyridil-based π - π^* -allowed ligand centered (¹LC) transitions. The two bands at 240 and

453 nm are assigned to metal-to-ligand charge transfer $^1\text{MLCT}$ $d-\pi^*$ transitions. The shoulders visible at 320 and 340 nm are related to MC transitions. The maximum at 450 nm results slightly red-shifted probably due to a rigidity of the hybrid system respect to the free metal complex.

For Ir-NCNDs, the absorption band at around 250 nm is assigned to the ligand centered (^1LC) $\pi-\pi^*$ transition, while the bands at 300-400 nm are a mixture of singlet-manifold ligand-to-ligand charge transfer ($^1\text{LLCT}$) and $^1\text{MLCT}$ transitions. The band at 456 nm is attributed to both singlet and triplet metal to ligand charge transfer transition, $^1\text{MLCT}$ and $^3\text{MLCT}$, respectively.

Subsequently, the excited state was investigated in both hybrids by exciting Ru-NCNDs and Ir-NCNDs at 340 and 380 nm, respectively, and compared with the metal complexes and NCNDs alone as references.

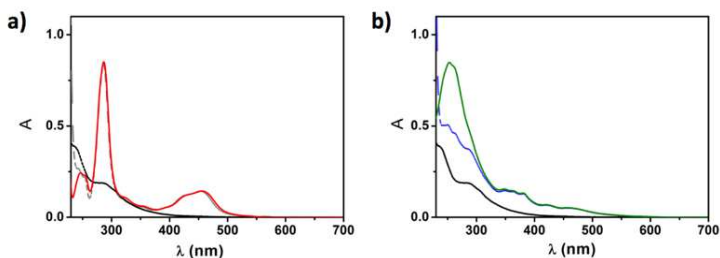


Figure 3.28 UV-Vis absorption spectra of a) Ru (grey line), NCNDs (black line) and Ru-NCNDs (red line), b) Ir (blue line), NCNDs (black line) and Ir-NCNDs (green line), in ProCell[®] solution. $[\text{Ru}] = 10^{-5}\text{M}$, $[\text{Ir}] = 10^{-5}\text{M}$.

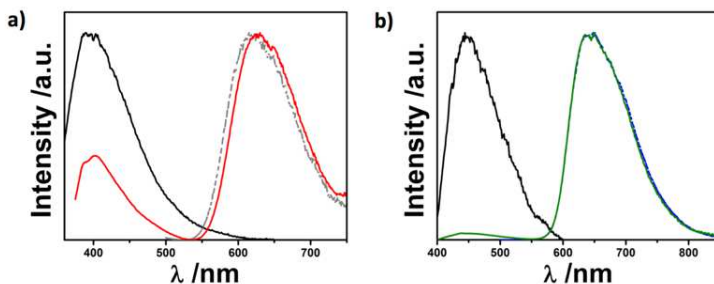


Figure 3.29 PL emission spectra of a) Ru (grey line), NCNDs (black line) and Ru-NCNDs (red line), $\lambda_{\text{exc}}=340$ nm, b) Ir (blue line), NCNDs (black line) and Ir-NCNDs (green line), $\lambda_{\text{exc}}=380$ nm, in ProCell[®] solution. $[\text{Ru}] = 10^{-5}\text{M}$, $[\text{Ir}] = 10^{-5}\text{M}$.

The PL spectra of both nano hybrids showed the two contribution corresponding to the NCND-centered emission (at around 400 nm) and to the metal complexes. While the Ru-NCNDs broad emission profile at 630 nm, corresponding to the ³MLCT emission of the ruthenium bipyridine complex, is slightly shifted to lower energy as compared to the ruthenium complex, for Ir-NCNDs the fluorescence spectrum at 650 nm does not show any bathochromic shift.

The PL excited state lifetimes are mono-exponentials when detected in the metal complex emission band, while a complex decay (tri-exponential) is observed for the NCNDs emission, without significative variations respect to the free components in the same solvent (**Table 3.2**). The absolute photoluminescence quantum yields (PLQYs) of the metal complexes in the hybrids, calculated as 4% and 12% for Ru-NCNDs and Ir-NCNDs (**Table 3.2**), respectively, do not show considerable variations as compared to the bare metal complexes. These results suggest that no quenching processes occur upon the metal complexes attachment on the NCNDs. Therefore, the multiple redox centers at the peripheries of nanodots retain the ground- and excited-state photophysical properties of the references,

which is a crucial requirement for the effective use of the nanohybrids as ECL labels.

Table 3.2 Lifetimes and PLQYs data of NCNDs, ruthenium and iridium complexes (Ru and Ir), and Ru-NCND and Ir-NCND nanohybrids.

	Lifetime / ns	PLQY / %
NCNDs	$\tau_1=14.0$ (2.3%) $\tau_2=5.1$ (34%) $\tau_3=2.1$ (63.7%) ^a	8 ^d
Ru	329.1 ^b	4 ^e
Ru-NCNDs	$\tau_1=11.7$ (11.8%) $\tau_2=3.6$ (26.3%) $\tau_3=1.0$ (61.9%) ^a 363.0 ^b	4 ^{d,e}
Ir	734.4 ^c	14 ^f
Ir-NCNDs	$\tau_1=9.9$ (21.9%) $\tau_2=3.6$ (62.7%) $\tau_3=1.1$ (15.4%) ^a 785.5 ^c	12 ^f

a. $\lambda_{\text{exc}} = 375$ nm/ $\lambda_{\text{em}} = 420$ nm; b. $\lambda_{\text{exc}} = 440$ nm/ $\lambda_{\text{em}} = 625$ nm; c. $\lambda_{\text{exc}} = 440$ nm/ $\lambda_{\text{em}} = 640$ nm; d. $\lambda_{\text{exc}} = 300$ nm; e. $\lambda_{\text{exc}} = 460$ nm; f. $\lambda_{\text{exc}} = 380$ nm.

3.3.3 Electrochemical characterization

To shed light on the electronic properties of the hybrids, an extensive electrochemical investigation was carried out. The CVs in DMF of the Ru-NCND and Ir-NCND hybrids, as well as the metal complexes and NCNDs as references, are reported in **Figure 3.30**.

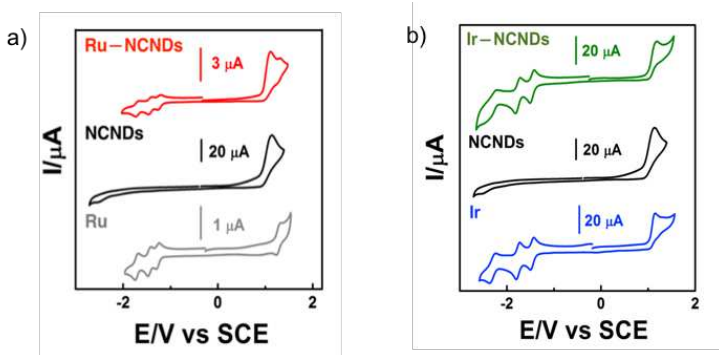


Figure 3.30 a) CVs of Ru-NCNDs (red line), $\text{Ru}(\text{bpy})_3^{2+}$ (grey line) 0.26 mM and NCNDs (black line) 1mg/mL in DMF; b) CVs of Ir-NCNDs (green line), Ir-COOH (blue line) 1 mM and NCNDs (black line) 1mg/mL in DMF. 0.1 M TBAPF₆ as supporting electrolyte and GC as working electrode. Scan rate 0.1 V/s.

The CV of the Ru-NCNDs hybrid (**Figure 3.30a**, red line) shows the electrochemical features of both NCNDs (**Figure 3.30a**, black line) and $\text{Ru}(\text{bpy})_3^{2+}$ (**Figure 3.30a**, grey line). The anodic region presents two distinctive oxidation peaks at +1.09 V and +1.30 V related, respectively, to the oxidation of the free amines on the NCNDs surface and to the oxidation of Ru^{2+} to Ru^{3+} . The presence of a single oxidation wave suggests that all the complexes, within electrode proximity, are electrochemically equivalent. On the other hand, in the cathodic region three reduction peaks are observed, at -1.24; -1.42 and -1.71 V, corresponding to the reduction of the three bipyridine ligands.^{135,136} Although in the anodic part of Ru-NCND hybrid both

features of NCNDs and $\text{Ru}(\text{bpy})_3^{2+}$ can be identified, for the Ir-NCND hybrid (**Figure 3.30b**, green line) only one peak is visible. This could be ascribed to the similar values for the oxidation peak of the iridium complex (at +1.12 V; **Figure 3.30b**, blue line) and the free amino groups on the NCNDs surface (at +1.09 V; **Figure 3.30b**, black line). On the contrary, the three peaks in reduction at -1.43 V, -1.74 V, -2.26 V present in the iridium complex alone can be observed in the Ir-NCND hybrid, with the last one, probably correlated to the picolinic ligand coupled with the NCNDs, less pronounced in the hybrid.

As diffusion limited processes, both electrochemistry and ECL are greatly influenced by the size and mobility of the electrochemically active species in solution. Therefore, we determined the diffusion coefficients of both nano hybrids. For this purpose, cyclic voltammetry at different scan rate (from 0.05 to 1 V/s) were measured and the diffusion coefficient was determined by using Randles–Sevcik equation.

In the CVs of both hybrids and metal complexes alone, the peak currents were proportional to the square root of the scan rate ($v^{1/2}$) and the intercepts were approaching zero, showing that oxidation and reduction processes were diffusion controlled and no adsorption phenomena on the electrode surface were occurring (**Figures 3.31, 3.32**). Then, the diffusion coefficients were determined on the oxidation peaks. The correlation between the peak currents and the square root of the scan rate ($v^{1/2}$) for both hybrids and metal complexes were estimated. The calculated diffusion coefficients for the nano hybrids were in agreement with those reported in the literature,^{137,138} for zero dimensional (spherical) nanoparticles with diameter ranging from 1 to 5 nm. Moreover, a comparison with the diffusion coefficients of the metal complexes alone indicate that the presence of NCNDs do not led to significant variations due to their

small dimension, suggesting that the electron transfer kinetics in ECL should not be affected.

Therefore, both hybrids promise a mobility towards the electrode surface comparable to the one of the single label, which should result in an unaffected electrochemical process efficiency.

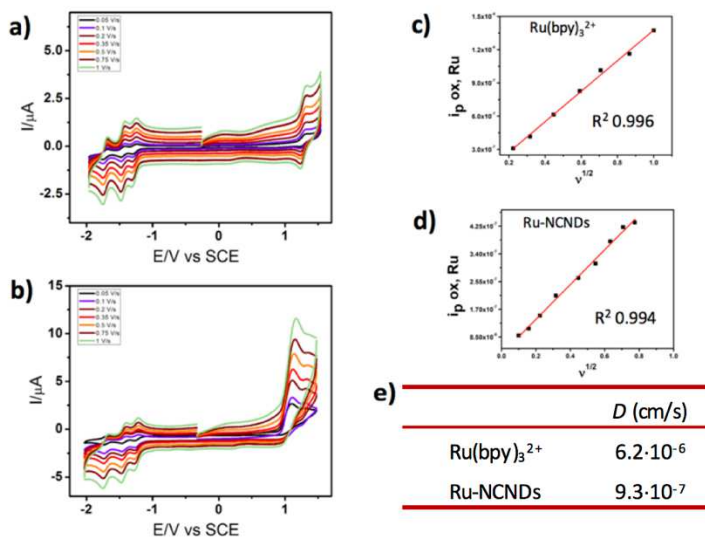


Figure 3.31 a) CVs of $\text{Ru}(\text{bpy})_3^{2+}$ 0.26 mM in DMF, b) CVs of Ru-NCNDs with $[\text{Ru}] = 0.26$ mM in DMF, using 0.1 M TBAPF_6 as supporting electrolyte and GC as working electrode. Scan rate from 0.05 V/s to 1 V/s. i_p vs $v^{1/2}$ of c) CVs of $\text{Ru}(\text{bpy})_3\text{PF}_6$ and d) CVs of Ru-NCNDs ; e) table reporting the diffusion coefficients (D , cm/s) for $\text{Ru}(\text{bpy})_3^{2+}$ and Ru-NCNDs .

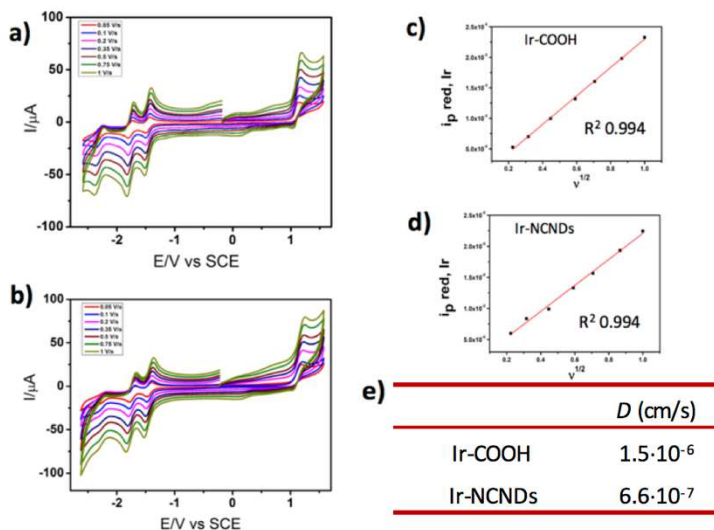


Figure 3.32 a) CVs of Ir-COOH 1 mM in DMF, b) CVs of Ir-NCNDs with $[\text{Ir}] = 1$ mM in DMF, using 0.1 M TBAPF₆ as supporting electrolyte and GC as working electrode. Scan rate from 0.05 V/s to 1 V/s. i_p vs $v^{1/2}$ of c) CVs of Ir-COOH and d) CVs of Ir-NCNDs; e) table reporting the diffusion coefficients (D , cm/s) for Ir-COOH and Ir-NCNDs.

3.3.4 Electrochemiluminescence

The ECL activity of both hybrids was evaluated studying the ECL intensity as function of voltage applied, time and emission profile, in comparison to the references with the same optical density at 450 nm. In agreement with what reported for the system $[\text{Ru}(\text{bpy})_3]^{2+}/\text{TPA}$ in aqueous solution in section 3.1.4, the ECL curve for a solution of $[\text{Ru}(\text{bpy})_3]^{2+}$ in ProCell[®] (10 μM) exhibit two waves at +0.93 V and +1.18 V vs Ag/AgCl (1M KCl), which can be associated to the generation of $[\text{Ru}(\text{bpy})_3]^{2+}$ excited state (**Figure 3.33a**, grey line). As shown in **Figure 3.33c** (Mechanism I), in the oxidative–reduction

mechanism, the first wave involves the electrochemical oxidation of TPA to $\text{TPA}^{\cdot+}$, which then oxidizes $[\text{Ru}(\text{bpy})_3]^+$ to the excited state $[\text{Ru}(\text{bpy})_3]^{2+*}$. The second wave is instead assigned to the classic mechanism (Mechanism II) that occur when electrogenerated $[\text{Ru}(\text{bpy})_3]^{3+}$ reacts with $\text{TPA}^{\cdot-}$ (**Figure 3.33d**). The ECL curve for the iridium complex in a ProCell[®] solution display the same features, showing a peak at +0.9 V associated to the mechanism I, which reaches its ECL maximum around +1.25 V with a small bump at +1.1 V correlated to mechanism II (**Figure 3.33b**, blue line).

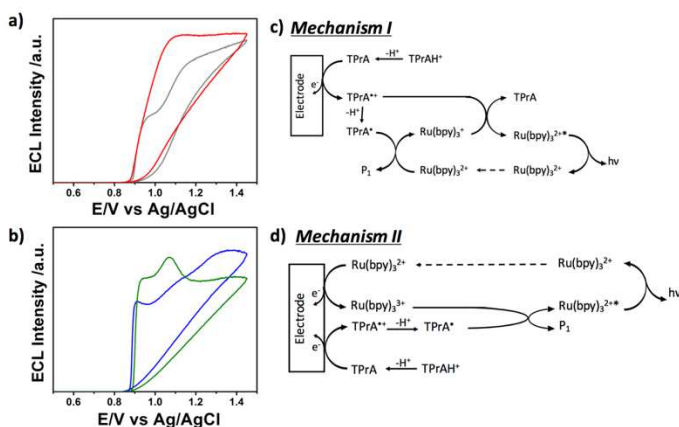


Figure 3.33 ECL intensities in Procell[®] of a) $\text{Ru}(\text{bpy})_3^{2+}$ (grey line) and Ru-NCNDs (red line), b) Ir-COOH (blue line), Ir-NCNDs (green line), using GC as working electrode. $[\text{Ru}] = [\text{Ir}] = 10^{-5}$ M. Potential scan rate 50 mV/s. c) Mechanism I and d) Mechanism II reported by Bard *et al.*⁷⁷ for the $\text{Ru}(\text{bpy})_3^{2+}/\text{TPA}$ system in aqueous solution containing $\text{Ru}(\text{bpy})_3^{2+}$ in low concentration.

The ECL curves for both hybrids Ru-NCNDs and Ir-NCNDs , studied in the same conditions than the metal complexes alone, show different profiles. Specifically, compared to the references, the ECL curve of the Ru-NCNDs is characterized by a broader emission between +0.95

V and +1.2 V (**Figure 3.33a**, red line), while for Ir-NCNDs two peaks at higher intensity than Ir-COOH appear at +0.9 V and at +1.05 V followed by a plateau (**Figure 3.33b**, green line). These evidences could be correlated to the generation of the excited state of Ru-NCNDs* and Ir-NCNDs* from a mixed contribution of the TPA (from the ProCell[®] solution) and the free amino groups of NCNDs. The latter are still present in the hybrids, as shown from the CVs, can be oxidized within this range and, as demonstrated in section 3.2, can act as co-reactant for ECL generation.

In order to investigate the nature of the electrogenerated emissive excited state, the ECL spectra of the two nanoconjugates were recorded (**Figure 3.34**). For this purpose, the ECL light was collected during 5 chronoamperometry pulses of 1 s between 0 V and +1.4 V vs Ag/AgCl, and the spectra were collected using a cooled EMCCD camera with the accumulation of 10 s. The as-obtained ECL spectra have the same features as the photoluminescence spectra in ProCell[®], confirming that the emission is the result of the decay of the same excited state, generated by either photo- or electrochemical excitation.

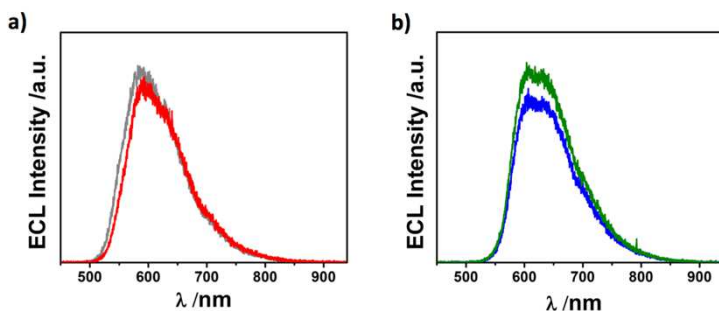


Figure 3.34 ECL emission spectra in ProCell[®] of a) Ru (grey line) and Ru-NCNDs (red line), b) Ir (blue line), Ir-NCNDs (green line).

From the intensities of the above mentioned ECL spectra, the ECL efficiencies for both hybrids can be evaluated. For this purpose, chronoamperometric experiments for the two hybrids and iso-absorptive solutions of metal complexes as standards were also performed. In these experiments, the ECL was generated by a chronoamperometry pulse at +1.4 V for 1 s and the light was detected by a photomultiplier tube (PMT) (**Figure 3.35**).

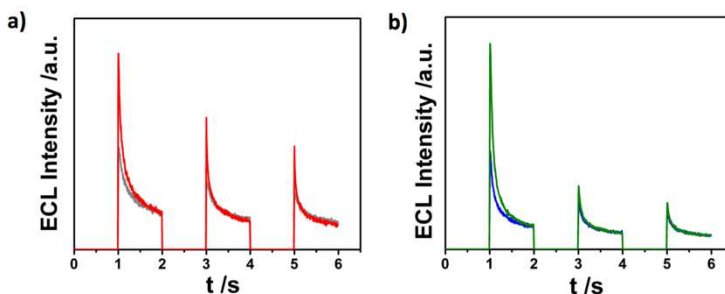


Figure 3.35 ECL intensities in time in ProCell[®] of a) Ru (grey line) and Ru-NCNDs (red line), b) Ir (blue line), Ir-NCNDs (green line).

The comparison of the ECL spectra and chronoamperometries of the hybrids and the references clearly show that the ECL efficiency of both conjugated systems are the same of the single labels. Thus, all the redox centers present in the nanoconjugates participate to the ECL emission. Notably, this is the highest result for ECL labels-coupled nanoparticles ever reported. This could be ascribed to the following findings for the nanohybrids studied: all the redox centers are in very close contact with the electrode surface and are electrochemically and ECL active, since diffusional problems are limited and quenching phenomena are avoided.

3.3.5 Self-enhanced and multi-label ECL platforms

In light of the above considerations, we moved forward the study of the previously discussed systems as ECL self-enhanced nanohybrids and we investigated the effect of their immobilization on the electrode surface on the ECL emission.

We evaluated the possible use of these nanoconjugates as self-enhanced ECL platform, investigating the efficiency of NCNDs as co-reactant when covalently linked to the metal complexes. For this purpose, it was studied the ECL generation of the Ru-NCNDs hybrid in PBS solution, without the presence of additional co-reactant species such as TPA.

On the other hand, the ECL efficiency of Ir-NCNDs immobilized on a gold surface was evaluated, in order to investigate if the ECL efficiency is proportional to the number of redox centers for nanodots.

3.3.5.1 Self-enhanced ECL platform

To evaluate the NCNDs co-reactant behavior in Ru-NCNDs, we recorded the ECL curve of the hybrid in PBS solution, comparing those obtained for $\text{Ru}(\text{bpy})_3^{2+}$ or for the uncoupled system NCNDs/ $\text{Ru}(\text{bpy})_3^{2+}$ in the same conditions and with the same optical density of $\text{Ru}(\text{bpy})_3^{2+}$ (**Figure 3.36a**). It was observed an ECL emission intensity two times higher for the Ru-NCNDs hybrid with respect to the uncoupled components (**Figure 3.36b**).

As discussed in section 3.1.3 and according to ECL self-enhanced systems already reported,⁹²⁻¹⁰² we hypothesize that in Ru-NCNDs the intramolecular electron transfer is more efficient compared to the intermolecular reaction due to the shorter electron-transfer path and consequent reduced energy loss.

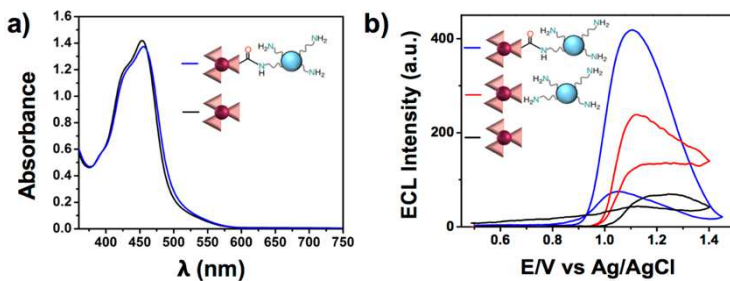


Figure 3.36 a) Absorption spectra at MLCT of $\text{Ru}(\text{bpy})_3^{2+}$ (black line) and Ru-NCNDs (blue line) in PBS at the same concentration of chromophore (10^{-4} M); b) ECL intensity during a scan potential of $\text{Ru}(\text{bpy})_3^{2+}$ 10^{-4} M PBS solution (black line), upon addition of NCNDs 0.1 mg/mL (red line) and of Ru-NCNDs (blue line) with a concentration of Ru of 10^{-4} M. Scan rate 0.05 V/s.

3.3.5.2 Multi-label ECL platform

Ir-NCNDs were immobilized onto a gold electrode surface, mediated by a SAM (**Figure 3.37b**; detailed procedure in experimental section). For comparison, the metal complex was also immobilized using the same procedure, starting from a solution with the same optical density (**Figure 3.37a**; detailed procedure in experimental section). The ECL behavior for the two modified electrodes was evaluated in a PBS/Triton X 100 solution with TPA 10 mM as co-reactant. The ECL curves obtained for the two surface-confined system showed an ECL enhancement for the Ir-NCNDs nano hybrid (**Figure 3.37c**, green line) respect to the metal complex alone (**Figure 3.37c**, black line). In particular, it was observed an ECL emission intensity two times higher for the nanoconjugate with respect to the reference, in agreement with the ICP-MS calculation, and thus confirming that the totality of the redox centers covalently linked to the nanodots are ECL active.

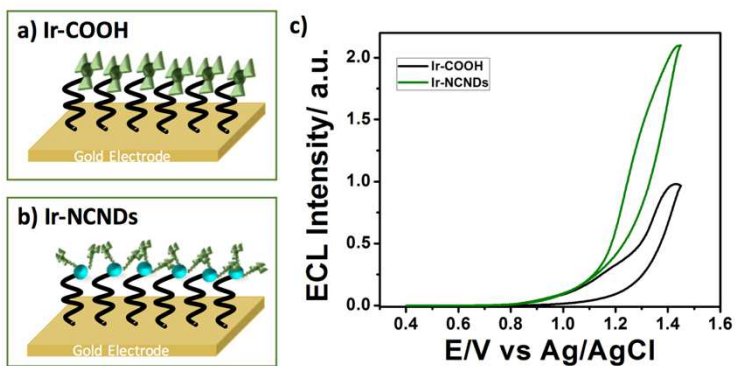


Figure 3.37 Schematic representation of a) Ir-COOH and b) Ir-NCNDs immobilized onto gold electrodes; c) ECL intensities recorded during a CV in PBS/ Triton X 100/ TPA 10 mM of Ir-NCNDs (green line) and Ir-COOH (black line) after immobilization onto gold electrodes.

3.4 Conclusions and perspectives

In the framework of ECL system based on nanomaterials, this chapter focused on the investigation of the largely unexplored application of NCNDs.

In the first part, NCNDs carrying primary or tertiary amino groups on the surface were studied as co-reactant to promote ECL. Their simple and cost effective production, high aqueous solubility and low toxicity have inspired us to investigate the possible use of NCNDs as alternative co-reactant species. The primary or tertiary amino groups, which are known to provide great efficiency as oxidative-reduction co-reactant, on the NCNDs surface have shown powerful co-reactant ability for $\text{Ru}(\text{bpy})_3^{2+}$ ECL generation. The co-reactant mechanism was investigated proving a NCNDs catalytic effect on the $\text{Ru}(\text{bpy})_3^{2+}$ oxidation. Our results show how the use of alkyl amines on a carbon nanodots for $\text{Ru}(\text{bpy})_3^{2+}$ ECL, would circumvent most of the drawbacks related to the use of the standard alkyl amines such as TPA, which is toxic, corrosive, volatile, scarcely soluble and need to be used in high concentrations. Notably, it was recorded the same $\text{Ru}(\text{bpy})_3^{2+}$ ECL intensity using a small amount of NCNDs and a concentration of TPA 20 mM, achieving an improvement of *c.a.* 150 times by using nanodots. We proposed a mechanism in which, upon oxidation, the amino groups of NCNDs become a reductive unstable intermediate able to form the excited-state $\text{Ru}(\text{bpy})_3^{2+*}$, through highly energetic electron transfer. Then $\text{Ru}(\text{bpy})_3^{2+*}$ emits light and produces $\text{Ru}(\text{bpy})_3^{2+}$, which in turn can be re-oxidized for a new cycle. Impressively, it was observed that, in contrast to TPA, our NCNDs can be used for further cycles. Indeed, NCNDs provide constant ECL response for more than 20 cycles due to a great electrochemical stability and abundant presence of amines for further cycles.

In light of these results, we finally explored the use of our Ru(bpy)₃²⁺/NCNDs ECL system for biosensing, reporting a simple methodology for the detection of epinephrine, which showed competitive performance when compared to already reported systems. Therefore, the use of our NCNDs can pave the route towards sensitive biosensing platform for the detection of interesting bioanalytes.

In the second part, we reported the use of NCNDs in covalently-linked systems with ECL labels. We prepared NCND-based hybrids bearing ruthenium or iridium complexes, thus reporting a straightforward synthetic strategy for assembling more signal-generating units into the nanodots platform. Notably, a deep spectroscopic and electrochemical investigation demonstrated that the totality of the redox centers retains their properties in the hybrids.

Optical characterizations showed that no quenching phenomena of the redox centers occur in the hybrids. Moreover, the electrochemical studies shed light on the mobility of the hybrids towards the electrode through the determination of the diffusion coefficients. It was observed that due to the small dimensions of the nanoconjugates, the electron transfer kinetics in ECL should not be significantly modified compared to the bare metal complexes.

These results have prompted us to investigate the ECL behaviors of the hybrids. From ECL spectra and chronoamperometries, no significant difference in the ECL efficiency of the nanoconjugates when compared to the metal complexes references (at the same concentration of redox units) were observed. These evidences substantiate the effective use of these hybrids as ECL platform. In particular, the results achieved are the highest for ECL labels-coupled nanoparticles ever reported, since in nanostructured architectures both the optical properties of the redox centers and their accessibility to the electrode surface can be affected. To summarize, it was

demonstrated that the totality of the redox centers in the presented hybrids are ECL actives, in close contact with the electrode and able to diffuse towards it.

Furthermore, we probed that our NCNDs-based hybrids exhibit great self-enhanced ECL without the addition of co-reactants such as TPA. Our hybrids provide an ECL emission intensity two times higher with respect to the uncoupled components.

The observed ECL enhancement is due to the presence of NCNDs amino groups in the hybrids, which act as co-reactant. Therefore, the luminophores and its co-reactive groups are integrated in a single hybrids entity. Thus, in contrast to the common intermolecular ECL reaction, the electrons are transferred intramolecularly to the redox centers, leading to enhanced ECL intensity due to shorter electron-transfer path and reduced energy loss. Our results provide a new method for signal amplification, opening interesting possibilities towards self-enhanced systems which would extend bionalytical applications.

Finally, we evaluated the direct effect on the ECL signal of the more signal-generating unit assembly into the same nanometric object. Thus, it was investigated the immobilization of the hybrids on an electrode and it was observed a signal enhancement proportional to the number of ECL probes present in each NCNDs due to their raised density on the electrode surface. Therefore, the use of NCNDs as novel platform for higher ECL efficiency was demonstrated and we believe that our encouraging results would offer the possibility to make outstanding steps forward in this field.

3.5 Experimental section

3.5.1 Materials

The synthesis of NCNDs is reported in *Chapter 2*. Ruthenium-tris(2,2'-bipyridyl) dihexafluorophosphate ($\text{Ru}(\text{bpy})_3(\text{PF}_6)_2$), piperidine, phenethylamine, benzylamine, aniline, quinoline, tripropylamine, L-epinephrine, paraformaldehyde (95%), potassium hydroxide ($\geq 85\%$), formic acid ($\geq 96\%$), N-hydroxysulfosuccinimide (Sulfo-NHS), 1-ethyl-3-[3-dimethylaminopropyl]carbodiimide hydrochloride (EDC \cdot HCl), Phosphate Buffer Saline (PBS, pH = 7.4) were purchased from Sigma-Aldrich and used without purification. Paraformaldehyde (Sigma-Aldrich, 95%), KOH (Sigma-Aldrich, $\geq 85\%$) and formic acid (Sigma-Aldrich; $\geq 96\%$) were used without further purifications.

Bis-(2,2-bipyridyl) (4-carboxypropyl,4'-methyl-2,2'-bipyridine) ruthenium(II) chloride (Ru-COOSu), was supplied by Roche diagnostics. $\text{Ir}(6\text{-phenylphenanthridine})_2$ 2-(carboxyethylphenyl) pyridine-2-carboxylic acid (Ir-COOH) was kindly supplied from the group of Prof. L. De Cola.¹³⁹

Kaiser test kit was purchased from Sigma-Aldrich.

Dialysis tubes with molecular weight cutoff 0.5-1 KDa were bought from Spectrum Labs.

Size exclusion chromatography was carried out using Sephadex TMLH-20 (Amersham Biosciences).

Ultrapure fresh water obtained from a Millipore water purification system ($>18\text{M}\Omega$ Milli-Q, Millipore). Dimethylformamide (DMF) was purchased at Acros organics and used without any purification. ProCell[®] solution was acquired from Roche (Product number, 1662988) and consists in a solution of phosphate buffer (PBS, pH = 6.8) 300 mM, tripropylamine 180 mM, a proprietary surfactant (0.1%) and preservative.

3.5.2 Apparatus and characterization

Transmission Electron Microscopy (TEM) images were obtained with a Jeol-JEM 2011 system operated at 200 kV equipped with a Cs-probe corrector, an Energy Dispersive X-ray Spectrometer and a GIF Tridiem filter. The drop cast of samples in methanol (concentration of few mg/mL) on a lacey carbon grid was used as general procedure.

ICP-MS experiments were performed to evaluate the amount of ruthenium complexes in Ru-NCNDs. The instrument employed was a "X series II" from Thermo Electron. From the determination of the absolute ruthenium and iridium content in Ru-NCNDs and Ir-NCNDs, a loading of 200 mg/g for ruthenium complex and 440 mg/g for iridium complex were calculated. Through the following calculations, it was estimated a number of three ruthenium and iridium complexes for each NCNDs. The ICP-MS measurement of a Ru-NCNDs and Ir-NCNDs sample with a concentration of 0.0096 mg/mL and 0.0330 mg/mL, respectively, in nitric acid, revealed a concentration (C) of NCNDs and Ru equal to 0.0074 and 0.0022 mg/mL (corresponding to $2.3 \cdot 10^{-9}$ mol/mL), respectively, and of NCNDs and Ir equal to 0.0290 and 0.0054 mg/mL (corresponding to $5.5 \cdot 10^{-9}$ mol/mL). By assuming NCNDs as spherical nanoparticles with a diameter equal to 2.47 nm,¹⁴⁰ and considering the density of amorphous carbon as 2.0 g/cm³,⁷⁶ it was calculated the mass (m) of a single NCNDs:

$$V = 4/3 \pi r^3 = 7,89 \cdot 10^{-21} \text{ cm}^3$$

$$m = d \cdot V = 2 \cdot 7,9 \cdot 10^{-21} = 1,58 \cdot 10^{-20} \text{ g}$$

From the ratio between the concentration (C) of NCNDs in the sample and the mass (m) of one NCNDs, it was calculated the number (N_0) of NCNDs in the Ru-NCNDs nano hybrid:

$$\frac{0,0074 \cdot 10^{-3}}{1,58 \cdot 10^{-20}} = 4,7 \cdot 10^{14} \text{ } N_0 \text{ of NCNDs in Ru-NCNDs}$$

$$\frac{0,029 \cdot 10^{-3}}{1,58 \cdot 10^{-20}} = 1,8 \cdot 10^{15} \text{ N}_o \text{ of NCNDs in Ir-NCNDs}$$

The number (N_o) of Ru in the Ru-NCNDs and Ir in the Ir-NCNDs nano hybrid was calculated as follow:

$$n \cdot N_A = N_o$$

$$2,3 \cdot 10^{-9} \cdot 6,022 \cdot 10^{23} = 1,4 \cdot 10^{15} \text{ N}_o \text{ of Ru in Ru-NCNDs}$$

$$5,5 \cdot 10^{-9} \cdot 6,022 \cdot 10^{23} = 3,4 \cdot 10^{15} \text{ N}_o \text{ of Ir in Ir-NCNDs}$$

where N_A is the Avogadro number and n are the number of moles of Ru and Ir in the nano hybrid. From the N_o as calculated, it was estimated the number of ruthenium and iridium complexes on each NCNDs:

$$\frac{1,4 \cdot 10^{15}}{4,7 \cdot 10^{14}} \cong 3 \text{ Ru/NCNDs}$$

$$\frac{3,4 \cdot 10^{15}}{1,8 \cdot 10^{15}} \cong 2 \text{ Ir/NCNDs}$$

FT-IR spectroscopy was performed in the solid state using an attenuated total reflectance (ATR-FTIR) accessory on a Shimadzu IR Affinity-1 spectrometer.

Modified Ir-COOH and Ir-NCNDs gold electrodes: **Figure S3.1** illustrates the fabrication process of the modified electrodes. A Gold working electrode (Au, 2 mm in diameter) was polished repeatedly with 0.3 and 0.05 mm alumina slurry, followed by successive sonication in acetone, ethanol and distilled water for 5 min and dried in air. The electrodes were then modified in two different ways since the complex is carboxy-terminated while the Ir-NCNDs is amino terminated. For the Ir-COOH the electrode was modified with a 1 mM ethanolic solution of 11-amino-1-undecanethiol and for the Ir-NCNDs with a 1 mM ethanolic solution of 16 mercapto-decanodic acid, for 48 hours. Electrodes were then washed in PBS (pH 7.4), then

the carboxy-terminated parts were immersed in a mixture of EDC and NHS (1:3) PBS solution for approximately 15 minutes at room temperature (Ir-COOH and SAM for Ir-NCNDs). Finally, the electrode was immersed in activated Ir-COOH or Ir-NCNDs PBS solution ($[Ir] = 10^{-4}$ M) for approximately 1 hour, at 37°C. Each electrode was then washed with PBS Tween (PBST 0.05% v/v) three times and other three times with PBS.

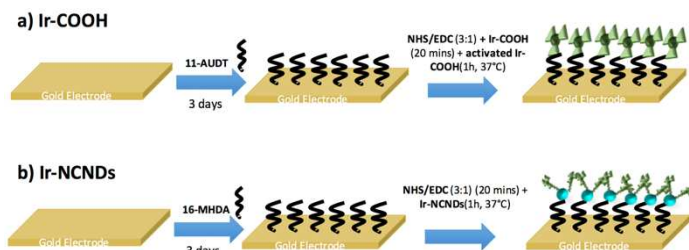


Figure S3.1 Schematic representation of the procedures used to prepare modified Ir-COOH and Ir-NCNDs electrodes.

The electrochemical characterizations of NCNDs, mNCNDs, different amines for the co-reactant section, Ru-NCNDs, Ir-NCNDs, $\text{Ru}(\text{bpy})_3^{2+}$ and Ir-COOH were performed in DMF with 0.1M tetrabutylammonium hexafluorophosphate (TBAPF_6) as supporting electrolyte. The electrochemistry on the $\text{Ru}(\text{bpy})_3^{2+}$ (0.1 mM)/NCNDs (0.1 mg/mL) system has been studied in PBS (pH = 7.4). For the electrochemical experiments, a CHI750C Electrochemical Workstation (CH Instruments, Inc., Austin, TX, USA) was used. The experiments were performed in a glass cell under an argon atmosphere. Feedback correction was employed in order to minimize the ohmic drop between the working and reference electrodes. A glassy carbon electrode (GC, 3 mm diameter 66-EE047 Cypress Systems) was employed as the working electrode (WE), while a platinum and a silver wires were used as counter (CE) and quasi-

reference (QRE) electrodes. The GC electrode was stored in ethanol and, before the experiments, polished with a 0.05 μm diamond suspension (Metadi Supreme Diamond Suspension, Buehler) and ultrasonically rinsed with water for 10 minutes and ethanol for 10 minutes. It was electrochemically activated in the electrolyte solution by means of several voltammetric cycles at 0.5 Vs^{-1} between the anodic and cathodic solvent/electrolyte discharges. The RE was separated from the catholyte by glass frits. It was calibrated at the end of each experiment against the ferrocene/ferricenium ($\text{Fc}|\text{Fc}^+$) couple, whose formal potential is 0.460 V against KCl-saturated calomel electrode (SCE). All potential values were reported against SCE. The standard potentials were calculated as the average value between cathodic and anodic peak potentials, when the processes were reversible or quasi-reversible.

We determined the diffusion coefficients of NCNDs and mNCNDs, $\text{Ru}(\text{bpy})_3^{2+}$ through cyclic voltammetric experiments at different scan rates (from 0.05 to 1 V/s) and applying the Randles–Sevcik equation:

$$i_p = 2.69 \cdot 10^5 n^{3/2} A D^{1/2} C v^{1/2}$$

where n is the number of electrons transferred in the redox event (usually 1), A the electrode surface (cm^2), D the diffusion coefficient (cm^2/s), v the scan rate (V/s) and C the concentration (mol/cm^3). The CV experiments and the diffusion coefficients (D) were determined on the oxidation peaks. It was observed that the peak currents are proportional to the square root of the scan rate ($v^{1/2}$), indicating that all the oxidation/reduction processes were diffusion controlled and no adsorption phenomena on the electrode surface were occurring.

For the ECL characterization a custom system was used, consisting in an electrochemical cell based on a glassy carbon (Tokai Inc.) disk electrode (3 mm diameter) as the WE, which was closely facing (a few mm) the photomultiplier tube (PMT, Hamamatsu, H10723-01,

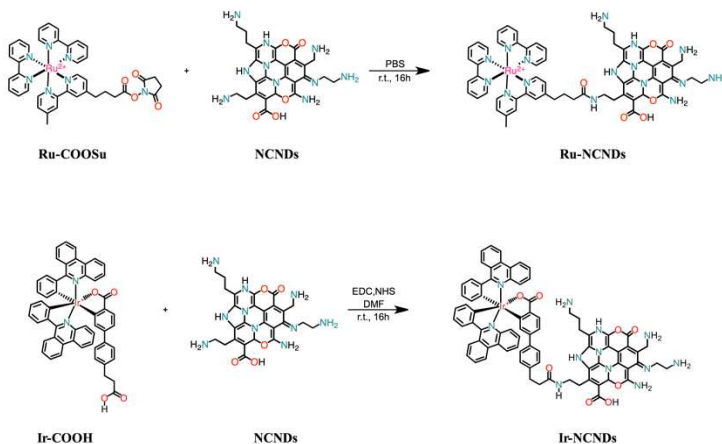
Japan) detector controlled by an Autolab electrochemical workstation PGSTAT101 (Metrohm, The Netherlands). The RE employed was an Ag/AgCl (1M KCl) from CHI-Instruments and it was separated from the catholyte by glass frit. A platinum wire served as the CE. For potentiodynamic measurements (Cyclic Voltammetry), the solution was scanned at 0.05 V/s from +0.5 V to +1.45 V. For chronamperometric experiments, used for the detection of EP, the pulsing potential was set at +1.4 V vs Ag/AgCl (1M KCl). The pulse width was 1 s. The transients and the faradic currents were managed by using the software NOVA provided with the Autolab. The ECL spectrum was acquired using a calibrated electron multiplying charge couple device (EM-CCD) camera (A-DU970N-UVB Andor technology, Newton EM-CCD) coupled with a spectrograph (Andor Technology, Shamrock 163). The working electrode was mechanically cleaned before each run as above mentioned for the electrochemical measurements.

The ECL relative intensity of the complexes was compared to Rubpy, (I/I_{Ru}), where I is the integrated signal of the complex for 1s and I_{Ru} is the integrated signal of Rubpy under the same conditions. The values were the average of three different measurements. The working electrode was mechanically cleaned before each run as described for the electrochemical measurements. A $Ru(bpy)_2PF_6$ solution (10^{-5} M in Procell[®]) was used as reference.

Absorption spectra were measured on a Shimadzu UV-3600 double-beam UV-Vis-NIR spectrometer and baseline corrected. Steady-state emission spectra were recorded on HORIBA Jobin-Yvon IBH FL-322 Fluorolog 3 spectrometer equipped with a 450W xenon-arc lamp, double-grating excitation and emission monochromators (2.1 nm/mm dispersion, 1200 grooves/mm blazed at 500 nm), and a TBX-04 detector. Emission and excitation spectra were corrected for source intensity (lamp and grating) and emission spectral response (detector

and grating) by standard correction curves. The quantum yield measurements were performed by using an absolute photoluminescence quantum yield spectrometer Quantaaurus C11347 (Hamamatsu, Japan). Time-resolved measurements were performed by using time-correlated single-photon counting (TCSPC) electronics PicoHarp300 of a PicoQuant FluoTime 300 (PicoQuant GmbH, Germany), equipped with a PDL 820 laser pulse driver. The excitation wavelength was 375 nm (NCNDs and the hybrids) and 440 nm ($[\text{Ru}(\text{bpy})_3]^{2+}$, Ir-COOH and the hybrids) using a laser source LDH-P-C-375 and the time-correlated single photon counting (TCSPC) option was used for decays times. The laser was mounted directly on the sample chamber at 90° to a Czerny-Turner type emission monochromator (2.7 nm mm^{-1} of dispersion; $1200 \text{ grooves mm}^{-1}$). The photons were collected with a PMA-C-192 photomultiplier (PMT) single-photon-counting detector. For anisotropy measurements, the solvent used was ethylene glycol. The polarization was in the configuration VV (vertical-vertical) and VH (vertical-horizontal). The data were acquired by using the commercially available software EasyTau (PicoQuant GmbH, Germany), and data analysis was performed by using the commercially available software FluoFit (PicoQuant GmbH, Germany). The goodness-of-fit was assessed by minimizing the reduced chi-square function (χ^2) and visual inspection of the weighted residuals.

3.5.3 Syntheses of the hybrids

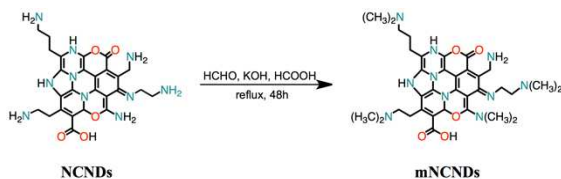


For Ru-NCNDs, NCNDs (40.0 mg, 1.0 eq) were added into a solution of bis-(2,2-bipyridyl) (4-carboxypropyl,4'-methyl-2,2'-bipyridine) ruthenium(II) (Ru-COOSu) (39.0 mg, 1.4 eq) in MeOH (1.5 mL), then PBS (2.0 mL) was added.

For Ir-NCNDs, NCNDs (40.0 mg, 1.0 eq) were added into a solution containing EDC, NHS and Ir (6-phenylphenanthridine)₂ 2-(carboxyethyl-phenyl)pyridine-2-carboxylic acid (Ir-COOH) (30.34 mg, 1.0 eq) in DMF (5.0 mL).

The mixtures were then stirred at room temperature for 16 h. The solvent was removed under reduced pressure and the crude mixture was dissolved in MeOH (1.5 mL) and separated by SEC using a column packed with Sephadex LH-20 (eluting with MeOH). Finally, MeOH was removed under reduced pressure obtaining two orange-red solids as the final products Ru-NCNDs and Ir-NCNDs (26.0 mg and 30.0 mg, respectively).

3.5.4 Synthesis of mNCNDs



The synthetic procedure was adapted from the literature.¹⁴¹⁻¹⁴³ NCNDs (80.0 mg, 0.11 mmol amines) were dissolved in a mixture of formalin (37 % w/v, 3.0 mL, 0.01 mol) and formic acid (99 %, 4 mL, 106.0 mmol). The solution was heated to reflux for 48 h and then cooled to room temperature. Volatiles were removed under vacuum together with the solvent and the residue was taken up in water and dialyzed against pure water through a dialysis membrane for 2 days. The aqueous solution of NCNDs was lyophilized, yielding a slightly brownish solid (mNCNDs: 47.5 mg). Kaiser Tests performed on NCNDs and mNCNDs result respectively in 1350 $\mu\text{mol/g}$ and 26 $\mu\text{mol/g}$ of amines.

3.6 References

- (1) A.J. Bard. Electrogenerated Chemiluminescence. *Marcel Dekker, New York* **2004**.
- (2) Richter, M. M. Electrochemiluminescence (ECL). *Chem. Rev.* **2004**, *104*, 3003–3036.
- (3) Miao, W. Electrogenerated Chemiluminescence and Its Biorelated Applications. *Chem. Rev.* **2008**, *108*, 2506–2553.
- (4) Richter, M. M. Electrochemiluminescence (ECL). *Chem. Rev.* **2004**, *104*, 3003–3036.
- (5) Hu, L.; Xu, G. Applications and Trends in Electrochemiluminescence. *Chem. Soc. Rev.* **2010**, *39*, 3275–3304.
- (6) Dennany, L.; Forster, R. J.; White, B.; Smyth, M.; Rusling, J. F. Direct Electrochemiluminescence Detection of Oxidized DNA in Ultrathin Films Containing [Os(bpy)₂(PVP)₁₀]²⁺. *J. Am. Chem. Soc.* **2004**, *126*, 8835–8841.
- (7) Dennany, L.; Forster, R. J.; Rusling, J. F. Simultaneous Direct Electrochemiluminescence and Catalytic Voltammetry Detection of DNA in Ultrathin Films. *J. Am. Chem. Soc.* **2003**, *125*, 5213–5218.
- (8) Sardesai, N. P.; Barron, J. C.; Rusling, J. F. Carbon Nanotube Microwell Array for Sensitive Electrochemiluminescent Detection of Cancer Biomarker Proteins. *Anal. Chem.* **2011**, *83*, 6698–6703.
- (9) Hvastkovs, E. G.; So, M.; Krishnan, S.; Bajrami, B.; Tarun, M.; Jansson, I.; Schenkman, J. B.; Rusling, J. F. Electrochemiluminescent Arrays for Cytochrome P450-Activated Genotoxicity Screening. DNA Damage from Benzo[a]pyrene Metabolites. *Anal. Chem.* **2007**, *79*, 1897–1906.
- (10) Sun, B.; Qi, H.; Ma, F.; Gao, Q.; Zhang, C.; Miao, W. Double Covalent Coupling Method for the Fabrication of Highly

-
- Sensitive and Reusable Electrogenerated Chemiluminescence Sensors. *Anal. Chem.* **2010**, *82*, 5046–5052.
- (11) So, M.; Hvastkovs, E. G.; Schenkman, J. B.; Rusling, J. F. Electrochemiluminescent/voltammetric Toxicity Screening Sensor Using Enzyme-Generated DNA Damage. *Biosens. Bioelectron.* **2007**, *23*, 492–498.
- (12) Juris, A.; Balzani, V.; Barigelletti, F.; Campagna, S.; Belser, P.; von Zelewsky, A. Ru(II) Polypyridine Complexes: Photophysics, Photochemistry, Electrochemistry, and Chemiluminescence. *Coord. Chem. Rev.* **1988**, *84*, 85–277.
- (13) Rubinstein, I.; Bard, A. J. Electrogenerated Chemiluminescence. 37. Aqueous Ecl Systems Based on tris(2,2'-bipyridine)ruthenium(2+) and Oxalate or Organic Acids. *J. Am. Chem. Soc.* **1981**, *103*, 512–516.
- (14) Ege, D.; Becker, W. G.; Bard, A. J. Electrogenerated Chemiluminescent Determination of tris(2,2'-bipyridine)ruthenium Ion (Ru(bpy)₃²⁺) at Low Levels. *Anal. Chem.* **1984**, *56*, 2413–2417.
- (15) Zhou, M.; Robertson, G. P.; Roovers, J. Comparative Study of Ruthenium(II) Tris(bipyridine) Derivatives for Electrochemiluminescence Application. *Inorg. Chem.* **2005**, *44*, 8317–8325.
- (16) Wei, H.; Wang, E. Electrochemiluminescence of tris(2,2'-Bipyridyl)ruthenium and Its Applications in Bioanalysis: A Review. *Luminescence* **2011**, *26*, 77–85.
- (17) Li, J.; Wang, E. Applications of tris(2,2'-bipyridyl)ruthenium(II) in Electrochemiluminescence. *Chem. Rec.* **2012**, *12*, 177–187.
- (18) Huang, B.; Zhou, X.; Xue, Z.; Lu, X. Electrochemiluminescence Quenching of tris(2,2'-Bipyridyl)ruthenium. *TrAC Trends Anal. Chem.* **2013**, *51*, 107–116.
-

- (19) Zhang, S.; Ding, Y.; Wei, H. Ruthenium Polypyridine Complexes Combined with Oligonucleotides for Bioanalysis: A Review. *Molecules* **2014**, *19*, 11933–11987.
- (20) Kenten, J. H.; Casadei, J.; Link, J.; Lupold, S.; Willey, J.; Powell, M.; Rees, A.; Massey, R. Rapid Electrochemiluminescence Assays of Polymerase Chain Reaction Products. *Clin. Chem.* **1991**, *37*, 1626–1632.
- (21) Blackburn, G. F.; Shah, H. P.; Kenten, J. H.; Leland, J.; Kamin, R. A.; Link, J.; Peterman, J.; Powell, M. J.; Shah, A.; Talley, D. B. Electrochemiluminescence Detection for Development of Immunoassays and DNA Probe Assays for Clinical Diagnostics. *Clin. Chem.* **1991**, *37*, 1534–1539.
- (22) YU, H. Detection of Biological Threat Agents by Immunomagnetic Microsphere-Based Solid Phase Fluorogenic- and Electro-Chemiluminescence. *Biosens. Bioelectron.* **2000**, *14*, 829–840.
- (23) Jameison, F.; Sanchez, R. I.; Dong, L.; Leland, J. K.; Yost, D.; Martin, M. T. Electrochemiluminescence-Based Quantitation of Classical Clinical Chemistry Analytes. *Anal. Chem.* **1996**, *68*, 1298–1302.
- (24) Namba, Y.; Usami, M.; Suzuki, O. Highly Sensitive Electrochemiluminescence Immunoassay Using the Ruthenium Chelate-Labeled Antibody Bound on the Magnetic Micro Beads. *Anal. Sci.* **1999**, *15*, 1087–1093.
- (25) Deaver, D. R. A New Non-Isotopic Detection System for Immunoassays. *Nature* **1995**, *377*, 758–760.
- (26) Luttmmer, J. D.; Bard, A. J. Electrogenerated Chemiluminescence. 38. Emission Intensity-Time Transients in the tris(2,2'-bipyridine)ruthenium(II) System. *J. Phys. Chem.* **1981**, *85*, 1155–1159.
- (27) Lai, R. Y.; Chiba, M.; Kitamura, N.; Bard, A. J. Electrogenerated Chemiluminescence. 68. Detection of Sodium Ion with a Ruthenium(II) Complex with Crown Ether

- Moiety at the 3,3'-Positions on the 2,2'-Bipyridine Ligand. *Anal. Chem.* **2002**, *74*, 551–553.
- (28) Schmittl, M.; Lin, H.-W. Quadruple-Channel Sensing: A Molecular Sensor with a Single Type of Receptor Site for Selective and Quantitative Multi-Ion Analysis. *Angew. Chem. Int. Ed.* **2007**, *46*, 893–896.
- (29) Li, M.-J.; Chen, Z.; Zhu, N.; Yam, V. W.-W.; Zu, Y. Electrochemiluminescence of Ruthenium(II) Complexes Functionalized with Crown Ether Pendants and Effects of Cation Binding. *Inorg. Chem.* **2008**, *47*, 1218–1223.
- (30) Hu, L.; Bian, Z.; Li, H.; Han, S.; Yuan, Y.; Gao, L.; Xu, G. [Ru(bpy)₂dppz]²⁺ Electrochemiluminescence Switch and Its Applications for DNA Interaction Study and Label-Free ATP Aptasensor. *Anal. Chem.* **2009**, *81*, 9807–9811.
- (31) Staffilani, M.; Höss, E.; Giesen, U.; Schneider, E.; Hartl, F.; Josel, H.-P.; De Cola, L. Multimetallic ruthenium(II) Complexes as Electrochemiluminescent Labels. *Inorg. Chem.* **2003**, *42*, 7789–7798.
- (32) Richter, M. M.; Bard, A. J.; Kim, W.; Schmehl, R. H. Electrogenerated Chemiluminescence. 62. Enhanced ECL in Bimetallic Assemblies with Ligands That Bridge Isolated Chromophores. *Anal. Chem.* **1998**, *70*, 310–318.
- (33) Zhou, M.; Roovers, J. Dendritic Supramolecular Assembly with Multiple Ru(II) Tris(bipyridine) Units at the Periphery: Synthesis, Spectroscopic, and Electrochemical Study. *Macromolecules* **2001**, *34*, 244–252.
- (34) Zhou, M.; Roovers, J.; Robertson, G. P.; Grover, C. P. Multilabeling Biomolecules at a Single Site. 1. Synthesis and Characterization of a Dendritic Label for Electrochemiluminescence Assays. *Anal. Chem.* **2003**, *75*, 6708–6717.
- (35) Chikhaliwala, P.; Chandra, S. Dendrimers: New Tool for Enhancement of Electrochemiluminescent Signal. *J.*
-

Organomet. Chem. **2016**, *821*, 78–90.

- (36) Puodziukynaite, E.; Oberst, J. L.; Dyer, A. L.; Reynolds, J. R. Establishing Dual Electrogenenerated Chemiluminescence and Multicolor Electrochromism in Functional Ionic Transition-Metal Complexes. *J. Am. Chem. Soc.* **2012**, *134*, 968–978.
- (37) Evariste, S.; Sandroni, M.; Rees, T. W.; Roldán-Carmona, C.; Gil-Escrig, L.; Bolink, H. J.; Baranoff, E.; Zysman-Colman, E. Fluorine-Free Blue-Green Emitters for Light-Emitting Electrochemical Cells. *J. Mater. Chem. C* **2014**, *2*, 5793.
- (38) Barbante, G. J.; Doeven, E. H.; Kerr, E.; Connell, T. U.; Donnelly, P. S.; White, J. M.; López, T.; Laird, S.; Wilson, D. J. D.; Barnard, P. J.; *et al.* Understanding Electrogenenerated Chemiluminescence Efficiency in Blue-Shifted Iridium(III)-Complexes: An Experimental and Theoretical Study. *Chem. - A Eur. J.* **2014**, *20*, 3322–3332.
- (39) Tordera, D.; Bünzli, A. M.; Pertegás, A.; Junquera-Hernández, J. M.; Constable, E. C.; Zampese, J. A.; Housecroft, C. E.; Ortí, E.; Bolink, H. J. Efficient Green-Light-Emitting Electrochemical Cells Based on Ionic Iridium Complexes with Sulfone-Containing Cyclometalating Ligands. *Chem. - A Eur. J.* **2013**, *19*, 8597–8609.
- (40) Fernández-Hernández, J. M.; Ladouceur, S.; Shen, Y.; Iordache, A.; Wang, X.; Donato, L.; Gallagher-Duval, S.; de Anda Villa, M.; Slinker, J. D.; De Cola, L.; *et al.* Blue Light Emitting Electrochemical Cells Incorporating Triazole-Based Luminophores. *J. Mater. Chem. C* **2013**, *1*, 7440–7452.
- (41) Meier, S. B.; Sarfert, W.; Junquera-Hernández, J. M.; Delgado, M.; Tordera, D.; Ortí, E.; Bolink, H. J.; Kessler, F.; Scopelliti, R.; Grätzel, M.; *et al.* A Deep-Blue Emitting Charged Bis-Cyclometallated iridium(III) Complex for Light-Emitting Electrochemical Cells. *J. Mater. Chem. C* **2013**, *1*, 58–68.
- (42) Li, M.-J.; Jiao, P.; Lin, M.; He, W.; Chen, G.-N.; Chen, X. High Electrochemiluminescence of a New Water-Soluble
-

- iridium(III) Complex for Determination of Antibiotics. *Analyst* **2011**, *136*, 205–210.
- (43) Ding, Z.; Quinn, B. M.; Haram, S. K.; Pell, L. E.; Korgel, B. A.; Bard, A. J. Electrochemistry and Electrogenenerated Chemiluminescence from Silicon Nanocrystal Quantum Dots. *Science* **2002**, *296*, 1293–1297.
- (44) Miao, J.-J.; Ren, T.; Dong, L.; Zhu, J.-J.; Chen, H.-Y. Double-Template Synthesis of CdS Nanotubes with Strong Electrogenenerated Chemiluminescence. *Small* **2005**, *1*, 802–805.
- (45) Gill, R.; Polsky, R.; Willner, I. Pt Nanoparticles Functionalized with Nucleic Acid Act as Catalytic Labels for the Chemiluminescent Detection of DNA and Proteins. *Small* **2006**, *2*, 1037–1041.
- (46) Chen, Z.; Zu, Y. Gold Nanoparticle-Modified ITO Electrode for Electrogenenerated Chemiluminescence: Well-Preserved Transparency and Highly Enhanced Activity. *Langmuir* **2007**, *23*, 11387–11390.
- (47) Shen, L.; Cui, X.; Qi, H.; Zhang, C. Electrogenenerated Chemiluminescence of ZnS Nanoparticles in Alkaline Aqueous Solution. *J. Phys. Chem. C* **2007**, *111*, 8172–8175.
- (48) Lin, Z.; Chen, J.; Chen, G. An ECL Biosensor for Glucose Based on Carbon-nanotube/Nafion Film Modified Glass Carbon Electrode. *Electrochim. Acta* **2008**, *53*, 2396–2401.
- (49) Chang, Y.-L.; Palacios, R. E.; Fan, F.-R. F.; Bard, A. J.; Barbara, P. F. Electrogenenerated Chemiluminescence of Single Conjugated Polymer Nanoparticles. *J. Am. Chem. Soc.* **2008**, *130*, 8906–8907.
- (50) Fang, Y.-M.; Song, J.; Li, J.; Wang, Y.-W.; Yang, H.-H.; Sun, J.-J.; Chen, G.-N. Electrogenenerated Chemiluminescence from Au Nanoclusters. *Chem. Commun.* **2011**, *47*, 2369–2371.
- (51) Li, L.; Liu, H.; Shen, Y.; Zhang, J.; Zhu, J.-J. Electrogenenerated Chemiluminescence of Au Nanoclusters for
-

-
- the Detection of Dopamine. *Anal. Chem.* **2011**, *83*, 661–665.
- (52) Li, L.-L.; Ji, J.; Fei, R.; Wang, C.-Z.; Lu, Q.; Zhang, J.-R.; Jiang, L.-P.; Zhu, J.-J. A Facile Microwave Avenue to Electrochemiluminescent Two-Color Graphene Quantum Dots. *Adv. Funct. Mater.* **2012**, *22*, 2971–2979.
- (53) Xu, Y.; Wu, M.; Feng, X.-Z.; Yin, X.-B.; He, X.-W.; Zhang, Y.-K. Reduced Carbon Dots versus Oxidized Carbon Dots: Photo- and Electrochemiluminescence Investigations for Selected Applications. *Chem. - A Eur. J.* **2013**, *19*, 6282–6288.
- (54) Wu, L.; Wang, J.; Ren, J.; Li, W.; Qu, X. Highly Sensitive Electrochemiluminescent Cytosensing Using Carbon nanodot@Ag Hybrid Material and Graphene for Dual Signal Amplification. *Chem. Commun.* **2013**, *49*, 5675–5677.
- (55) Wu, P.; Hou, X.; Xu, J.-J.; Chen, H.-Y. Electrochemically Generated versus Photoexcited Luminescence from Semiconductor Nanomaterials: Bridging the Valley between Two Worlds. *Chem. Rev.* **2014**, *114*, 11027–11059.
- (56) Amelia, M.; Lincheneau, C.; Silvi, S.; Credi, A. Electrochemical Properties of CdSe and CdTe Quantum Dots. *Chem. Soc. Rev.* **2012**, *41*, 5728–5743.
- (57) Liu, X.; Jiang, H.; Lei, J.; Ju, H. Anodic Electrochemiluminescence of CdTe Quantum Dots and Its Energy Transfer for Detection of Catechol Derivatives. *Anal. Chem.* **2007**, *79*, 8055–8060.
- (58) Myung, N.; Lu, X.; Johnston, K. P.; Bard, A. J. Electrogenerated Chemiluminescence of Ge Nanocrystals. *Nano Lett.* **2004**, *4*, 183–185.
- (59) Bae, Y.; Myung, N.; Bard, A. J. Electrochemistry and Electrogenerated Chemiluminescence of CdTe Nanoparticles. *Nano Lett.* **2004**, *4*, 1153–1161.
- (60) Rampazzo, E.; Bonacchi, S.; Genovese, D.; Juris, R.; Marcaccio, M.; Montalti, M.; Paolucci, F.; Sgarzi, M.;
-

- Valenti, G.; Zaccheroni, N.; *et al.* Nanoparticles in Metal Complexes-Based Electrogenerated Chemiluminescence for Highly Sensitive Applications. *Coord. Chem. Rev.* **2012**, *256*, 1664–1681.
- (61) Bertocello, P.; Forster, R. J. Nanostructured Materials for Electrochemiluminescence (ECL)-Based Detection Methods: Recent Advances and Future Perspectives. *Biosens. Bioelectron.* **2009**, *24*, 3191–3200.
- (62) Miao, W.; Bard, A. J. Electrogenerated Chemiluminescence. 80. C-Reactive Protein Determination at High Amplification with [Ru(bpy)₃]²⁺-Containing Microspheres. *Anal. Chem.* **2004**, *76*, 7109–7113.
- (63) Miao, W.; Bard, A. J. Electrogenerated Chemiluminescence. 77. DNA Hybridization Detection at High Amplification with [Ru(bpy)₃]²⁺-Containing Microspheres. *Anal. Chem.* **2004**, *76*, 5379–5386.
- (64) Bagwe, R. P.; Yang, C.; Hilliard, L. R.; Tan, W. Optimization of Dye-Doped Silica Nanoparticles Prepared Using a Reverse Microemulsion Method. *Langmuir* **2004**, *20*, 8336–8342.
- (65) Sun, X.; Du, Y.; Dong, S.; Wang, E. Method for Effective Immobilization of Ru(bpy)₃(3)²⁺ on an Electrode Surface for Solid-State Electrochemiluminescence Detection. *Anal. Chem.* **2005**, *77*, 8166–8169.
- (66) Wang, L.; Yang, C.; Tan, W. Dual-Luminophore-Doped Silica Nanoparticles for Multiplexed Signaling. *Nano Lett.* **2005**, *5*, 37–43.
- (67) Zhang, L.; Liu, B.; Dong, S. Bifunctional Nanostructure of Magnetic Core Luminescent Shell and Its Application as Solid-State Electrochemiluminescence Sensor Material. *J. Phys. Chem. B* **2007**, *111*, 10448–10452.
- (68) Qian, L.; Yang, X.-R. One-Step Synthesis of Ru(2,2'-Bipyridine)₃Cl₂-Immobilized Silica Nanoparticles for Use in Electrogenerated Chemiluminescence Detection. *Adv. Funct.*
-

- Mater.* **2007**, *17*, 1353–1358.
- (69) Zhang, L.; Wang, F.; Dong, S. Layer-by-Layer Assembly of Functional Silica and Au Nanoparticles for Fabricating Electrogenenerated Chemiluminescence Sensor. *Electrochim. Acta* **2008**, *53*, 6423–6427.
- (70) Li, J.; Guo, L.-R.; Gao, W.; Xia, X.-H.; Zheng, L.-M. Enhanced Electrochemiluminescence Efficiency of Ru(II) Derivative Covalently Linked Carbon Nanotubes Hybrid. *Chem. Commun.* **2009**, 7545–7547.
- (71) Zhu, X.; Chen, L.; Lin, Z.; Qiu, B.; Chen, G. A Highly Sensitive and Selective “signal-On” Electrochemiluminescent Biosensor for Mercury. *Chem. Commun.* **2010**, *46*, 3149–3151.
- (72) Zheng, L.; Chi, Y.; Wang, B.; Han, L.; Chen, G. Strong Electrochemiluminescence Based on Electron Transfer between Tris(2,2'-bipyridine)ruthenium(III) and SnO NPs@MWCNTs. *Chem. Commun.* **2010**, *46*, 5734–5736.
- (73) Zamolo, V. A.; Valenti, G.; Venturelli, E.; Chaloin, O.; Marcaccio, M.; Boscolo, S.; Castagnola, V.; Sosa, S.; Berti, F.; Fontanive, G.; *et al.* Highly Sensitive Electrochemiluminescent Nanobiosensor for the Detection of Palytoxin. *ACS Nano* **2012**, *6*, 7989–7997.
- (74) Bozorgzadeh, S.; Haghghi, B.; Gorton, L. Fabrication of a Highly Efficient Solid State Electrochemiluminescence Sensor Using Ru(bpy)₃²⁺ Incorporated nanoZnO-MWCNTs-Nafion Composite Film. *Electrochim. Acta* **2015**, *164*, 211–217.
- (75) Yu, Y.; Zhou, M.; Cui, H. Synthesis and Electrochemiluminescence of bis(2,2'-bipyridine)(5-Amino-1,10-Phenanthroline) ruthenium(II)-Functionalized Gold Nanoparticles. *J. Mater. Chem.* **2011**, *21*, 12622–12625.
- (76) Zanarini, S.; Rampazzo, E.; Ciana, L. Della; Marcaccio, M.; Marzocchi, E.; Montalti, M.; Paolucci, F.; Prodi, L. Ru(bpy)₃
-

- Covalently Doped Silica Nanoparticles as Multicenter Tunable Structures for Electrochemiluminescence Amplification. *J. Am. Chem. Soc.* **2009**, *131*, 2260–2267.
- (77) Miao, W.; Choi, J.-P.; Bard, A. J. Electrogenerated Chemiluminescence 69: The Tris(2,2'-bipyridine)ruthenium(II), (Ru(bpy)₃²⁺)/Tri-N-Propylamine (TPrA) System Revisited-A New Route Involving TPrA^{•+} Cation Radicals. *J. Am. Chem. Soc.* **2002**, *124*, 14478–14485.
- (78) Lee, S. K.; Zu, Y.; Herrmann, A.; Geerts, Y.; Müllen, K.; Bard, A. J. Electrochemistry, Spectroscopy and Electrogenerated Chemiluminescence of Perylene, Terrylene, and Quaterylene Diimides in Aprotic Solution. *J. Am. Chem. Soc.* **1999**, *121*, 3513–3520.
- (79) Bolleta, F.; Ciano, M.; Balzani, V.; Serpone, N. Polypyridine Transition Metal Complexes as Light Emission Sensitizers in the Electrochemical Reduction of the Persulfate Ion. *Inorganica Chim. Acta* **1982**, *62*, 207–213.
- (80) White, H. S.; Bard, A. J. Electrogenerated Chemiluminescence. 41. Electrogenerated Chemiluminescence and Chemiluminescence of the Ru(2,2-bpy)₃²⁺-S₂O₈²⁻ System in Acetonitrile-Water Solutions. *J. Am. Chem. Soc.* **1982**, *104*, 6891–6895.
- (81) Rubinstein, I.; Bard, A. J. Electrogenerated Chemiluminescence. 37. Aqueous Ecl Systems Based on tris(2,2'-bipyridine)ruthenium(2+) and Oxalate or Organic Acids. *J. Am. Chem. Soc.* **1981**, *103*, 512–516.
- (82) Chang, M.-M.; Saji, T.; Bard, A. J. Electrogenerated Chemiluminescence. 30. Electrochemical Oxidation of Oxalate Ion in the Presence of Luminescers in Acetonitrile Solutions. *J. Am. Chem. Soc.* **1977**, *99*, 5399–5403.
- (83) Leland, J. K. Electrogenerated Chemiluminescence: An Oxidative-Reduction Type ECL Reaction Sequence Using Tripropyl Amine. *J. Electrochem. Soc.* **1990**, *137*, 3127–3131.
-

-
- (84) Gross, E. M.; Pastore, P.; Wightman, R. M. High-Frequency Electrochemiluminescent Investigation of the Reaction Pathway between Tris(2,2'-bipyridyl)ruthenium(II) and Tripropylamine Using Carbon Fiber Microelectrodes. *J. Phys. Chem. B* **2001**, *105*, 8732–8738.
- (85) Xu, J.; Huang, P.; Qin, Y.; Jiang, D.; Chen, H. Analysis of Intracellular Glucose at Single Cells Using Electrochemiluminescence Imaging. *Anal. Chem.* **2016**, *88*, 4609–4612.
- (86) Liu, X.; Shi, L.; Niu, W.; Li, H.; Xu, G. Environmentally Friendly and Highly Sensitive Ruthenium(II) Tris(2,2'-Bipyridyl) Electrochemiluminescent System Using 2-(Dibutylamino)ethanol as Co-Reactant. *Angew. Chem. Int. Ed.* **2007**, *46*, 421–424.
- (87) Han, S.; Niu, W.; Li, H.; Hu, L.; Yuan, Y.; Xu, G. Effect of Hydroxyl and Amino Groups on Electrochemiluminescence Activity of Tertiary Amines at Low tris(2,2'-bipyridyl)ruthenium(II) Concentrations. *Talanta* **2010**, *81*, 44–47.
- (88) Kitte, S. A.; Wang, C.; Li, S.; Zholudov, Y.; Qi, L.; Li, J.; Xu, G. Electrogenerated Chemiluminescence of tris(2,2'-bipyridine)ruthenium(II) Using N-(3-Aminopropyl)diethanolamine as Coreactant. *Anal. Bioanal. Chem.* **2016**, *408*, 7059–7065.
- (89) Downey, T. M.; Nieman, T. A. Chemiluminescence Detection Using Regenerable tris(2,2'-bipyridyl)ruthenium(II) Immobilized in Nafion. *Anal. Chem.* **1992**, *64*, 261–268.
- (90) Milutinovic, M.; Sallard, S.; Manojlovic, D.; Mano, N.; Sojic, N. Glucose Sensing by Electrogenerated Chemiluminescence of Glucose-Dehydrogenase Produced NADH on Electrodeposited Redox Hydrogel. *Bioelectrochemistry* **2011**, *82*, 63–68.
- (91) Sentic, M.; Arbault, S.; Goudeau, B.; Manojlovic, D.; Kuhn,
-

- A.; Bouffier, L.; Sojic, N. Electrochemiluminescent Swimmers for Dynamic Enzymatic Sensing. *Chem. Commun.* **2014**, *50*, 10202–10205.
- (92) Swanick, K. N.; Ladouceur, S.; Zysman-Colman, E.; Ding, Z. Self-Enhanced Electrochemiluminescence of an iridium(III) Complex: Mechanistic Insight. *Angew. Chem. Int. Ed.* **2012**, *51*, 11079–11082.
- (93) Liang, W.; Zhuo, Y.; Xiong, C.; Zheng, Y.; Chai, Y.; Yuan, R. Ultrasensitive Cytosensor Based on Self-Enhanced Electrochemiluminescent Ruthenium-Silica Composite Nanoparticles for Efficient Drug Screening with Cell Apoptosis Monitoring. *Anal. Chem.* **2015**, *87*, 12363–12371.
- (94) Li, P.; Jin, Z.; Zhao, M.; Xu, Y.; Guo, Y.; Xiao, D. Self-Enhanced Electrogenerated Chemiluminescence of ruthenium(II) Complexes Conjugated with Schiff Bases. *Dalton Trans.* **2015**, *44*, 2208–2216.
- (95) Wang, H.; Liu, Y.; Li, M.; Huang, H.; Xu, H. M.; Hong, R. J.; Shen, H. Multifunctional TiO₂ Nanowires-Modified Nanoparticles Bilayer Film for 3D Dye-Sensitized Solar Cells. *Optoelectron. Adv. Mater. Rapid Commun.* **2010**, *4*, 1166–1169.
- (96) Zhuo, Y.; Liao, N.; Chai, Y. Q.; Gui, G. F.; Zhao, M.; Han, J.; Xiang, Y.; Yuan, R. Ultrasensitive Apurinic/aprimidinic Endonuclease 1 Immunosensing Based on Self-Enhanced Electrochemiluminescence of a Ru(II) Complex. *Anal. Chem.* **2014**, *86*, 1053–1060.
- (97) Wang, H.; Yuan, Y.; Zhuo, Y.; Chai, Y.; Yuan, R. Self-Enhanced Electrochemiluminescence Nanorods of Tris(bipyridine) Ruthenium(II) Derivative and Its Sensing Application for Detection of N-Acetyl- β -D-Glucosaminidase. *Anal. Chem.* **2016**, *88*, 2258–2265.
- (98) Wang, H.; He, Y.; Chai, Y.; Yuan, R. A Super Intramolecular Self-Enhanced Electrochemiluminescence Immunosensor Based on Polymer Chains Grafted on Palladium Nanocages.
-

- Nanoscale* **2014**, *6*, 10316–10322.
- (99) Gui, G.-F.; Zhuo, Y.; Chai, Y.-Q.; Xiang, Y.; Yuan, R. In Situ Generation of Self-Enhanced Luminophore by β -Lactamase Catalysis for Highly Sensitive Electrochemiluminescent Aptasensor. *Anal. Chem.* **2014**, *86*, 5873–5880.
- (100) Pinaud, F.; Russo, L.; Pinet, S.; Gosse, I.; Ravaine, V.; Sojic, N. Enhanced Electrogenenerated Chemiluminescence in Thermo-responsive Microgels. *J. Am. Chem. Soc.* **2013**, *135*, 5517–5520.
- (101) Zhang, L.; He, Y.; Wang, H.; Yuan, Y.; Yuan, R.; Chai, Y. A Self-Enhanced Electrochemiluminescence Immunosensor Based on L-Lys-Ru(dcbpy)₃²⁺ Functionalized Porous Six Arm Star Column Nanorods for Detection of CA15-3. *Biosens. Bioelectron.* **2015**, *74*, 924–930.
- (102) Zhou, L.; Huang, J.; Yu, B.; You, T. A Novel Self-Enhanced Electrochemiluminescence Immunosensor Based on Hollow Ru-SiO₂@PEI Nanoparticles for NSE Analysis. *Sci. Rep.* **2016**, *6*, 22234–22242.
- (103) Miao, W. Electrogenenerated Chemiluminescence. In *Handbook of Electrochemistry*; Zoski, C. G.; Elsevier: Amsterdam, T. N., Ed.; 2007; pp. 541–590.
- (104) Zu, Y.; Bard, A. J. Electrogenenerated Chemiluminescence. 66. The Role of Direct Coreactant Oxidation in the Ruthenium Tris(2,2')bipyridyl/Tripropylamine System and the Effect of Halide Ions on the Emission Intensity. *Anal. Chem.* **2000**, *72*, 3223–3232.
- (105) Kanoufi, F.; Zu, Y.; Bard, A. J. Homogeneous Oxidation of Trialkylamines by Metal Complexes and Its Impact on Electrogenenerated Chemiluminescence in the Trialkylamine / Ru(bpy)₃²⁺ System. *J. Phys. Chem. B* **2001**, *105*, 210–216.
- (106) Arora, A.; de Mello, A. J.; Manz, A. Sub-Microliter Electrochemiluminescence Detector-A Model for Small Volume Analysis Systems. *Anal. Commun.* **1997**, *34*, 393–
-

395.

- (107) Yuan, J.; Li, T.; Yin, X.; Guo, L.; Jiang, X.; Jin, W.; Yang, X.; Wang, E. Characterization of Prolidase Activity Using Capillary Electrophoresis with Tris(2,2'-bipyridyl)ruthenium(II) Electrochemiluminescence Detection and Application To Evaluate Collagen Degradation in Diabetes Mellitus. *Anal. Chem.* **2006**, *78*, 2934–2938.
- (108) Li, J.; Yan, Q.; Gao, Y.; Ju, H. Electrogenated Chemiluminescence Detection of Amino Acids Based on Precolumn Derivatization Coupled with Capillary Electrophoresis Separation. *Anal. Chem.* **2006**, *78*, 2694–2699.
- (109) Morita, H.; Konishi, M. Electrogenated Chemiluminescence Derivatization Reagent, 3-Isobutyl-9,10-Dimethoxy-1,3,4,6,7,11b-Hexahydro-2H-pyrido[2,1-a]isoquinolin-2-Ylamine, for Carboxylic Acid in High-Performance Liquid Chromatography Using Tris(2,2'-bipyridine)ruthenium(II). *Anal. Chem.* **2003**, *75*, 940–946.
- (110) Zhao, X.; You, T.; Liu, J.; Sun, X.; Yan, J.; Yang, X.; Wang, E. Drug-Human Serum Albumin Binding Studied by Capillary Electrophoresis with Electrochemiluminescence Detection. *Electrophoresis* **2004**, *25*, 3422–3426.
- (111) Forbes, G. A.; Nieman, T. A.; Sweedler, J. V. On-Line Electrogenated Ru(bpy)₃³⁺ Chemiluminescent Detection of β -Blockers Separated with Capillary Electrophoresis. *Anal. Chim. Acta* **1997**, *347*, 289–293.
- (112) Pérez-Ruiz, T.; Martínez-Lozano, C.; García, M. D. High-Performance Liquid Chromatography–post-Column Chemiluminescence Determination of Aminopolycarboxylic Acids at Low Concentration Levels Using tris(2,2'-bipyridyl)ruthenium(III). *J. Chromatogr. A* **2007**, *1169*, 151–157.
- (113) Li, Y.; Zhang, Z. Tris(2,2-bipyridyl)ruthenium(II) [Ru(bpy)₃²⁺]-Modified Single Pt Wire Electrogenated

- Chemiluminescence Detector for High-Performance Liquid Chromatography and Its Application in the Determination of Antiemetic Drugs in Human Serum. *Anal. Methods* **2012**, *4*, 4014–4018.
- (114) Gross, E. M.; Maddipati, S. S.; Snyder, S. M. A Review of Electrogenenerated Chemiluminescent Biosensors for Assays in Biological Matrices. *Bioanalysis* **2016**, *8*, 2071–2089.
- (115) Hsueh, Y.-T.; Collins, S. D.; Smith, R. L. DNA Quantification with an Electrochemiluminescence Microcell. *Sensors Actuators B Chem.* **1998**, *49*, 1–4.
- (116) Long, Y.-M.; Bao, L.; Zhao, J.-Y.; Zhang, Z.-L.; Pang, D.-W. Revealing Carbon Nanodots As Coreactants of the Anodic Electrochemiluminescence of Ru(bpy)₃²⁺. *Anal. Chem.* **2014**, *86*, 7224–7228.
- (117) Li, L.; Yu, B.; Zhang, X.; You, T. A Novel Electrochemiluminescence Sensor Based on Ru(bpy)₃²⁺ /N-Carbon Nanodots System for the Detection of Bisphenol A. *Anal. Chim. Acta* **2015**, *895*, 104–111.
- (118) Knight, A. W.; Greenway, G. M. Relationship between Structural Attributes and Observed Electrogenenerated Chemiluminescence (ECL) Activity of Tertiary Amines as Potential Analytes for the tris(2,2-bipyridine)ruthenium(II) ECL Reaction. A Review. *Analyst* **1996**, *121*, 101R.
- (119) Evans, D. H. One-Electron and Two-Electron Transfers in Electrochemistry and Homogeneous Solution Reactions. *Chem. Rev.* **2008**, *108*, 2113–2144.
- (120) Lytle, F. E.; Hercules, D. M. Chemiluminescence from the Reduction of Aromatic Amine Cations and ruthenium(III) Chelates. *Photochem. Photobiol.* **1971**, *13*, 123–133.
- (121) Jonah, C. D.; Matheson, M. S.; Meisel, D. Reaction of Eaq- into Excited States of tris(2,2'-bipyridine)ruthenium(2+). *J. Am. Chem. Soc.* **1978**, *100*, 1449–1456.
- (122) Wallace, W. L.; Bard, A. J. Electrogenenerated
-

- Chemiluminescence. 35. Temperature Dependence of the ECL Efficiency of tris(2,2'-bipyridine)ruthidium(2+) in Acetonitrile and Evidence for Very High Excited State Yields from Electron Transfer Reactions. *J. Phys. Chem.* **1979**, *83*, 1350–1357.
- (123) Hercules, D. M.; Lytle, F. E. Chemiluminescence from Reduction Reactions. *J. Am. Chem. Soc.* **1966**, *88*, 4745–4746.
- (124) Kanoufi, F.; Zu, Y.; Bard, A. J. Homogeneous Oxidation of Trialkylamines by Metal Complexes and Its Impact on Electrogenerated Chemiluminescence in the Trialkylamine / Ru(bpy)₃²⁺ System. *J. Phys. Chem. B* **2001**, *105*, 210–216.
- (125) Kang, J.; Yin, X.-B.; Yang, X.; Wang, E. Electrochemiluminescence Quenching as an Indirect Method for Detection of Dopamine and Epinephrine with Capillary Electrophoresis. *Electrophoresis* **2005**, *26*, 1732–1736.
- (126) Guo, Y.; Yang, J.; Wu, X.; Du, A. A Sensitive Fluorimetric Method for the Determination of Epinephrine. *J. Fluoresc.* **2005**, *15*, 131–136.
- (127) Li, F. Determination of Noradrenaline and Dopamine in Pharmaceutical Injection Samples by Inhibition Flow Injection Electrochemiluminescence of Ruthenium Complexes. *Talanta* **2003**, *59*, 627–636.
- (128) Babaei, A.; Mirzakhani, S.; Khalilzadeh, B. A Sensitive Simultaneous Determination of Epinephrine and Tyrosine Using an iron(III) Doped Zeolite-Modified Carbon Paste Electrode. *J. Braz. Chem. Soc.* **2009**, *20*, 1862–1869.
- (129) Guo, Z.; Dong, S. Electrogenerated Chemiluminescence Determination of Dopamine and Epinephrine in the Presence of Ascorbic Acid at Carbon Nanotube/Nafion-Ru(bpy) Composite Film Modified Glassy Carbon Electrode. *Electroanalysis* **2005**, *17*, 607–612.
- (130) Xu, Z.; Yu, J.; Liu, G. Fabrication of Carbon Quantum Dots
-

- and Their Application for Efficient Detecting Ru(bpy)₃²⁺ in the Solution. *Sensors Actuators B Chem.* **2013**, *181*, 209–214.
- (131) Ameloot, M.; Acuña, A. U.; Valeur, B.; Hasselt, U.; Building, C. Fluorescence Anisotropy Measurements in Solution: Methods and Reference Materials (IUPAC Technical Report). *Pure Appl. Chem.* **2013**, *85*, 589–608.
- (132) Barbero, N.; Napione, L.; Quagliotto, P.; Pavan, S.; Barolo, C.; Barni, E.; Bussolino, F.; Viscardi, G. Fluorescence Anisotropy Analysis of Protein-Antibody Interaction. *Dye. Pigment.* **2009**, *83*, 225–229.
- (133) De Cola, L.; Belser, P. Photoinduced Energy and Electron Transfer Processes in Rigidly Bridged Dinuclear Ru/Os Complexes. *Coord. Chem. Rev.* **1998**, *177*, 301–346.
- (134) Kalyanasundaram, K. Photophysics, Photochemistry and Solar Energy Conversion with tris(bipyridyl)ruthenium(II) and Its Analogues. *Coord. Chem. Rev.* **1982**, *46*, 159–244.
- (135) Miao, W.; Choi, J.-P.; Bard, A. J. Electrogenerated Chemiluminescence 69: The Tris(2,2'-bipyridine)ruthenium(II), (Ru(bpy)₃²⁺)/Tri-N-Propylamine (TPrA) System Revisited-A New Route Involving TPrA^{•+} Cation Radicals. *J. Am. Chem. Soc.* **2002**, *124*, 14478–14485.
- (136) Tokel-Takvoryan, N. E.; Hemingway, R. E.; Bard, A. J. Electrogenerated Chemiluminescence. XIII. Electrochemical and Electrogenerated Chemiluminescence Studies of Ruthenium Chelates. *J. Am. Chem. Soc.* **1973**, *95*, 6582–6589.
- (137) Roberts, J. J. P.; Vuong, K. T.; Murray, R. W. Synthesis and Electrochemistry of 6 Nm Ferrocenated Indium–Tin Oxide Nanoparticles. *Langmuir* **2013**, *29*, 474–479.
- (138) Bhatt, P. A.; Pratap, A.; Jha, P. K. Size and Dimension Dependent Diffusion Coefficients of SnO₂ Nanoparticles. In *AIP Conference Proceedings*; 2013; Vol. 1536, pp. 237–238.
- (139) Cysewski, R.; De Cola, L.; Fernandez Hernandez, J. M.;

- Josel, H.-P.; Lopez-Calle, E.; Zarnt, T. *Iridium-Based Complexes for ECL. US 8835637 B2*, 2014.
- (140) Arcudi, F.; Đorđević, L.; Prato, M. Synthesis, Separation, and Characterization of Small and Highly Fluorescent Nitrogen-Doped Carbon NanoDots. *Angew. Chemie* **2016**, *128*, 2147–2152.
- (141) Martin, L. J.; Koegl, M.; Bader, G.; Cockcroft, X.-L.; Fedorov, O.; Fiegen, D.; Gerstberger, T.; Hofmann, M. H.; Hohmann, A. F.; Kessler, D.; *et al.* Structure-Based Design of an in Vivo Active Selective BRD9 Inhibitor. *J. Med. Chem.* **2016**, *59*, 4462–4475.
- (142) Tomassoli, I.; Gündisch, D. The Twin Drug Approach for Novel Nicotinic Acetylcholine Receptor Ligands. *Bioorg. Med. Chem.* **2015**, *23*, 4375–4389.
- (143) Moegling, J.; Benischke, A. D.; Hammann, J. M.; Vepřek, N. A.; Zoller, F.; Rendenbach, B.; Hoffmann, A.; Sievers, H.; Schuster, M.; Knochel, P.; *et al.* Bis(pyrazolyl)methane Copper Complexes as Robust and Efficient Catalysts for Sonogashira Couplings. *European J. Org. Chem.* **2015**, *2015*, 7475–7483.

4 Carbon Nanodots-based Hybrid Materials

This chapter focus on the study of nitrogen-doped carbon nanodots (NCNDs)-based hybrid materials. It is divided into three main sections. Firstly, a brief and general overview on photofunctional nanocarbon-based hybrids and supramolecular gels is presented. Then, novel covalent and supramolecular systems based on NCNDs and porphyrin are discussed, together with their extensive photophysical characterization in order to shed light on the dynamics of charge-transfer and related processes. Finally, CNDs-based ionogels and their comprehensive characterization are reported.

The work presented in Section 2 has been accomplished with the aid of *Dr. Luka Đorđević* (University of Trieste, Italy) for the materials preparation and of *Dr. Volker Strauss* and *Dr. Alejandro Cadranel* from *Prof. Dirk Guldi* group (Friedrich-Alexander-Universität Erlangen-Nürnberg, Germany) for their photophysical characterization. The materials preparation and characterization presented in Section 3 have been accomplished in collaboration with the group of *Prof. Francesca D'Anna* (University of Palermo, Italy), with the aid of *Dr. Carla Rizzo* and *Prof. Nadka Tz. Dintcheva*.

Part of the work presented in this chapter has been used in the preparation of the manuscripts: “Porphyrin Antennaes on Carbon Nanodots: Excited State Energy and Electron Transduction” and “Nitrogen-doped carbon nanodots/ionogels with powerful radical scavenging activity”.

4.1 Introduction

4.1.1 Photofunctional nanocarbon-based hybrids

The photosynthetic system is considered the most elaborate nano-scale biological machine in nature. Photosynthesis involves the capture of excitation energy by a light-harvesting antenna and its transfer to the reaction center. The reaction center converts it to chemical energy, in the form of transmembrane charge separation, via a multistep electron-transfer reaction. The stored electrochemical energy is later converted into other forms of biologically useful energy such as proton motive force.^{1,2}

All forms of renewable energy will play important roles to solve today's energy issues, however solar energy is clearly the most viable long-term solution. As a consequence, researchers have paid great attention to artificial photosynthesis, which showcases of the nanotechnology ability to address problem of societal importance.³ Artificial photosynthesis involves the mimicry of natural photosynthetic processes through the application of their basic principles for the design and assembly of simpler systems, which can efficiently process solar energy. In this context, the study of photo-induced electron transfer reactions is pivotal for the design of efficient artificial photosynthetic systems. A variety of donor-acceptor systems have been extensively investigated aiming at mimicking the natural photosynthetic process. Many synthetic methods have inspired chemists during the last two decades to modulate photoinduced electron transfer processes in donor-acceptor systems through the control of their supramolecular ensembles or covalent attachment.^{4,5} In particular, porphyrins and carbon nanomaterials have shown to be promising building blocks for photoinduced electron transfer systems.^{3,6-17}

Porphyrins (Por) have been selected by the evolution as the pigment of life in *heme* as well as in chlorophyll.¹⁸ They are the usual chromophores of choice to be employed as molecular components of artificial photosynthetic systems, since they hold some advantages with respect to other types of electro- and photo-active compounds.¹⁹⁻²² Porphyrins are macrocycles consisting of 18 π -electrons spread over four pyrroles and four methyne bridges. The trivial nomenclature can be found in (**Figure 4.1**). They are thermally and chemically stable compounds and possess an intense optical absorption in the red/NIR region of the solar spectrum. Additionally, the possibility of tailoring their redox potentials by the careful choice of the metal atom in the macrocycles' cavity and/or through adequate functionalization of the *meso*- and β -positions, represents an appealing feature for their use in energy-related areas.¹⁸

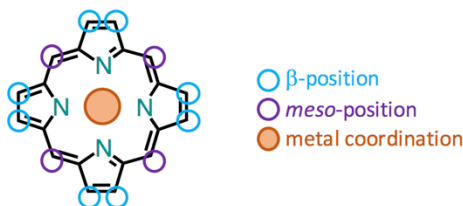


Figure 4.1 Typical structure of a porphyrin showing the four *meso*-, the eight β -positions and the metal coordination site.

Their ability to harvest light efficiently and, once photoexcited, to act as an electron donor moiety, have prompted their use for the preparation of a variety of donor-acceptor hybrids. Their high electronic excitation energy powers a strong exergonic electron transfer, which subsequently intercedes the conversion between light and chemical/electrical energy.^{23,24}

Among the acceptor moieties employed for the preparation of

porphyrin-based donor-acceptor ensembles, carbon nanostructures such as fullerenes, carbon nanotubes and graphene hold a privileged position.²⁵

Fullerenes have been found to be an excellent electron transfer partners for porphyrins and the wide variety of their ensembles have exerted a noteworthy impact on the improvement of light-induced charge-separation systems.²⁶ Indeed, fullerenes possesses excellent electron acceptor properties, which were exploited, together with its small reorganization energy, its ability to promote ultrafast CS (charge separation) and slow CR (charge recombination), for the construction of a large number of attractive photo- and electro-active systems.^{27,28}

Likewise to fullerenes, carbon nanotubes and graphene can act as electron acceptor materials when coupled with appropriate electron-donor dyes.^{29,30}

In this context, carbon nanodots (CNDs) are beginning to emerge. CNDs can act either as electron donors or as electron acceptors depending on the counterpart. Until now, a large variety of covalent and supramolecular systems based on porphyrin and carbon nanostructures have been described. However, beside the extensive studies on their ‘carbon cousins’, the application of CNDs in this context is still in its infancy.

Pioneering work showed that CND photoluminescence can be quenched either by electron acceptors (4-nitrotoluene and 2,4-dinitrotoluene) or donors (*N,N*-diethylaniline) through an electron transfer process, since they can act as electron donors or acceptors in their excited state.³¹ Following these pioneering charge-transfer studies, a few CND-based hybrids were reported. Leading examples are supramolecular assemblies SWCNT/CND,³² PBI/CND,³³ and graphene oxide/CND,³⁴ featuring a remarkable charge-transfer

activity and suggesting that CNDs are valuable building-blocks for the design of photoactive hybrids.

In the following sections, an overview of the porphyrin-nanocarbon-based strategy for the construction of artificial photosynthetic mimics is presented.

4.1.1.1 Supramolecular porphyrin-nanocarbon ensembles

The supramolecular strategy is based on the assembly through the “toolbox” of non-covalent interactions, such as hydrogen bonding, metal–ligand, cation-crown ether or π - π interactions (**Figure 4.2**).

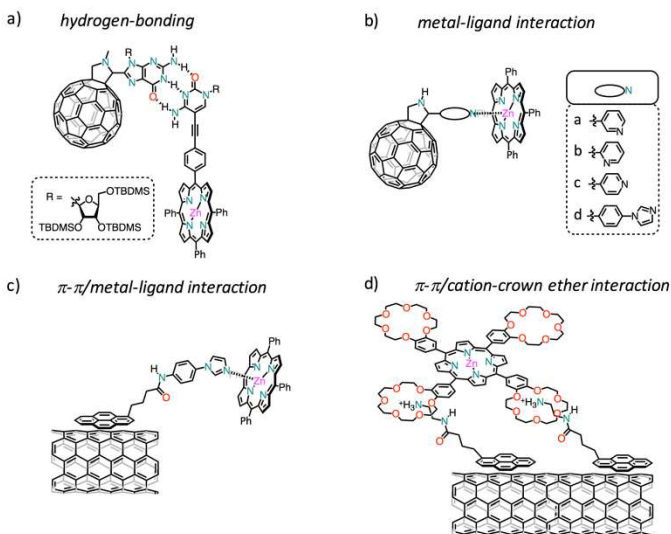


Figure 4.2 Representative examples of carbon nanostructures-porphyrin supramolecular systems: a) hydrogen bonding; b) metal-ligand interaction; c) π - π /metal-ligand interactions; d) π - π /cation-crown ether interactions.

Hydrogen bonding interactions, by choosing the appropriate motifs,

allow the fine-tuning of the strength in the resulting supramolecular complexes and the electronic coupling between the components. Several elegant model systems, including conjugates held by DNA base-pairs such as G:C and A:T type Watson–Crick hydrogen bonding motifs, have been designed and studied.^{35–40} For instance, supramolecular Por/C₆₀ dyads, based on Watson–Crick hydrogen bonding interactions by complexation of a fulleropyrroline bearing a guanosine moiety with cytidine-substituted porphyrin, have been reported (**Figure 4.2a**).³⁷ The self-assembly of the guanosine–cytidine moieties *via* Watson–Crick three-point hydrogen has been observed through fluorescence studies in dichloromethane on the emission of the cytidine-porphyrin as a function of increasing fullerene derivative concentration. Finally, transient absorption experiments revealed the formation of radical ion pair species with a lifetime of 2.02 μ s.

Metal-directed self-assembly is another simple yet elegant approach for forming self-assembled supramolecular donor–acceptor dyads. Several examples of systems based on functionalized fullerenes, bearing a nitrogenous ligand (such as pyridine or imidazole), in order to coordinate the central metal (zinc or magnesium) of porphyrins have been synthesized and studied.^{8,12,41,42} The choice of metal ion depends on the strength of the metal–nitrogen coordination bond, in addition to the redox behavior and photophysical properties of the macrocyclic compounds. It has been found that the ligand nature, as well the relative spatial orientation of porphyrin and fullerene within the ensemble, affects the communication between the donor and the acceptor units. For example, a series of Por/C₆₀ systems, shown in **Figure 4.2b**, bearing an *o*- (b), *m*-(a), *p*-pyridine (c) or imidazole (d) ligands have been studied.^{13,15} A 1:1 assembly stoichiometry was revealed for all the systems, by means of UV-Vis, ¹H-NMR, mass spectrometry and computational studies. The K_a followed the order *o*-pyridyl < *m*-pyridyl \approx *p*-pyridyl \ll *N*-phenyl Im. *Ab initio* methods showed that the majority of the HOMO was located on the porphyrin unit, while the LUMO was entirely located on the fullerene moiety.

Further photophysical studies demonstrated significant interaction between the two entities. Moreover, the deactivation pathway was found to be strongly dependent on the solvent media. While in *o*-DCB the main quenching pathway for all the systems involved charge separation (CS) from the singlet excited porphyrin to C₆₀, on the contrary in a coordinating solvent (like benzonitrile) intermolecular electron transfer takes place mainly from the triplet excited porphyrin to C₆₀.

The use of non-covalent π - π interactions between appropriately functionalized molecules and the CNT wall is a valuable strategy for designing supramolecular assemblies where the electronic properties of the nanotube remains almost unaffected. In this context, a variety of Por-CNT systems taking advantage of the strong π - π interactions between pyrenes (Py) and CNTs walls have been reported. More so, the combination of Py-CNT π - π stacking and metal-ligand coordination has been used for the preparation of sophisticated three-component systems with porphyrins and an example is depicted in **Figure 4.2c**.⁴³ In such assemblies, imidazole-substituted Py (Im-Py) acts as a “bridging” unit thanks to the phenylimidazole moiety that is able to strongly coordinate to the zinc center of porphyrin while interacting with the CNT surface through the Py moiety. The supramolecular assembly of the donor-acceptor moieties was confirmed through absorption and fluorescence titration studies in *o*-DCB. The titration of the porphyrin, with an increasing amount of Im-Py/CNT, resulted in quenching and red-shifting of the emission bands of the macrocycles with respect to the uncomplexed porphyrin. Interestingly, the fluorescence titration of the porphyrin against a Py/CNT ensemble in which the Py derivative did not have the Im moiety resulted in a less pronounced quenching, as compared to the one observed from the system bearing the Im moiety. This result suggests that the axial coordination between the zinc metal of the porphyrin and the Im entity, in the bridging Im-Py compound, facilitates the system formation. Nanosecond transient absorption spectra of Por/Im-Py/CNT ensembles revealed that the

photoexcitation of the porphyrin moiety resulted in the one-electron oxidation of the donor unit and the simultaneous one-electron reduction of the CNT, leading to the formation of the charge-separated specie $\text{Zn(II)Por}^{\bullet+}/\text{Im-Py/SWCNT}^{\bullet-}$.

A combination of π - π and ammonium-crown ether interactions have also been used to assemble a Por/Py/CNT hybrid, constituted by a porphyrin peripherally substituted with four crown ether moieties and a Py “bridging” unit bearing an alkyl ammonium cation group (**Figure 4.2d**).⁴⁴ The presence of four crown ether moieties on the Por macrocycle resulted in complexation of multiple CNT-immobilized, ammonium-substituted Py units and led to the formation of stable supramolecular Por/Py/SWCNT complexes.

Therefore, the supramolecular approach allows the preparation, in a convergent strategy, of thermodynamically reversible assemblies, whose stabilities are influenced by the careful choice of the supramolecular interactions, as well as by some external conditions such as the temperature or the solvent polarity. Rationalizing the effects of the structural and electronic features on electron/energy-transfer dynamics open extensive possibilities for influencing/modulating the systems properties.

4.1.1.2 Covalent porphyrin-nanocarbon hybrid

The covalent approach could be considered as a highly versatile and simple approach. More so, a substantial impact on the ground and excited state interactions between porphyrins and fullerenes, carbon nanotubes, or graphene have been documented in covalently linked systems. In most cases, however, the covalent functionalization involves multi-step synthetic processes. Moreover, fullerenes, carbon nanotubes and graphene have limited solubility in organic and aqueous solvents, which hampers their large-scale synthesis and use. Furthermore, direct covalent functionalization converts some of their

sp^2 carbons to sp^3 carbons, breaking-off the π -conjugations, possibly altering their electronic properties, and finally impacting their electronic conductivities and light absorption abilities. In these ensembles, parameters such as electronic coupling, geometrical overlap and the nature of the spacer connecting the donor and the acceptor moieties (short/long, rigid/flexible, conjugated/nonconjugated), have been varied with the aim of rationalizing how these changes affect the formation and recombination of the photogenerated charged species.

Functionalization of various porphyrin moieties to C_{60} has been achieved by standard reactions in fullerene chemistry, which imply relatively simple steps, such as cyclopropanation reactions (so called Bingel-Hirsch reaction),⁴⁵ 1,3-dipolar cycloaddition (such as the Prato reaction), and other cycloadditions.⁴⁶ Systems built up from fullerene and porphyrin display among the fastest photoinduced charge separation and slowest charge recombination to yield a long-lived charge-separated state with a high quantum yield.

One of the first porphyrin- C_{60} -linked dyad is shown in **Figure 4.3a**, where fullerene is covalently tethered to a *meso*-porphyrin aryl ring at the *para*-position via an amide bond.¹⁷ After excitation of the porphyrin, the transient absorption due to the porphyrin excited singlet state appeared. As the absorption decayed, concomitant rise and decay of the transient bands due to the zinc porphyrin (ZnP) radical cation ($ZnP^{+\bullet}$) and the C_{60} radical anion ($C_{60}^{\bullet-}$) were unambiguously detected, demonstrating photo-induced electron transfer from the porphyrin excited singlet state to the C_{60} moiety.

Later on, further studies have shown photo-induced charge separation and subsequent charge recombination in a series of systems prepared by changing the linking position at the *meso*-phenyl ring from *para* to *ortho*.¹⁶

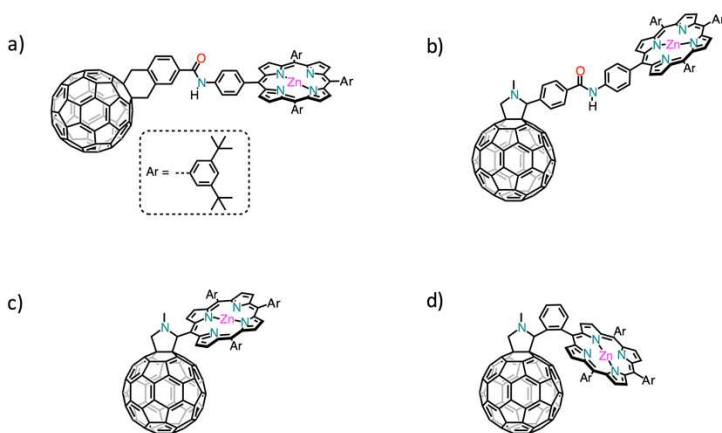


Figure 4.3 Representative examples of porphyrin-fullerene covalently linked dyads.

Systematic studies on the solvent-dependent changes and the separation distance between porphyrins and fullerenes have been found crucial in determining the energy balance between the charge separation states and the exciplex. A representative example of zinc porphyrin- C_{60} dyads, in which the distance between the two moieties is varied, is reported in **Figure 4.3b-d**, with the calculated edge-to-edge distance between the two moieties for the optimized geometries increases as follow: c) (2.6 Å) < d) (3.4 Å) << b) (11.9 Å).^{14,47,48} Irrespective of the solvent polarity, photoinduced electron transfer of the porphyrin-fullerene dyads with a rather long-length linear spacer (**Figure 4.3b**) takes place from the porphyrin singlet excited state to the C_{60} moiety producing a charge-separated state ($ZnP^{++}-C_{60}^{\bullet-}$). However, the charge-recombination process is solvent-dependent and can be rationalized by the small reorganization energy of the two moieties in the electron transfer processes. Indeed, the charge-separated state decays to different energy states depending on the energy level of the charge-separated state relative to the C_{60} singlet and triplet excited states. In polar solvents, such as benzonitrile, THF and DMF, since the energy level of the charge-separated state is lower

than those of the porphyrin and fullerene triplet excited states, all of the excited states (*i.e.* the porphyrin and C₆₀ excited singlet and triplet states) lead to the production of the charge-separated state with a total formation efficiency of 99% (in benzonitrile), which slowly decays to the ground state. On the contrary, in non polar solvents, such as benzene, the charge-separated state undergoes charge recombination to yield the C₆₀ singlet excited state, followed by intersystem crossing to the C₆₀ triplet excited state, since the energy level of the charge-separated state is higher than that of the C₆₀ singlet excited state.

The two dyads with shorter spacers **Figure 4.3c,d** disclose different photophysical behavior. The photoexcitation of **c** in both benzonitrile and toluene results in the formation of a new intermediate state, assigned to an exciplex state, which decays rapidly to the ground state without forming the charge-separated state. Therefore, the strong interaction between the ZnP and the C₆₀ due to the small distance between the two moieties, leads to the exclusive formation of the exciplex. This results can be rationalized by the fact that the energy of the exciplex is lower than that of the charge-separated state even in a polar solvent such as benzonitrile. On the contrary, the photoexcitation in benzonitrile of **d** having a slightly larger edge-to-edge distance value, results in the formation of the charge-separated state via the exciplex formation, which is higher in energy than the charge-separated state, but in toluene the exclusive formation and decay of the exciplex occurs, as observed in **c**.

Among the large number of available covalent functionalization methodologies for SWCNTs and graphene, such as reactions using azomethine ylides and aryl diazonium compounds, oxidation is the most commonly used approach. It involves the treatment under strongly acidic and oxidative conditions, and results in the formation of different oxygenated functionalities, mainly carboxylic groups.

Interesting covalently linked graphene oxide (GO) and porphyrin composites were prepared by amidation or esterification of the carboxylate moieties of the nanocarbon materials.^{7,10,11,49-52} Examples of covalent linking of porphyrin to oxidized SWCNTs or graphene oxide by reacting their carboxylic groups with porphyrin moieties are illustrated in **Figure 4.4a,b**, where the strong porphyrin emission quenching was attributed to a possible electron transfer process.^{7,10} Moreover, as in the case of porphyrin-C₆₀ linked dyads, the geometry as well as the disposition of the two moieties have large impacts on the photodynamics of covalently linked CNTs- or graphene-porphyrin hybrids. For instance, for the hybrid reported in **Figure 4.4c,d** it was observed the evolution of an exciplex between the porphyrin excited singlet state and the SWCNT or graphene. The exciplex decays to the ground state without generating the charge-separated state, due to the strong interaction between the porphyrin and CNTs through the short spacers.^{6,9}

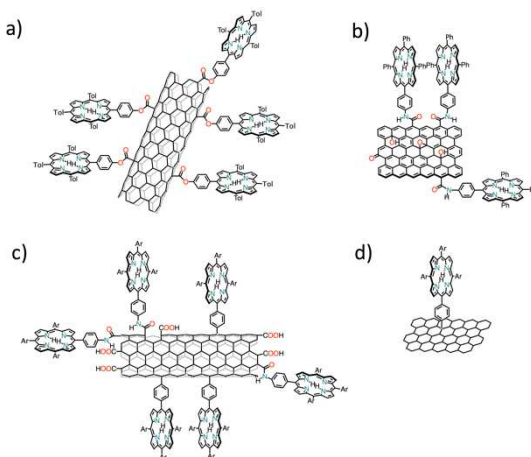


Figure 4.4 Representative examples of porphyrin-CNTs or graphene covalently linked dyads.

4.1.2 Supramolecular gel

Soft materials have been attracting increasing attention as a ‘transformable’ functional class of materials due to their flexibility, that enables them to change their shape and properties depending on the conditions.⁵³ Gels are soft and jelly-like materials formed from colloidal mixtures. They are colloidal in nature because of the dispersion of the gelator (the solid, continuous phase) within a solvent (the liquid, dispersed phase).⁵⁴ They are defined as dilute cross-linked systems, and it is the crosslinks within the fluid responsible of their structure and stickiness.⁵⁵

The term supramolecular gel is often used to describe gels that consist of low molecular weight compounds (often referred to as low molecular weight gelators, LMWGs) that can self-assemble under the proper conditions (*i.e.* temperature, concentration, solvent, etc.) into nano- or micro-scale network structures, resulting in the formation of 3D networks, which are interconnected by multiple non-covalent interactions, such as hydrogen bonding, metal coordination, Van der Waals interactions, π - π stacking interactions, solvophobic or hydrophobic forces. (**Figure 4.5**).⁵⁶

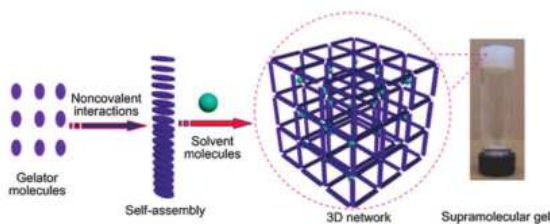


Figure 4.5 Schematic representation of a supramolecular gel formation.⁵⁶

The high versatility of LMWGs towards synthetic modification allows a great control of the properties of the gel-phase assemblies. Moreover, the weak and reversible nature of the non-covalent

interactions that holds these network structures together results in the inherent ability of these gels to respond to external stimuli and can impart interesting mechanical properties. Thus, supramolecular gels are highly promising candidates for a diverse range of applications: they have been applied in the photographic, food, cosmetic and petroleum industries and they have potential uses as biomaterials, scaffolds (such as in tissue engineering), stimuli-responsive, liquid crystalline and electronic materials, sensors and catalytic supports, to name a few.⁵⁷⁻⁶⁶

Supramolecular gels can be classified either as organogels, hydrogels or ionogels depending on the solvent medium being either an organic solvent, water or ionic liquid, respectively. Among them, gelation of ionic liquids (ILs) by low molecular mass organic compounds is of current interest because of the many favorable properties of the ILs. ILs are organic salts, which exhibit low melting temperature, by convention below 100 °C. The physicochemical properties of ILs can be tuned by the choice of the anion-cation pair, which opens millions of possibilities.⁶⁷ Their peculiarity is the negligible vapor pressure, the thermal stability of the liquid phase, and the high conductivity, that is usually quite similar to the conductivities of the neat ILs, since the presence of the gelator usually do not affect the ionic mobility of the ions present in the ILs.⁶⁸ Therefore, ionogels are stable materials over time, resistant up to high temperatures, and represent an attractive replacement for organic electrolytes, which are generally volatile and flammable.

The intrinsic hybrid character of ionogels relies on the intimate combination of an IL and a solid-like network. The solid-like network may be organic (typically using LMWGs or polymers), inorganic (typically using oxide nanoparticles or carbon nanotubes), or hybrid organic-inorganic (typically polymers reinforced with inorganic

fillers), and the properties of the ionogels derive both from those of the IL and those of the component forming the solid-like network.

In the presence of another component an additional level of hierarchical control can be introduced in the self-organization process.⁶⁹ This is the case of carbon materials incorporation, that has been widely applied to increase strength and performances of supramolecular gels.⁷⁰ It has been reported an extensive use of SWCNTs dispersed gels of ionic liquids as soft functional materials.⁷¹ Aida *et al.* reported for the first time that grinding a suspension of SWCNTs with imidazolium based ionic liquids led to the formation of physical gels, the so called ‘bucky gel’.⁷² They have high potential for electrochemical applications since they simultaneously contain dispersed a π -conjugated materials (nanotubes) and an electrolyte (the ionic liquid). These gels have been used in electric double layer capacitors,⁷³ where the carbon nanotubes act as nanoelectrodes and the ionic liquid serves as an electrolyte, or for the construction of a bucky gel-based plastic actuator that works in air.⁷⁴

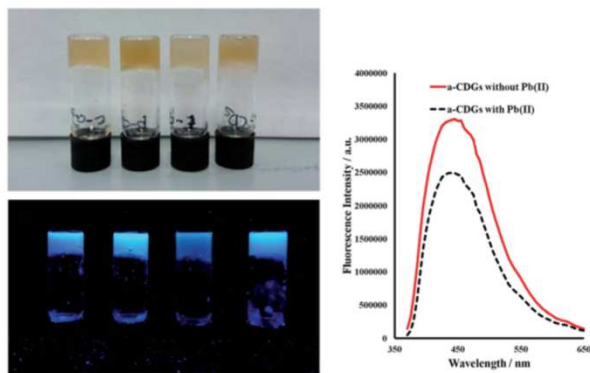


Figure 4.6 On the left: photographs of CNDs-containing hydrogels based on bis(urea) gelators, in daylight and under UV light (365 nm) illumination. On the right:

fluorescence emission spectra of a CNDs-hydrogel with (black line) and without (red line) Pb^{2+} (10 $\mu\text{g}/\text{mL}$).⁷⁵

While several nanocarbons (especially CNTs and graphene) have been incorporated in gel matrices forming composite material with superior properties,⁷⁶ only a few examples of supramolecular gels with CNDs have been so far reported.^{75,77–79} Recently, Steed *et al.* reported the first example of CNDs incorporation within a LMWG-based hydrogel (**Figure 4.6**).⁷⁵ It was shown that CNDs increase the rate of self-assembly and the novel hybrid were successfully used as hydrophobic environment suitable for fluorescent ion sensing within an aqueous medium.

4.1.3 Aim of the project

The aim of this project is to explore the use of CNDs for the design of functional hybrid systems. As previously discussed, various fullerenes, carbon nanotubes or graphene-based hybrid systems have been the subject of extensive investigation, representing an active and fascinating area of research of paramount importance. In this context, CNDs seems to be a promising candidate, but the research in this field can be considered at the early stage.

The first part focuses on the use of the NCNDs, presented in *Chapter 2*, for the covalent and supramolecular decoration with porphyrins as photoactive building blocks towards CND-based hybrid materials. Indeed, CNDs seems to be a very promising candidates for the formation of charge-transfer hybrids with either electron donors or acceptors. Contrary to other nanocarbons, the surface of CNDs is rich in functional groups, which provides high intrinsic solubility, on one hand, and reactive sites for the easy labeling with electroactive groups, on the other hand. Therefore, we investigated systems in which for the first time the light harvesting and electron donating

properties of porphyrins are combined with the electron accepting features of our NCNDs.

Finally, in light of the outstanding advantages that have been reported in the recent years on the incorporation on carbon nanostructures in supramolecular gels, the second part is devoted to the study of the effect of NCNDs in ionogels.

4.2 NCNDs with porphyrin antennas: covalent and non-covalent electron donor-acceptor hybrids

In this section we report the first detailed photophysical study of an electron donor-acceptor nanoconjugate employing our NCNDs (synthesis and characterization are described in *Chapter 2*) as electron acceptors, and porphyrins as electron donors.

In the first part, the non-covalent system is studied, in which porphyrins and NCNDs interact supramolecularly with each other, by means of photophysical studies in the form of spectrophotometric titrations. In the next step, the intramolecular interactions in the porphyrin-NCND covalent hybrid are investigated by transient absorption measurements, in order to shed light on the dynamics of charge-transfer and related processes (**Figure 4.7**).

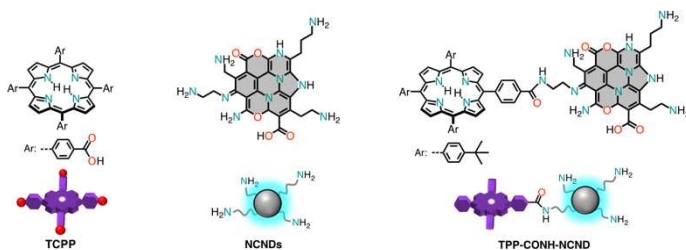


Figure 4.7 Systems studied in this section. Tetrakis(4-carboxyphenyl)porphyrin (TCPP) and nitrogen doped CNDs (NCNDs) on the left, and covalently linked porphyrin-NCND (TPP-CONH-NCND) nanoconjugate on the right.

4.2.1 Porphyrin/NCNDs supramolecular ensemble

Firstly, we probed the NCNDs in non-covalent ensembles with porphyrins. To this end, a free-base porphyrin featuring four

carboxyphenyl acids in its meso positions (5,10,15,20-tetrakis(4-carboxyphenyl)porphyrin, (TCPP)) was employed (**Figure 4.7**).⁸⁰

The ground and excited state interactions between NCNDs and TCPP were studied through titration experiments in phosphate-buffered H₂O (pH 7.2) of a TCPP solution (3×10^{-6} M) with variable concentrations of NCNDs (0–1.6 g/L), and monitoring the corresponding absorption and fluorescence changes (**Figure 4.8**). Upon increasing the concentration of NCNDs, the Soret band of TCPP significantly decreases, together with an 8 nm red-shift relative to the TCPP reference and the appearance of an isosbestic point at 420 nm (**Figure 4.8a**). In addition, the Q-bands shift from 517, 554, 581, and 635 nm to 520, 557, 594, and 650 nm when NCNDs are added. The large shifts of the Q_x-bands relative to the small shifts of the Q_y-bands reflect an increase of the symmetry in the porphyrin electronic structure from D_{2h} toward toward D_{4h}.⁸¹

When turning to the fluorescence assays of TCPP with NCNDs, similar trends were observed (**Figure 4.8b**): the two typical free-base porphyrin maxima are shifted from 645 and 701 nm to 652 and 715 nm, respectively. Additionally, an overall quenching of the TCPP centered fluorescence was observed and reached 40% relative to the TCPP reference. In an attempt to quantify the interactions between TCPP and NCNDs the integrated fluorescence intensity was plotted versus the NCND concentrations (inset **Figure 4.8b**). The corresponding exponential behavior in the Stern-Volmer plot indicates that fluorescence quenching, within the newly formed assembly TCPP/NCND, is static rather than dynamic.

Reversed titration experiments, during which variable amounts of TCPP were added to NCNDs, showed quantitatively similar observations, with the spectra reported in **Figure S4.2** (experimental section). As the amount of TCPP increases, the absorptions shift from 422, 519, 556, 591, and 645 nm to 414, 518, 555, 579, and 637 nm,

respectively. In addition, the NCND centered fluorescence, which was selectively excited at 300 nm, is quenched with increasing amounts of TCPP.

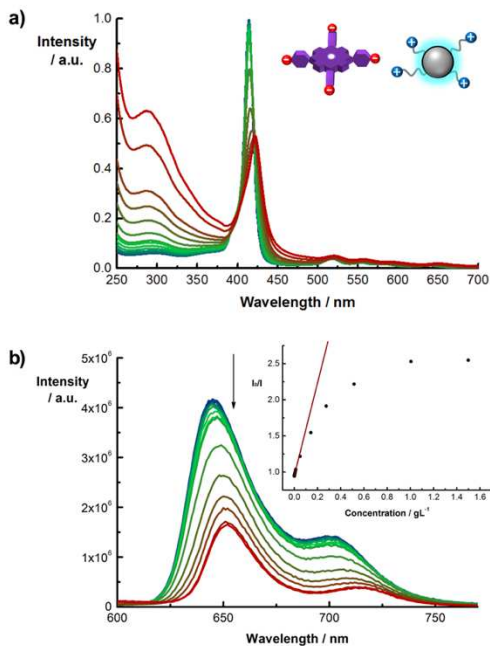


Figure 4.8 a) Absorption spectra of TCPP (blue, 3×10^{-6} M) during the course of a titration with NCNDs (blue>green>red, 0 – 1.6 g/L) in phosphate-buffered H_2O (pH 7.2) at room temperature; b) fluorescence spectra of TCPP (blue, 3×10^{-6} M) during the course of a titration with NCNDs (blue>green>red, 0 – 1.6 g/L) in phosphate-buffered H_2O (pH 7.2) upon excitation at 550 nm at room temperature. Inset: Relationship of I_0/I of TCPP, using the wavelength corrected integrated emission intensities, versus the concentration of NCNDs.

Notably, none of the above spectral changes were present in $\text{H}_2\text{O}/\text{THF}$ (1:1 v/v, **Figure S4.3**, experimental section), suggesting

that hydrophobic interactions are pivotal in the formation of the TCPP/NCND assembly.

The excited state dynamics of TCPP were found to be affected by the presence or absence of NCNDs by means of femtosecond transient absorption. The differential absorption spectra of TCPP reference alone (in H₂O at pH 7.2) showed, upon photoexcitation, the evolution of typical absorption pattern of a free-base porphyrin (**Figure S4.5**, experimental section).⁸² Particularly, the minima at 520, 584, and 650 nm reflect the ground-state bleaching of the Q-bands while the broad positive signal spanning through the entire visible range is assigned to excited state absorptions. At time delays as early as 500 ps, the growth of the triplet excited state absorptions is noted at 460 nm. As a matter of fact, the formation via intersystem crossing takes place with a lifetime of 17 ns, while for the decay via ground state recovery, a lifetime of 220 μ s is derived.

On the other hand, the differential absorption spectra of the supramolecular TCCP/NCNDs complex (TCPP in presence of an excess of NCNDs, in H₂O at pH 7.2) are depicted in **Figure 4.9**. The minima at 521, 593, and 654 nm correspond again to the Q-band absorptions. Most importantly, new transients, which are at ~460 and in the 600–750 nm range, are neither detected for TCPP nor for NCNDs alone. We assign these features, in line with spectroelectrochemical investigations, to the one-electron oxidized form of TCPP. The accordingly formed charge separated state converts into ground state with a lifetime of 1270 ps.

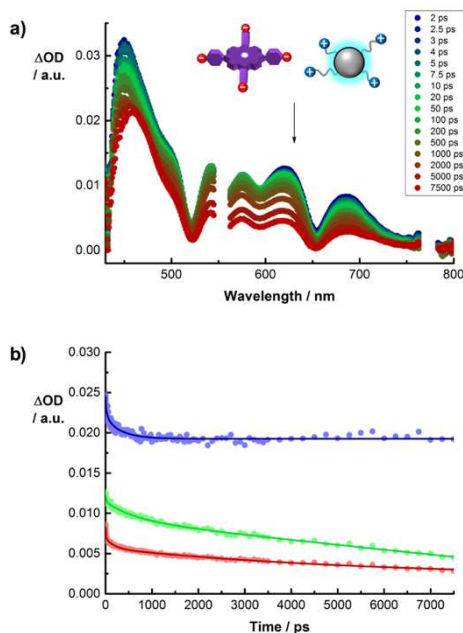


Figure 4.9 a) Differential absorption spectra obtained upon femtosecond pump probe experiments ($\lambda_{\text{ex}} = 550$ nm) of TCP/NCNDs (TCP: 3×10^{-5} M; NCNDs: 5 g/L) with several time delays between 2 and 5000 ps in phosphate-buffered H_2O at room temperature; b) corresponding time profiles at 470 (blue), 620 (green), and 685 nm (red).

4.2.2 Porphyrin-NCNDs covalently linked system

The porphyrin-NCND nanoconjugate was prepared through the covalent coupling (carbodiimide condensation reaction) of the free amino functional groups of NCNDs with a carboxyphenyl peripheral moiety on the porphyrin (5,10,15-tri(4-*tert*-butylphenyl)-20-(4-carboxyphenyl)porphyrin (TPP-COOH)) in a DMF solution, overnight.³⁶ The hybrid material, denoted as TPP-CONH-NCND, is

obtained as a purple solid by washing with organic solvents and dialyzing against H₂O to remove the unbound molecules (details in the experimental section).

The TPP-CONH-NCND nanoconjugate has been found to be soluble in H₂O and in polar organic solvents such as MeOH or EtOH, forming stable solutions at least for several weeks (**Figure S4.8**, experimental section). Thus, the coupling of TPP to NCNDs results in the solubility in aqueous media of a porphyrin otherwise almost completely insoluble.

The formation of TPP-CONH-NCND was monitored by FT-IR spectroscopy. The spectrum of the nanoconjugate (**Figure 4.10**, red line) shows the typical bands of NCNDs, as reported in *Chapter 2*, and the typical 820 cm⁻¹ band due to the out-of-plane bending vibration of the pyrrole C-H groups, two well defined peaks at 1642 and 1570 cm⁻¹ that are characteristic of stretching and bending modes of carbonyl and N-H groups, respectively, of the amide units, and the disappearance of the 1695 cm⁻¹ band due to the carboxylic acid of the free TPP-COOH.

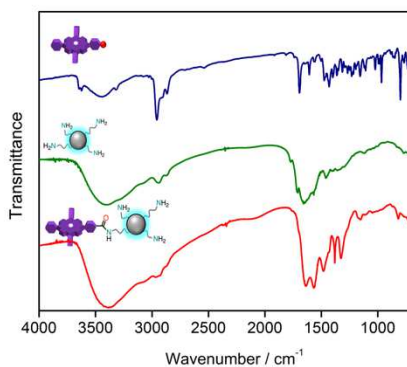


Figure 4.10 FT-IR spectra of TPP-COOH (blue line), NCNDs (green line), and TPP-CONH-NCNDs (red line).

The size of the TPP-CONH-NCNDs was found to be around 5 nm (**Figure 4.11**), by atomic force microscopy in contrast to 2.5 nm for the free NCNDs (as reported in *Chapter 2*).

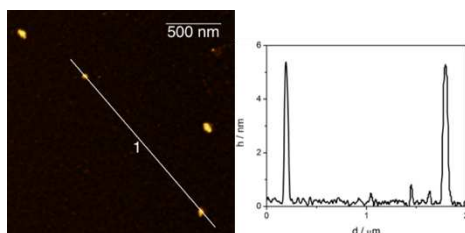


Figure 4.11 Representative tapping mode AFM image of TPP-CONH-NCND conjugate ($2.0 \times 2.0 \mu\text{m}$) on a mica substrate (left) and height profile (right).

The steady-state absorption and fluorescence spectroscopic measurements of the TPP-CONH-NCND hybrid and references (TPP-COOH and NCNDs) are reported in **Figure 4.12**. The absorption spectrum of the reference TPP-COOH reveals the typical Soret band at 414 nm and Q bands at 518, 555, 581, 636 nm (**Figure 4.12a**, blue line). On the other hand, NCNDs (**Figure 4.12a**, green line) exhibit a broad maximum at 287 nm and a featureless absorption trailing into the visible. In the case of the hybrid material (in H_2O), the Soret and Q bands of the TPP-CONH-NCND nanoconjugate are broadened and significantly red-shifted to 444, and 523, 556, 597, and 650 nm, respectively. The absorption corresponding to the covalently grafted NCNDs is blue-shifted by 6 nm as compared to free NCNDs (**Figure 4.12a**, red line). From the latter shift, we deduce the close proximity between TPP and NCNDs and mutual electronic communication in the ground state.

Subsequently, the excited state of the TPP-CONH-NCNDs was investigated, by exciting NCNDs and TPP at 300 and 422 nm,

respectively, and comparing them with references NCNDs and TPP-COOH alone (after adjusting to the same optical density) (**Figure 4.12b**). Upon excitation at 300 nm, a drastic quenching of the intense NCNDs fluorescence at 360 nm and the evolution of an additional fluorescent feature at ~ 450 nm was observed. Likewise, when the TPP moiety of the TPP-CONH-NCNDs is selectively excited at 422 nm, which correlates with the isosbestic point seen in the titration experiments with TCPP and NCNDs, a significant fluorescence decrease is observed. Additionally, the fluorescence peaks are red-shifted from 645 and 715 nm in the TPP-COOH reference, to 651 and 721 nm, confirming the electronic interactions between TPP and the NCNDs.

In contrast to the results obtained in H₂O, complementary absorption and fluorescence assays in H₂O/THF (1:1 v/v) showed only subtle changes. The absorption spectrum of TPP-CONH-NCNDs is only slightly broadened in the Soret band range, while the NCND-centered absorption is, like in H₂O, blue-shifted by ~ 8 nm (**Figure S4.4**).

When comparing the fluorescence spectrum of TPP-CONH-NCNDs, upon excitation at either 290 or 550 nm, with that of either the TPP-COOH or the NCND references, a significant quenching evolves in all cases (**Figure S4.4**). Similarly to the H₂O experiments, an additional shoulder at ~ 445 nm appears upon 300 nm excitation of TPP-CONH-NCNDs. In contrast, the porphyrin fluorescence in TPP-CONH-NCND is quenched by 40%, but was not shifted with respect to the reference experiments with TPP-COOH.

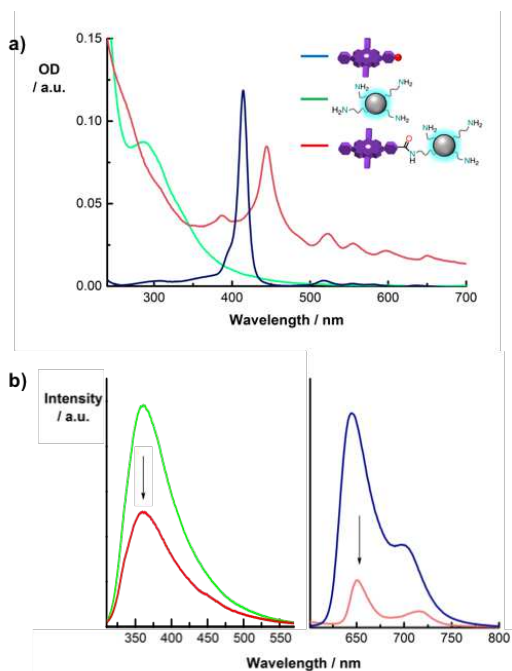


Figure 4.12 a) Absorption spectra of TPP-COOH (blue line), NCNDs (green line), and TPP-CONH-NCNDs (red line) in phosphate buffered H₂O; b) fluorescence spectra of TPP (blue line), NCNDs (green line), and TPP-CONH-NCNDs (red line) in phosphate buffered H₂O upon excitation at 300 nm (left panel) and 422 nm (right panel) at room temperature.

Following this, the TPP-CONH-NCNDs and TPP-COOH excited state nature and dynamics were investigated in H₂O/THF (1:1 v/v) or in H₂O (pH 7) (**Figure S4.7**). The transient absorption measurements of reference TPP-COOH (**Figure S4.6**), upon excitation at 550 nm, showed minima at 515, ~550, 593, and 691 nm that reflect the ground state absorption of the Q-bands. Notably, the entire visible range is superimposed by a broad positive transient stemming from excited

state absorptions. Moreover, the singlet excited state decays within 7.5 ns via intersystem crossing to the triplet excited state. For the latter, a lifetime of 2.2 μ s was determined.

On the other hand, the situation in TPP-CONH-NCNDs is quite different, as can be observed in **Figure 4.13**. In this case, the minima, which are discernable at 593 and 651 nm, confirm the porphyrin excitation. Within about 500 ps, two rather broad transient maxima evolve at \sim 650 and \sim 1090 nm in sound agreement with the presence of the one-electron oxidized form of the porphyrin. From the latter we conclude that the charge separation evolves from the TPP singlet excited state. On a longer time-scale, charge recombination sets in, for which we determined a lifetime of \sim 3.5 ns. In contrast to TPP-COOH alone, no evidence for ISC was noted.

Thus, these results corroborate an efficient charge separation between the electron donating TPP and the electron accepting NCNDs. The excited state deactivation via a charge separated state was observed upon excitation into either the second singlet excited state of TPP at 387 nm or into the first singlet excited state of TPP at 550 nm (**Figure 4.14**).

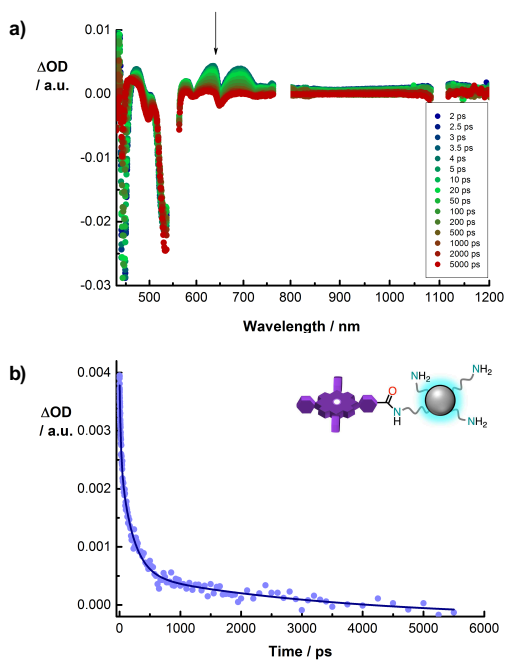


Figure 4.13 a) Differential absorption spectra obtained upon femtosecond pump probe experiments ($\lambda_{ex} = 550$ nm) of TPP-CONH-NCNDs with several time delays between 2 and 5000 ps in H_2O/THF (1:1 v/v) at room temperature; b) corresponding time profiles at 680 nm.

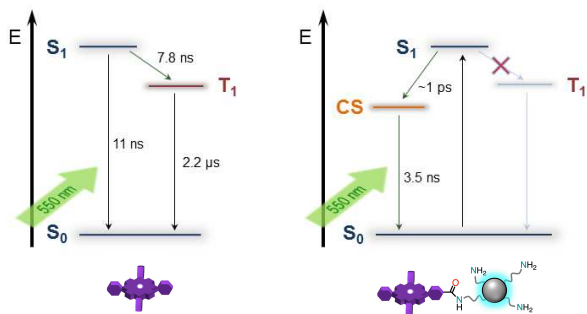


Figure 4.14 Energy diagrams illustrating the excited state decay for TPP (left) and TPP-CONH-NCNDs (right) upon excitation into the porphyrin S_1 state (550 nm).

4.3 NCNDs/Ionogels

In this section we report CND-based ionogels and the systems studied are illustrated in **Figure 4.15**.

We focused our attention on two dicationic organic salts (DOSs) as gelators, formed by *meta*- or *para*-substituted diimidazolium (3,3'-di-*n*-dodecyl-1,1'-(1,3-phenylenedimethylene) diimidazolium or 3,3'-di-*n*-dodecyl-1,1'-(1,4-phenylenedimethylene) diimidazolium) cation- 1,4-benzenedicarboxylate anion, hereafter named as *m*-C₁₂ or *p*-C₁₂, which exhibit good gelation ability in some ionic liquid solutions.⁸³ We tested their gelling ability in the presence of NCNDs (synthesis and characterization are described in *Chapter 2*), by using some of the most common ionic liquids (ILs). In order to shed light on the ability of NCNDs to cooperate in the gelation process, we selected 1-butyl-3-methylimidazolium tetrafluoroborate [bmim][BF₄] and 1-butyl-3-methylimidazolium N-bis-trifluoromethanesulfonylimide [bmim][NTf₂], since in the first the chosen gelators are able to form the gel, while the second is a non-gelating solvent.

In the first part we have investigated the gel properties. We studied the critical gelation concentration, as well as the thermal and photophysical properties of the novel hybrid gels. The gel phase formation was followed by opacity measurements and resonance light scattering (RLS) analysis. The rheological response of gel phases, their ability to self-repair after disruption and their morphology have been also investigated. Finally, we tested also their radical scavenging activity, by using the common 1,1-diphenyl-2-picryl radical (DPPH) test.

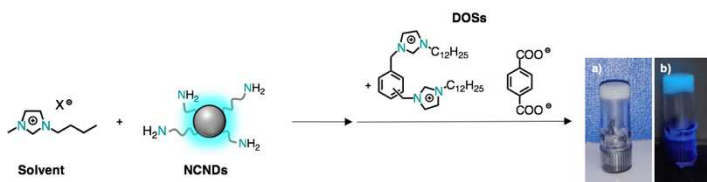


Figure 4.15 Schematic representation of the gels components. Solvents: [bmim][BF₄] (X = BF₄) or [bmim][NTf₂] (X = NTf₂). Nitrogen-doped CNDs (NCNDs). DOSs: 3,3'-di-*n*-dodecyl-1,1'-(1,3-phenylenedimethylene) diimidazolium- or 3,3'-di-*n*-dodecyl-1,1'-(1,4-phenylenedimethylene) diimidazolium- 1,4-benzene-dicarboxylate anion (*m*-C₁₂ or *p*-C₁₂). The combination of ILs, NCNDs and DOSs (as reported in the experimental section) resulted in a) white opaque gel in daylight and b) blue-emitting gel under UV light (365 nm) illumination.

4.3.1 Gelation tests

Gelation tests have been performed in presence of different quantities of NCNDs (**Table 4.1**). Thermoreversible and white opaque gels have been obtained, as evidenced by the tube-inversion test,⁸⁴ that exhibited blue emission under UV irradiation (**Figure 4.15**).

Table 4.1 Gelation tests of diimidazolium salts in the presence or in the absence of different amount of NCNDs.

DOS	[bmim][BF ₄]				[bmim][NTf ₂]			
	NCNDs ^a	DOS ^a	appear. ^b	T _{gel} ^c	DOS ^a	appear. ^b	T _{gel} ^c	
<i>m</i> -C ₁₂	0	5.0	OG ^d	SM	5.0	P ^d		
		3.3*	OG ^d	24.3	3.3	P ^d		
	0.05	5.2*	OG	26.3	6.0	PG		
		3.7	PG					
	0.1	5.0	OG	28.5	5.2*	OG	SM	
		3.6*	OG	31.2	4.2	S		

4 Carbon Nanodots-based Hybrid Materials

		2.5	PG				
<i>p</i> -C ₁₂	0	5.0	OG ^d	53.4	5.0	P ^d	
		3.3*	OG ^d	44.5	3.3	P ^d	
	0.025				5.0	OG	41.2
		3.7*	OG	SM	3.6	OG	38.9
		2.5	S		2.5*	OG	41.1
	0.05				1.6	PG	
					5.0	OG	42.9
		3.7*	OG	48.8	3.5	OG	35.4
		2.5	S		2.7	OG	39.0
					1.8*	OG	34.2
	0.1				0.8	S	
		5.0	OG	48.3	5.0	OG	42.8
		3.5*	OG	49.0	4.1	OG	43.6
		2.3	S		3.1	OG	40.9
					2.2*	OG	41.0
				1.1	S		

a. Concentration of NCNDs in ILs or gels, and concentration of DOS in gel, (% w/w);
b. appearances: OG = opaque gel; P = precipitate; PG = gel-like precipitate; S = soluble;
SM = soft material (the gel did not support the weight of the lead-ball for T_{gel}
determination); c. T_{gel} (°C) determined by the lead ball-method and reproducible in 1
°C; d. data from reference 85; *critical gelation concentration (CGC) values.

Gels of both DOSs in [bmim][BF₄] were stable also in presence of NCNDs. In general, these gels pertain almost the same properties of the corresponding pure gels as evidenced by the critical gelation concentration (CGC) and the thermal stability, *i.e.* the temperature of phase transition from gel to solution (T_{gel}). Indeed, only in the case of gel formed by *m*-C₁₂ in [bmim][BF₄] with 0.05 wt % of NCNDs, the

CGC was higher in respect to pure gel (5.2 wt % instead of 3.3 wt %, respectively).

To simplify, now on, all gels will be indicated as DOS acronym/anion of ionic liquid used as gelation solvent-NCND with the corresponding concentration, meaning for the above gel: $m\text{-C}_{12}/[\text{BF}_4]\text{-NCND}_{0.05}$.

On one hand, NCNDs do not disturb gel phase formation and their properties, on the other hand they are not able to favour gel formation at lower DOS concentrations, respect to CGC values of pure gels, as was reported for hybrid organogel containing carbon nanotubes.⁸⁵ Nevertheless, a small amount of NCNDs was able to induce gel formation in solutions of $[\text{bmim}][\text{NTf}_2]$ and DOSs, that without nanodots resulted in precipitate formation after heating and cooling. We hypothesized a positive contribution of nanodots as centres for hydrophobic nucleation and cross-linking nodes for self-assembled fibrillar network. Indeed, nanodots should be able to interact with fibres by hydrophobic and $\pi\text{-}\pi$ stacking interactions.⁷⁵ In our NCNDs, the amino and carboxylic groups present on their surface should give a hydrophilic contribution, resulting in a counterbalance of $\pi\text{-}\pi$ stacking and hydrophilic interactions among NCNDs, DOS and IL, that favors the gel formation also for solutions in which gelation is normally inhibited.

Interestingly, CGC values of $p\text{-C}_{12}$ in $[\text{bmim}][\text{NTf}_2]$ are lower than the ones of the corresponding gels in $[\text{bmim}][\text{BF}_4]$ (2.5 wt % vs 3.5 wt %). In agreement on what previously observed for ionogels,⁸³ the largest CGC values were obtained in the IL having the largest hydrogen-bond accepting ability, β ($\beta = 0.376$ and 0.243 for $[\text{bmim}][\text{BF}_4]$ and $[\text{bmim}][\text{NTf}_2]$, respectively).⁸⁶

Additionally, also small quantities of NCNDs cooperate in gel formation obtaining soft materials with comparable thermal stability. Generally, NCNDs-gel reflects properties of pure ionogels, *i.e.* $p\text{-C}_{12}$ form more thermal stable gel than $m\text{-C}_{12}$, and with lower CGC values.

4.3.2 Rheological properties

For comparison purposes, rheological measurements of NCND-gels have been performed by using 5 wt % of DOS and 0.1 wt % of NCNDs for gel preparation. In addition, to study the effect of the NCNDs amount on the properties of the final gel the $p\text{-C}_{12}/\text{NTf}_2$ system was taken into account. Rheological properties of $m\text{-C}_{12}/\text{NTf}_2\text{-NCND}_{0.1}$ were not determined since its thermal stability at 25 °C was too low.

Soft materials behaved as classical gels, showing a dependence of moduli (G' , storage modulus and G'' , loss modulus) on % strain applied, γ (**Figures 4.16a, S4.9**). In particular, storage moduli were larger than loss ones until they reached the crossover point (γ at $G' = G''$) where they were inverted. The crossover point represents the value at which disruption and collapse of the gel state can be ascribed. In addition, fixing a % value of strain within the linear viscoelastic region (LVR), the independence of moduli on the angular frequency has been observed (**Figures 4.16b, S4.9**). Values of G' were always larger than G'' in the last measurements.

To allow a better comparison of gel properties, values of moduli and rheological parameters such as the crossover point and $\tan\delta = G''/G'$ can be considered (**Table 4.2**).

The data show how the increasing quantity of NCNDs give rise to a stronger material. Indeed, even if the disruption of gel phase occurs at almost the crossover point (γ at $G' = G''$), the value of elastic modulus for $p\text{-C}_{12}/[\text{NTf}_2]\text{-NCND}_{0.1}$ is doubled in respect to the one of $p\text{-C}_{12}/[\text{NTf}_2]\text{-NCND}_{0.05}$, but the further decrease of NCNDs concentration do not cause a further decrease in gel strength. The observed trend, *i.e.* the increase of gel strength as function of increasing amount of nanomaterials was also evidenced for hybrid-organogels and hydrogels already reported.^{87,88}

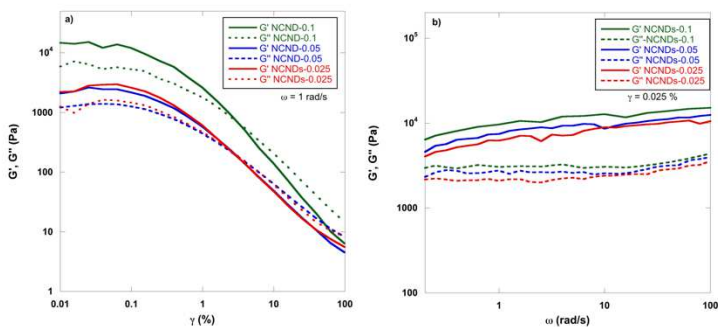


Figure 4.16 a) Strain sweeps and b) frequency sweeps for gels of p -C₁₂/NTf₂-NCND at 5 wt % of DOS and at different concentrations of NCNDs.

Table 4.2 Elastic and viscous moduli, G' and G'' ; $\tan \delta$ and γ value at $G' = G''$ at 5 wt % DOS concentrations and 25 °C. Error limits are based on the average of three different measurements with different aliquots.

Gel	G' (Pa)	G'' (Pa)	$\tan \delta$	γ at $G'=G''$
p -C ₁₂ /[NTf ₂]-NCND _{0.1}	12400±1600 ^a	4900±1200 ^a	0.39±0.06 ^a	2.49±0.01%
p -C ₁₂ /[NTf ₂]-NCND _{0.05}	6000±2000 ^a	2400±700 ^a	0.43±0.06 ^a	2.0±0.5%
p -C ₁₂ /[NTf ₂]-NCND _{0.025}	6600±400 ^a	2600±500 ^a	0.39±0.06 ^a	2.6±0.1%
p -C ₁₂ /[BF ₄]-NCND _{0.1}	180±20 ^b	90±10 ^b	0.51±0.01 ^b	9±1%
m -C ₁₂ /[BF ₄]-NCND _{0.1}	2000±400 ^a	500±190 ^a	0.24±0.04 ^a	70±10%

a. values at $\gamma = 0.025\%$; b. values at $\gamma = 0.063\%$.

Despite this positive effect of NCND on gels formed in [bmim][NTf₂], NCND-gels in [bmim][BF₄] seem much weaker than the corresponding pure gels ($G' \approx 4000$ Pa and $G' \approx 20000$ Pa for p -

C₁₂ and *m*-C₁₂ pure ionogels). As a comparison, we should consider that low values of G' , comparable to ours, have been also observed for hybrid-hydrogels reported by Steed *et al.*, that are the most similar systems to our ionogels.⁷⁵ However, also in [bmim][BF₄]/NCND-gels, the presence of NCNDs is advantageous, as in both cases the crossover point of hybrid gels is obtained at larger γ percentage than pure gels ($\approx 9\%$ vs $\approx 3\%$ for *p*-C₁₂/[BF₄]-NCND_{0.1} and corresponding pure gel; $\gamma \approx 70\%$ vs $\approx 7\%$ for *m*-C₁₂/[BF₄]-NCND_{0.1} and corresponding pure gel). This suggests that the presence NCNDs in the gel made the organization of the composite flow harder than the one-component gel. The prolonged LVR could be attributed to the effect of good dispersion of NCNDs in the gel matrix, as previously reported for some carbon nanotubes hybrid organogels.^{85,89} Therefore, our NCNDs enhance the properties of systems not able to gel in their absence, but exert a slightly destabilizing effect on the rheological properties of systems able to self-assemble without NCNDs. Considering the *p*-C₁₂ gels with the same amount of NCNDs, it is clear that gel formed in [bmim][NTf₂] shows higher resistance than the one formed in [bmim][BF₄]. In addition, *m*-C₁₂/[BF₄]-NCND_{0.1} is surprisingly stronger than the corresponding gel formed by *para*-substituted DOS.

To conclude, the presence of NCNDs influences properties of the materials. Indeed, for pure ionogels, as general trend, gelator presenting *para*-substituted cations exerted better rheological response than *meta*-substituted ones. These data well support the previous hypothesis of a NCNDs stabilizing effect on systems less organized and a destabilizing one for more organized gels.

4.3.3 Self-healing properties

The ability to self-repair after exposure to external stimuli could be pivotal for the implementation of gels in devices. Indeed, a gel should

be more manageable if we imagine spreading it on a surface when it is more fluid. On the other hand, it should be able to restore its strength after rest. This property has been extensively studied for hydro- and organogel,⁹⁰ but it has been scarcely analysed for hybrid ionogels. For these reasons we investigated the ability of our gels to self-repair after exposure to magnetic stirring (thixotropy) and ultrasound irradiation (sonotropy) (**Table 4.3**).

The ability to restore after disruption of a mechanical force was observed only for hybrid gels formed in [bmim][NTf₂], according to their best rheological response. The thixotropy of the gel was further confirmed with a rheological test (**Figures 4.17, S4.10**). Additionally, all the gels resisted to the action of ultrasound irradiation with the only exception of *m*-C₁₂[BF₄]-NCND_{0.1}, which showed sonotropic behaviour.

Table 4.3 Results of self-healing ability tests of the gels at 5 wt % of DOS, in terms of sonotropy and thixotropy.

Gel	Thixotropy	Sonotropy
<i>p</i> -C ₁₂ [NTf ₂]-NCND _{0.1}	Yes	Stable
<i>p</i> -C ₁₂ [NTf ₂]-NCND _{0.05}	Yes	Stable
<i>p</i> -C ₁₂ [NTf ₂]-NCND _{0.025}	Yes	Stable
<i>p</i> -C ₁₂ [BF ₄]-NCND _{0.1}	No	Stable
<i>m</i> -C ₁₂ [BF ₄]-NCND _{0.1}	No	Yes

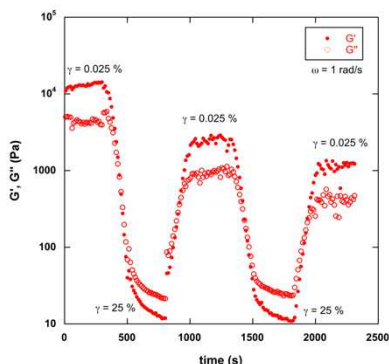


Figure 4.17 G' and G'' at 25 °C as a function of time for $p\text{-C}_{12}/[\text{NTf}_2]\text{-NCND}_{0.1}$: at low ($G' > G''$ regimes, $\gamma = 0.025\%$) and destructive strain ($G'' > G'$ regimes, $\gamma = 68\%$).

When low levels of strain in the LVR were applied after the disruption of the gels, G' was higher than G'' , demonstrating its recovery. The percentage of gel recovery was estimated comparing initial G' values with the ones obtained in the LVR after disruption (**Table 4.4**).

Table 4.4 Percentage of G' recovered after gel disruption.

Gel	1° cycle recovery	2° cycle recovery
$p\text{-C}_{12}/[\text{NTf}_2]\text{-NCND}_{0.1}$	19%	9%
$p\text{-C}_{12}/[\text{NTf}_2]\text{-NCND}_{0.05}$	27%	26%
$p\text{-C}_{12}/[\text{NTf}_2]\text{-NCND}_{0.025}$	67%	41%

Interestingly, the recovery depends on the amount of NCNDs in gel matrix, as it increases with low quantity of NCNDs. These data indicated a good response of gels to the external force applied. Indeed,

gel networks were restored also after the second disruption. In addition, a further partial loss of G' was observed only for p - C_{12} /[NTf₂]-NCND_{0.1}, while for other gels it stayed almost constant.

4.3.4 Kinetic of gel formation

Kinetic of gel formation was also investigated for all the gels of p - C_{12} , since gels formed by m - C_{12} gelators presented a really slow kinetic of formation that could not be followed. This trend recalls what previously reported also for some pure ionogels by m - C_{12} gelators.⁸³

Gel formation was determined by recording the absorbance of gel phases at 568 nm (**Figures 4.18, S4.11**). In this way, it is possible to have information on the opacity of the gel, which is qualitatively related to the number and the size of polydisperse nanostructures in a system, and also to the crystallinity of a gel.⁹¹

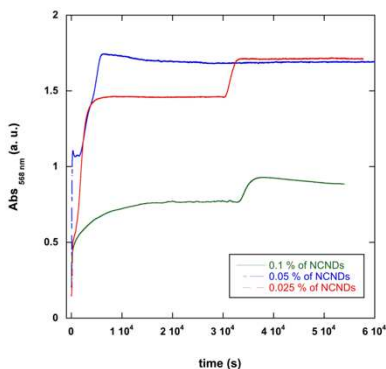


Figure 4.18 Kinetic of gel formation for p - C_{12} /[NTf₂] with different amount of NCNDs at 25 °C.

In all cases we can observe that the gel formation occurred through a two-step mechanism. Indeed, the absorbance rapidly increases

keeping constant for a long interval of time, and this first step could be ascribed to the aggregate nucleation, while in the second step, the absorbance further increases until reaches a constant value corresponding to the completion of gelation. Bearing in mind that the self-assembly process can involve fibers (*i.e.* 1D objects) formation before the 3D networks of self-assembled fibrillar networks are completed, we attribute the kinetic trend to initial formation of aggregates that subsequently rearrange to form gel phases.

According to Liu *et al.* carbon materials slow down the kinetic of gel formation due to a strong interaction between nanotubes and the gelator,⁸⁵ and the same effect seems to be also induced by our NCNDs. Indeed, the comparison between the kinetic of formation for $p\text{-C}_{12}/[\text{BF}_4]\text{-NCND}_{0.1}$ and the corresponding pure gel reveals that the hybrid gel presents an induction period of nucleation equal to 7 h while for pure gel it was equal to 1.5 h. Furthermore, the gradual increase of NCNDs caused a different kinetic of gel formation as small amount of NCND-gels shows a quite faster kinetic, while the increase of NCNDs in gel matrix extended the nucleation period and subsequently the gel formation occurred at larger interval of time. Additionally, for $p\text{-C}_{12}/[\text{NTf}_2]\text{-NCND}_{0.1}$ a drop in crystallinity values can be observed in respect to hybrid-gels with fewer amounts of NCNDs.

4.3.5 Fluorescence properties

Differently from water solutions (data reported in *Chapter 2*) the optimal excitation wavelength of NCNDs in ILs was shifted to 340 nm or 355 nm inducing the highest emission band at ≈ 420 and ≈ 450 nm, for [bmim][BF₄] and [bmim][NTf₂] solutions, respectively. The dissolution of NCNDs in both ILs induced a significant increase in fluorescence emission by increasing the NCNDs amount from 0.025 to 0.1 wt %. The enhanced emission was more consisted in

[bmim][BF₄] than in [bmim][NTf₂] (**Figure S4.12**). This result underlines how the different nature of the IL's anion plays an important role in the interaction with carbon dots. Dupont *et al.* attributed this phenomenon to the IL charged stabilising layer that could affect the nanoparticle electrostatic potential.⁹²

Fluorescence spectra of the NCNDs-IL solutions in presence of DOS (all measurements were carried out at 5 wt % of gelator concentration) showed a fluorescence intensity drop, probably due to the strong interaction hold between diimidazolium salt and NCNDs. The fluorescence decrease is even more evident in the condensed phase (**Figures 4.19, S4.13**).

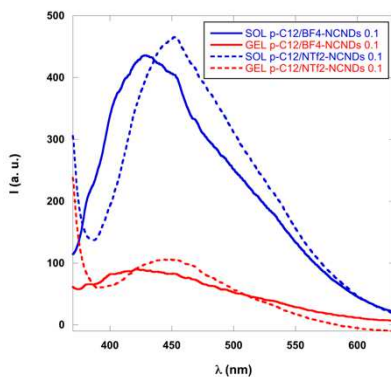


Figure 4.19 FL emission spectra of hot solutions and hybrid-ionogels recorded at the optimal excitation wavelength of 340 and 355 nm for [bmim][BF₄] and [bmim][NTf₂] solutions, respectively.

The decrease of NCNDs emission could be ascribed both to the interaction of nanoparticles with DOSs and to the opacity of the matrices. Similar results were previously obtained for organogels formed by a gelator capped with CdSe/ZnS quantum dots and for the

hybrid sol-gel matrices used for the obtained of thin films. In the last case, the fluorescence is highly reduced when compared to solution.⁹³ FLQYs of the gels ranged from 2.87% to 6.83% (**Table S4.1**). According to the NCNDs emission in IL solutions, the gel fluorescence increases with a larger NCNDs amount, in addition the least opaque gel (*p*-C₁₂/[NTf₂]-NCND_{0.1}) presents the higher FLQY. On the other hand, in contrast to solution measurements, gels formed in [bmim][NTf₂] are more emissive than the ones in [bmim][BF₄]. Interestingly, the comparison of gels with different DOSs as gelators shows the higher fluorescence for *m*-C₁₂ gels than *p*-C₁₂, and this is probably related to the opacity of the gels.

Therefore, it is clear that the combination of NCNDs with ionogels drastically changes properties of pure materials. Nevertheless, NCNDs keep their characteristic features, and even if the fluorescence is reduced in the hybrids when compared to the solutions, this result is consistent for a gel phase.

4.3.6 Morphological investigation

The realistic representation of the hybrid-gel morphology could be achieved with a technique that allows observing both nanoparticles and gel network in their forms. To this aim, AFM measurements were performed on *p*-C₁₂/[NTf₂]-NCND_{0.1} as a representative gel, that showed the best performance.

From height images (**Figure 4.20a,d**) it is possible to recognize the gel 3D network, which seems characterized by a thick texture, where trunk-like fibers tightly intertwine. The thick texture morphology was consistent with the one reported for pure ionogel,⁸³ and a fiber dense 3D network was observed also for carbon dots-hydrogels.^{75,79} In **Figure 4.20b,c,e,f** are reported amplitude images, that being equivalent to a map of the slope of the sample, often display the shape of the sample more easily. Quasispherical nanoparticles arranged on

the compact gel network can be identified, having nanometric dimensions respect to the micrometric ones of the gel network. Unfortunately, the size of NCNDs could not be measured due to the presence of the gel matrix. Interestingly, in **Figure 4.20f** a cross-linked structure formed around the nanodots can be observed, strengthening the hypothesis that NCNDs are active components in the gel network formation. This tight interaction between carbon nanomaterials and gelators could be confirmed also by comparison with other hybrid gels. Indeed, fibers crossed over the surface of graphene oxide sheets were also observed for some hybrid organogels.⁸⁹ Furthermore, it has been reported that the addition of carbon nanotubes in organogels gave rise to fibers.^{87,94}

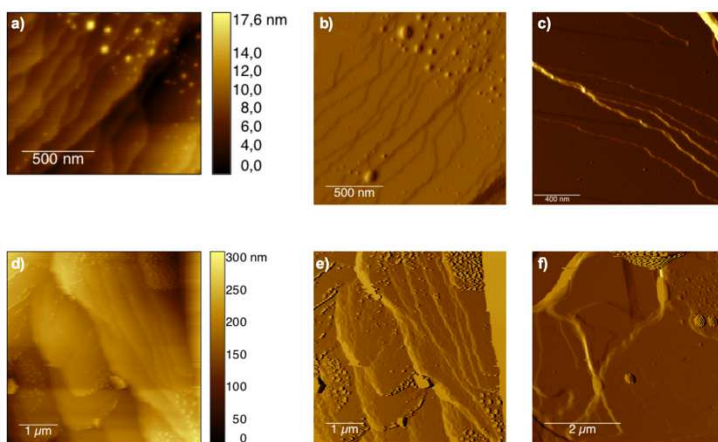


Figure 4.20 Tapping-mode AFM images of the hybrid-ionogel drop-casted on a mica surface. a), d) Heights images; b), c), e), f) amplitude images.

4.3.7 Aggregation studies

To have insights on the presence of aggregates in the hybrid gels, RLS investigation was performed, since it allows detecting the presence of

aggregates formed by different systems in solution, especially chromophores.⁹⁵ In addition, RLS intensity can be related to the size of aggregates and, generally, it simultaneously increases with the size of aggregates.⁹⁶ **Figure 4.21** shows values of RLS intensity maxima for hot solutions and gels (**Table S4.2**).

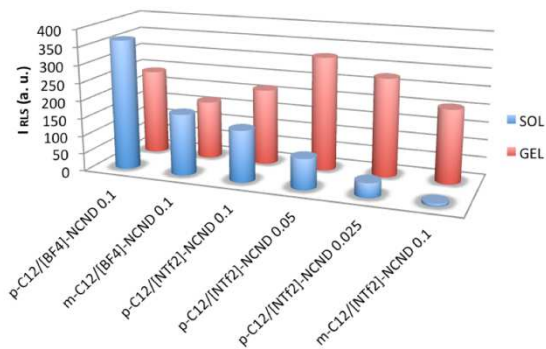


Figure 4.21 Histogram showing the values of RLS intensity maxima for solutions and gels.

As stated above, the nature of the IL used as gelation solvent drastically changes the gel properties. This particularity can be observed also from RLS measurements; indeed, aggregates in solution of [bmim][BF₄] are unpredictably larger than the one of the gel, while the opposite trend can be recognized for systems in [bmim][NTf₂]. This behaviour, once again, underlines the different interaction among NCNDs, DOS and IL. In the first case, larger aggregates rearrange in smaller ones for the obtainment of the self-assembled fibrillar network according to pure ionogels.⁸³ In the second case, the self-assembly process probably involves fiber formation of 1D objects with smaller size before the 3D networks is formed with aggregates presenting larger size. Interestingly, the

amount of NCNDs significantly influences the size of the aggregates in solution, as more nanoparticles in solution form larger aggregates. The only exception is observed for $m\text{-C}_{12}/[\text{NTf}_2]\text{-NCND}_{0.1}$ that is the weakest gel. In addition, lowest I_{RLS} values were detected for $m\text{-C}_{12}$ -gels, and the presence of smaller aggregates could also explain the higher fluorescence of these gel phases.

4.3.8 Anti-radical activity

The anti-radical activity of CNDs has been recently reported, and their potentiality in quenching reactive radical oxygenated species is due to the presence of defects and unpaired electrons on the surface. Moreover, their π -conjugated nature is likely to facilitate charge transfer and electron storage.⁹⁷ The use of CNDs anti-oxidant properties has been studied especially for biological purposes, but, it is well known that processes of auto-oxidation can involve also the conservation, hence preservation, of cultural heritage.^{98,99} For this reason, we envisage that our hybrid ionogels might be used as sensors for the detection of radicals or as coating materials for artworks in order to prevent auto-oxidation processes. To this aim we analysed the radical scavenger efficiency of our hybrid ionogel. For this test, the gel $p\text{-C}_{12}/[\text{NTf}_2]\text{-NCND}_{0.1}$ was chosen, since is the most fluorescent gel among the ones tested, and an interesting relation between fluorescence and radical scavenger efficiency has been recently reported for carbon dots solutions.¹⁰⁰

The gel was exposed to a DPPH solution, modifying opportunely the procedure of the most common free radical assay used gel system.^{101,102}

The solution of DPPH in contact with the gel rapidly changed its colour from dark purple to light yellow (**Figure S4.14**). The efficiency of the gel scavenger activity was measured by monitoring the disappearance of the radical absorbance peak at 517 nm in relation

to the absorbance of a DPPH solution unexposed to the gel phase (**Figure 4.22**).

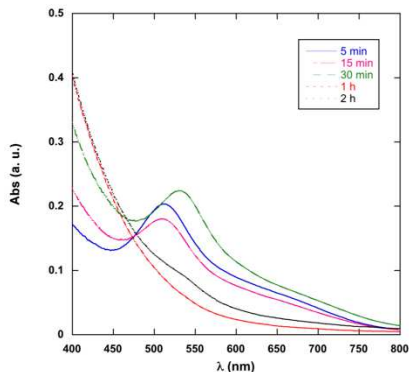


Figure 4.22 UV-Vis absorption spectra of DPPH solutions in contact with p - C_{12} /[NTf₂]-NCND_{0.1} at different intervals of time.

The efficiency of the gel was surprisingly high even after just 5 minutes of contact between the radical solution and the gel and it reaches the maximum value in 1 hour (**Table S4.3**). Interestingly, the gel phase keeps its nature even after long exposure to the radical solution, so, we are confident that this matrix could be used as coating materials keeping high efficiency also for prolonged exposure.

In order to understand which component gave rise to the anti-radical efficiency, we exposed to the DPPH solution the NCNDs and the DOS-IL solution, separately (**Table S4.4**). It is worth mentioning that the CNDs in contact with the etheric DPPH solution were not soluble and did not exhibit any anti-radical activity, but when they were dissolved in methanol, the DPPH solution turned yellow. Therefore, it seems that the solubilization of CNDs in a matrix is crucial for them to behave as radical scavenger, indeed their activity has been so far reported only in solution.^{100,103}

The efficiency of DOS-IL solution is moderate compared to the NCNDs one, however even the NCNDs alone cannot achieve the strong efficiency of the hybrid gel. Therefore, the interaction between NCNDs and ionogel generates a positive effect on the final properties of the material.

Additionally, the radical scavenger activity of the hybrid gel is comparable with the one of L-ascorbic acid. In the same conditions used for gels, the radical scavenger activity of the well-known anti-oxidant was tested for the pure acid and for a solution of DOS-IL in which an amount of acid was previously dissolved. After 15 minutes, both systems presented the same anti-radical efficiency (76% for L-ascorbic acid system and 78% for $p\text{-C}_{12}/[\text{NTf}_2]\text{-NCND}_{0.1}$, **Table S4.4**).

4.4 Conclusions and perspectives

In this chapter we have reported novel functional NCNDs-hybrid materials.

The first part focused on an electron donor-acceptor nanoconjugate, in which the light harvesting and electron donating properties of porphyrins were, for the first time, combined with the electron accepting features of NCNDs. We self-assembled porphyrins with NCNDs and we demonstrated the formation of a charge separated state. These results may lead to the supramolecular constructions of nano-architectures using multiple combinations of these two moieties being able to generate large libraries of electron-donor/electron-acceptor ensembles. Moreover, we showed that visible light excitation transforms the strongly quenched porphyrin singlet excited states in the conjugate into a several nanoseconds lasting charge separated states. The optimization of the coupling in the porphyrin-CNDs composites is far behind that in the porphyrin–fullerene or SWCNTs composites, and there is plenty of room for improvement. To conclude, it has been shown a promising and leading beginning for CNDs-based hybrid materials possessing covalently linked or supramolecularly arranged porphyrins as photoactive moieties, towards the development of novel functional architectures. We believe that our key finding of photoinduced charge separation between CNDs and porphyrins will give a significant contribution to scientists working in the arising field of CNDs. Thus, the CNDs may open the door to a host of unforeseen applications and could be a target of choice for the development of novel photoactive materials. In the second part, we have reported the first example of CNDs-based ionogels, by using diimidazolium organic salts. It has been demonstrated that NCNDs induce gel formation for no gelating systems and module properties of pure gels. This is likely due to a counterbalance of π - π stacking and hydrophilic interactions among

the gel components. Thermal stability of hybrid gels and critical gelation concentration are not affected by NCNDs, while other properties like rheological ones are heavily influenced. Interestingly, increasing the amount of NCNDs makes the gel stronger, while an opposite trend respect to the rheological properties of pure ionogels can be observed. Furthermore, the presence of nanomaterials seems to induce a stabilizing effect on systems less organized and a slightly destabilizing one on more organized gels. For example, it was observed that NCNDs could slow down the gelation process. An important feature of our soft materials, especially for future applications, is their ability to restore after repeated mechanical disruptions.

The strong connection between the gel components was confirmed through the morphological analysis of gel phases. Indeed, we were able to observe the spherical nanoparticles crosslinked to the fibers of the 3D gel network.

Our ionogels keep the fluorescence of the carbon dots, even if it resulted partially quenched due to the opacity of the gel phases. Finally, it was demonstrated that the dissolution of the NCNDs in the gel matrix enhances their antiradical activity. Indeed, the hybrid gels exert a great potential as radical scavenger, property that opens the possibility to use them as coating materials, for instance for the preservation of artworks.

4.5 Experimental section

4.5.1 Materials

The synthesis of NCNDs is reported in *Chapter 2*.

Diimidazolium organic salts, *p*-C₁₂ and *m*-C₁₂, were synthesized according to literature.⁸³

Reagents were bought from Sigma-Aldrich, TCI, VWR Int. and used as received, unless otherwise specified.

Dialysis tubes with molecular weight cut-off 1 kDa were bought from Spectrum Labs.

Column chromatography was carried out using Merck silica gel 60 Å (particle size 40-63 μm).

Thin layer chromatography (TLC) was conducted on pre-coated aluminum sheets with 0.20 mm Merck Silica Gel F254.

Ultrapure fresh water was obtained from a Millipore water purification system (>18MΩ Milli-Q, Millipore).

4.5.2 Apparatus and characterization

NMR experiments were carried out with a Varian Inova 500 MHz and 125 MHz (¹H and ¹³C).

Steady-state absorption spectra were recorded at room temperature on a Perkin Elmer Lambda 2 spectrophotometer. Steady-state fluorescence spectra were recorded at room temperature on a Horiba Fluormax 3 spectrofluorometer. Femtosecond transient-absorption studies were carried out using a mode-locked Ti: sapphire laser CPA-2101 (Clark-MXR, Inc.) in connection with a Helios transient absorption pump/probe (Ultrafast systems). The excitation wavelength was tuned by means of noncollinear optical parametric amplification of the fundamental laser beam.

IR spectra (KBr) were recorded on a Perkin Elmer 2000 spectrometer.

Atomic force microscopy (AFM) images were obtained with a Nanoscope IIIa, VEECO Instruments. As a general procedure to perform AFM analyses, tapping mode with a HQ:NSC19/ALBS probe (80kHz; 0.6 N/m) (MikroMasch) from drop cast of samples in an aqueous solution (concentration of few mg/mL) on a mica substrate was performed. The obtained AFM-images were analyzed in Gwyddion 2.35.

RLS measurements were carried out with a spectrofluorophotometer, by using a synchronous scanning mode in which the emission and excitation monochromators were preset to identical wavelengths. The RLS spectrum was recorded from 300 to 800 nm with both the excitation and emission slit widths set at 1.5 nm. We chose as working wavelength the one corresponding to the intensity maximum of the emission spectrum. Samples were prepared by injecting into a quartz cuvette (light path 0.2 cm) the limpid hot solution. The measurements were carried out at 25 °C. Spectra were recorded for the hot solution and the gel phase. The gel phase obtained at the end of the measurement was stable after the tube inversion test.

Opacity measurements were recorded with a spectrophotometer. The opacity of the gel phases was determined with UV-Vis measurements as a function of time, at a wavelength of 568 nm and a temperature of 25 °C. Samples for a typical kinetic analysis were prepared by injecting into a quartz cuvette (light path 0.2 cm) a hot dispersion of salt. Spectra were recorded until gel formation. The gel phase obtained at the end of the measurement was stable according to the tube inversion test.

Rheology measurements were recorded at room temperature on ARES G2 (TA Instruments) strain-controlled rheometer using a plate-plate (PP 25-2) tool, the sample was placed between the shearing

plates of the rheometer. Rheological properties, such as strain sweep and frequency sweep, were recorded three times on three different aliquots of gels.

Strain sweeps were carried at angular frequency of 1 rad/s and frequency sweeps at strain of 0.025%. These values were chosen to be within the linear viscoelastic region (LVR) of gels.

Self-healing properties of gel phases were also tested by rheometer. They were carried out at room temperature and at angular frequency of 1 rad/s, varying the strain from low to high percentage values for fixed time intervals of 5 minutes (values of yield strain to apply were chosen from linear viscoelastic region and destructive strain of the gel). Rotational strain was kept at 0 % for 0.05 s before changing from destructive strain to linear viscoelastic region conditions. When the moduli reached plateau values after the cessation of disruptive strain, it was possible to calculate the percentage of recovery of the initial G' value.

Thixotropic and sonotropic behaviour: the gel phases were subjected to two different external stimuli. The mechanical stimulus involved stirring the gel phase at 1000 rpm for 5 min, using a stirring bar (length 8 mm, height 3 mm). The sonotropic behaviour of the gel phases was tested by irradiating in an ultrasound water bath for 5 min with a power of 200 W and a frequency of 45 kHz. Thereafter, the materials were stored at 4 °C overnight.

When the samples were stable to the tube-inversion test, the gels were defined as thixotropic or sonotropic.

DPPH test: the 1,1-diphenyl-2-picryl free radical scavenging assay was carried out to assess antiradical efficiency of gel phases modifying the published procedures.^{101,102} To verify the efficiency of gels it was necessary to use the gel phase in its form, for this reason the direct contact of the gel with the methanol solution of DPPH was avoided. Therefore, samples for a typical measurement were prepared

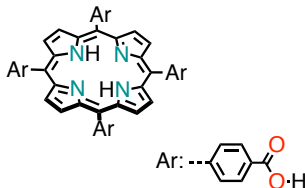
by placing in a screw-capped vial, containing 250 mg of NCNDs-gel, 250 μL of a diethyl-ether solution of DPPH (10^{-3} M). All samples were thermostated at 25 $^{\circ}\text{C}$ for the time required by the measurement. Gel phases were stable for the entire duration of the experiments. At fixed intervals of time, the vial containing the gel and the supernatant liquid were concentrated in vacuum to remove solvent traces and they were subsequently dissolved in 1 mL of methanol. The final solution ([DPPH] $\sim 10^{-4}$ M) was analysed recording the corresponding UV-Vis spectrum with a Beckmann DU-800 spectrophotometer equipped with a Peltier temperature controller. Scavenging activities were determined from the drop in absorbance at 517 nm of each sample compared with that of the DPPH solution in the absence of contact with the gel. The control was treated in the same way as gel phases: 250 μL of DPPH solution dissolved in diethyl ether were placed in an empty vial and, at the same interval of time of the sample, the control solution was concentrated in vacuum and dissolved in methanol. Scavenging efficiency values were calculated by the following equation:

$$\text{Radical Scavenging Efficiency (\%)} = [(A-B) / (A-0.1)] \times 100$$

where A is the absorbance of the DPPH solution and B the absorbance of the DPPH solution after the contact with the gels.

The above procedure was used also to test the efficiency of CNDs, a partially formed gel in absence of CNDs, L-ascorbic acid and a partially formed gel in presence of 0.1 wt % of L-ascorbic acid.

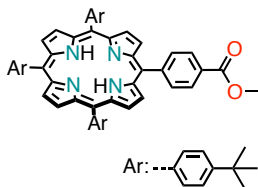
4.5.3 Synthesis of TCPP



The 5,10,15,20-tetrakis(4-carboxyphenyl) porphyrin (TCPP) was synthesized according to a slightly modified literature procedure.⁸⁰ A solution of 4-formylbenzoic acid (0.50 g, 3.33 mmol) in propionic acid (20 mL) was heated to 80 °C until the aldehyde was fully dissolved. At this point, pyrrole (0.23 mL, 3.33 mmol) was added and the temperature was brought to reflux for 2 hrs. The reaction mixture was allowed to cool down to r.t. and left at -20 °C overnight. The crystals were collected, washed with CH₂Cl₂ and dried to obtain product as dark purple solid (0.68 g, 26 % yield).

m.p. > 250 °C. ¹H NMR (500 MHz, Dimethylsulfoxide-*d*₆): δ 13.19 (s, 4H, Ar-COOH), 8.85 (s, 8H, Pyr-*H*), 8.38 (d, *J* = 8.0 Hz, 8H, Ar-*H*), 8.33 (d, *J* = 8.1 Hz, 8H, Ar-*H*), -2.91 (bs, 2H, Pyr-NH). IR (KBr): cm⁻¹ 3433, 1697, 1605, 1401, 1263, 1177, 1102, 1019, 965, 866, 797, 714. ES (MS -): 789.2 (M - H⁺), C₄₈H₃₀N₄O₈ requires 790.21. Characterization in accordance with literature.⁸⁰

4.5.4 Synthesis of TPP-COOCH₃

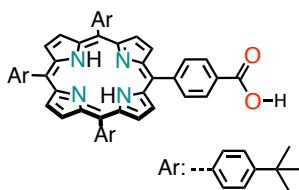


The 5,10,15-tri(4-*tert*-butylphenyl)-20-(4-carboxymethylphenyl) porphyrin (TPP-COOCH₃) was synthesized according to a slightly modified literature procedure.³⁶ To a solution of 4-*tert*-butylbenzaldehyde (0.37 mL, 2.19 mmol), methyl 4-formylbenzoate (330 mg, 2.19 mmol) and freshly distilled pyrrole (0.30 mL, 4.38 mmol) in CHCl₃ (1.0 L with 0.75 % EtOH) was added BF₃·OEt₂ (0.36 mL), at r.t. and under Ar. The solution was stirred for 1 hr before adding Chloranil (400 mg, 1.63 mmol) and was left stirring for another hour. Finally, Et₃N (0.28 mL) was added and all was stirred for 15 min. The reaction mixture was concentrated under reduced pressure and passed over a silica plug (CHX/CH₂Cl₂ 1:1) to obtain a dark purple solid as a mixture of TPP and porphyrin esters. The crude was purified by column chromatography with product eluting as the second band (SiO₂, CHX → CHX/AcOEt 95:5) and finally crystallized from CH₂Cl₂ with pentane to obtain the purple product (294 mg, 15 % yield).

m.p. > 250 °C. ¹H-NMR (500 MHz, Chloroform-*d*): δ 8.91 (d, *J* = 4.9 Hz, 2H), 8.89 (s, 4H), 8.77 (d, *J* = 4.6 Hz, 2H), 8.44 (d, *J* = 8.1 Hz, 2H), 8.32 (d, *J* = 8.1 Hz, 2H), 8.20 – 8.09 (m, 6H), 7.79 – 7.74 (m, 6H), 4.12 (s, 3H), 1.62 (s, 27H), -2.74 (s, 2H). ¹³C-NMR (126 MHz, Chloroform-*d*): δ 167.65, 150.82, 147.50, 139.37, 139.31, 134.89, 134.76, 134.71, 129.71, 128.12, 123.88, 123.85, 121.01, 120.72,

118.40, 52.65, 35.17, 31.96. MS (ES +): found 841.5 ($M + H^+$), $C_{58}H_{56}N_4O_2$ requires = 840.44. Characterization was in accordance with literature.³⁶

4.5.5 Synthesis of TPP-COOH

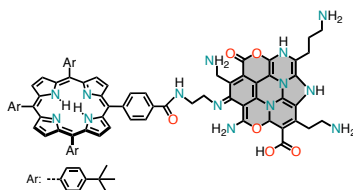


The 5,10,15-tri(4-tert-butylphenyl)-20-(4-carboxyphenyl) porphyrin (TPP-COOH) was synthesized according to a slightly modified literature procedure.¹⁰⁴ To a suspension of 5-(4-carboxymethylphenyl)-10,15,20-(4-tert-butyltriphenyl) porphyrin (100 mg, 0.12 mmol) in EtOH (50 mL) was added an excess of aq. KOH and the mixture was refluxed overnight. The reaction mixture was acidified with 2 M aq. HCl and was concentrated under reduced pressure. The crude was extracted with $CHCl_3$ and the organic phase was washed with 1 M aq. $NaHCO_3$ and brine, dried (Na_2SO_4) and removed under reduced pressure. The crude was purified by column chromatography (SiO_2 , $CH_2Cl_2 \rightarrow CH_2Cl_2/MeOH$ 9:1) to obtain pure product as purple solid (86 mg, 89 % yield).

m.p. > 250 °C. 1H -NMR (500 MHz, Chloroform- d /dimethylsulfoxide- d_6 9:1): δ 12.60 (s, 1H, Ar-COOH), 8.90 (d, $J = 4.9$ Hz, 2H, Pyr-H), 8.88 (s, 4H, Pyr-H), 8.80 (d, $J = 4.7$ Hz, 2H, Pyr-H), 8.44 (d, $J = 7.9$ Hz, 2H, Ar-H), 8.29 (d, $J = 7.9$ Hz, 2H, Ar-H), 8.15 – 8.10 (m, 6H, Ar-H), 7.78 (d, $J = 7.8$ Hz, 6H, Ar-H), 1.61 (s, 27H, Ar-(CH_3)₃), -2.82 (s, 2H, Pyr-NH). ^{13}C -NMR (126 MHz, Chloroform-

d/dimethylsulfoxide- d_6 9:1): δ 169.52, 151.68, 147.53, 139.87, 139.82, 135.55, 135.49, 135.46, 131.61, 129.13, 124.81, 124.79, 121.73, 121.49, 119.53, 35.96, 32.77. IR (KBr): cm^{-1} 3437, 2957, 1694, 1607, 1474, 1431, 1398, 1362, 1313, 1267, 1231, 1195, 1156, 1108, 1023, 982, 967, 800, 767, 734. MS (ES +): found 827.5 ($M + H^+$), $C_{58}H_{56}N_4O_2$ requires = 862.42. Characterization was in accordance with literature.¹⁰⁴

4.5.6 Synthesis of TPP-CONH-NCNDs



To a solution of 5,10,15-Tri(4-*tert*-butylphenyl)-20-(4-carboxyphenyl) porphyrin (44.8 mg, 0.05 mmol) in anhydrous DMF (4.0 mL), 1-(3 dimethylaminopropyl)-3-dimethylaminopropyl)-3-ethylcarbodiimide hydrochloride (EDC · HCl) (19.2 mg, 0.10 mmol) and N-hydroxysuccinimide (11.5 mg, 0.1 mmol) were added. The mixture was stirred at r.t. for 20 min. NCNDs (25.0 mg) were added and the resulting mixture was stirred overnight. The solvent was removed under reduced pressure. Slightly acidic water was added to the reaction mixture (0.1 M aq. HCl) and the excess of porphyrin was removed by washing with copious amounts of CHCl_3 . The aqueous phase was dialyzed against pure water through a dialysis membrane for 2 days to obtain a purple solid (17.5 mg).

4.5.7 Preparation of gels and T_{gel} determination

A dispersion of NCNDs in the selected IL (0.1; 0.05 and 0.025 wt %) was obtained adding a small amount of MeOH (200 μ L for 2 mL of IL). The mixture was, then, concentrated under high vacuum to remove methanol residues.

Gels were prepared by weighing into a screw-capped sample vial (diameter 1 cm) the amount of diimidazolium salt and the NCNDs/IL dispersion (\sim 250 mg). The mixture was heated in an oil bath at 100 $^{\circ}$ C until a clear solution was obtained (\sim 1 h). The vial was then cooled and stored overnight at 4 $^{\circ}$ C. The tube inversion test method was used to examine gel formation.⁸⁴

T_{gel} were determined by the lead ball-method. A lead ball (weighing 46.23 mg and 2 mm of diameter) was placed on the top of the gel and the vial was put into a water bath. The bath temperature was gradually increased (2 $^{\circ}$ C / min) until the gel melted and the lead ball reached the bottom of the vial (T_{gel}). The T_{gel} values were reproducible within 1 $^{\circ}$ C.

4.5.8 Supporting figures

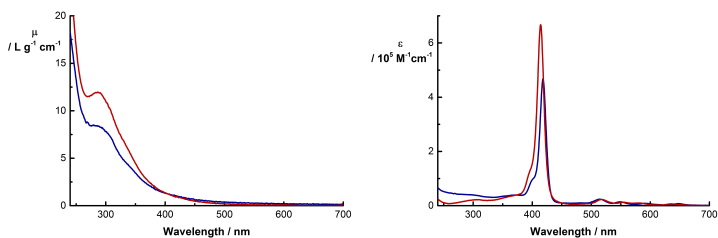


Figure S4.1 Left: mass extinction coefficients of NCNDs (6×10^{-3} g/L) in H₂O/THF (1:1 v/v) (blue line) and in phosphate buffered H₂O (pH = 7.2) (red line) at room temperature. Right: molar extinction coefficients of TCPP in H₂O/THF (1:1 v/v) (blue line) and in phosphate buffered H₂O (red line) at room temperature.

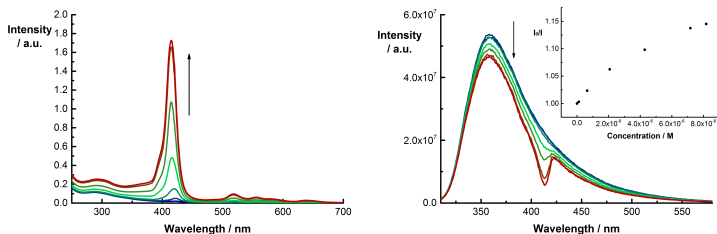


Figure S4.2 Left: absorption spectra of NCNDs (blue line, 0.02 g/L) during the course of a titration with TCPP (blue>green>red, 0 - 8×10^{-6} M) in phosphate-buffered H₂O (pH 7.2) at room temperature. Right: fluorescence spectra of NCNDs (blue line, 0.02 g/L) during the course of a titration with TCPP (blue>green>red, 0 - 8×10^{-6} M) in phosphate-buffered H₂O (pH 7.2) at room temperature. Inset: relationship of I_0/I , using the wavelength corrected integrated emission intensities, versus the concentration of TCPP.

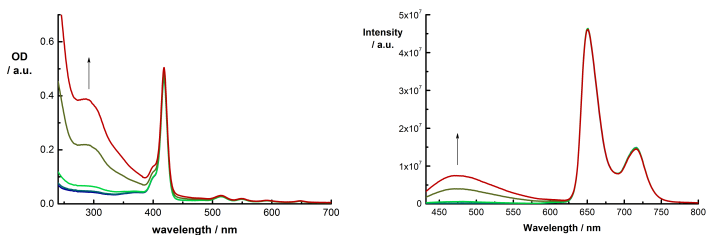


Figure S4.3 Left: absorption spectra of TCPP (blue line, 1.5×10^{-6} M) during the course of a titration with NCNDs (blue>green>red, 0 - 5×10^{-2} g/L) in H₂O/THF (1:1 v/v) at room temperature. Right: fluorescence spectra of TCPP (blue line, 1.5×10^{-6} M) during the course of a titration with NCNDs (blue>green>red, 0 - 5×10^{-2} g/L) in H₂O/THF (1:1 v/v) upon excitation at 422 nm at room temperature.

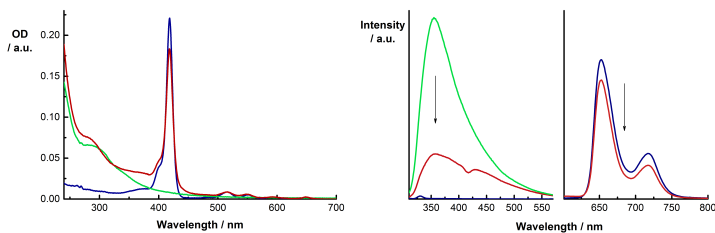


Figure S4.4 Left: absorption spectra of TPP-COOH (blue line), NCNDs (green line) and TPP-CONH-NCNDs (red line) in H₂O/THF (1:1 v/v). Right: fluorescence spectra of TPP-COOH (blue line), NCNDs (green line) and TPP-CONH-NCND (red line) in H₂O/THF (1:1 v/v) upon excitation at 300 nm (left panel) and 550 nm (right panel) at room temperature.

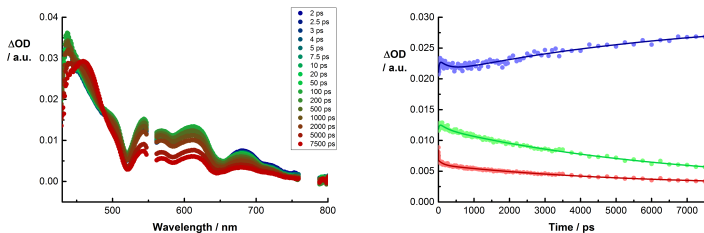


Figure S4.5 Left: differential absorption spectra obtained upon femtosecond pump probe experiments ($\lambda_{\text{ex}} = 550$ nm) of TCP in H_2O at room temperature. Right: corresponding time profiles at 470 (blue) 620 (green), and 685 nm (red).

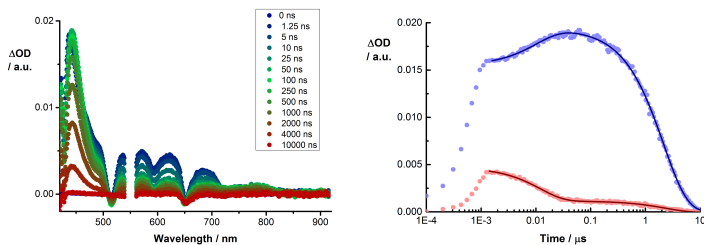


Figure S4.6 Left: differential absorption spectra obtained upon femtosecond pump probe experiments ($\lambda_{\text{ex}} = 550$ nm) of TPP-COOH with several time delays between 0 and 10 μs in $\text{H}_2\text{O}/\text{THF}$ (1:1 v/v) at room temperature. Right: corresponding time profiles at 440 (blue) and 630 nm (red).

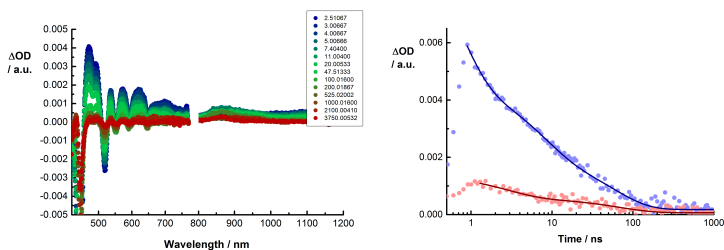


Figure S4.7 Left: differential absorption spectra obtained upon femtosecond pump probe experiments ($\lambda_{\text{ex}} = 387$ nm) of TPP-CONH-NCND with several time delays between 0 and 3750 ps in H_2O (pH = 7.2) at room temperature. Right: corresponding time profiles at 470 (blue) and 680 nm (red).

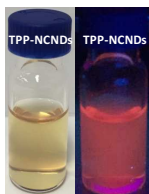


Figure S4.8 Photographs of an aqueous solution of TPP-CONH-NCNDs in daylight (left) and under UV light (365 nm) illumination (right).

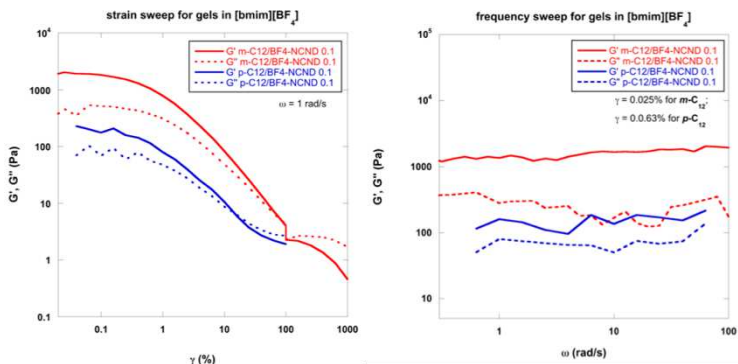


Figure S4.9 Rheological measurements of NCND-gels.

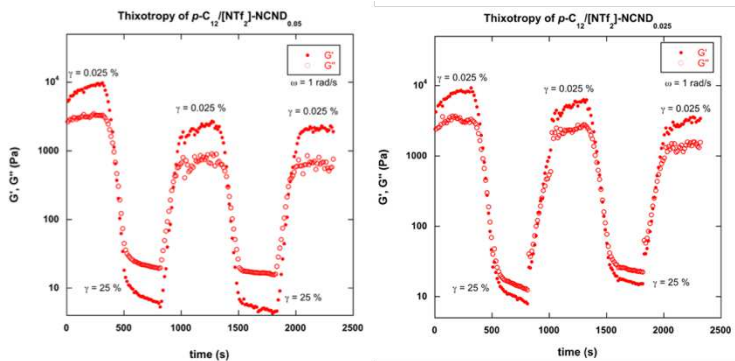


Figure S4.10 Thixotropic measurements of NCND-gels by rheological test.

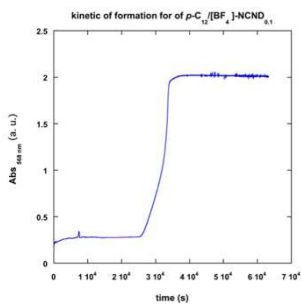


Figure S4.11 Opacity measurements for $p\text{-C}_{12}/[\text{BF}_4]\text{-NCND}_{0.1}$.

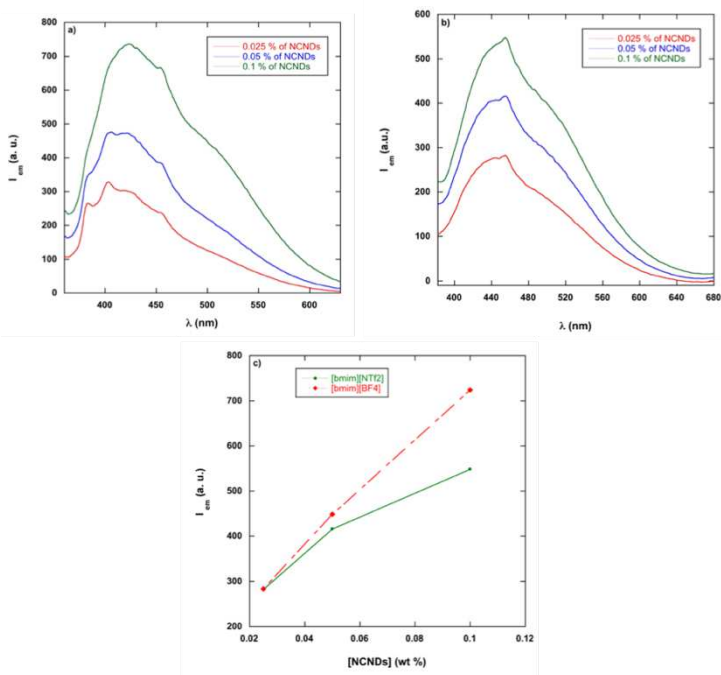


Figure S4.12 FL emission spectra in a) [bmim][BF4] at $\lambda_{\text{exc}} = 340$ nm, b) [bmim][NTf2] at $\lambda_{\text{exc}} = 355$ nm; c) maxima of intensity fluorescence of the difference spectra between solution with lowest and highest concentration of NCNDs.

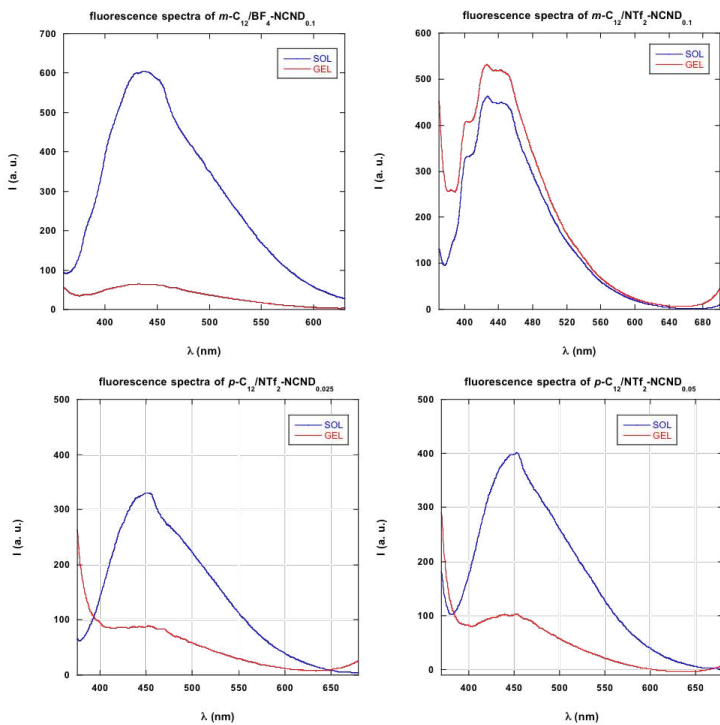


Figure S4.13 Fluorescence spectra of hot solutions and hybrid-ionogels recorded at $\lambda_{\text{exc}} = 340$ nm or 355 nm for [bmim][BF₄] and [bmim][NTf₂].



Figure S4.14 a) DPPH solution at $t = 0$ on empty vial; b) DPPH solution at $t = 0$ in contact with NCND-gel; c) DPPH solution unexposed to gel phase at $t = 1$ h; d) DPPH solution exposed to gel phase at $t = 1$ h.

Table S4.1 Maxima of fluorescence intensity peaks and quantum yields recorded at $\lambda_{\text{ex}} = 340$ nm and $\lambda_{\text{ex}} = 355$ nm for systems in [bmim][BF₄] and in [bmim][NTf₂], respectively.

Hybrid systems	I_{max} (a. u.)		Φ	
	<i>SOL</i>	<i>GEL</i>	<i>SOL</i>	<i>GEL</i>
<i>p</i> -C ₁₂ /[BF ₄]-NCND _{0.1}	435.9	90.4	3.13 %	2.87 %
<i>m</i> -C ₁₂ /[BF ₄]-NCND _{0.1}	605.7	65.1	3.55 %	3.05 %
<i>p</i> -C ₁₂ /[NTf ₂]-NCND _{0.1}	465.2	105.2	5.62 %	4.34 %
<i>p</i> -C ₁₂ /[NTf ₂]-NCND _{0.05}	401.2	103.2	4.85 %	3.63 %
<i>p</i> -C ₁₂ /[NTf ₂]-NCND _{0.025}	330.3	88.2	2.91 %	2.64 %
<i>m</i> -C ₁₂ /[NTf ₂]-NCND _{0.1}	458.0	532.0	5.45 %	6.36 %

Table S4.2 Maxima of RLS intensity peaks for systems in [bmim][BF₄] and in [bmim][NTf₂].

Hybrid systems	I _{max} RLS (a. u.)	
	<i>SOL</i>	<i>GEL</i>
<i>p</i> -C ₁₂ /[BF ₄]-NCND _{0.1}	365.8	242.0
<i>m</i> -C ₁₂ /[BF ₄]-NCND _{0.1}	172.9	165.8
<i>p</i> -C ₁₂ /[NTf ₂]-NCND _{0.1}	145.4	215.4
<i>p</i> -C ₁₂ /[NTf ₂]-NCND _{0.05}	86.0	320.7
<i>p</i> -C ₁₂ /[NTf ₂]-NCND _{0.025}	40.6	276.6
<i>m</i> -C ₁₂ /[NTf ₂]-NCND _{0.1}	7.5	206.7

Table S4.3 Anti-radical efficiency of *p*-C₁₂/[NTf₂]-NCND_{0.1} as function of time.

Time (min)	E (%)
5	71
15	78
30	75
45	72
60	100
120	96

Table S4.4 Anti-radical efficiency after the contact of DPPH solution with the individual components of the hybrid gel, hybrid gel and L-ascorbic acid alone and dispersed on gel matrix.

Matrix	Time (min)	E (%)
DOS-IL solution	60	38
NCNDs	60	88
<i>p</i> -C ₁₂ /[NTf ₂]-NCND _{0.1}	60	100
L-ascorbic acid	60	100
<i>p</i> -C ₁₂ /[NTf ₂]-L-ascorbic acid _{0.1}	15	76

4.6 References

- (1) McConnell, I.; Li, G.; Brudvig, G. W. Energy Conversion in Natural and Artificial Photosynthesis. *Chem. Biol.* **2010**, *17*, 434–447.
- (2) Gust, D.; Moore, T. A.; Moore, A. L. Mimicking Photosynthetic Solar Energy Transduction. *Acc. Chem. Res.* **2001**, *34*, 40–48.
- (3) Imahori, H.; Mori, Y.; Matano, Y. Nanostructured Artificial Photosynthesis. *J. Photochem. Photobiol. C Photochem. Rev.* **2003**, *4*, 51–83.
- (4) Wasielewski, M. R. Photoinduced Electron Transfer in Supramolecular Systems for Artificial Photosynthesis. *Chem. Rev.* **1992**, *92*, 435–461.
- (5) Gust, D.; Moore, T. A.; Moore, A. L. Molecular Mimicry of Photosynthetic Energy and Electron Transfer. *Acc. Chem. Res.* **1993**, *26*, 198–205.
- (6) Umeyama, T.; Mihara, J.; Tezuka, N.; Matano, Y.; Stranius, K.; Chukharev, V.; Tkachenko, N. V.; Lemmetyinen, H.; Noda, K.; Matsushige, K.; *et al.* Preparation and Photophysical and Photoelectrochemical Properties of a Covalently Fixed Porphyrin-Chemically Converted Graphene Composite. *Chem. - A Eur. J.* **2012**, *18*, 4250–4257.
- (7) Xu, Y.; Liu, Z.; Zhang, X.; Wang, Y.; Tian, J.; Huang, Y.; Ma, Y.; Zhang, X.; Chen, Y. A Graphene Hybrid Material Covalently Functionalized with Porphyrin: Synthesis and Optical Limiting Property. *Adv. Mater.* **2009**, *21*, 1275–1279.
- (8) D'Souza, F.; Ito, O. Supramolecular Donor-Acceptor Hybrids of Porphyrins/phthalocyanines with Fullerenes/carbon Nanotubes: Electron Transfer, Sensing, Switching, and Catalytic Applications. *Chem. Commun.* **2009**, 4913–4928.
- (9) Umeyama, T.; Fujita, M.; Tezuka, N.; Kadota, N.; Matano, Y.; Yoshida, K.; Isoda, S.; Imahori, H. Electrophoretic

-
- Deposition of Single-Walled Carbon Nanotubes Covalently Modified with Bulky Porphyrins on Nanostructured SnO₂ Electrodes for Photoelectrochemical Devices. *J. Phys. Chem. C* **2007**, *111*, 11484–11493.
- (10) Baskaran, D.; Mays, J. W.; Zhang, X. P.; Bratcher, M. S. Carbon Nanotubes with Covalently Linked Porphyrin Antennae: Photoinduced Electron Transfer. *J. Am. Chem. Soc.* **2005**, *127*, 6916–6917.
- (11) Li, H.; Martin, R. B.; Harruff, B. A.; Carino, R. A.; Allard, L. F.; Sun, Y.-P. Single-Walled Carbon Nanotubes Tethered with Porphyrins: Synthesis and Photophysical Properties. *Adv. Mater.* **2004**, *16*, 896–900.
- (12) El-Khouly, M. E.; Ito, O.; Smith, P. M.; D'Souza, F. Intermolecular and Supramolecular Photoinduced Electron Transfer Processes of Fullerene–porphyrin/phthalocyanine Systems. *J. Photochem. Photobiol. C Photochem. Rev.* **2004**, *5*, 79–104.
- (13) D'Souza, F.; Deviprasad, G. R.; Zandler, M. E.; Hoang, V. T.; Klykov, A.; VanStipdonk, M.; Perera, A.; El-Khouly, M. E.; Fujitsuka, M.; Ito, O. Spectroscopic, Electrochemical, and Photochemical Studies of Self-Assembled via Axial Coordination Zinc Porphyrin–Fulleropyrrolidine Dyads. *J. Phys. Chem. A* **2002**, *106*, 3243–3252.
- (14) Imahori, H.; El-Khouly, M. E.; Fujitsuka, M.; Ito, O.; Sakata, Y.; Fukuzumi, S. Solvent Dependence of Charge Separation and Charge Recombination Rates in Porphyrin–Fullerene Dyad. *J. Phys. Chem. A* **2001**, *105*, 325–332.
- (15) D'Souza, F.; Deviprasad, G. R.; Rahman, M. S.; Choi, J. Self-Assembled Porphyrin–C₆₀ and Porphycene–C₆₀ Complexes via Metal Axial Coordination. *Inorg. Chem.* **1999**, *38*, 2157–2160.
- (16) Imahori, H.; Hagiwara, K.; Aoki, M.; Akiyama, T.; Taniguchi, S.; Okada, T.; Shirakawa, M.; Sakata, Y. Linkage and Solvent Dependence of Photoinduced Electron Transfer
-

-
- in Zincporphyrin-C60 Dyads. *J. Am. Chem. Soc.* **1996**, *118*, 11771–11782.
- (17) Liddell, P. a; Sumida, J. P.; Macpherson, A. N.; Noss, L.; Seely, G. R.; Clark, K. N.; Moore, A. L.; Moore, T. a; Gust, D. Preparation and Photophysical Studies of Porphyrin-C60 Dyads. *Photochem. Photobiol.* **1994**, *60*, 537–541.
- (18) *Handbook of Porphyrin Science*; Kadish, K. M.; Smith, K. M.; Guillard, R., Eds.; World Scientific: Singapore, 2010.
- (19) Auwärter, W.; Écija, D.; Klappenberger, F.; Barth, J. V. Porphyrins at Interfaces. *Nat. Chem.* **2015**, *7*, 105–120.
- (20) Holten, D.; Bocian, D. F.; Lindsey, J. S. Probing Electronic Communication in Covalently Linked Multiporphyrin Arrays. A Guide to the Rational Design of Molecular Photonic Devices. *Acc. Chem. Res.* **2002**, *35*, 57–69.
- (21) Sengupta, S.; Würthner, F. Chlorophyll J-Aggregates: From Bioinspired Dye Stacks to Nanotubes, Liquid Crystals, and Biosupramolecular Electronics. *Acc. Chem. Res.* **2013**, *46*, 2498–2512.
- (22) Miyatake, T.; Tamiaki, H. Self-Aggregates of Natural Chlorophylls and Their Synthetic Analogues in Aqueous Media for Making Light-Harvesting Systems. *Coord. Chem. Rev.* **2010**, *254*, 2593–2602.
- (23) Hasobe, T. Porphyrin-Based Supramolecular Nanoarchitectures for Solar Energy Conversion. *J. Phys. Chem. Lett.* **2013**, *4*, 1771–1780.
- (24) Drain, C. M.; Varotto, A.; Radivojevic, I. Self-Organized Porphyrinic Materials. *Chem. Rev.* **2009**, *109*, 1630–1658.
- (25) Umeyama, T.; Imahori, H. Photofunctional Hybrid Nanocarbon Materials. *J. Phys. Chem. C* **2013**, *117*, 3195–3209.
- (26) Kirner, S.; Sekita, M.; Guldi, D. M. 25th Anniversary Article: 25 Years of Fullerene Research in Electron Transfer
-

-
- Chemistry. *Adv. Mater.* **2014**, *26*, 1482–1493.
- (27) Hiroshi, I.; Kiyoshi, H.; Tsuyoshi, A.; Masanori, A.; Seiji, T.; Tadashi, O.; Masahiro, S.; Yoshiteru, S. The Small Reorganization Energy of C60 in Electron Transfer. *Chem. Phys. Lett.* **1996**, *263*, 545–550.
- (28) Guldi, D. M.; Asmus, K.-D. Electron Transfer from C76(C2v⁺) and C78(D2) to Radical Cations of Various Arenes: Evidence for the Marcus Inverted Region. *J. Am. Chem. Soc.* **1997**, *119*, 5744–5745.
- (29) Dirian, K.; Herranz, M. Á.; Katsukis, G.; Malig, J.; Rodríguez-Pérez, L.; Romero-Nieto, C.; Strauss, V.; Martín, N.; Guldi, D. M. Low Dimensional Nanocarbons – Chemistry and Energy/electron Transfer Reactions. *Chem. Sci.* **2013**, *4*, 4335.
- (30) D'Souza, F.; Ito, O. Photoinduced Electron Transfer Processes of Functionalized Nanocarbons; Fullerenes, Nanotubes and Graphene. *Sci. Prog.* **2013**, *96*, 369–397.
- (31) Wang, X.; Cao, L.; Lu, F.; Meziani, M. J.; Li, H.; Qi, G.; Zhou, B.; Harruff, B. a; Kermarrec, F.; Sun, Y.-P. Photoinduced Electron Transfers with Carbon Dots. *Chem. Commun.* **2009**, 3774–3776.
- (32) Strauss, V.; Margraf, J. T.; Clark, T.; Guldi, D. M. A Carbon–carbon Hybrid – Immobilizing Carbon Nanodots onto Carbon Nanotubes. *Chem. Sci.* **2015**, *6*, 6878–6885.
- (33) Strauss, V.; Margraf, J. T.; Dirian, K.; Syrgiannis, Z.; Prato, M.; Wessendorf, C.; Hirsch, A.; Clark, T.; Guldi, D. M. Carbon Nanodots: Supramolecular Electron Donor-Acceptor Hybrids Featuring Perylenediimides. *Angew. Chem. Int. Ed.* **2015**, *54*, 8292–8297.
- (34) Yu, P.; Wen, X.; Toh, Y.-R.; Lee, Y.-C.; Huang, K.-Y.; Huang, S.; Shrestha, S.; Conibeer, G.; Tang, J. Efficient Electron Transfer in Carbon Nanodot–graphene Oxide Nanocomposites. *J. Mater. Chem. C* **2014**, *2*, 2894–2901.
-

-
- (35) Sánchez, L.; Sierra, M.; Martín, N.; Myles, A. J.; Dale, T. J.; Rebek, J.; Seitz, W.; Guldi, D. M. Exceptionally Strong Electronic Communication through Hydrogen Bonds in Porphyrin–C60 Pairs. *Angew. Chem. Int. Ed.* **2006**, *45*, 4637–4641.
- (36) Wessendorf, F.; Gnichwitz, J.-F.; Sarova, G. H.; Hager, K.; Hartnagel, U.; Guldi, D. M.; Hirsch, A. Implementation of a Hamilton-Receptor-Based Hydrogen-Bonding Motif toward a New Electron Donor–Acceptor Prototype: Electron versus Energy Transfer. *J. Am. Chem. Soc.* **2007**, *129*, 16057–16071.
- (37) Sessler, J. L.; Jayawickramarajah, J.; Gouloumis, A.; Torres, T.; Guldi, D. M.; Maldonado, S.; Stevenson, K. J. Synthesis and Photophysics of a Porphyrin–fullerene Dyad Assembled through Watson–Crick Hydrogen Bonding. *Chem. Commun.* **2005**, 1892–1894.
- (38) de Rege, P.; Williams, S.; Therien, M. Direct Evaluation of Electronic Coupling Mediated by Hydrogen Bonds: Implications for Biological Electron Transfer. *Science* **1995**, *269*, 1409–1413.
- (39) D'Souza, F.; Gadde, S.; Islam, D.-M. S.; Pang, S.-C.; Schumacher, A. L.; Zandler, M. E.; Horie, R.; Araki, Y.; Ito, O. Photoinduced Electron Transfer in a Watson–Crick Base-Paired, 2-Aminopurine:uracil-C60 Hydrogen Bonding Conjugate. *Chem. Commun.* **2007**, *60*, 480–482.
- (40) Sessler, J. L.; Wang, B.; Harriman, A. Long-Range Photoinduced Electron Transfer in an Associated but Non-Covalently Linked Photosynthetic Model System. *J. Am. Chem. Soc.* **1993**, *115*, 10418–10419.
- (41) D'Souza, F.; Ito, O. Photoinduced Electron Transfer in Supramolecular Systems of Fullerenes Functionalized with Ligands Capable of Binding to Zinc Porphyrins and Zinc Phthalocyanines. *Coord. Chem. Rev.* **2005**, *249*, 1410–1422.
- (42) Chitta, R.; D'Souza, F. Self-Assembled Tetrapyrrole–fullerene and Tetrapyrrole–carbon Nanotube Donor–acceptor
-

-
- Hybrids for Light Induced Electron Transfer Applications. *J. Mater. Chem.* **2008**, *18*, 1440–1471.
- (43) Chitta, R.; Sandanayaka, A. S. D.; Schumacher, A. L.; D'Souza, L.; Araki, Y.; Ito, O.; D'Souza, F. Donor–Acceptor Nanohybrids of Zinc Naphthalocyanine or Zinc Porphyrin Noncovalently Linked to Single-Wall Carbon Nanotubes for Photoinduced Electron Transfer. *J. Phys. Chem. C* **2007**, *111*, 6947–6955.
- (44) D'Souza, F.; Chitta, R.; Sandanayaka, A. S. D.; Subbaiyan, N. K.; D'Souza, L.; Araki, Y.; Ito, O. Self-Assembled Single-Walled Carbon Nanotube:Zinc–Porphyrin Hybrids through Ammonium Ion–Crown Ether Interaction: Construction and Electron Transfer. *Chem. - A Eur. J.* **2007**, *13*, 8277–8284.
- (45) *Fullerenes and Related Structures*; A. Hirsch, Ed.; Springer: Berlin, 1999; Vol. 199.
- (46) Prato, M.; Maggini, M. Fullero-pyrrolidines: A Family of Full-Fledged Fullerene Derivatives. *Acc. Chem. Res.* **1998**, *31*, 519–526.
- (47) Tkachenko, N. V.; Lemmetyinen, H.; Sonoda, J.; Ohkubo, K.; Sato, T.; Imahori, H.; Fukuzumi, S. Ultrafast Photodynamics of Exciplex Formation and Photoinduced Electron Transfer in Porphyrin–Fullerene Dyads Linked at Close Proximity. *J. Phys. Chem. A* **2003**, *107*, 8834–8844.
- (48) Kesti, T. J.; Tkachenko, N. V.; Vehmanen, V.; Yamada, H.; Imahori, H.; Fukuzumi, S.; Lemmetyinen, H. Exciplex Intermediates in Photoinduced Electron Transfer of Porphyrin–Fullerene Dyads. *J. Am. Chem. Soc.* **2002**, *124*, 8067–8077.
- (49) Karousis, N.; Sandanayaka, A. S. D.; Hasobe, T.; Economopoulos, S. P.; Sarantopoulou, E.; Tagmatarchis, N. Graphene Oxide with Covalently Linked Porphyrin Antennae: Synthesis, Characterization and Photophysical Properties. *J. Mater. Chem.* **2011**, *21*, 109–117.
-

-
- (50) Bala Murali Krishna, M.; Venkatramaiah, N.; Venkatesan, R.; Narayana Rao, D. Synthesis and Structural, Spectroscopic and Nonlinear Optical Measurements of Graphene Oxide and Its Composites with Metal and Metal Free Porphyrins. *J. Mater. Chem.* **2012**, *22*, 3059–3068.
- (51) Zhao, H.; Zhu, Y.; Chen, C.; He, L.; Zheng, J. Synthesis, Characterization, and Photophysical Properties of Covalent-Linked Ferrocene–porphyrin–single-Walled Carbon Nanotube Triad Hybrid. *Carbon* **2012**, *50*, 4894–4902.
- (52) Giordani, S.; Colomer, J.-F.; Cattaruzza, F.; Alfonsi, J.; Meneghetti, M.; Prato, M.; Bonifazi, D. Multifunctional Hybrid Materials Composed of [60]fullerene-Based Functionalized-Single-Walled Carbon Nanotubes. *Carbon* **2009**, *47*, 578–588.
- (53) Maeda, H. Anion-Responsive Supramolecular Gels. *Chem. - A Eur. J.* **2008**, *14*, 11274–11282.
- (54) Lloyd, G. O.; Steed, J. W. Anion-Tuning of Supramolecular Gel Properties. *Nat. Chem.* **2009**, *1*, 437–442.
- (55) Banerjee, S.; Das, R. K.; Maitra, U. Supramolecular Gels “in Action.” *J. Mater. Chem.* **2009**, *19*, 6649.
- (56) Yu, G.; Yan, X.; Han, C.; Huang, F. Characterization of Supramolecular Gels. *Chem. Soc. Rev.* **2013**, *42*, 6697–6722.
- (57) Hirst, A. R.; Escuder, B.; Miravet, J. F.; Smith, D. K. High-Tech Applications of Self-Assembling Supramolecular Nanostructured Gel-Phase Materials: From Regenerative Medicine to Electronic Devices. *Angew. Chem. Int. Ed.* **2008**, *47*, 8002–8018.
- (58) Kitamura, T.; Nakaso, S.; Mizoshita, N.; Tochigi, Y.; Shimomura, T.; Moriyama, M.; Ito, K.; Kato, T. Electroactive Supramolecular Self-Assembled Fibers Comprised of Doped Tetrathiafulvalene-Based Gelators. *J. Am. Chem. Soc.* **2005**, *127*, 14769–14775.
- (59) Kato, T.; Hirai, Y.; Nakaso, S.; Moriyama, M. Liquid-
-

- Crystalline Physical Gels. *Chem. Soc. Rev.* **2007**, *36*, 1857–1867.
- (60) Mukhopadhyay, P.; Iwashita, Y.; Shirakawa, M.; Kawano, S.; Fujita, N.; Shinkai, S. Spontaneous Colorimetric Sensing of the Positional Isomers of Dihydroxynaphthalene in a 1D Organogel Matrix. *Angew. Chem. Int. Ed.* **2006**, *45*, 1592–1595.
- (61) Cravotto, G.; Cintas, P. Molecular Self-Assembly and Patterning Induced by Sound Waves. The Case of Gelation. *Chem. Soc. Rev.* **2009**, *38*, 2684.
- (62) Stupp, S. I. Self-Assembly and Biomaterials. *Nano Lett.* **2010**, *10*, 4783–4786.
- (63) Sangeetha, N. M.; Maitra, U. Supramolecular Gels: Functions and Uses. *Chem. Soc. Rev.* **2005**, *34*, 821.
- (64) van Esch, J. H.; Feringa, B. L. New Functional Materials Based on Self-Assembling Organogels: From Serendipity towards Design. *Angew. Chem. Int. Ed.* **2000**, *39*, 2263–2266.
- (65) Estroff, L. A.; Hamilton, A. D. Water Gelation by Small Organic Molecules. *Chem. Rev.* **2004**, *104*, 1201–1218.
- (66) Terech, P.; Weiss, R. G. Low Molecular Mass Gelators of Organic Liquids and the Properties of Their Gels. *Chem. Rev.* **1997**, *97*, 3133–3160.
- (67) Welton, T. Room-Temperature Ionic Liquids. Solvents for Synthesis and Catalysis. *Chem. Rev.* **1999**, *99*, 2071–2084.
- (68) Le Bideau, J.; Viau, L.; Vioux, A. Ionogels, Ionic Liquid Based Hybrid Materials. *Chem Soc Rev* **2011**, *40*, 907–925.
- (69) Buerkle, L. E.; Rowan, S. J. Supramolecular Gels Formed from Multi-Component Low Molecular Weight Species. *Chem. Soc. Rev.* **2012**, *41*, 6089–6102.
- (70) Delbecq, F. Supramolecular Gels from Lipopeptide Gelators: Template Improvement and Strategies for the in-Situ Preparation of Inorganic Nanomaterials and for the
-

-
- Dispersion of Carbon Nanomaterials. *Adv. Colloid Interface Sci.* **2014**, *209*, 98–108.
- (71) Fukushima, T.; Aida, T. Ionic Liquids for Soft Functional Materials with Carbon Nanotubes. *Chem. - A Eur. J.* **2007**, *13*, 5048–5058.
- (72) Fukushima, T. Molecular Ordering of Organic Molten Salts Triggered by Single-Walled Carbon Nanotubes. *Science* **2003**, *300*, 2072–2074.
- (73) Katakabe, T.; Kaneko, T.; Watanabe, M.; Fukushima, T.; Aida, T. Electric Double-Layer Capacitors Using “Bucky Gels” Consisting of an Ionic Liquid and Carbon Nanotubes. *J. Electrochem. Soc.* **2005**, *152*, A1913–A1916.
- (74) Fukushima, T.; Asaka, K.; Kosaka, A.; Aida, T. Fully Plastic Actuator through Layer-by-Layer Casting with Ionic-Liquid-Based Bucky Gel. *Angew. Chem. Int. Ed.* **2005**, *44*, 2410–2413.
- (75) Cayuela, A.; Kennedy, S. R.; Soriano, M. L.; Jones, C. D.; Valcárcel, M.; Steed, J. W. Fluorescent Carbon Dot-molecular Salt Hydrogels. *Chem. Sci.* **2015**, *6*, 6139–6146.
- (76) Bhattacharya, S.; Samanta, S. K. Soft-Nanocomposites of Nanoparticles and Nanocarbons with Supramolecular and Polymer Gels and Their Applications. *Chem. Rev.* **2016**, *116*, 11967–12028.
- (77) Quaranta, A.; Carturan, S.; Campagnaro, A.; Dalla Palma, M.; Giarola, M.; Daldosso, N.; Maggioni, G.; Mariotto, G. Highly Fluorescent Xerogels with Entrapped Carbon Dots for Organic Scintillators. *Thin Solid Films* **2014**, *553*, 188–192.
- (78) Dolai, S.; Bhunia, S. K.; Jelinek, R. Carbon-Dot-Aerogel Sensor for Aromatic Volatile Organic Compounds. *Sensors Actuators B Chem.* **2017**, *241*, 607–613.
- (79) Cayuela, A.; Soriano, M. L.; Kennedy, S. R.; Steed, J. W.; Valcárcel, M. Fluorescent Carbon Quantum Dot Hydrogels for Direct Determination of Silver Ions. *Talanta* **2016**, *151*,
-

100–105.

- (80) Daly, D.; Al-Sabi, A.; Kinsella, G. K.; Nolan, K.; Dolly, J. O. Porphyrin Derivatives as Potent and Selective Blockers of Neuronal Kv1 Channels. *Chem. Commun.* **2015**, *51*, 1066–1069.
- (81) Rudolf, M.; Feng, L.; Slanina, Z.; Wang, W.; Nagase, S.; Akasaka, T.; Guldi, D. M. Strong Electronic Coupling and Electron Transfer in a Ce2@Ih-C80-H2P Electron Donor Acceptor Conjugate. *Nanoscale* **2016**, *8*, 13257–13262.
- (82) Huang, X.; Nakanishi, K.; Berova, N. Porphyrins and Metalloporphyrins: Versatile Circular Dichroic Reporter Groups for Structural Studies. *Chirality* **2000**, *12*, 237–255.
- (83) Rizzo, C.; D’Anna, F.; Noto, R.; Zhang, M.; Weiss, R. G. Insights into the Formation and Structures of Molecular Gels by Diimidazolium Salt Gelators in Ionic Liquids or “Normal” Solvents. *Chem. - A Eur. J.* **2016**, *22*, 11269–11282.
- (84) Weiss, R.; Terech, P. Molecular Gels. In: Raghavan, S.; Cipriano, B., Eds.; Eds. Springer: Dordrecht, 2006; p. 241.
- (85) Tian, Y.; Zhang, L.; Duan, P.; Liu, F.; Zhang, B.; Liu, C.; Liu, M. Fabrication of Organogels Composed from Carbon Nanotubes through a Supramolecular Approach. *New J. Chem.* **2010**, *34*, 2847.
- (86) Crowhurst, L.; Mawdsley, P. R.; Perez-Arlandis, J. M.; Salter, P. A.; Welton, T. Solvent–solute Interactions in Ionic Liquids. *Phys. Chem. Chem. Phys.* **2003**, *5*, 2790–2794.
- (87) Samanta, S. K.; Pal, A.; Bhattacharya, S.; Rao, C. N. R. Carbon Nanotube Reinforced Supramolecular Gels with Electrically Conducting, Viscoelastic and near-Infrared Sensitive Properties. *J. Mater. Chem.* **2010**, *20*, 6881–6890.
- (88) Adhikari, B.; Banerjee, A. Short Peptide Based Hydrogels: Incorporation of Graphene into the Hydrogel. *Soft Matter* **2011**, *7*, 9259–9266.
-

- (89) Zhang, Y.; Wang, H.; Wu, Y.; Li, M. Effects of Carbon Nanomaterials on the Aggregation of a Bi-Oxadiazole Derivative (BOXD-T8) in DMF and Its Gel Properties. *New J. Chem.* **2014**, *38*, 4823–4829.
- (90) Mallia, V. A.; George, M.; Blair, D. L.; Weiss, R. G. Robust Organogels from Nitrogen-Containing Derivatives of (R)-12-Hydroxystearic Acid as Gelators: Comparisons with Gels from Stearic Acid Derivatives. *Langmuir* **2009**, *25*, 8615–8625.
- (91) Terech, P.; Pasquier, D.; Bordas, V.; Rossat, C. Rheological Properties and Structural Correlations in Molecular Organogels. *Langmuir* **2000**, *16*, 4485–4494.
- (92) Castro, H. P. S.; Souza, V. S.; Scholten, J. D.; Dias, J. H.; Fernandes, J. A.; Rodembusch, F. S.; dos Reis, R.; Dupont, J.; Teixeira, S. R.; Correia, R. R. B. Synthesis and Characterisation of Fluorescent Carbon Nanodots Produced in Ionic Liquids by Laser Ablation. *Chem. - A Eur. J.* **2016**, *22*, 138–143.
- (93) Peveler, W. J.; Bear, J. C.; Southern, P.; Parkin, I. P. Organic–inorganic Hybrid Materials: Nanoparticle Containing Organogels with Myriad Applications. *Chem. Commun.* **2014**, *50*, 14418–14420.
- (94) Zou, J.; He, X.; Fan, J.; Raymond, J. E.; Wooley, K. L. Supramolecularly Knitted Tethered Oligopeptide/Single-Walled Carbon Nanotube Organogels. *Chem. - A Eur. J.* **2014**, *20*, 8842–8847.
- (95) Anglister, J.; Steinberg, I. Z. Resonance Rayleigh Scattering of Cyanine Dyes in Solution. *J. Chem. Phys.* **1983**, *78*, 5358–5368.
- (96) Pasternack, R.; Collings, P. Resonance Light Scattering: A New Technique for Studying Chromophore Aggregation. *Science* **1995**, *269*, 935–939.
- (97) Chong, Y.; Ge, C.; Fang, G.; Tian, X.; Ma, X.; Wen, T.;
-

-
- Wamer, W. G.; Chen, C.; Chai, Z.; Yin, J.-J. Crossover between Anti- and Pro-Oxidant Activities of Graphene Quantum Dots in the Absence or Presence of Light. *ACS Nano* **2016**, *10*, 8690–8699.
- (98) Cavicchioli, A.; de Faria, D. L. A.; Neves, C. A.; Antunes, M. T. Automatic Devices for Monitoring Environmentally Induced Auto-Oxidative Degradation of Artistic Materials in Conservation Sites. *Sensors Actuators B Chem.* **2008**, *131*, 462–469.
- (99) Dietemann, P.; Higgitt, C.; Kälın, M.; Edelmann, M. J.; Knochenmuss, R.; Zenobi, R. Aging and Yellowing of Triterpenoid Resin Varnishes—Influence of Aging Conditions and Resin Composition. *J. Cult. Herit.* **2009**, *10*, 30–40.
- (100) Wu, S.; Weng, P.; Tang, Z.; Guo, B. Sustainable Carbon Nanodots with Tunable Radical Scavenging Activity for Elastomers. *ACS Sustain. Chem. Eng.* **2016**, *4*, 247–254.
- (101) Dintcheva, N. T.; Arrigo, R.; Teresi, R.; Megna, B.; Gambarotti, C.; Marullo, S.; D’Anna, F. Tunable Radical Scavenging Activity of Carbon Nanotubes through Sonication. *Carbon* **2016**, *107*, 240–247.
- (102) Shieh, Y.-T.; Wang, W.-W. Radical Scavenging Efficiencies of Modified and Microwave-Treated Multiwalled Carbon Nanotubes. *Carbon* **2014**, *79*, 354–362.
- (103) Zhao, S.; Lan, M.; Zhu, X.; Xue, H.; Ng, T.-W.; Meng, X.; Lee, C.-S.; Wang, P.; Zhang, W. Green Synthesis of Bifunctional Fluorescent Carbon Dots from Garlic for Cellular Imaging and Free Radical Scavenging. *ACS Appl. Mater. Interfaces* **2015**, *7*, 17054–17060.
- (104) Zhang, X.; Li, Y.; Qi, D.; Jiang, J.; Yan, X.; Bian, Y. Linkage Dependence of Intramolecular Fluorescence Quenching Process in Porphyrin-Appended Mixed (Phthalocyaninato)(Porphyrinato) Yttrium(III) Double-Decker Complexes. *J. Phys. Chem. B* **2010**, *114*, 13143–13151
-

5 Rationally Designed Carbon Nanodots

In this chapter, the rational design of carbon nanodots (CNDs) with tailored properties is discussed. Firstly, a general overview on multicolored, optically active and electroactive materials is presented. Then, the synthesis and characterization of novel CNDs using properly designed functional units as precursors are presented. One-pot, bottom-up, cost-effective and time-saving synthetic methods, built on commercially available or easy to synthesize organic building blocks, were employed.

The first two parts deal with the preparation of CNDs with desired optical properties, by incorporating fluorophores in the nanostructures for the creation of nanodots with novel features. Naphthalene dianhydride derivatives (NDAs) and boron-dipyrromethenes (BODIPYs) have been selected as candidates. Through the use of NDA as precursors, CNDs with emission from blue-white, to pure white and further to red-white are described, resulting in tunable white emission, ranging from cool to warm colors, which could find applications according to requirements. On the other hand, preliminary studies on the BODIPY-based CNDs effect on the natural killer cell maturation process and activation are presented, showing their high potential in bio-related applications.

Then, the preparation of inherently chiral CNDs by using chiral small organic molecules as precursors is described, and their role as template for the induction of preferential chirality to porphyrin aggregates is investigated.

Finally, the use of small oxidants precursors as dopants for the tuning of the CNDs redox properties is presented.

The work presented in this chapter has been done in a collaborative work with *Dr. Luka Dorđević* (University of Trieste, Italy) that played

a critical role in the discussion of the experimental design, projects direction and results. The work presented in Sections 3 and 5 has been done in a collaborative work with *Mr. Francesco Rigodanza* (University of Trieste, Italy) that carried out part of the nanodots characterization. *Dr. Blanca Arnaiz* (CIC biomaGUNE, San Sebastián, Spain) acquired the image with the confocal microscope reported in Section 3. The project on the natural killer cells of Section 3 has been done in collaboration with *Prof. Alessandro Moretta* (University of Genova, Italy), with the aid of *Prof. Simona Sivori* and *Dr. Simona Carlomagno*. The project on porphyrin chiral supramolecular assembly of Section 4 has been done thanks to a collaboration, that started with my stay in Catania, with *Prof. Roberto Purrello* (University of Catania, Italy), with the aid of *Dr. Alessandro D'Urso*.

Part of the work presented in this chapter has been published as “Rationally Designed Carbon Nanodots towards Pure White-Light Emission” in *Angewandte Chemie Int. Ed.* **2017**, *56*, 4179-4173. Other parts of this chapter have been used to prepare the following manuscripts: “Customizing energy levels in carbon nanodots through bottom-up quinone-doped synthesis”; “BODIPY-based carbon nanodots promote natural killer cells activation and maturation”; “Synthesis of inherently chiral carbon nanodots and their use as template for chiral porphyrin aggregates”.

5.1 Introduction

5.1.1 Multicolored emission

Carbon nanodots are attractive light-emitting materials with a potential to overcome organic dyes and inorganic quantum dots (see *Chapter 1*).

Photostability is a key property for fluorescent materials and represents one of the major advantage of CNDs.¹⁻⁴ As shown in **Figure 5.1**, which compares the photostability of the most commonly used fluorescent probes,³ CNDs preserve more than 90% of the initial intensity under *c.a.* 60 minutes of excitation and are more stable than dye-doped silica or polymer nanoparticles.^{5,6} Moreover, the fluorescence of fluorescein isothiocyanate (FITC), which is one of the most widely used fluorescent dyes, is quickly quenched within 5 minutes under excitation due to severe photobleaching. The inorganic quantum dots CdTe QDs⁷ is more photostable, retaining more than 30% of the original photoluminescence intensity after 20 minutes of excitation.

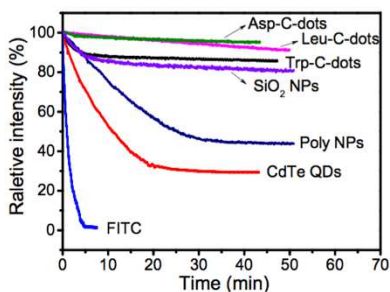


Figure 5.1 Photostability comparison of fluorescein isothiocyanate (FITC), CdTe QDs, polymer nanoparticles (Poly NPs), dye-doped silica nanoparticles (SiO₂ NPs) and CNDs prepared from different amino acids as precursors.³

However, the development of facile and efficient approaches for controllable syntheses of high-quality multicolored CNDs on a large scale remains challenging.

The fluorescence quantum yields of CNDs have been increasingly improved along the way, but the relatively low value (usually less than 20%) for wavelength emissions beyond the blue region has so far hindered most of their applications.⁸ For instance, through the hydrothermal treatment of a polythiophene derivative as the carbon source, red emissive CNDs with quantum yield of 2.3% in water were reported (**Figure 5.2**, left).⁹ Moreover, as showed in **Figure 5.2**, right, CNDs having green, blue and red emission were prepared under solvothermal conditions starting from the three isomers *o*-phenylenediamine, *m*-phenylenediamine, *p*-phenylenediamine, as precursors. The fluorescence quantum yields of the green, blue and red CNDs, were calculated as 10.4, 4.5 and 20.6%, respectively, in ethanol solution. Only the sizes and nitrogen contents of the three CNDs were distinctly different, and although they were believed responsible for the different optical features, their mutual relation was not clearly understood.¹⁰

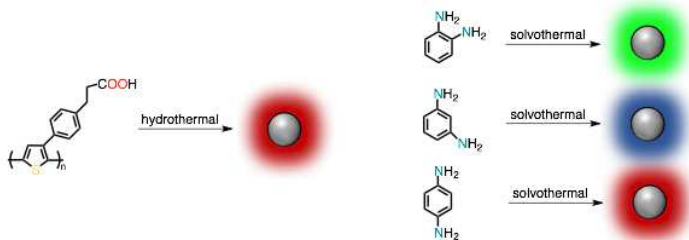


Figure 5.2 CNDs prepared starting from a polythiophene derivative (on the left, red emissive) and from phenylenediamine isomers (on the right, green, blue and red emissive).

Moreover, it has been reported that a higher degree of oxidation on the CNDs surfaces implies more surface defects and introduces more emission sites, resulting in red-shifted emission (**Figure 5.3**).^{11,12} Additionally, surface epoxide or hydroxyl groups were found predominantly responsible for the fluorescence red-shift.¹³

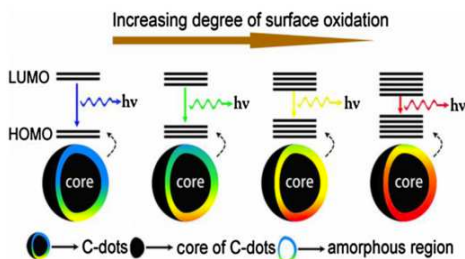


Figure 5.3 Tunable CNDs fluorescence with different degrees of oxidation.¹¹

Therefore, although some progresses regarding the understanding of the fluorescence mechanisms of CNDs have been achieved, it is still not clear how the fluorescence is influenced by the numerous factors, such as defects, functional groups, and doping.

Despite the diverse structures of CNDs prepared from different approaches and with different precursors, they often share some similar optical properties in terms of absorption and fluorescence characteristics.

Currently, one of the most important challenges to address this issue is to develop an efficient method for large-scale production of high-quality CNDs with a well-defined structure in order to sort out their fluorescence emission.

5.1.1.1 White-light emission

One of the dream-goals in photonics is the production of white-light emission. In order to observe colors in the visible region, we require

illumination of white-light, which is, in general, considered as the optimized composition of the three primary colors *i.e.* red (R), green (G) and blue (B) (**Figure 5.4a,b**).

In 1931, the Commission Internationale d'Éclairage (CIE) set up a standard colorimetric system, referred to as CIE 1931, which is the most widely used colorimetric standard so far.¹⁴ In a CIE plot, all the colors generated from the visible spectra are represented by two coordinates, x and y , which are called color coordinates. According to CIE regulation, the color coordinates for equal energy point of white-light are (0.33, 0.33) (**Figure 5.4c**).

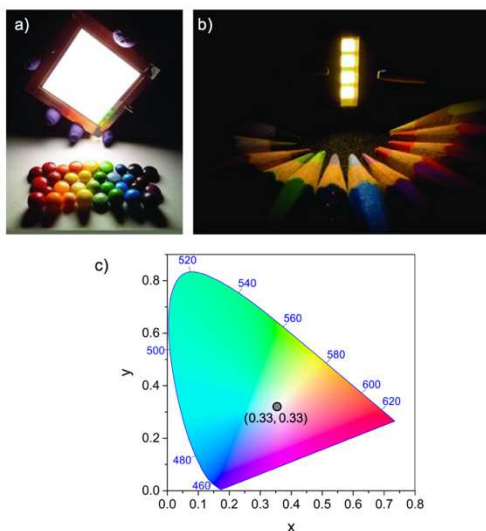


Figure 5.4 a,b) Photographs of WOLEDs illuminating colored materials,^{15,16} c) a typical 1931 CIE plot showing the coordinates of pure white-light (0.33, 0.33).

Among artificial ways to generate light, the white organic light-emitting diode (WOLED) technology is considered the next generation of solid-state light source. WOLEDs offer a range of

attractive characteristics (**Figure 5.5a**), including being conceptually different from other light sources, resulting in glare-free and homogenous illumination.¹⁷

Ideally, a WOLED should emit a continuous spectrum over the whole visible range. In order to mimic the spectral distribution of natural sunlight, a combination of luminophores is usually employed to cover the visible spectrum. The overall emission, which combines red, green and blue luminophores in the right composition, yields white-light (**Figure 5.5b**).

Typically employed fluorescent low-molecular-weight emitters used in WOLEDs can be found in **Figure 5.5c**, which include rare earth metals complexes of iridium.

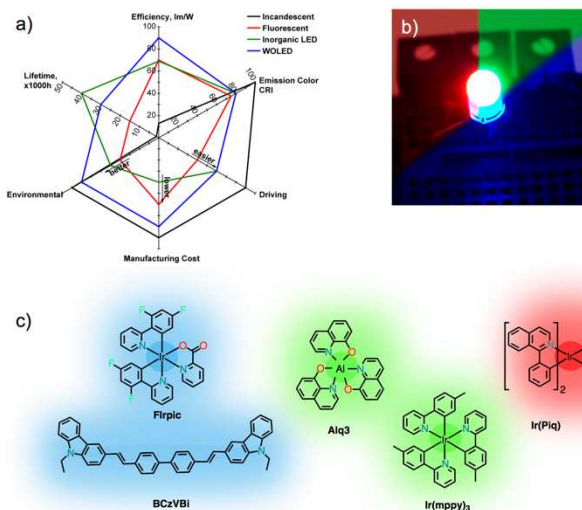


Figure 5.5 a) Semiquantitative comparison of the key performance parameters of WOLEDs relative to incandescent lamps, fluorescent tubes, and inorganic white LEDs;¹⁷ b) photograph of a RGB LED;¹⁸ c) typical fluorescent low-molecular-weight emitters used in WOLEDs with the corresponding color emission.

The different luminophores can be combined in different ways, *i.e.*, whether they are blended in a single layer, separated in different layers of the same OLED, or contained in several formally independent devices each of which emits light of a different color (**Figure 5.6**).¹⁷

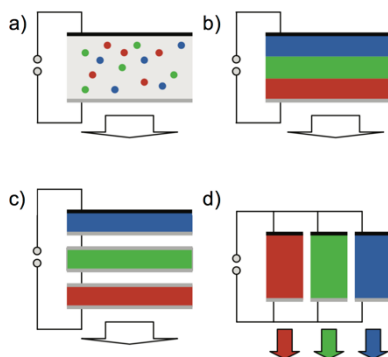


Figure 5.6 Approaches to generate WOLEDs: a) blending luminophores emitting different colors into a single layer, b) multi-layer concept using a single device stack with several layers emitting in different regions of the spectrum on top of each other, c) tandem approach using multiple monochrome OLED stacks connected by charge-generation layers, and d) striped approach generating the white emission by adjacent monochrome OLEDs. Reflective electrodes are illustrated in black; semi-transparent electrodes are shown in gray.¹⁷

Blending different luminophores in a single layer is an attractive approach since it's generally considered to offer simpler and low cost device fabrication (**Figure 5.6a**). If all components required to generate white-light are mixed into one material, WOLEDs can be fabricated with a single active layer that is sandwiched between two electrodes. This reduces the number of processing steps for device fabrication and allows straightforward deposition of the active layer

using conventional solution- or evaporation-based processes. However, morphology of the emitting layer and careful control of components ratio play crucial roles in the management of energy transfer phenomena and thus in the device optimization.

White-light can be also produced from device architectures where individual emitting layers are combined in a stacked architecture, and in some cases physically separated using barrier films in order to prevent interlayer mixing, undesired exciton migration and energy transfer phenomena (**Figure 5.6b**).

The general challenge in designing multilayer architectures is that the simultaneous emission from the stacked layers required that the thickness of each individual film and the dopant concentrations need to be properly adjusted on the basis of the luminescence spectra and efficiency of the single emitters. As a major drawback, the multiplicity of layers adds complexity to the device manufacture and operating voltages are superior to those required for WOLEDs based on a single emitting film, due to the increased overall thickness of the multilayer architectures.

Other approaches to generate white-light include tandem and striped WOLEDs (**Figure 5.6c,d**). These methods imply that a set of complete OLED stacks, emitting in different regions of the spectrum, are positioned in close proximity. Despite they hold some advantages, such as an easy adjustment of the color emitted by changing the ratio of red, green, and blue emission, the fabrication process is more elaborate and examples of these devices are rare.

Much effort has been devoted to preparing organic materials, aiming at low cost, easier fine-tuning and solution processability, low toxicity and better flexibility for device fabrication. However, increasing the number of synthetic steps and blending of the luminophores increase the cost and complexity of the system.

On the other hand, obtain panchromatic white-light emission from a single molecule system is a highly challenging task. Indeed, according to the Kasha's rule,^{19,20} fluorophores always tend to attain the lowest possible vibrational states resulting, generally, in monochromatic emission (**Figure 5.7**). The presence of blue, green and red fluorophores in a single molecular backbone often results in complex intramolecular FRET (Föster resonance energy transfer) or TBET (through-bond energy transfer) processes leading to enhanced emission from the red-emitting fluorescent units which act as the energy acceptors (**Figure 5.7**).^{19–25} Moreover, controlling the relative intensity ratios of the individual emission bands is almost unmanageable.²⁶

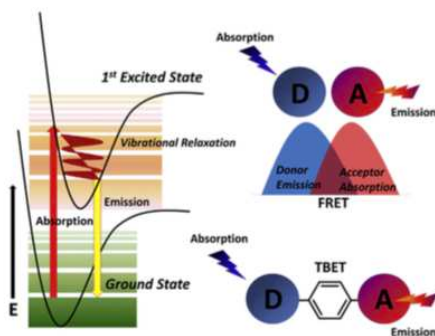


Figure 5.7 Schematic representation of Kasha's rule (left), FRET in separated dye pairs and TBET in conjugated fluorescent dyads (right).²⁶

These are possibly the reason for somewhat scattered literature reports of white-light emissive molecules.

Interestingly, a few strategies have been reported in the past few years to obtain simultaneous RGB luminescence from single molecular species. The rare examples reported so far include, for instance, *N*-aryl-2,3-naphthalimides with low symmetry (**Figure 5.8**).^{23,27} These dyes show efficient panchromatic emission, in which the relative

intensities of the individual emission bands depend on the energy of excitation that, in turn, controls the relative populations of the different excited states. Compound **2** exhibits a three-color emission over the entire visible region (**Figure 5.8**). When excited at 423 nm dye **2** displays three-color peaks, *i.e.* blue, green and orange emission (450-700) with relatively balanced emissions (inset **Figure 5.8**: middle photographs of white-light emission). Upon shorter wavelength excitation (390 nm), dye **2** displays intense blue color emission whereas at longer wavelength excitation (450 nm) it displays intense green color emission.

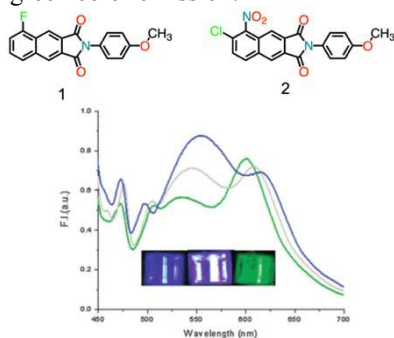


Figure 5.8 Structure of dyes **1** and **2**, and emission spectra of 20 mM compound **2** in water with 0.10% DMSO at different excitation wavelengths (390 nm, 423 nm and 450 nm, corresponding to blue, white and green photographs, respectively).^{23,27}

Other examples include halochromic^{28–31} or ES IPT (excited-state-intramolecular-proton-transfer)^{32,33} based white-light emitters. The former one is built up on fluorophores with large spectral widths and significantly different emission features in neutral and protonated (or deprotonated) forms, which can show full color RGB luminescence at precisely optimized conditions. In the latter case, the RGB luminescence is attained thanks to the absence of intermolecular and intramolecular energy transfer processes. Moreover, apart from intramolecular origin, RGB luminescence can also arise from

intermolecular interactions or complex formations, *i.e.* excimers and exciplexes.^{32,34,35}

Few examples of white emission from self-assembled³⁶⁻⁴¹ and polymeric systems⁴²⁻⁴⁵ have been also reported, however, especially in the latter case, complex FRET and TBET processes usually occur.

Other strategies imply composite systems or doping. White-emitting materials were obtained upon doping of organogels,^{46,47} by using luminescent organic liquids,⁴⁸ or through organic-inorganic hybrids, such as silica nanoparticles with organic dyes on their surface or inside their core.⁴⁹⁻⁵¹

In this context, fluorescent organic nanoparticles have attracted a lot of attention in the last years.⁵²⁻⁵⁸

One of the first examples of white-light emissive fluorescent organic nanoparticles was reported by Würthner and co-workers (**Figure 5.9**).⁵² In situ polymerization on vesicles with bilayer membrane structures was used to prepare nanocapsules that are stable in all aqueous pH ranges. An in-situ synthesis of perylene bisimide (PBI)-based nanocapsules in a water solution of the donor (compound **33**) lead to the incorporation of pyrene-based energy donors inside the capsules. While under acidic pH the bispyrene derivative showed blue emission arising from its unlocked state (which is favorable due to electrostatic repulsions), it was observed that in basic pH the locked conformation is preferred, resulting in π - π stacking interactions between the pyrene moieties and consequent green emission from the excimers. The excimer emission band overlaps considerably with the PBIs absorption profiles and thus close range FRET can only occur from the locked conformation rather than the unlocked blue emissive states. At pH \sim 9.0 the vesicles were found to emit white-light (with CIE coordinates of (0.32, 0.31)) from a balance of blue, green and red emissions.

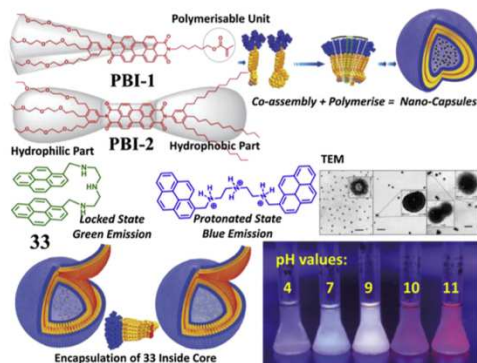


Figure 5.9 Schematic representation of the white-light-emitting nanocapsules preparation as followed by Würthner *et al.*. Co-assembly of PBI-1 and PBI-2 followed by polymerization of PBI-1, resulted in the formation of the bilayer nanocapsules with water encapsulation inside the core. The pyrene derivative **33** can be encapsulated inside the core and can act as a FRET energy donor forming excimers. The excimer formation process is pH dependent as at lower pH, repulsions between cationic ammonium groups resulted in an unlocked conformation of **33**. At pH 9.0 the nanostructures showed white-light emission with CIE coordinates (0.32, 0.31).⁵²

In light of the above examples and discussion, it is clear that achieving precise control over the structure and/or energy transfer processes towards white emission can be tedious and time consuming.

In order to overcome some of the issues in producing white-light-emitting materials, a few examples of carbon and graphene quantum- and nano-dots have been so far proposed,^{59–62} by blending with other chromophores or different dots,^{10,63–65} or by energy transfer that originates from PVK (poly(*N*-vinylcarbazole) as emissive layer) to the carbon quantum dots.⁶⁶

For instance, a white-light-emitting film has been prepared by incorporating carbon dots and lanthanide complexes (Eu(DBM)₃ and Tb(DBM)₃ (DBM: dibenzoylmethide)) into poly(methyl

methacrylate) (PMMA) matrix (**Figure 5.10**). The dots were functionalized by copolymerization with methacrylate to improve the compatibility with PMMA. The lanthanide complexes were dispersed in the matrix due to the possible interaction between the lanthanide ions and the oxygen atoms in the PMMA chains. White-light emission with CIE coordinates of (0.31, 0.32) could be observed by carefully adjusting the ratio of the components and excitation wavelengths.⁶³

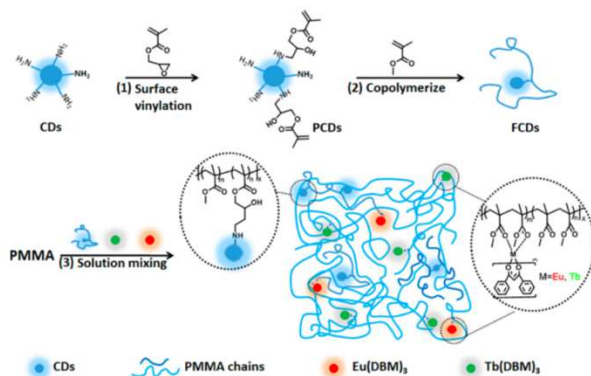


Figure 5.10 Schematic representation of the white-light-emitting film preparation by incorporating carbon dots and lanthanide complexes into PMMA matrix.⁶³

Alternatively, white-light emission with CIE coordinates of (0.33, 0.34) was obtained by mixing green- (*o*-CDs), blue- (*m*-CDs), and red- (*p*-CDs) emitting dots in a poly(vinyl alcohol) (PVA) film with appropriate ratios (2:4:1 (weight)) (**Figure 5.11**).¹⁰

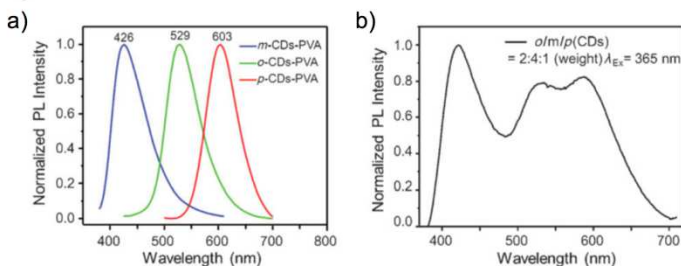


Figure 5.11 Normalized PL spectra upon excitation at 365 nm of a) *m*-CDs, *o*-CDs, and *p*-CDs PVA composite films and b) a white-light emission from a PVA composite film by mixing *m*-CDs, *o*-CDs, and *p*-CDs.¹⁰

5.1.2 Tunable electrochemistry

CNDs could play an important role in applications such as energy conversion and photocatalysis. Recently CNDs have been successfully employed as primary photocatalysts for hydrogen evolution and carbon dioxide reduction.^{67,68} Mastering control over the electrochemical properties of CNDs is essential in order to produce high-quality nanomaterials with desired energy levels for such applications. However, the control of CNDs electrochemical properties remains still an elusive task and no efforts have been yet accomplished in tuning the energy levels of CNDs.

This effort acquires even more importance if we compare how the control of redox activity is currently achieved in other type of nanoparticles. For example, electrochemical properties of semiconductor quantum dots (QDs) or graphene quantum dots (GQDs) can be tuned by preparing hybrids through the (non)covalent attachment of electroactive molecular species.

The chemical functionalization of the QDs surface is a powerful and versatile strategy to tune their electronic structure.⁶⁹

Recently, the tuning of the energy levels and gaps in GQDs have been achieved through their functionalization with different functional groups, by the nucleophilic substitution and dehydration of the amines on a precursor with the epoxide bridges and the hydroxyls on oxidized GQDs (*o*-GQDs) (**Figure 5.12**).⁷⁰ All the functionalized GQDs showed almost identical size and shape, and the photoluminescence and electronic tunability was attributed to their different surface functionalities. The change in the HOMO/LUMO levels of GQDs upon functionalization is depicted in **Figure 5.12**. The energy levels have been tuned as a consequence of the strength of the orbital interactions. HOMO-LUMO gap was varied from 1.30 to 2.23 eV. GQDs functionalized with primary (NH₂-GQDs) or dimethyl amines (Me₂N-GQDs) showed the HOMO orbital at higher energy level due to strong orbital interactions. On the other hand, GQDs functionalized with *o*-phenylenediamine (OPD-GQDs), diamionaphthalene (DAN-GQDs), azo (Azo-GQDs), or *p*-methyl red (*p*MR- GQDs) had the LUMO orbital at lower energy level. The tuned energy gap resulted also in the red-shift of the photoluminescence band maxima and UV absorption edges with narrowing of the gap, and the photoluminescence quantum yields were found to be $\approx 9.7\%$, $\approx 18.2\%$, $\approx 6.9\%$, and $\approx 15.4\%$, respectively, for Azo-GQDs, NH₂-GQDs, OPD-GQDs, and DAN-GQDs.

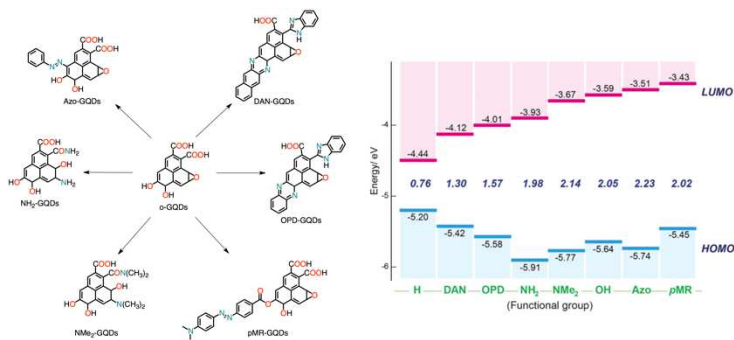


Figure 5.12 Functionalized GQDs and measured energy level diagram.⁷⁰

5.1.3 Optical activity

Optical activity is the physical phenomenon associated to the rotation of linearly polarized light when it propagates through chiral compounds.⁷¹ Linearly polarized light can be seen as the superposition of left (L) and right (R) circularly polarized light. When light passes through an absorbing optically active system, it absorbs differently L and R circularly polarized light, and, as shown in **Figure 5.13**, linearly polarized light becomes elliptically polarized.⁷² This phenomenon is known as circular dichroism (CD), and can be measured, together with other related effects, by using chiroptical techniques like electronic and vibrational CD, which detect differences in absorption between L and R circularly polarized light, or measure the ellipticity defined as the ratio of the minor and major axis of the ellipse formed by the leaving electromagnetic amplitude.^{71,73}

The origin of biological homochirality has puzzled scientists since the chiral nature of molecules was discovered by Louis Pasteur more than 150 years ago,⁷⁴ and on a molecular-level represents an intrinsic property of the building blocks of life. Indeed, chirality is a key aspect

in the evolution of life and plays an important role in molecular recognition.^{75,76}

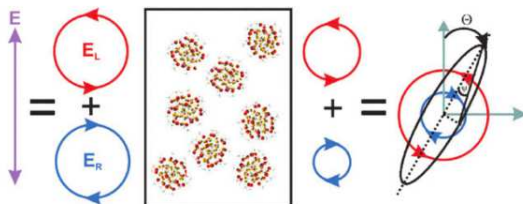


Figure 5.13 From left to right: a linearly polarized beam (E) composed by the sum of left (E_L) and right (E_R) circularly polarized light traveling in an absorbing medium made of a collection of randomly oriented chiral nanoparticles. The system absorbs differently left and right circularly polarized light, presenting the circular dichroism phenomenon, and resulting in elliptical polarized beam.⁷²

Because of the connection between the chirality of molecules and their chemical function, a great amount of research has been carried out in the field of chemistry, pharmacology, biology, and medicine with respect to control over chirality. Interest in this property extends from fundamental particle physics and optics through organic and inorganic chemistry to complex biological systems, such as proteins and nucleic acids.

Chirality has also been envisaged to play an important role in nanotechnology, but the understanding of the fundamental concepts relevant to chirality in nanostructures is pivotal for further advancements.⁷⁷ Chiral nanostructures have been rising steeply and show great promise for applications in photonics, biochemistry and medicine.⁷⁸

Nanoscale hybrid organic-inorganic materials, chiral ligand-protected metal clusters and nanoparticles have been investigated extensively.^{72,79-83} They are promising candidates for a variety of

applications, including biosensing, catalysis, and may open exciting possibilities in the development of innovative metamaterials.⁸⁴⁻⁸⁷

In semiconductor quantum dots (QDs) chirality can be originate concurrently from (i) the intrinsic dissymmetry of a nanocrystal, (ii) the ligand-induced chiral surface of QDs, (iii) the electronic coupling between chiral capping ligands and achiral QDs, or (iv) chiral assemblies of achiral QDs.⁸⁸⁻⁹³ Since capping ligands can influence chemical and electronic properties of QDs,^{94,95} the post-synthetic functionalization of achiral QDs with chiral capping ligands is an ideal approach to induce and control chirality in semiconductor nanomaterials. For instance, chiral thiol capping ligands L- and D-cysteines induced chiro-optical properties in achiral selenide QDs (CdSe) (**Figure 5.14**).^{96,97}

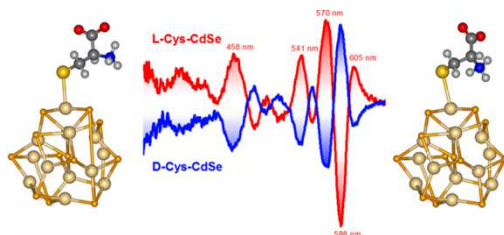


Figure 5.14 Chiral QDs prepared by post-synthetic phase transfer ligand exchange on achiral QDs: D- and L-cysteine functionalized CdSe QDs display mirror image circular dichroism.⁹⁷

Currently, only very few examples are known on chiral carbon-based dots. Recently, the chirality of GQDs was first reported by Martin *et al.*⁹⁸ Chiral GQDs were prepared by covalent functionalization with enantiomerically pure (*R*) or (*S*)-2-phenyl-1-propanol (**Figure 5.15**, top).⁹⁸ The concept that GQDs could become chiral after covalent functionalization with chiral organic ligands was demonstrated only by adding pyrene in the solution. It was observed that the chiro-optical

property could be transferred to a supramolecular structure built with pyrene molecules, where the GQDs/pyrene ensembles showed a characteristic chiro-optical response depending on the configuration of the chiral organic ligands introduced, although the measured spectra are not specular images probably due to different degrees of functionalization.

Almost at the same time, Kotov *et al.* reported chiral GQDs by covalent attachment of *L*- or *D*-cysteine with nearly mirror image optical activity (**Figure 5.15**, bottom).⁹⁹ The high-energy chiro-optical peaks at 210–220 nm correspond to the hybridized molecular orbitals involving the chiral centers of amino acids and atoms of graphene edges. Diverse experimental and modeling data, including DFT calculations of CD spectra with probabilistic distribution of GQDs isomers, indicate that the newly formed band at 250–265 nm originates from the three-dimensional twisting of the graphene sheet and can be attributed to the chiral excitonic transitions.

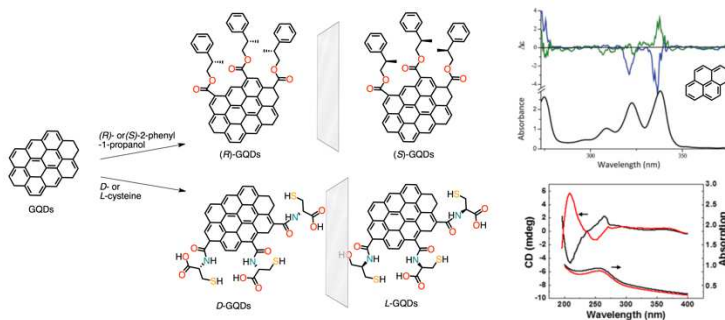


Figure 5.15 Top: chiral GQDs prepared by covalent functionalization with (*R*) or (*S*)-2-phenyl-1-propanol, CD spectra in NMP for aggregates (*R*)-GQDs/pyrene (blue line) and (*S*)-GQDs/pyrene (green line) and UV-Vis absorption spectrum of pyrene in NMP.⁹⁸ Bottom: chiral GQDs prepared by covalent functionalization with *L*- or *D*-cysteine, CD spectra for *L*-GQDs (red line) and *D*-GQDs (black line) dispersions and their UV-Vis absorption spectra.⁹⁹

5.1.4 Aim of the project

In order to produce high-quality CNDs, besides the appropriate synthetic conditions, a proficient choice of the starting precursors is of pivotal importance. For example, heteroatoms such as nitrogen, can be inherited from nitrogen-rich precursors to yield excellent optical properties and, usually, blue-shifted fluorescence (FL), as showed in *Chapter 2*. Regrettably, besides element doping, there are no rational synthetic approaches to obtain materials with predictable optical properties, leaving this field driven mainly by empirical evidence. Moreover, by mastering the CND properties, applications in optoelectronic and biological fields could be more successfully targeted.

It is with this goal in mind that the aim of this project is to develop a simple strategy, based on the design of small molecular building blocks as CNDs precursors, which are able to induce the desired physicochemical properties from the molecular level to the nanoscale in a controlled fashion. Conscious that realizing real-word applications requires time- and cost-effective procedures, a cost-efficiency parameter will be used to guide the design of the synthetic procedures and the choice of the molecular precursors.

To this end, our approach aims at the formation of the desired nanodots in only one synthetic step, without the need of sophisticated equipment or additional post-synthetic processes, through a quick and controlled microwave heating of commercially available, or easy-to-synthesize, precursors.

The first part of the project is particularly devoted to the preparation of CNDs with the desired fluorescent properties, by a careful choice of the proper chromophores as starting materials. Arginine and ethylenediamine that lead to “blue” dots, namely they emit in the blue region of the spectrum (300-450 nm), will be combined with organic fluorophores for the preparation of multicolored CNDs. In particular,

naphthalene dianhydride derivatives (NDAs) and boron-dipyrromethenes (BODIPYs) have been identified as valuable classes of candidates. Two strategies for the incorporation of the fluorophores in the nanostructures have been identified: (i) through their core, manipulating their optical properties for the creation of CNDs with novel features, with the final aim of white-light-emitting nanodots, as in the case of the NDA-based nanodots; (ii) through their periphery, so as to retain the starting characteristics and achieve a high level of prediction of the final CNDs properties, as in the case of the BODIPY-based nanodots.

In the second part, chiral small molecules will be evaluated as building blocks and will be properly selected among the variety of potential commercial candidate, *i.e.* they should be able of chiral inheritance and/or transfer chirality to the final CNDs nanostructures at the high temperatures needed for the reaction.

Finally, it will be investigated the role of small oxidant molecules as dopants for CNDs with tunable redox properties, as a proof of concept of a strategy aimed at the preparation of a redox library of nanodots.

5.2 White-light-emitting CNDs

5.2.1 Design and synthesis

As previously discussed, in the context of white emissive molecules/materials, the common approach consists of several synthetic steps in preparing the R-G-B luminophores, which can be combined in several ways. However, increasing the number of synthetic step, blending of the luminophores and control, for instance, the structure and/or energy transfer processes, increases the cost and complexity of the system.

To this end, we aim at the formation of white-emitting carbon nanodots (WCNDs) in only one synthetic step and employing commercial organic building blocks, which is highly desirable as a cost-effective and time-saving method (**Figure 5.16**).

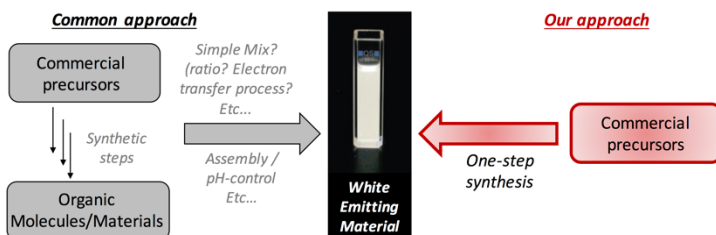


Figure 5.16 Approaches towards white-emitting materials. Common approach: synthesize molecules with tunable emission and control the overall emission with, for instance, their assembly or pH. Our approach: use commercially available precursors and perform a one-step synthesis.

While plenty of organic molecules are able to emit across the whole visible spectrum, we focused our attention on naphthalene diimides (NDIs), due to a number of reasons. First of all, we expect that, under our experimental conditions (microwave-assisted hydrothermal controlled conditions) not only arginine and ethylenediamine

participate in the formation of nanodots, but also naphthalenes anhydrides are able to react. Indeed, NDIs can be synthesized in high yields, starting from naphthalene dianhydrides (NDAs) and amines (**Figure 5.17a**). Highly efficient (and green) imidization of dianhydrides was recently found to proceed quantitatively, without using organic solvents, catalysts or bases.¹⁰⁰

Secondly, proper functionalization at the naphthalene core with electron-donating substituents (yielding core-substituted naphthalene diimides, cNDIs) confers them the ability to absorb and fluoresce in all colors, without significantly changing their structure.¹⁰¹ Furthermore, the cNDI chemistry and spectroscopy are well known, giving us a fair amount of predictability.^{102,103} By employing bromo-substituted naphthalenes diimides, nucleophiles can displace the bromine in a nucleophilic aromatic substitution reaction, in order to functionalize the core (**Figure 5.17b**). Significantly, different substitutions of the naphthalene core result in a modification of the frontier orbitals energies leading to different absorption/emission properties (**Figure 5.17c**).

We had to consider also our hydrothermal synthetic conditions, where small π -conjugated cores should be able to react, while other (larger) aromatic chromophores would be inhibited to take part, due to their insolubility and/or aggregation. In this respect, alkylamino di-substituted cNDIs play an important role, since they have been proposed as the smallest, most 'atom-efficient' chlorophyll mimic.¹⁰⁴

5 Rationally Designed Carbon Nanodots

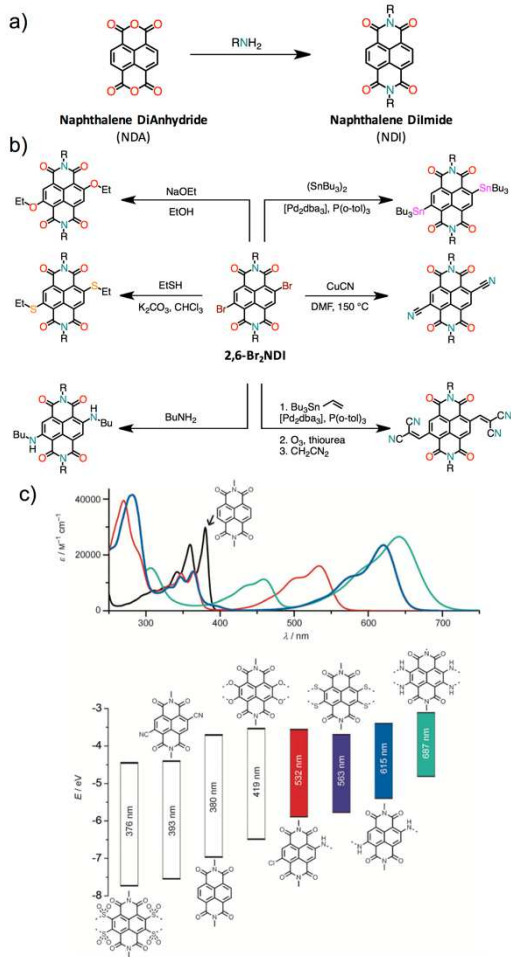


Figure 5.17 Syntheses and optical properties of naphthalene diimides: a,b) synthesis of diimides from anhydrides and common reactions on the naphthalene core; c) modification of the frontier orbitals energies by core modification of selected NDI derivatives and corresponding UV-Vis absorption spectra.¹⁰²

‘Doped’ CNDs were prepared via MW-assisted hydrothermal synthesis by using Arginine (Arg), ethylenediamine (EDA), 1,4,5,8-naphthalenetetracarboxylic acid-1,8:4,5-dianhydride (NDA) and 2,6-dibromonaphthalene-1,4:5,8-tetracarboxylic dianhydride (Br₂NDA) as precursors. We expect that naphthalene anhydrides (NDAs) react with amines in order to form naphthalene diimides (NDIs), and at least one Br atom of the cNDI would be substituted. The formation of amino-substituted cNDIs ultimately would be responsible for shifting the absorption/emission to the red region of the spectrum.

In order to validate our approach, we designed the appropriate experimental conditions that would lead to CNDs ‘doped’ with both NDIs and cNDIs, resulting in a material that emits across the entire visible emission spectrum (**Figure 5.18**).

Arg and EDA, in the presence of an appropriate ratio of NDA and Br₂NDA, led to the formation of pure white-light-emitting carbon nanodots (WCNDs), with 1931 CIE coordinates of (0.33, 0.33).

The MW parameters were optimized to obtain the desired optical performances of the final material, by using appropriate viscosity and temperature control for a uniform carbonization that leads to processes of condensation, polymerization and aromatization, resulting in the formation of NDI-incorporated CNDs.

WCNDs were obtained at 230 °C, 217 psi, 300 W with a MW heating time of 200 seconds using water as reaction medium (see experimental section for details). Large carbon nanoparticles were removed by filtration and the solution was dialyzed against Milli-Q water. The obtained nanodots exhibited a high solubility in water and also in common polar organic solvents.

Besides the white-emitting CNDs, we also prepared the reference materials NDI•CNDs and cNDI•CNDs, obtained by employing either NDA or Br₂NDA, respectively, in the presence of Arg and EDA under

the same MW-assisted conditions (see experimental section for details).

The tuning of emission colors, by employing different ratio of starting materials, are presented in **Table 5.1** together with CIE chromaticity diagram.

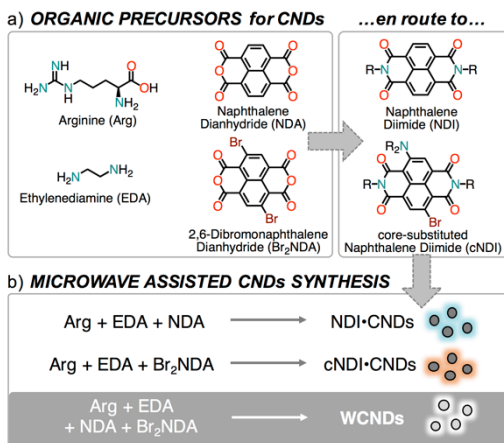


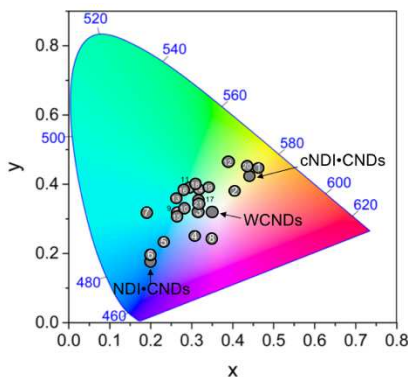
Figure 5.18 Organic precursors used to produce carbon nanodots with tunable emission. a) Molecular structures of the organic precursors that include arginine (Arg), ethylenediamine (EDA), 1,4,5,8-naphthalenetetracarboxylic acid-1,8:4,5-dianhydride (NDA) and 2,6-dibromonaphthalene-1,4:5,8-tetracarboxylic dianhydride (Br₂NDA); b) MW-assisted synthesis starting from the depicted organic precursors yielding NDI•CNDs, cNDI•CNDs and white-light-emitting carbon nanodots (WCNDs).

5 Rationally Designed Carbon Nanodots

Table 5.1 Starting materials molar ratio, molarity and temperature used for optimization experiments. CIE coordinates obtained (summarized in the 1931 CIE chromaticity diagram below).

Entry	Arg:EDA:NDA:Br ₂ NDA mol	[M]/H ₂ O ^a	T(°C)	CIE ^b
WCNDs	1.0:0.5:0.9:0.8	0.46	230	0.33,0.33
NDI-CNDs	1.0:0.5:0.9:0.0	0.46	230	0.20,0.18
cNDI-CNDs	1.0:0.5:0.0:0.9	0.46	230	0.41,0.44
1	1.0:0.5:0.3:0.8	0.46	230	0.46,0.42
2	1.0:0.5:0.6:0.8	0.46	230	0.40,0.36
3	1.0:0.5:0.9:0.25	0.46	230	0.31,0.33
4	1.0:0.5:0.9:0.5	0.46	230	0.24,0.30
5	1.0:1.0:0.0:0.5	3.43	180	0.28,0.26
6	0.5:1.0:0.3:0.2	1.50	200	0.20,0.20
7	0.5:0.5:0.0:1.0	0.40	160	0.19,0.32
8	0.0:1.0:0.0:0.5	6.00 ^c	160	0.33,0.23
9	0.5:0.0:1.0:0.5	0.27	240	0.26,0.33
10	0.25:0.5:1.0:0.7	0.11	230	0.28,0.34
11	0.3:0.6:1.0:1.0	0.11	230	0.29,0.38
12	0.4:0.4:0.0:1.0	0.11	230	0.38,0.43
13	0.25:0.25:1.0:0.7	0.11	230	0.26,0.35
14	0.5:0.5:1.0:0.7	0.21	230	0.31,0.37
15	0.6:0.7:1.0:0.3	0.21	230	0.26,0.32
16	0.7:0.6:1.0:0.8	0.29	230	0.28,0.37
17	0.9:0.55:1.0:1.0	0.38	230	0.31,0.36
18	1.0:0.6:0.9:1.0	0.36	230	0.30,0.37
19	1.0:0.5:0.75:0.8	0.43	230	0.32,0.38
20	1.0:0.4:0.4:0.7	0.54	230	0.43,0.43
21	0.8:0.5:0.65:1.0	0.36	230	0.31,0.35

a) Arg concentration; b) calculated from FL emission spectra upon excitation at 350 nm; c) EDA concentration. Reaction time 200 seconds for all the samples.



5.2.2 Photophysical characterization

The successful synthesis of WCNDs was first observed by acquiring absorption and emission spectra. The UV-Vis absorption spectra (**Figure 5.19**) of WCNDs and the reference materials NDI•CNDs and cNDI•CNDs showed the effective formation of naphthalene diimides under our experimental conditions, with characteristic absorption features in the 300-400 nm region. Moreover, in the case of WCNDs and cNDI•CNDs, the 400-600 nm region displayed the successful formation of core-substituted naphthalene diimides. More specifically, the absorption profile in this region is representative of 2,6-NDIs substituted with one bromine and one amino substituent, which brings their absorption/fluorescence towards the red region of the visible spectrum, as predicted.^{101,102,105}

The fluorescence emission spectra of the three different nanodots (**Figure 5.20**) showed that NDI•CNDs cover mostly the blue region (CIE coordinates of (0.20, 0.18)), the cNDI•CNDs emit mainly in the red region (CIE coordinates of (0.41, 0.44)), while WCNDs exhibited a broad emission from 400 to 700 nm (CIE coordinates of (0.33, 0.33)).

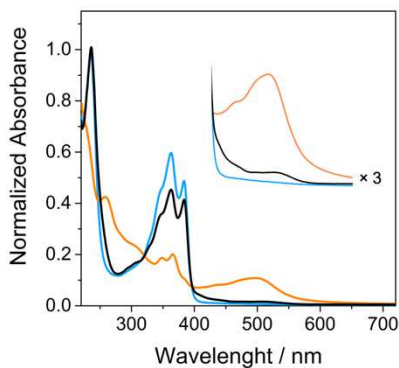


Figure 5.19 Normalized UV-Vis absorption spectra in water of WCNDs (black line), NDI•CNDs (blue line) and cNDI•CNDs (orange line), with the inset showing a zoomed region of the spectra (400-650 nm).

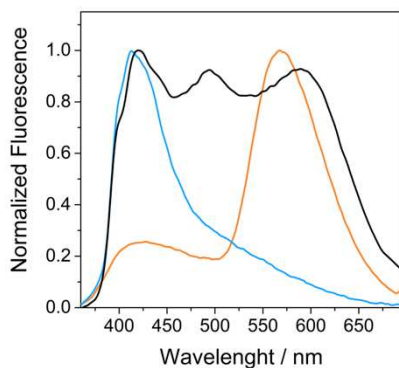


Figure 5.20 Normalized FL emission spectra in water (298 K and $\lambda_{\text{ex}} = 350$ nm) of WCNDs (black line), NDI•CNDs (blue line) and cNDI•CNDs (orange line).

Fluorescence matrix scan experiments (**Figure 5.21**) confirmed the broad emission of WCNDs, the blue- and red-emitting NDI•CNDs

and cNDI•CNDs, respectively, with the emission being tunable by using different excitation wavelengths (**Figure 5.22**).

Therefore, preparing the three types of nanodots unveiled that this methodology could be used to tune and achieve emission from blue-white, to pure white and further to red-white (**Figure 5.23**). This is of particular importance in order to realize tunable white emission, ranging from cool (blue-white) to warm (yellow-white) colors, which find applications according to requirements.

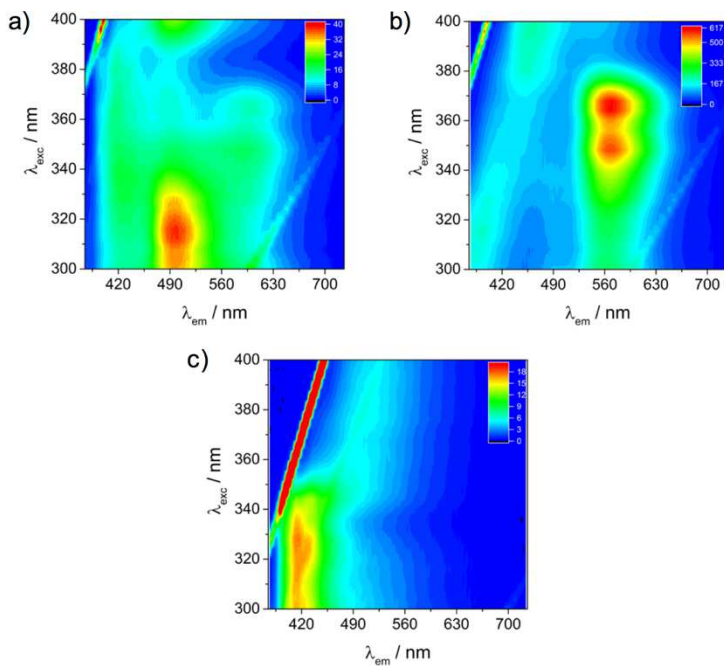


Figure 5.21 FL matrix scan experiments in water (298 K) for a) WCNDs, b) cNDI•CNDs, c) NDI•CNDs, showing the fluorescence mapping by exciting at different wavelengths (300-400 nm).

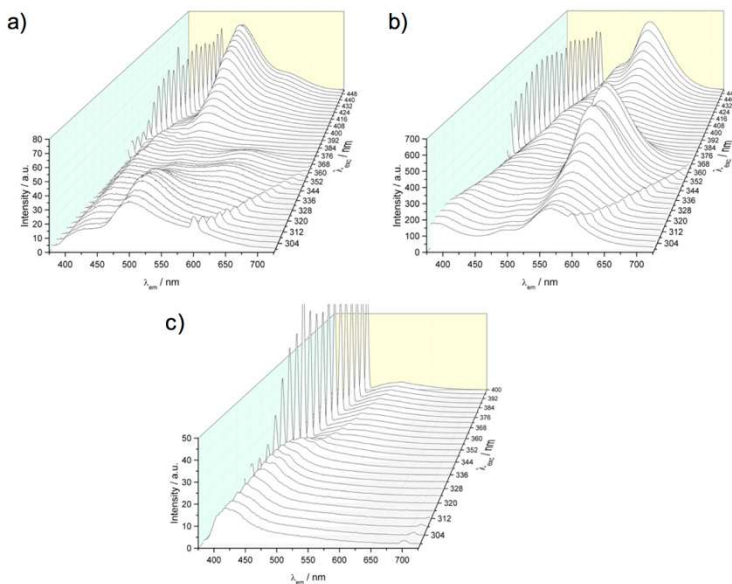


Figure 5.22 FL emission spectra in water (298 K) of a) WCNDs, b) cNDI•CNDs, c) NDI•CNDs, by exciting at different wavelengths (300-400 nm).

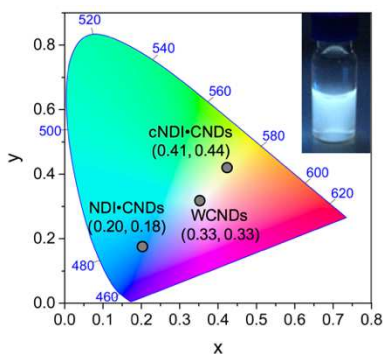


Figure 5.23 1931 CIE chromaticity diagram showing coordinates of WCNDs (0.33, 0.33), NDI•CNDs (0.20, 0.18) and cNDI•CNDs (0.41, 0.44); the inset shows a solution of WCNDs in water exposed to UV light (365 nm).

Additionally, there were no changes in FL intensity after 5 h of continuous UV excitation, confirming the photostability of our material (**Figure S5.2**).

Absolute FL quantum yields (QYs) were measured and found to be 8% for WCNDs, 12% for cNDI•CNDs and less than 1% for NDI•CNDs. While the low QY of NDI•CNDs can be attributed to the electron-acceptor nature of the naphthalene diimide core,¹⁰³ the QYs of cNDI•CNDs and WCNDs gave promising results, given their emission in the red region and the entire visible spectrum, respectively.

5.2.3 Morphological and structural characterization

All three materials were further characterized in order to obtain structural (by FT-IR and X-ray photoelectron spectroscopy) and morphological information (by atomic force microscopy).

AFM confirmed the quasi-spherical morphology and showed that the three CNDs have a rather homogeneous size distribution. By statistical analysis of about one hundred WCNDs nanoparticles, we estimated an average size of 3.70 ± 0.86 nm (FWHM: 2.021) (**Figure 5.24**).

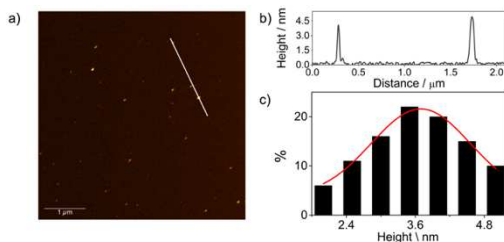


Figure 5.24 a) Tapping mode AFM image of WCNDs ($5.0 \times 5.0 \mu\text{m}$) drop-casted on a mica substrate; b) height profile of WCNDs; c) size histogram of WCNDs with curve fit to the data using a Gaussian model.

For comparison, AFM analysis of NDI•CNDs and cNDI•CNDs showed similar sizes and distribution (**Figures 5.25, 5.26**).

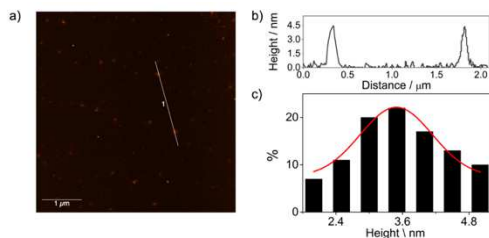


Figure 5.25 a) Tapping mode AFM image of cNDI•CNDs ($5.0 \times 5.0 \mu\text{m}$) on a mica substrate; b) height profile of cNDI•CNDs; c) size histogram of cNDI•CNDs with curve fit to the data using a Gaussian model. Average size of $3.5 \pm 0.65 \text{ nm}$ (FWHM: 1.530).

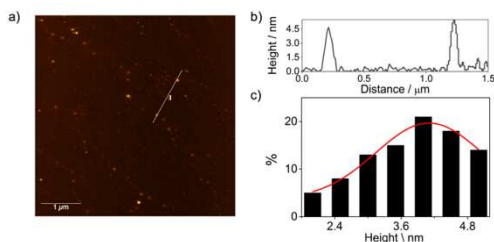


Figure 5.26 a) Tapping mode AFM image of NDI•CNDs ($5.0 \times 5.0 \mu\text{m}$) on a mica substrate; b) height profile of cNDI•CNDs; c) size histogram of cNDI•CNDs with curve fit to the data using a Gaussian model. Average size of of $4.1 \pm 0.96 \text{ nm}$ (FWHM: 2.265).

The FT-IR spectrum (**Figure 5.27**) displayed that WCNDs have many oxygenated functional groups on their surface such as imide, carboxylic acid, epoxy, alkoxy, hydroxyl and carbonyl groups. Absorptions at 1186 and 1114 cm^{-1} can be attributed to the C-O-C bond, while absorptions at 1384 , 1347 , 1275 and 1254 cm^{-1} confirmed the presence of C-O bonds. Peaks at 1456 and 1442 cm^{-1} were

indicative of C-N bonds, while 1584 cm^{-1} showed the presence of C=N/C=C. Additionally, the absorption at 1705 , 1655 and 1619 cm^{-1} displayed C=O bonds, whereas the broad peak centered at 3424 cm^{-1} revealed O-H/N-H bonding. Finally, peaks at 2931 and 2847 cm^{-1} were related to the C-H bond stretching vibrations.

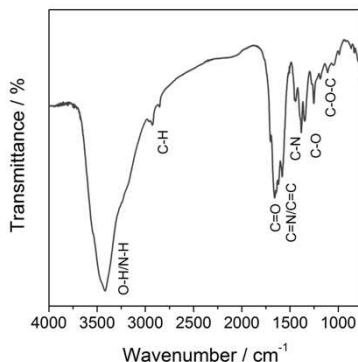


Figure 5.27 FT-IR spectrum of WCNDs.

NDI•CNDs and cNDI•CNDs have similar IR spectra, suggesting a similar functional groups distribution (**Figures S5.3, S5.4**).

X-ray photoelectron spectroscopy was then carried out to further confirm the functional groups present on the surface of carbon nanodots. From the full-scan XPS spectra of WCNDs (**Figure 5.28a**) Br3d at 69.3 eV , Br3p 182.3 eV , Br3s 263.1 eV , C1s 285.5 eV , N1s 400.5 eV , O1s 531.8 eV were clearly discernible. In the case of WCNDs, the atomic percentage for C, N, O and Br were as follows: 65.9, 11.7, 17.2 and 5.2, respectively. The XPS survey spectra for NDI•CNDs and cNDI•CNDs are reported in **Figures S5.5 and 5.28b**, respectively. The binding energies of Br3p and Br3d (only in WCNDs and cNDI•CNDs samples) corresponded to bromine covalently bonded to carbon atoms,¹⁰⁶⁻¹⁰⁹ confirming our observations from UV-

Vis experiments, which showed the presence of the 2-bromo-7-substituted naphthalene diimide core.^{101,102,105}

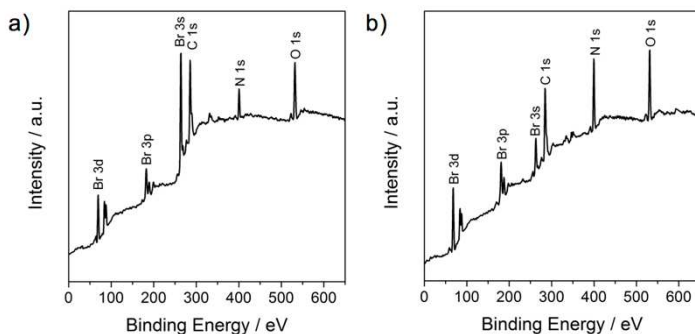


Figure 5.28 XPS survey of a) WCNDs and b) cNDI•CNDs.

To determine the C and N configurations in the CNDs, a detailed peak fitting analysis was performed (**Figures 5.29-5.31**). The XPS spectrum of C1s was deconvoluted into six surface components corresponding to sp^2 (C=C) at 284.5 eV, sp^3 (C-C, C-H) at 285.4 eV, C-O/C-N/C-Br at 286.5 eV, C=O/C=N at 288.5 eV, as well as O-C=O at 289.6 eV and a component at 290.7 eV attributed to the shake-up satellite ($\pi-\pi^*$).¹⁰⁶ The N1s spectrum was deconvoluted into four peaks centered at 398.3, 399.5, 400.4, 401.3 eV corresponding to C=N, NH₂, C-N-C and N-C₃, respectively.¹¹⁰ No significant differences were found in the composition of the C1s and N1s functional groups between the three CNDs (**Table 5.2**). The surface components of CNDs, as determined by XPS, were in good agreement with the observations from FT-IR experiments.

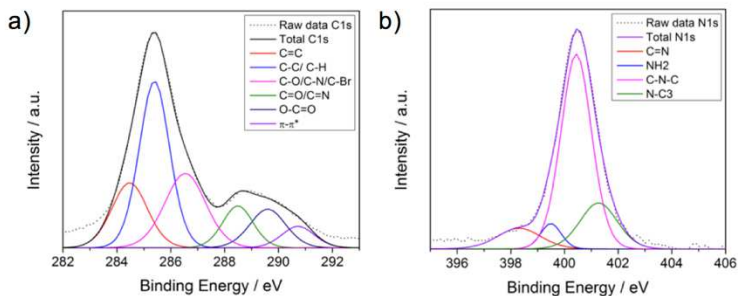


Figure 5.29 Deconvoluted a) C1s and b) N1s spectra of WCNDs.

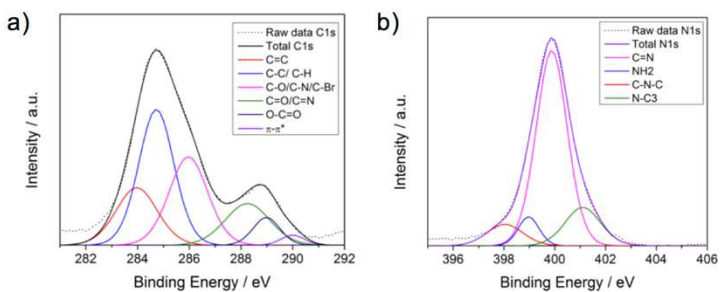


Figure 5.30 Deconvoluted a) C1s and b) N1s spectra of cNDI•CNDs.

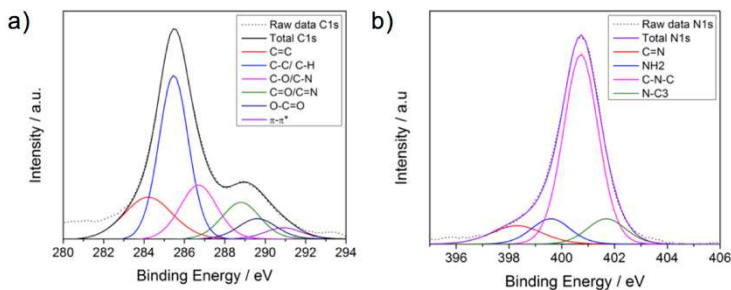


Figure 5.31 Deconvoluted a) C1s and b) N1s spectra of NDI•CNDs.

5 Rationally Designed Carbon Nanodots

Table 5.2 Percentages of C, N, O, Br atoms in WCNDs, cNDI•CNDs and NDI•CNDs, as determined by XPS measurements.

Entry	WCNDs	cNDI•CNDs	NDI•CNDs
C%	65.9	51.2	67.4
C=C	16.8	17.6	18.1
C-C/C-H	36.7	35.6	42.1
C-O/C-N/C-Br ^a	22.1	25.5	17.4
C=O/C=N	9.2	13.9	12.1
O-C=O	10.1	5.6	6.7
Shake-up satellite (π - π^*)	5.1	1.8	3.6
N%	11.7	25.3	18.3
C=N	9.8	8.9	9.8
NH ₂	5.7	6.8	10.3
C-N-C	65.7	68.9	69.6
N-C3	18.8	15.4	10.3
O%	17.2	17.6	14.3
Br%	5.2	5.9	-

a. C-Br only for WCNDs and cNDI•CNDs.

5.3 BODIPY-based CNDs

5.3.1 Design and synthesis

4,4'-difluoro-4-bora-3a,4a-diaza-*s*-indacene (abbreviated to BODIPY) dyes have gained a great deal of attention recently because of their many distinctive and desirable properties such as high extinction coefficients, narrow absorption and emission bands, high quantum efficiencies of fluorescence, relative insensitivity to environmental perturbations.¹¹¹

They are commonly described as being a boradiazaindacene due to the analogy with the all-carbon tricyclic ring, and the numbering system follows rules set up for the carbon polycycle (**Figure 5.32**), where the 8-position is often referred as meso site by analogy with porphyrinic systems.

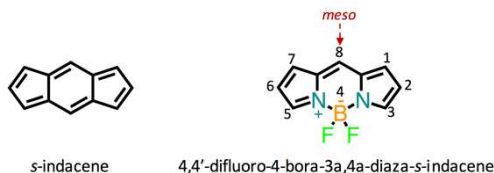


Figure 5.32 Numbering scheme used for BODIPY derived from indacene.

Small modifications to their structure enable tuning of their fluorescence characteristics and they are known as a photostable substitute for fluorescein.¹¹²

However, BODIPY also have undesirable characteristics for many applications in biotechnology. For instance, only a handful of water-soluble derivatives have been made and they display the tendency to decrease solvent contact by forming non-emissive aggregates.¹¹¹ Thus, there is the potential that BODIPY framework will lead to probes that can be used for imaging in living cells, but that is largely unrealized.

To improve water solubility, sophisticated functionalization of BODIPY skeletons is usually required. Moreover, the synthetic methodologies are limited and the preparation of large quantities represents a bottleneck for biomedical studies. Strategies to water-soluble BODIPY involve the introduction of oligo(ethylene glycol), *N,N*-bis(2-hydroxyethyl)amine, carbohydrates, nucleotides, or ionic hydrophilic groups such as carboxylic acid, sulfonic acid, or ammonium groups.¹¹³⁻¹²² For instance, highly water-soluble BODIPY were obtained by introducing branched oligo(ethylene glycol)methyl ether at the meso position with a fluorescence quantum yield of 4.2%, that can be enhanced up to 35.7% introducing steric hindrance to the BODIPY core through the replacement of the fluorine atoms with ethynyl subunits via a Grignard reaction.¹²² However, despite great synthetic efforts, little success was achieved in order to avoid multi-step synthesis and tedious purification for water-soluble BODIPY.

BODIPY-based CNDs (BCNDs) were synthesized using 8-(4-carboxyphenyl)-1,3,7,9-tetramethyl-BODIPY (hereafter abbreviated to BODIPY-COOH), which was prepared with a one-pot synthesis adapting a standard synthetic methodology.¹²² Substituents in position 1,7 result in enhanced quantum yield since they prevent free rotation of the phenyl group and therefore reduce loss of energy from the excited states via non-irradiative molecular motions.¹¹¹

BCNDs were prepared via MW-assisted hydrothermal synthesis by using Arginine (Arg), ethylenediamine (EDA) and BODIPY-COOH as precursors (**Figure 5.33**). We expect that, under our experimental conditions the carboxyphenyl group of the BODIPY reacts with the amino moieties of arginine and ethylenediamine. This results in the incorporation of the BODIPY-COOH in the final CNDs, which show a high solubility in water and in polar solvents. We hypothesized that the incorporation of BODIPY dyes into CNDs could effectively enhance their enthalpic interactions with water and increase their

water solubility, and that the introduction of steric hindrance at the meso positions of BODIPY dyes could reduce their aggregation through π - π stacking interactions between BODIPY cores in aqueous solution, enhancing their fluorescence quantum yields.

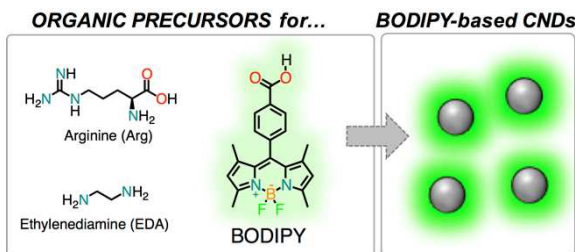


Figure 5.33 Molecular structures of the organic precursors that include arginine (Arg), ethylenediamine (EDA), 8-(4-carboxyphenyl)-1,3,7,9-tetramethyl-BODIPY (BODIPY-COOH) used to produce BODIPY-based carbon nanodots with green FL emission through a MW-assisted synthesis.

The MW parameters, as well as the molar ratio between the three organic precursors, were optimized to obtain the desired optical performances of the final material. By using appropriate viscosity and temperature controls for a uniform carbonization, processes of condensation, polymerization and aromatization resulted in the formation of BODIPY-incorporated CNDs.

BCNDs were obtained by employing Arg, EDA and BODIPY-COOH in a molar ratio of 1:0.5:0.25 mol, at 200 °C, 5 psi, 200 W with a MW heating time of 180 seconds, using water as reaction medium (see experimental section for details). Large carbon nanoparticles were removed by filtration and the solution was finally dialyzed against Milli-Q water.

5.3.2 Photophysical characterization

The photophysical properties of the novel BCNDs were measured in water. The absorption spectrum of BCNDs (**Figure 5.34**) is characterized by a strong $S_0 \rightarrow S_1$ ($\pi\text{-}\pi^*$) transition at 496 nm and a weaker broad band around 350 nm attributed to the $S_0 \rightarrow S_2$ ($\pi\text{-}\pi^*$) of the BODIPY moiety. Moreover, the absorption band around 307 nm could be ascribed to the $\pi\text{-}\pi^*$ transition of the C=C units from the nanoparticle core.¹¹⁰

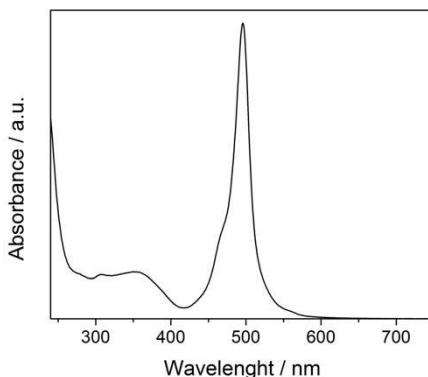


Figure 5.34 UV-Vis absorption spectrum in water of BCNDs.

The fluorescence emission spectrum of BCNDs showed the typical excitation wavelength-dependence phenomenon of CNDs arising from the presence of different functional groups with different surface state level, that dominate the emission at characteristic excitation wavelengths.¹¹⁰ A fluorescence peak shift from 352 to 470 nm when the excitation wavelength changes from 300 to 420 nm, according to the NCNDs previously reported, was observed.¹¹⁰ The incorporation of the dye in the BCNDs resulted in a double emission with an additional and more intense fluorescence peak centered at 507 nm, that became predominant exciting at 500 nm (**Figure 5.35**).

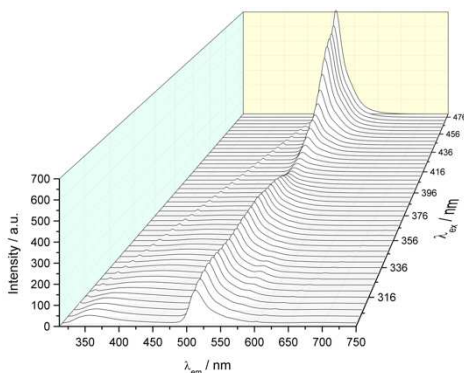


Figure 5.35 FL emission spectra of BCNDs in water (298 K), by exciting at different wavelengths (300–480 nm).

Fluorescence matrix scan experiments confirmed their mainly green emission (**Figure 5.36**); the BCNDs emitted from the blue-green to the green region upon excitation from 300 to 500 nm (**Figure 5.37**), showing CIE coordinates of (0.17, 0.39) exciting at 340 nm and of (0.15, 0.69) exciting at 500 nm (**Figure 5.38**). Finally, the fluorescence QY of BCNDs was determined in water and was found to be 20%, which is a remarkable result considering the usually low emission of BODIPY dyes in water, as discussed above. This could be attributed to the nanodots surrounding, which could prevent the aggregation of the dye in an aqueous solution through stacking or hydrophobic interactions between BODIPY cores. Notably, there were no changes in FL intensity after 4 h of continuous UV excitation in water, revealing the photostability of BCNDs (**Figure S5.7**).

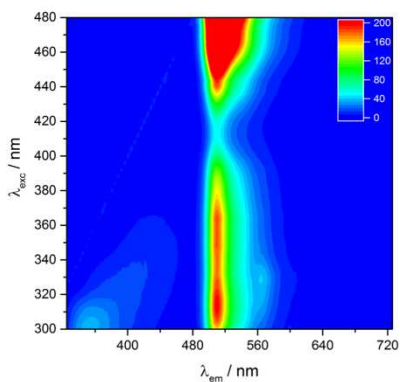


Figure 5.36 FL matrix scan experiment for BCNDs in water (298 K) showing the fluorescence mapping by exciting at different wavelengths (300-480 nm).

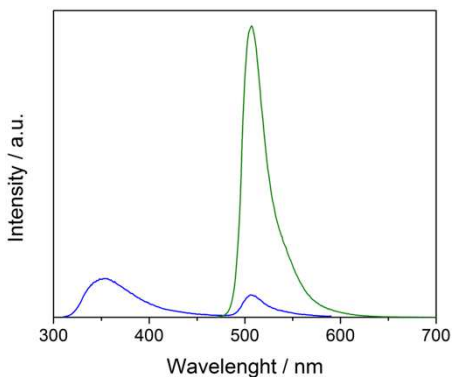


Figure 5.37 FL emission spectra of BCNDs in water by exciting at 300 nm (blue line) and 500 nm (green line).

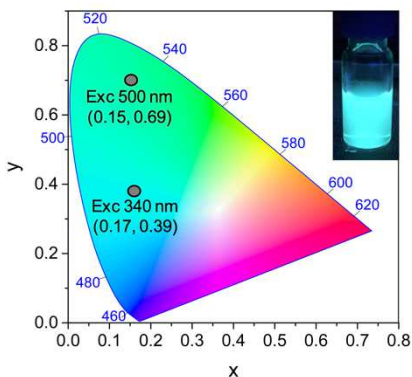


Figure 5.38 1931 CIE chromaticity diagram showing coordinates of BCNDs by exciting at 340 nm (0.17, 0.39) and 500 nm (0.15, 0.69); the inset shows a solution of BCNDs in water exposed to UV light (365 nm).

5.3.3 Morphological and structural characterization

Morphological information of BCNDs were obtained by AFM. AFM images showed the quasi-spherical morphology of the dots and a rather homogeneous size distribution. By statistical analysis of about one hundred of nanodots, we estimated an average size of 2.17 ± 0.64 nm (FWHM: 1.524).

The structure and the composition of BCNDs was determined by FT-IR spectroscopy and X-ray photoelectron spectroscopy.

The BCNDs FT-IR spectrum (**Figure 5.40**) showed the presence of many functional groups on their surface, similar to the ‘undoped’ nanodots presented in *Chapter 2*. Interestingly, the peak at 1683 cm^{-1} in the FT-IR spectrum of the BODIPY precursor and indicative of the carboxylic acid moiety (**Figure S5.6**), disappeared in the BCNDs spectrum. Instead, absorptions at 1669 and 1623 cm^{-1} showed the presence of C=O bonds, while absorptions at 1342 cm^{-1} confirmed the presence of C-O. Additionally, peaks at 1178 , 1155 and 1108 cm^{-1} displayed C-O-C bonds, and the broad peak centered at 3353 cm^{-1}

revealed O-H/N-H bonding. Absorptions at 2945 and 1385 cm^{-1} were indicative of C-H and B-N stretching, respectively. Furthermore, C=N/C=C (1545 and 1511 cm^{-1}) and C-N (1470 and 1452 cm^{-1}) functional groups can be identified.

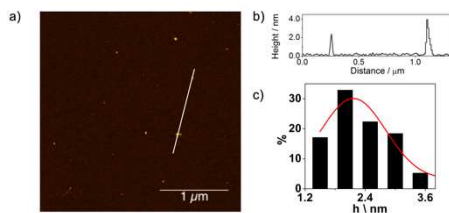


Figure 5.39 a) Tapping mode AFM image of BCNDs ($3.0 \times 3.0 \mu\text{m}$) drop-casted on a mica substrate; b) height profile of BCNDs; c) size histogram of BCNDs with curve fit to the data using a Gaussian model.

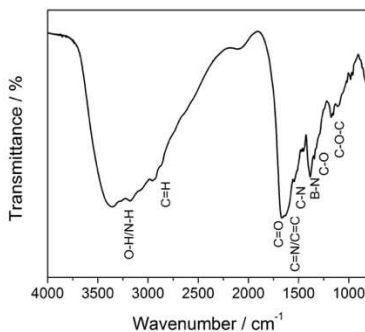


Figure 5.40 FT-IR spectrum of BCNDs.

The surface components as determined by FT-IR spectroscopy, were in good agreement with XPS results. From the full-scan XPS spectrum of BCNDs (**Figure 5.41a**) C1s at 286.3 eV, N1s at 401.0 eV, O1s at 532.3 eV, B1s at 190.3 eV, F1s at 685.8 eV were detected. The atomic percentages for C, N, O, B and F were as follows: 61.1,

22.4, 13.2, 1.2 and 2.1, respectively. To determine the C and N configurations in the BCNDs, a detailed peak fitting analysis was performed (**Figure 5.41b,c**).

The XPS spectrum of C1s was deconvoluted into five surface components corresponding to sp^2 (C=C) at 284.8 eV (5.0%), sp^3 (C-C/C-H) at 285.9 eV (29.8%), C-O/C-N/C-Br at 286.9 eV (47.9%), C=O/C=N at 288.8 eV (5%), and a component attributed to O-C=O at 289.9 eV (12.3%). The N1s spectrum was deconvoluted into four peaks centered at 398.9 (4.5%), 399.9 (8.0%), 400.9 (58.2%), 401.9 (29.3%) eV corresponding to C=N, NH₂, C-N-C and N-C₃, respectively.

The presence of primary amino groups was confirmed by a positive Kaiser test. It was estimated a value of 845 $\mu\text{mol/g}$ of amino groups, making BCNDs prompt to the easy insertion of further functional groups and/or interesting molecules/ions through standard organic chemistry protocols.

The electrochemical properties of BCNDs have been studied, in order to investigate the electronic effect of the BODIPY moiety in the nanodots. Usually, BODIPY dyes show reversible reduction and oxidation waves with peaks near -1.4 V and +1.3 V, respectively, which depend on the substituents present.¹²³⁻¹²⁵

The CV of BCNDs is reported in **Figure 5.42**. The anodic region presented an oxidation peak at +1.20 V, which is related to the oxidation of the amines present on the nanodots surface observed also in the CV of NCNDs (as reported in *Chapter 2*), and its broader shape as compared to the ‘undoped’ ones might result from the merging of the peak relative to amines and the oxidation peak of the BODIPY moiety. In the cathodic part, apart from a peak at -2.50 V associated to the reduction of the oxidized amines as in the case of NCNDs, a new irreversible peak at -1.90 V can be identified. This can be attributed to the presence of the BODIPY on the nanodots surface,

and the difference observed in its potential value compared to the typical ones of the dyes, suggested a ‘novel’ surrounding for the BODIPY, which requires more energy to be reduced, and thus their implementation in the dots nanostructure.

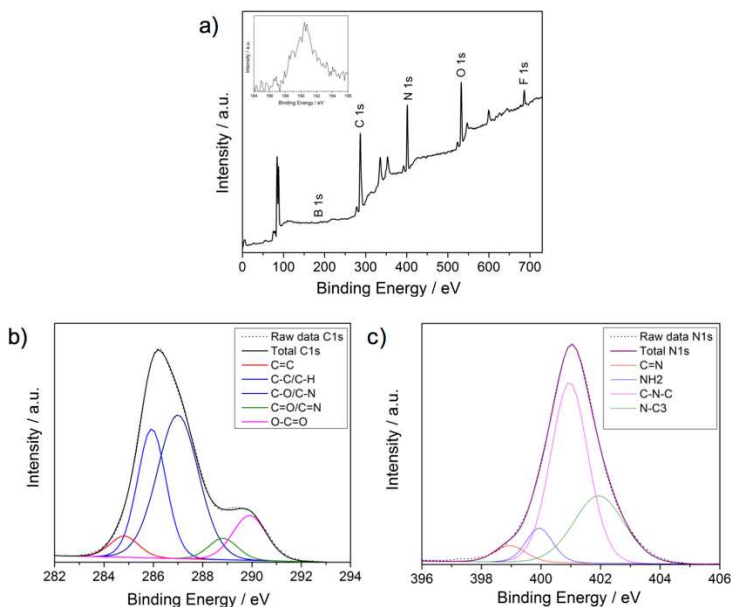


Figure 5.41 a) XPS survey of BCNDs (inset: zoom of the B1s region); deconvoluted b) C1s and c) N1s spectra of BCNDs.

The frontier orbital energies calculated from CV data were found to be -5.75 and -3.23 eV for HOMO and LUMO, respectively. A comparison with the ones of the ‘undoped’ NCNDs (HOMO: -5.7 eV; LUMO: -2.3 eV) showed that the presence of the BODIPY in the nanodots resulted in an unvaried HOMO level and in a more stabilized LUMO energy. The latter revealed that the BODIPY moiety strongly modify the nanodots surface and the reduced bandgap

observed for BCNDs (2.52 eV) respect to NCNDs (3.4 eV) is responsible of the observed optical bathochromical shift.

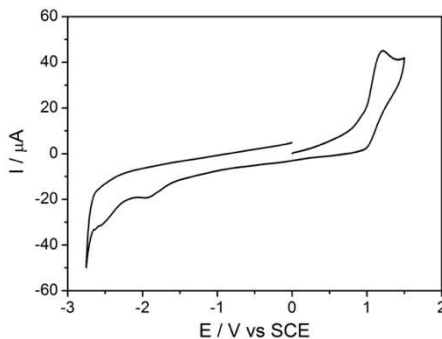


Figure 5.42 CV of BCNDs in DMF using TBAPF₆ as supporting electrolyte.

5.3.4 BCNDs effects on human natural killer cells

As reported in *Chapter 2*, NCNDs show a low cytotoxicity at relatively high concentrations. BCNDs should display an improved cellular imaging ability due to their bathochromically-shifted emission. Therefore, preliminary investigation using a confocal microscope, showed (**Figure 5.43**) that BCNDs are efficiently taken up by human cervix cancer C33-A cell line.

In light of these results, we investigated for the first time the effect of carbon nanodots on Natural Killer (NK) cells function and differentiation, and some preliminary results are reported below.

NK cells are lymphocytes of the innate immune system, that is the first line of defence against pathogens, together with epithelial barriers, phagocytes, dendritic cells, the complement system and cytokines.

They were first described in mice in 1975 as granular lymphoid cells with cytotoxic function against Moloney leukaemia cells.¹²⁶

Subsequently, these cells were identified as NK cells due to their ability to lyse certain tumor cells without prior stimulation.

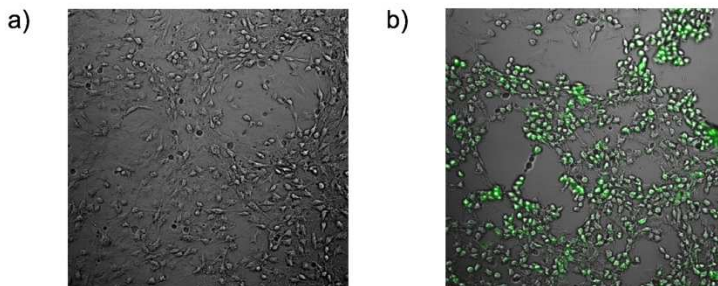


Figure 5.43 Confocal microscope images showing the uptake of BCNDs (10 $\mu\text{g/mL}$, 24 h exposure time at 37°C) by C33-A cell line. a) cells under bright field and b) by excitation at 488 nm. Magnification 20X.

Human natural killer cell function is regulated by a balance between activating and inhibitory receptors. Some inhibitory receptors recognize HLA class I molecules, which are expressed by virtually all healthy cells and prevent their killing by autologous NK cells. These inhibitory receptors include the clonally distributed Killer Ig-like Receptors (KIRs) that are able to distinguish among different HLA-A, -B and -C allotypes and the CD94/NKG2A heterodimer that directly recognizes HLA-E.¹²⁷ In the absence of interactions between NK inhibitory receptors and self-HLA class I molecules, a series of activating receptors transduces signals that result in NK-mediated attack of allogeneic, tumor- or virus-transformed cells.¹²⁸

NK cells derive from haemopoietic stem cells (HSC), which give rise to all blood cells. Their stages of differentiation are characterized by the sequential acquisition (or loss) of markers and functional properties. Different soluble factors play a key role in NK cell development, activation, expansion, trafficking and survival. In particular, IL-15 is responsible of NK cell development and

proliferation, and it is abundantly present in the bone marrow where NK cell development and differentiation occurs.

NK cells are currently defined as large granular lymphocytes, comprising about 5-15 % of total mononuclear cells in peripheral blood mononuclear cells (PBMCs), and they are identified by CD56⁺CD3⁻CD19⁻ surface phenotype.¹²⁹

On the basis of CD56 expression intensity, circulating NK cells are divided into two major subsets based on the intensity of CD56 expression: CD56^{bright} and CD56^{dim} NK cells (**Figure 5.44**). These two subsets display a different tissue distribution as well as distinct phenotypic characteristics and functions. While CD56^{dim} NK cells are largely predominant in PB where they represent about 90%, CD56^{bright} NK cells are more frequent in certain tissues and secondary lymphoid organs. Differently from CD56^{dim} NK cells, CD56^{bright} NK cells are characterized by low expression of lytic granules and by production of high amounts of cytokines, such as IFN- γ , TNF- α , and GM-CSF. Thus, CD56^{bright} NK cells have been usually considered as “regulatory NK cells” and CD56^{dim} NK cells as “cytotoxic NK cells” (notably CD56^{dim} NK cells can also release large amounts of cytokines but only upon receptor-mediated triggering).

Different experimental evidences have now established that CD56^{bright} NK cells represent an early stage of peripheral NK cell maturation, further progressing to CD56^{dim} NK cells. In addition, analysis of mice with a humanized immune system revealed that infused CD34⁺ cells give rise to CD56^{bright} first and subsequently to CD56^{dim} NK cells that also become KIR⁺. Cells at later stages of NK cell differentiation in addition to KIRs also express high levels of CD16 (Fc γ R) and CD57, lose the expression of CD94/NKG2A and are characterized by a low proliferative capacity. CD56^{bright} NK cells express only CD94/NKG2A, whereas CD56^{dim} NK cells may also express KIRs, and/or LIR-1.¹³⁰

CD69, CD25 and NKp44 represent NK cell activation markers. In particular, CD69 is early acquired by NK cells in response to different stimuli and it marks NK cells characterized by enhanced effector functions including cytotoxicity, proliferation and cytokine production. CD25 also named as IL2R α is expressed later than CD69 by activated NK cells and allows higher IL-2 mediated responses. NKp44 is exclusively expressed by activated NK cells,¹³¹ and it is one of the natural cytotoxicity receptors (NCRs). NCRs (NKp46, NKp30 and NKp44) are a group of NK cell receptors that mediate direct killing of stressed cells and are acquired at early maturation stages of NK cells.¹²⁸

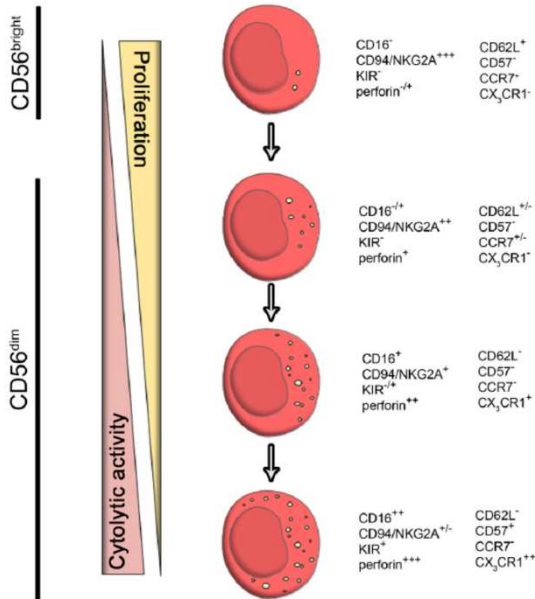


Figure 5.44 Peripheral NK cell subsets. Schematic representation of NK cell differentiation from CD56^{bright} to CD56^{dim}.

Firstly, the ability to visualize human NK cells by using BCNDs was investigated. For this purpose, flow cytometry analyses on resting NK cells (not cytokine pre-activated NK cells) from PBMCs were performed, comparing NK cells cultured with IL-15 (1 ng/ml) in the absence or in the presence of growing concentration of BCNDs.

The data were reported in two-dimensional dot plots in which each of the four quadrants (upper left: UL; upper right: UR; low left: LL; low right: LR) is defined by the two values obtained from the flow cytometer and the number reported in each quadrant is referred to the events recorded in terms of percentage. Therefore, the cells UL and LR are representative of single positive events, while UR of double positive events and LL of double negative events.

Figure 5.45 shows the BCNDs-dependent staining of NK cells (CD56^{bright} and CD56^{dim}) upon 30 minutes of exposure to different BNDs doses in the presence of IL-15. The exposure to higher doses of BNDs resulted in a clear and efficient uptake.

In order to evaluate the capability of BCNDs to induce NK cell activation, the surface expression of the CD69, CD25 and NKp44 activation markers was analyzed on NK cells upon 20 hours and 7 days of exposure to different doses of BCNDs.

After 20 hours of exposure (**Figure 5.46**), the presence of BCNDs induced a higher expression (especially with their higher dose employment) of the CD69 receptor, while an almost unchanged expression pattern for NKp44 and CD25 was observed.

However, after 7 days of BCNDs exposure (**Figure 5.47**), the expression of both CD69 and CD25 resulted enhanced compared to the results obtained after 20 hours of BCNDs exposure, and in a BCNDs dose-dependent manner, whereas the expression of NKp44 receptors appeared to be influenced only by the IL-15 cytokine stimulation.

5 Rationally Designed Carbon Nanodots

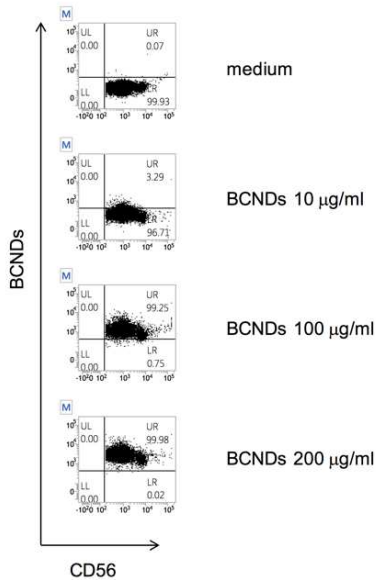


Figure 5.45 Two-dimensional dot plots showing the uptake of different doses of BCNDs (10 µg/mL, 100 µg/mL, 200 µg/mL at 37°C and in the presence of IL-15 1 ng/mL) by NK cells (CD56^{bright} and CD56^{dim}) after 30 min of exposure.

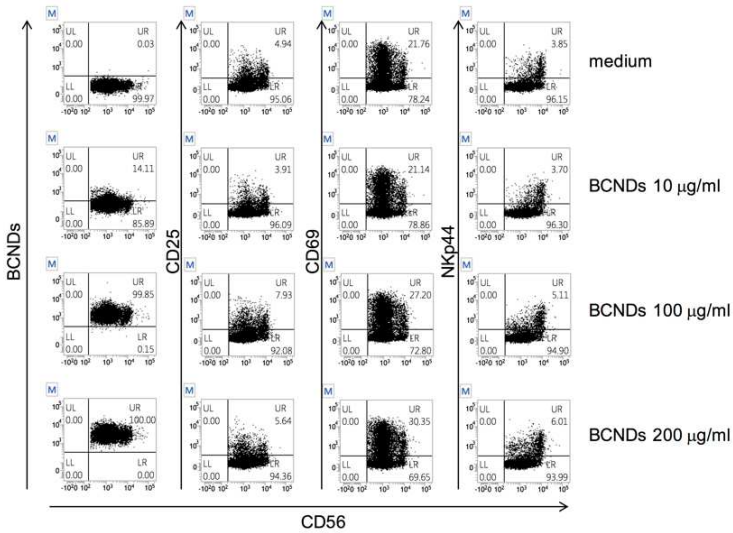


Figure 5.46 Two-dimensional dot plots showing the expression of the CD69, CD25 and Nkp44 activation markers on NK cells after 20 h of exposure of different doses of BCNDs (10 µg/mL, 100 µg/mL, 200 µg/mL at 37°C and in the presence of IL-15 1 ng/mL).

Prompted by these results, we investigated the BCNDs effect on the NK cell maturation process. Since the PBMCs is composed by NK cells at different differentiation stages, we evaluated whether PBMC exposure to BCNDs could change the ratio of the different NK cell subsets and favor the development of specific NK cell subsets.

Herein, the analysis performed after 20 hours and 7 days of BCNDs at different doses exposure are reported (**Figure 5.48**).

In the presence of BCNDs, an increment of NKG2A+ KIR+ NK cell subset and a decrease of NKG2A+ KIR- NK cell subset was observed especially for the higher BCNDs doses and the longer exposure time, suggesting a role of BCNDs in inducing an increment of more mature NK cells.

5 Rationally Designed Carbon Nanodots

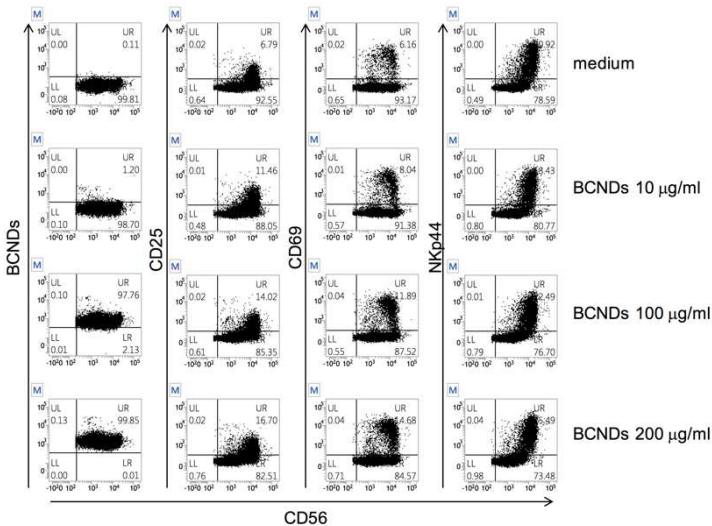


Figure 5.47 Two-dimensional dot plots showing the expression of the CD69, CD25 and NKp44 activation markers on NK cells after 7 days of exposure of different doses of BCNDs (10 µg/mL, 100 µg/mL, 200 µg/mL at 37°C and in the presence of IL-15 1 ng/mL).

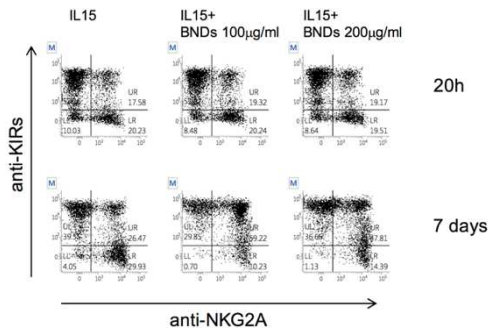


Figure 5.48 Two-dimensional dot plots showing the expression of the increment of NKG2A+ KIR+ NK cell subset after 20 h and 7 days of exposure of different doses of BCNDs (100 µg/mL, 200 µg/mL at 37°C and in the presence of IL-15 1 ng/mL).

5.4 Chiral CNDs

5.4.1 Design and synthesis

For the preparation of chiral carbon nanodots we build on our synthetic protocol for NCNDs discussed in *Chapter 2*. Chiral CNDs were prepared via MW-assisted hydrothermal synthesis by using arginine and *(RR)*-(—)-cyclohexanediamine or *(SS)*-(+)-cyclohexanediamine, instead of ethylenediamine, as precursors, at 240 °C, 60 psi, 200 W and with a MW heating time of 180 seconds in water (see experimental section for details). In the process of microwave heating, the solution changed color from transparent to dark brown, as a result of the formation of nanodots. Large carbon nanoparticles were removed by filtration and the yellow solution was finally dialyzed against Milli-Q water. The obtained nanodots exhibited a high solubility in water and also in common polar organic solvents, and are denoted here as (—)- and (+)-CNDs (**Figure 5.49**). Note that (—)- and (+)-CNDs notations refer here to the molecular chirality of the amines used as precursors, because the use of alternative notations requires a deep study on the origin of the chiroptical properties, which is among the goal of this project.

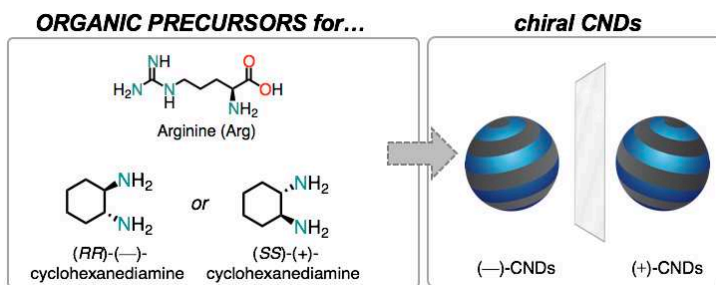


Figure 5.49 Molecular structures of the organic precursors that include arginine (Arg), and *(RR)*-(—)-cyclohexanediamine or *(SS)*-(+) cyclohexanediamine used to produce chiral carbon nanodots ((—)- or (+)-CNDs).

5.4.2 Morphological and structural characterization

The structure and the composition of (—)- and (+)-CNDs were determined by FT-IR spectroscopy and X-ray photoelectron spectroscopy, while morphological information were obtained by atomic force microscopy. As expected, the two enantiomers showed the same morphological and structural features. Therefore it is here reported the characterization of (+)-CNDs, while results for (—)-CNDs can be found in the experimental section.

AFM images showed the (+)-CNDs round shape and size of 2.62 ± 0.85 nm (FWHM: 2.001), comparable to the NCNDs (**Figure 5.50**).

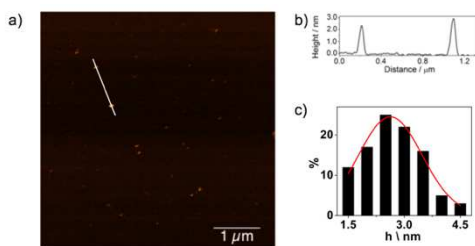


Figure 5.50 a) Tapping mode AFM image of (+)-CNDs (4.4×4.4 μm) drop-casted on a mica substrate; b) height profile of (+)-CNDs; c) size histogram of (+)-CNDs with curve fit to the data using a Gaussian model.

The (+)-CNDs FT-IR spectrum showed the presence of many functional groups on their surface, similar to the NCNDs prepared using EDA as amine precursor. Absorptions at 1174 and 1107 cm^{-1} can be attributed to C-O-C bond, while absorptions at 1386 , 1353 , 1342 cm^{-1} confirmed the presence of C-O bonds. Moreover, the absorption peaks at 1646 , 1703 and 1766 cm^{-1} are indicative of C=O bonds, whereas the broad peak centered at 3350 cm^{-1} revealed O-H/N-H bonding. In addition, C-N/C=N/C=C (1491 , 1470 , 1452 cm^{-1})

functional groups can be identified, while peaks at 2935, 2859 cm^{-1} are related to the C–H bond stretching vibrations (**Figure 5.51**).

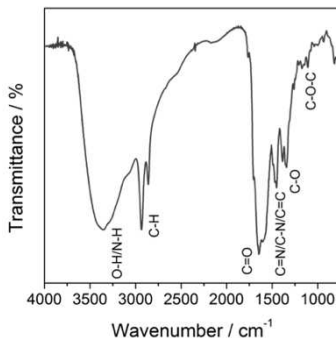


Figure 5.51 FT-IR spectrum of (+)-CNDs.

From the full-scan XPS spectrum of (+)-CNDs (**Figure 5.52a**) C, N, O were detected (C1s at 286.2 eV, N1s at 400.6 eV and O1s at 532.3 eV). The atomic percentages for C, N, O were as follows: 65.9, 23.7, 10.4, respectively, revealing that compared to NCNDs, chiral nanodots exhibit higher nitrogen and lower oxygen contents.

To determine the C and N configurations in the (+)-CNDs, a detailed peak fitting analysis was performed, and the surface components as determined were in good agreement with the observations from FT-IR experiments. The C1s spectrum of (+)-CNDs can be deconvoluted into five surface components corresponding to C=C at 284.8 eV (5.1%), C-C, and C-H at 285.8 eV (20.2%), C-O/C-N at 286.7 eV (56.8%), C=O/C=N at 288.5 eV (5.7%), as well as O-C=O at 289.6 eV (12.2%) (**Figure 5.52b**). The N1s spectrum of (+)-CNDs can be deconvoluted into four peaks centered at 398.7 (7.1%), 399.9 (25.7%), 400.9 (52.9%), 401.9 (14.3%) eV corresponding to C=N, NH_2 , C-N-C and N-C₃ respectively (**Figure 5.52c**).

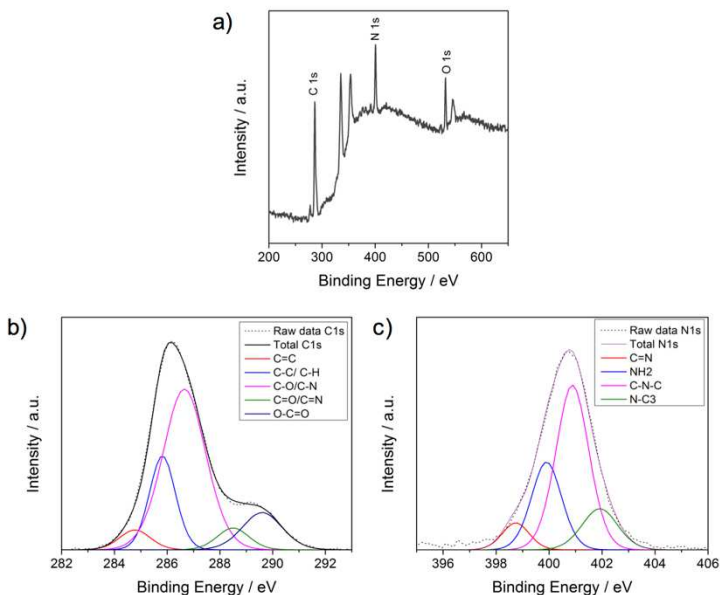


Figure 5.52 a) XPS survey of (+)-CNDs; deconvoluted b) C1s and c) N1s spectra of (+)-CNDs.

Therefore, FT-IR and XPS measurements show that the chiral nanodots surface contains similar multiple oxygen and nitrogen functional groups than NCNDs, but with different contents.

Finally, the presence of primary amino groups was confirmed by a positive Kaiser test, with an estimated value of 795 $\mu\text{mol/g}$ of amino groups, that is lower than the one founded for NCNDs according to XPS measure.

5.4.3 Photophysical and chiro-optical properties

The UV-Vis absorption spectra of (—)- and (+)-CNDs revealed two peaks at *c.a.* 270 nm and 330 nm, which are related to the electron transitions from π (or n) to π^* of C=C and C=O (**Figure 5.53**).

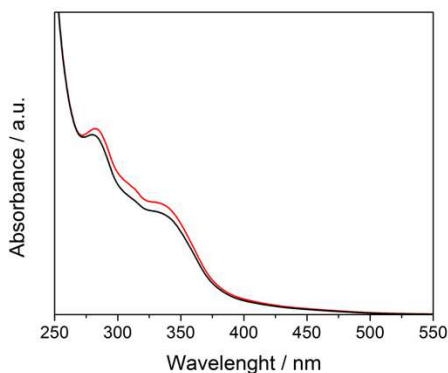


Figure 5.53 UV-Vis absorption spectra in water of (—)-CNDs (black line) and (+)-CNDs (red line).

The luminescence properties of the (—)- and (+)-CNDs have been explored. A broad emission peak at 425 nm is observed for both (—)- and (+)-CNDs when excited at the optimal excitation wavelength (340 nm) (**Figures 5.54, S5.13**). The fluorescence peak shifts from 419 nm to 466 nm when the excitation wavelength changes from 320 to 440 nm, with a slightly excitation-dependent emission profile. The FL quantum yield (QY) was found to be 20%.

These data reveal that the different surface functional groups of (—)- and (+)-CNDs, compared to the NCNDs (discussed in *Chapter 2*), which were synthesized and purified with the same protocol of the chiral nanodots, but using EDA as amine precursor, affect the optical properties, and that (—)- and (+)-CNDs show instead some optical similarities with the smaller NCNDs2-3 (discussed in *Chapter 2*). Indeed, the nanodots surface affects the FL properties since it determines the trapping of excitons under excitation.

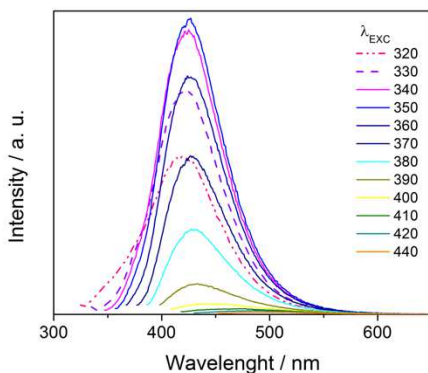


Figure 5.54 FL emission spectra in water (298 K) of (+)-CNDs at different excitation wavelengths.

The evidence of the successful synthesis of chiral nanodots was obtained from Electronic Circular Dichroism (ECD) spectroscopy. Two aqueous solutions of the enantiomers at a concentration of 0.7 mg mL^{-1} and pH 9.7 were measured (**Figure 5.55**).

The ECD spectrum of (—)-CNDs water solution presents two negative cotton effects at 260 nm and 320 nm in accordance with the UV absorption bands. As a result of the ECD analysis of enantiomer (+)-CNDs, the inversion of ECD signal was observed, indeed two positive cotton effects at 260 nm and 320 nm were detected.

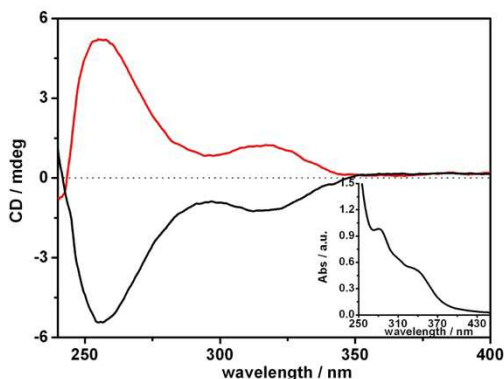


Figure 5.55 EDC spectra in water of (—)-CNDs (black line) and (+)-CNDs (red line).

5.4.4 Induced chiral supramolecular assemblies

In order to investigate the ability of chiral CNDs to transfer the chiral information to other molecules we studied their non-covalent interactions with porphyrins.

Porphyrins represent very attractive building blocks for the formulation of functional supramolecular materials. Over their unique spectroscopic and geometric properties, they are stable under a variety of conditions, exhibit unique optical and redox properties, and can be readily functionalized at different sites. Charged substituents make porphyrins water-soluble, even when maintaining the hydrophobic character of the macrocyclic core. Exploiting this dichotomy, it is possible to drive the tendency of the porphyrins to self-assemble in aqueous solutions and to modulate the aggregation from templates, inducing predefined architectures.¹³²⁻¹³⁷ One of their advantages is that they are ECD silent, but become ECD active upon binding to chiral molecules and show an induced ECD signal in their absorption region, as a specific spectroscopic signature of the chirality of the “host” molecule.

The porphyrin selected for our study is the tetranionic *meso*-tetrakis(4-sulfonatophenyl)porphyrin ($\text{H}_2\text{TPPS}^{4-}$, $\lambda_{\text{max}} = 413 \text{ nm}$, $\epsilon = 4.8 \cdot 10^5 \text{ M}^{-1} \text{ cm}^{-1}$), whose protonated form ($\text{H}_4\text{TPPS}^{2-}$, $\text{p}K_{\text{a}} = 4.8$) being zwitterionic molecules, forms both face to face (H-type, $\lambda_{\text{max}} = 420 \text{ nm}$) and edge to edge (J-type, $\lambda_{\text{max}} = 490 \text{ nm}$) aggregates.¹³⁸⁻¹⁴⁶

This supramolecular aggregation processes are based on hierarchical self-assembly showing different thermodynamically and kinetically controlled paths related to medium properties and experimental conditions such as concentration, pH, and ionic strength.¹⁴⁷⁻¹⁵¹ A challenging aspect in these systems is the possibility of modulating the structure and properties of the final aggregates. One of the most intriguing and controversial properties of $\text{H}_4\text{TPPS}^{2-}$ aggregates is a unpredictable chirality. $\text{H}_4\text{TPPS}^{2-}$ aggregates would be formed as a racemic mixture, exhibiting no optical activity,¹⁵² however traces of chiral contaminants shift the 1:1 racemate equilibrium.

To date only few studies have been performed on the induction of preferential chirality to $\text{H}_4\text{TPPS}^{2-}$ aggregates using chiral molecules as template.^{147,153} Here we report the effect of chiral CNDs as inducer of chirality and controller of the $\text{H}_4\text{TPPS}^{2-}$ aggregates size.

The addition of tetranionic $\text{H}_2\text{TPPS}^{4-}$ to a solution of CNDs at pH 9.7 induces spectroscopic evidence of interaction, *i.e.* hypochromic effect (H ~ 35%) and a slight broadening of the Soret band. Nevertheless, the surface of the CNDs is covered by amine residues, thus by changing the pH it is possible to tune the charges of the CNDs and modulate the interactions with the porphyrin. Indeed, decreasing the pH, from 9.7 to 6.5, of the $\text{H}_2\text{TPPS}^{4-}$ /CNDs solution the hypochromic effect and the broadening of the porphyrin Soret band becomes stronger. In particular, an intense hypochromic effect (H ~ 75%) and the splitting of the Soret band of the $\text{H}_2\text{TPPS}^{4-}$ (one more intense band at ~ 400 nm and the other at ~ 419 nm) are observed (**Figure 5.56**). This experiment indicates the important role played by electrostatic

interactions, since the porphyrin is tetranionic at pH 6.5, whilst the CNDs should carry positive charges.

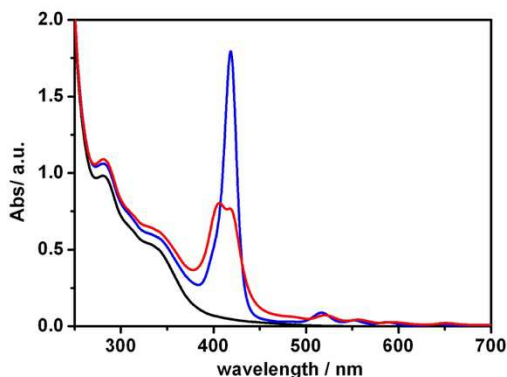


Figure 5.56 UV-Vis absorption spectra in water of chiral nanodots at pH 9.7 (black line), and in the presence of H₂TPPS⁴⁻ 6 μM at pH 9.0 (red line) and at pH 6.5 (blue line).

Subsequently, in order to induce the formation of H₄TPPS²⁻ aggregates, we decreased the pH to 2.5 (using hydrochloric acid) of the solutions of H₂TPPS⁴⁻/(—)-CNDs complex. The UV-Vis spectrum shows the complete formation of H-type and J-type H₄TPPS²⁻ aggregates in less than 1 hour (inset **Figure 5.57**). The ECD band of the CNDs drastically decreased and two small bidentate induced ECD bands (centered at 420 nm and 490 nm) appear in the porphyrin aggregates absorption region (**Figure 5.57**, black line). Mirror image ECD spectrum is obtained for the H₂TPPS⁴⁻/(+)-CNDs complex (**Figure 5.57**, red line).

The low intensity of the induced ECD signals of H₄TPPS²⁻ aggregates, might indicate a weak efficiency of the CNDs to transfer chiral information to porphyrin aggregates, owing to the almost disappearance of the ECD bands of the CNDs at acid pH. However, the ECD intensity is affected also by the size and the strength of the

communication of porphyrin aggregates. Indeed, resonance light scattering (RLS) measures indicate the formation of small porphyrin aggregates in the presence of CNDs, than the aggregates formed in the absence of CNDs (**Figure 5.58**).

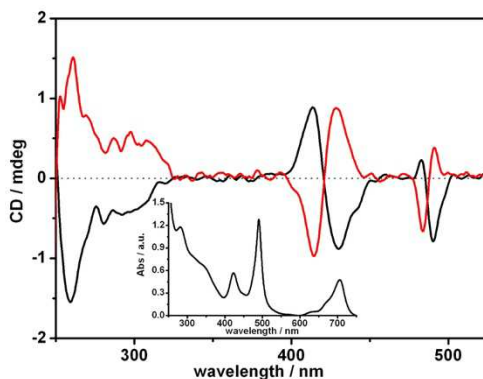


Figure 5.57 EDC spectra in water of (—)-CNDs (black line) and (+)-CNDs (red line) in the presence of $6 \mu\text{M}$ of $\text{H}_2\text{TPPS}^{4+}$ at pH 2.5. Inset shows the UV-Vis spectrum of the $\text{H}_2\text{TPPS}^{4+}$ /(—)-CNDs solution.

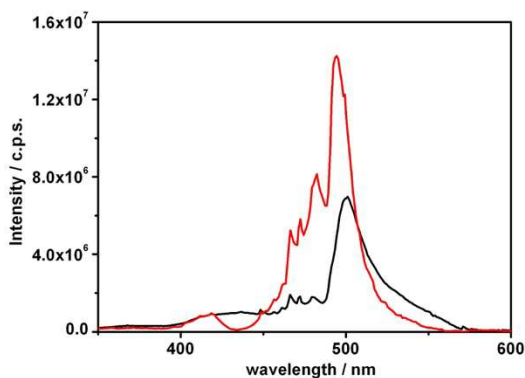


Figure 5.58 RLS spectra in water of $6 \mu\text{M}$ of $\text{H}_2\text{TPPS}^{4+}$ at pH 2.5 in the presence (black line) and in the absence (red line) of chiral nanodots.

5.5 Customizing energy-level in CNDs

5.5.1 Design and synthesis

As a proof of concept of our one-pot strategy for tuning the electrochemical properties of CNDs we focused on quinones, since it is well known that they are easily reduced to hydroquinones, being good oxidizing derivatives of aromatic compounds. Additionally, in our reaction conditions, we thought to take advantage of the quinones reactivity.^{154,155}

We employed arginine (Arg) and ethylenediamine (EDA) as precursors, which produce nitrogen-doped CNDs (NCNDs) under the hydrothermal MW-assisted protocol reported in *Chapter 2*, and we introduced the commercially available 2,3-dichloro-5,6-dicyano-1,4-benzoquinone (DDQ) as 'dopant' (**Figure 5.59**), in order to synthesize nanodots with much stronger oxidizing properties.

Quinone-doped CNDs (hereafter denoted as qCNDs) were obtained using Arg, EDA and DDQ as precursors, in a molar ratio of 1:1:0.5 mol, and by employing the MW parameters optimized for the 'undoped' NCNDs (240 °C, 26 bar, 200 W with a MW heating time of 180 seconds, using water as reaction medium. See experimental section for details). After the thermal treatment, the color of the reaction mixture turned to dark brown, as a result of the formation of CNDs. The reaction mixture was then filtered and the solution was dialyzed against Milli-Q water obtaining nanodots with a high solubility in water and also in common polar organic solvents.

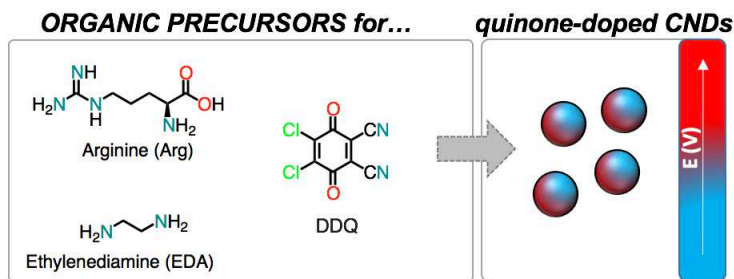


Figure 5.59 Molecular structures of the organic precursors, that include arginine (Arg), ethylenediamine (EDA) and 2,3-dichloro-5,6-dicyano-1,4-benzoquinone (DDQ), used to produce quinone-doped CNDs (qCNDs).

5.5.2 Morphological, structural and electrochemical characterization

The morphology of the novel qCNDs was investigated by atomic force spectroscopy (**Figure 5.60**), confirming their round shape and size of 2.18 ± 0.75 nm (FWHM: 1.766) comparable to the 'undoped' nanodots.

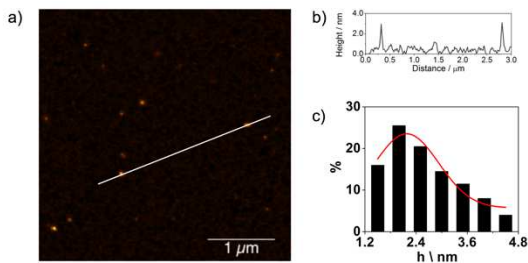


Figure 5.60 a) Tapping mode AFM image of qCNDs ($3.7 \times 3.7 \mu\text{m}$) drop-casted on a mica substrate; b) height profile of qCNDs; c) size histogram of qCNDs with curve fit to the data using a Gaussian model.

The structure and composition of CNDs were determined by FT-IR spectroscopy and X-ray photoelectron spectroscopy.

The FT-IR spectrum showed the presence of many oxygen and nitrogen functional groups on the qCNDs surface, similar to the 'undoped' NCNDs. Absorptions at 1766 and 1664 showed the presence of C=O bonds, while peaks at 1383, 1295 and 1169 cm^{-1} displayed C-O and C-O-C bonds. Absorptions at 1455, 1402 cm^{-1} suggest the presence of C=N/C=C/C-N bonds, the broad peaks centered at 3458 and 3172 cm^{-1} revealed O-H/N-H bonding, while peaks at 2926 and 2865 cm^{-1} were indicative of C-H stretching (**Figure 5.61**).

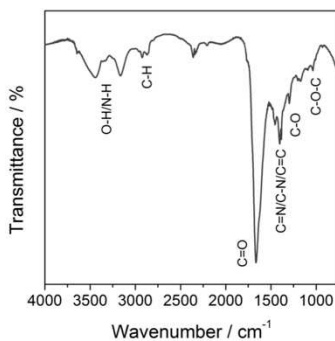


Figure 5.61 FT-IR spectrum of qCNDs.

Besides the above-mentioned groups, a peculiar characteristic of our carbon nanodots is the presence of amino groups on the surface, that was confirmed through a positive Kaiser test, estimating a value of 258 $\mu\text{mol g}^{-1}$ of free amino groups on the surface.

To further confirm the functional groups on the qCNDs surface, XPS measurements were performed. From the full-scan XPS spectrum of qCNDs (**Figure 5.62a**), the peaks related to C1s, N1s, O1s, at 286.1 eV, 400.5 eV, 532.2 eV, respectively, can be identified. Interestingly,

Cl atoms were not detected, suggesting their substitution during the nanodots formation. The atomic percentages were found as 67.4 for C1s, 20.5 for N1s and 12.1 in the case of O1s, indicating that doping with quinones alters the composition of nanodots, leading to higher nitrogen and lower oxygen contents.

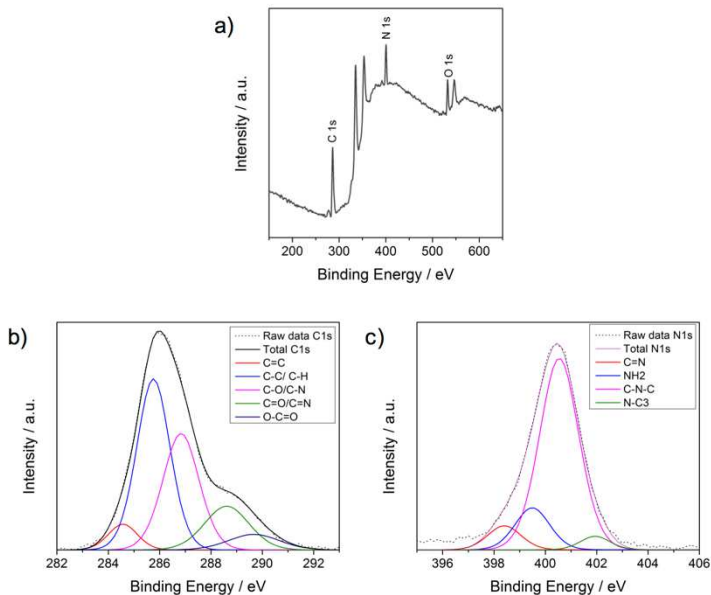


Figure 5.62 a) XPS survey of qCNDs; deconvoluted b) C1s and c) N1s spectra of qCNDs.

A detailed peak fitting analysis revealed the presence of surface components in good agreement with the observations from FT-IR measurements. The C1s and N1s of all the CNDs show the same multiple surface components, according to the nanodots without quinones, but with different contents. The C1s spectrum of qCNDs can be deconvoluted into five surface components corresponding to

C=C at 284.6 eV (5.6%), C-C, and C-H at 285.8 eV (42.4%), C-O/C-N at 286.8 eV (31.5%), C=O/C=N at 288.6 eV (14.6%), as well as O-C=O at 289.7 eV (5.9%) (**Figure 5.62b**). The N1s spectrum of qCNDs can be deconvoluted into four peaks centered at 398.7 (8.0%), 399.9 (14.2%), 400.9 (73.9%), 401.9 (3.9%) eV corresponding to C=N, NH₂, C-N-C and N-C₃ respectively (**Figure 5.62c**).

In addition, we investigated the electrochemical properties of the novel nanodots through cyclic voltammetry (**Figure 5.63**). As shown in *Chapter 2*, NCNDs prepared without quinones, showed very interesting electrochemical potentials that could be exploited for applications such as catalysis.^{156,157} Cyclic voltammetry exhibited a peak at -2.52 V and +1.18 V vs SCE (*Chapter 2*), so both the reduced and oxidized species were found to be good oxidant/reductant that could be coupled with a wide range of appropriate catalysts.

The anodic region of qCNDs presented an oxidation peak at +1.20 V vs SCE, similar to the one observed in the CV of NCNDs and related to the oxidation of the amines present on the nanodots surface. Concerning the reduction potentials, apart from a peak at -2.50 V vs SCE associated to the reduction of the oxidized amines, observed also in the case of NCNDs (as reported in *Chapter 3*), a new reversible peak at -1.90 V vs SCE can be identified and attributed to the doping with the quinone.

Therefore, the doping with quinone derivatives produces a new and interesting nanodots, with much stronger oxidizing properties. The potentials are sufficiently negative to efficiently inject electrons into the conduction band of TiO₂ ($E_F \approx -0.5$ V).¹⁵⁸ Thus, from the electrochemical point of view, these nanodots are good candidates for operation in DSSC as dyes or for proton reduction ($E_0 = -0.59$ V vs SCE).¹⁵⁹

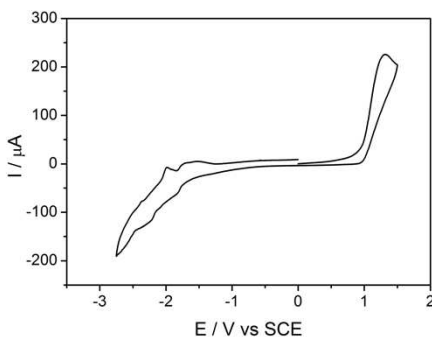


Figure 5.63 CV of qCNDs in DMF using TBAPF₆ as supporting electrolyte.

Finally, the frontier orbital energies calculated from CV data were found to be -5.75 and -3.1 eV for HOMO and LUMO, respectively, and a reduced bandgap for qCNDs (2.65 eV) respect to NCNDs (3.4 eV) was calculated. A comparison with the ‘undoped’ NCNDs (HOMO: -5.7 eV; LUMO: -2.3 eV) showed that the doping with quinones does not affect the HOMO level, while it leads to a more stabilized LUMO level suggesting that the doping modifies the nanodots surface.

5.5.3 Photophysical characterization

The optical properties of the nanodots are affected by chemical composition and surface functionalization. Therefore, we expect the quinones to affect this behavior showing variations in the absorption and emission features.

The UV-Vis absorption spectrum (**Figure 5.64**) of qCNDs revealed a peak at 284 nm, similar to the one observed for the ‘undoped’ NCNDs, and a new peak at 380 nm, that are related to the electron transitions from π (or n) to π^* of C=C and C=O.

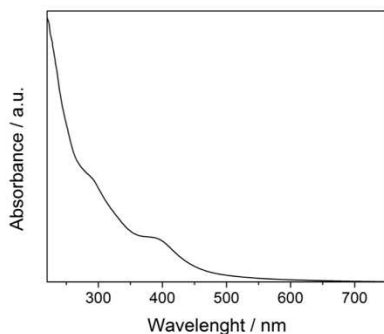


Figure 5.64 UV-Vis absorption spectrum in water of qCNDs.

qCNDs showed the typical wavelength depending emission (**Figure 5.65**). qCNDs showed the optimal emission upon excitation at 300 nm, and the fluorescence peaks shift from 355 nm to 550 nm when the excitation wavelength changes from 300 to 500 nm. Compared to the emission spectra of NCNDs, a lower decrease in intensity when the peak is red-shifted can be observed, as shown from the blue-green emission visible in the fluorescence matrix scan experiment (**Figure 5.66**). Moreover, FL quantum yields (QYs) were measured and found to be 15%, indicating that the quinone doping has not remarkable effect on the nanodots optical performance.

These data revealed that, as suggested from the structural investigations, the doping with quinone derivatives results in the presence of different surface functional groups compared to the NCNDs.

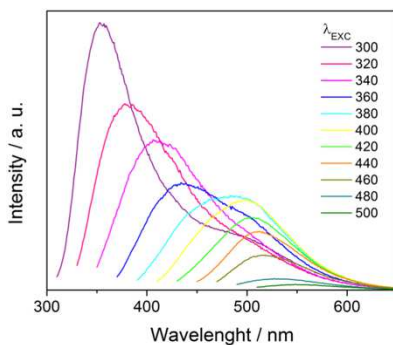


Figure 5.65 FL emission spectra of qCNDs in water (298 K) at different excitation wavelengths (300-500 nm).

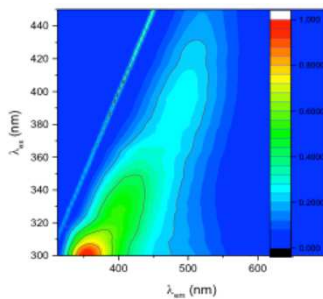


Figure 5.66 FL matrix scan experiment for qCNDs in water showing the fluorescence mapping by exciting at different wavelengths (300-450 nm).

5.6 Conclusions and perspectives

In summary, we have described a rational, simple and straightforward approach for tailor-made functional carbon nanodots. We built upon our previous work, showed in *Chapter 2*, in which we reported a simple and efficient method of producing small and highly fluorescent NCNDs via MW-assisted hydrothermal synthesis from arginine (Arg) and ethylenediamine (EDA). Herein, we employed commercial or easy to synthesize organic building blocks as ‘dopants’, which is highly desirable as a cost-effective and time-saving method.

In the first two parts of the chapter, we showed that it is possible to obtain CNDs with the desired fluorescent properties, by a careful choice of the organic precursors. The customized emission was achieved by adding organic chromophore precursors, based on naphthalene dianhydride (NDA) and dibromonaphthalene dianhydride (Br₂NDA) or 4,4'-difluoro-4-bora-3a,4a-diaza-s-indacene (BODIPY) as ‘dopants’.

We have shown that, by using an appropriate ratio of NDA and Br₂NDA precursors, carbon nanodots emit light across the entire visible spectrum, resulting in white-light emission. Accordingly, current efforts in our laboratory are directed towards the preparation of color displays and solid state lighting.

Moreover, novel BODIPY-based CNDs (BCNDs) were prepared and characterized, and preliminary studies showed that they play an important role in the natural killer cells maturation process and activation. Their functional use as carrier for interesting biomolecules, thanks to the presence of amino groups on their surface that makes BCNDs prompt for further functionalization through standard organic chemistry protocols, is currently under investigation in our laboratory.

In the third part of the chapter, the preparation of inherently chiral CNDs has been presented. Moreover, they have been successfully used as template for preferentially chiral porphyrin aggregates. Based on this approach, it is possible to construct more sophisticated chiral CNDs-based supramolecular organizations where chirality could play an important role in practical application. Moreover, we envisage that they may open exciting possibilities in field such as biosensing and catalysis, that are under investigation in our laboratory.

Finally, CNDs with strong oxidizing properties have been prepared by using a quinone derivative as ‘dopant’, in order to showcase the potentiality of our approach for the preparation of a redox library of nanoparticles with tunable energy levels. This is an on-going project in our laboratories, together with their ad-hoc application in fields such as hydrogen evolution and carbon dioxide reduction.

In conclusion, we expect our rational approach in preparing carbon dots may open the door to a host of unforeseen opportunities, targeted to their careful engineering, which, in turn, will guide the design of high performance materials.

5.7 Experimental section

5.7.1 Materials

Reagents and solvents were bought from Sigma-Aldrich, TCI, VWR Int. and used as received, unless otherwise specified.

SEC was performed with Sephadex LH-20 (Sigma-Aldrich).

Dialysis tubes with molecular weight cut-off 1 kDa were bought from Spectrum Labs.

Column chromatography was carried out using Merck silica gel 60 Å (particle size 40-63 µm).

Thin layer chromatography (TLC) was conducted on pre-coated aluminum sheets with 0.20 nm Merk Silica Gel F254.

Ultrapure fresh water was obtained from a Millipore water purification system (>18MΩ Milli-Q, Millipore).

5.7.2 Apparatus and characterization

The microwave syntheses were performed on a CEM Discover-SP.

UV-Vis spectra were recorded on a PerkinElmer Lambda 35 UV-Vis spectrophotometer.

Fluorescence spectra and fluorescence matrix scan measurements were recorded on a Varian Cary Eclipse Fluorescence Spectrophotometer. All the spectra were recorded at room temperature using 10 mm path-length cuvettes.

The absolute fluorescence quantum yields were measured on a Hamamatsu Quantaurus-QY integrating sphere in air-equilibrated condition using an empty quartz tube as a reference. The relative quantum yield measurements were performed with quinine sulphate

in 0.10 M H₂SO₄ (literature quantum yield 0.54) or coumarin 153 in ethanol (literature quantum yield 0.53) as standards.

The chromaticity coordinates were obtained using Osram Sylvania color calculator 6.61 software (available at: <https://www.osram-americas.com/en-us/tools-and-resources/Pages/led-color-calculator.aspx>) from fluorescence emission spectra recorded upon excitation at 350 nm.

CD spectra were recorded using Jasco J-815 at room temperature. A quartz cuvette with a 1 cm path length was used for all CD experiments. Conditions were as follows: scanning rate 50 nm/min, data pitch 0.2 nm, D.I.T 2 seconds. Each CD spectrum was an average of at least five scans.

Fourier-transform infrared spectra (KBr) were recorded on a Perkin Elmer 2000 spectrometer.

NMR spectra were obtained on a Varian Inova spectrometer (500 MHz ¹H and 125 MHz ¹³C). Chemical shifts are reported in ppm using the solvent residual signal as an internal reference (Dimethyl Sulfoxide-*d*₆: δ_H= 2.50 ppm). The resonance multiplicity is described as *s* (singlet), *d* (doublet), *t* (triplet), *q* (quartet), *m* (multiplet).

MALDI-MS were recorded using a Ultraflextreme III time-of-flight mass spectrometer equipped with a pulsed Nd:YAG laser (355 nm) in RP positive method. DHB was used as matrix, and diluted in acetonitrile. Samples were dissolved in methanol and air dried, then matrix was added and air dried for a second time.

The electrochemical characterization was carried out in DMF with 0.1M tetrabutylammonium hexafluorophosphate (TBAPF₆) as supporting electrolyte. Oxygen was removed by purging the DMF solution with high-purity nitrogen, and a cell CHI220 from CH. Instruments was used. A glassy carbon electrode (GC) was employed

as the working electrode (WE), while a platinum and a silver wires were used as counter (CE) and quasi-reference (QRE) electrodes. It was calibrated at the end of each experiment against the ferrocene/ferricenium (Fc/Fc^+) couple, whose formal potential is 0.460 V against KCl-saturated calomel electrode (SCE). All potential values were reported against SCE.

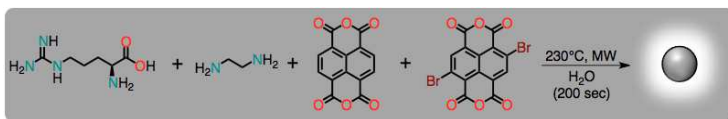
Atomic force microscopy (AFM) images were obtained with a Nanoscope IIIa, VEECO Instruments. As a general procedure to perform AFM analyses, tapping mode with a HQ:NSC19/ALBS probe (80kHz; 0.6 N/m) (MikroMasch) from drop cast of samples in an aqueous solution (concentration of few mg/mL) on a mica substrate was performed. The obtained AFM-images were analyzed in Gwyddion 2.35. The statistical analysis was performed on about one hundred nanoparticles and the average size was calculated from the size histogram with curve fit to the data using a Gaussian model.

X-ray photoemission spectroscopy (XPS) spectra were measured on a SPECS Sage HR 100 spectrometer using a non-monochromatized Mg-K α radiation of 1253.6 eV and 250 W, in an ultra-high vacuum chamber at pressure below $8 \cdot 10^{-7}$ mbar. For each analysis, an aqueous solution (c.a. 3 mg/mL) of material were deposited on a gold thin film. The calibration was done using the 3d5/2 line of Ag. Survey and high resolution spectra were collected with pass energy of 30 and 15 eV and 0.5 and 0.15 eV/step, respectively. CasaXPS 2.3.17 PR1.1 and Avantage (Thermo Fisher Scientific) software were used for data processing and fitting. Curve fittings of the C1s and N1s spectra were realized using a Gaussian-Lorentzian peak shape after performing a Shirley background correction, to finally obtain the relative percentage of each type of bond inside the analyzed sample.

Confocal Microscopy images were taken in a confocal microscope (Ism 500 meta, Zeiss) with laser 488nm, 505 LP filter and 20X

magnification objective with differential interference contrast for transmitted light. C33-A cells were seeded in 96-well plates with optical bottom (IBIDI) and cultured for 4 days. Supernatants were replaced by 150 μL media containing 100, 50 or 10 $\mu\text{g}/\text{ml}$ BNDs and incubated for 24 h at 37 $^{\circ}\text{C}$ and 5% CO_2 . Supernatants were discarded, cells were washed twice with sterile PBS prior to fixation with sterile PBS, 4% paraformaldehyde for 15 min at room temperature. Cells were washed twice as above and covered with mounting oil (IBIDI).

5.7.3 Synthesis of WCNDs



WCNDs were obtained via microwave irradiation of an aqueous solution of L-Arginine (Arg), ethylenediamine (EDA), 1,4,5,8-naphthalenetetracarboxylic acid-1,8:4,5-dianhydride (NDA) and 2,6-dibromonaphthalene-1,4:5,8-tetracarboxylic dianhydride (Br2NDA) (1:0.5:0.9:0.8 mol). Typically, Arg (20.0 mg), EDA (4.0 μL), NDA (30.0 mg), Br2NDA (43.0 mg) and Milli-Q water (260.0 μL) were heated at 230 $^{\circ}\text{C}$, 220 psi and 300 W for 200 seconds. In the process of microwave heating, the color changed from yellow to brown as a result of formation of CNDs. The reaction mixture was then diluted with a few milliliters of water and the solution (pH 0.8) was filtered through a 0.1 μm microporous membrane. The pH of the solution was adjusted to pH 7.2 and then filtered through a 0.1 μm microporous membrane separating an orange solution that was dialyzed against pure water through a dialysis membrane for 2 days. The aqueous solution was then lyophilized giving an orange solid (18.0 mg).

WCNDs were also separated by means of SEC (Sephadex LH-20), and according to their elution times, five fractions were collected.

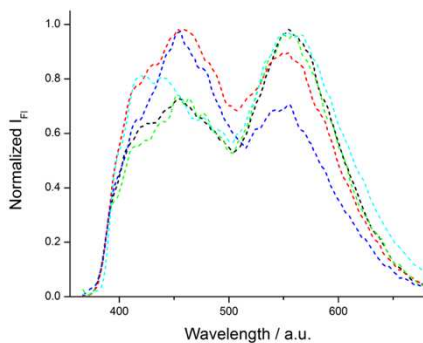
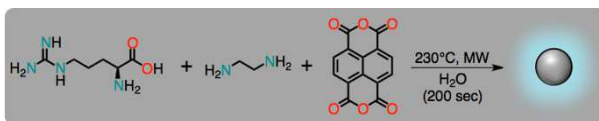


Figure S5.1 FL emission spectra recorded upon excitation at 350 nm for different fractions of WCNDs as separated from size-exclusion chromatography (in MeOH).

Interestingly, all of the fractions showed FL features that covered the entire emission spectra (the profiles slightly differ from main text due to the solvent – MeOH – used for the chromatography and recording the fluorescence spectra). Therefore, this is evidence that the white emission arises from WCNDs and could not be ascribed to a mixture of different emissive components.

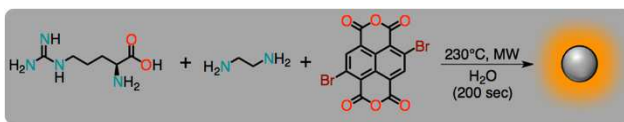
5.7.4 Synthesis of NDI•CNDs



NDI•CNDs were obtained via microwave irradiation of an aqueous solution of L-Arginine (Arg), ethylenediamine (EDA), 1,4,5,8-naphthalenetetracarboxylic acid-1,8:4,5-dianhydride (NDA) (1:0.5:0.9 mol). Typically, Arg (20.0 mg), EDA (4.0 μ L), NDA (30.0 mg) and Milli-Q water (260.0 μ L) were heated at 230 $^{\circ}$ C, 140 psi and 300 W for 200 seconds. In the process of microwave heating, the color changed from yellow to brown as a result of formation of CNDs. The reaction mixture was then diluted with a few milliliters of water and

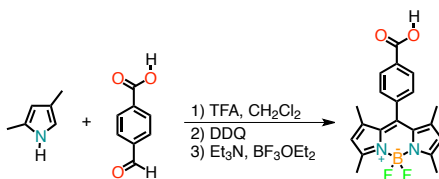
the solution (pH 8.9) was acidified (pH 1.3) and filtered through a 0.1 μm microporous membrane. The pH of the solution was adjusted to pH 7.2 and then filtered through a 0.1 μm microporous membrane separating a yellow solution that was dialyzed against pure water through a dialysis membrane for 2 days. The aqueous solution was then lyophilized giving a yellow solid (15.0 mg).

5.7.5 Synthesis of cNDI•CNDs



cNDI•CNDs were obtained via microwave irradiation of an aqueous solution of L-Arginine (Arg), ethylenediamine (EDA), 2,6-dibromonaphthalene-1,4:5,8-tetracarboxylic dianhydride (Br2NDA) (1:0.5:0.8 mol). Typically, Arg (20.0 mg), EDA (4.0 μL), Br2NDA (43.0 mg) and Milli-Q water (260.0 μL) were heated at 230 $^{\circ}\text{C}$, 140 psi and 300 W for 200 seconds. In the process of microwave heating, the color changed from yellow to brown as a result of formation of CNDs. The reaction mixture was then diluted with few milliliters of water and the solution (pH 1.2) was filtered through a 0.1 μm microporous membrane. The pH of the solution was adjusted to pH 7.2 and then filtered through a 0.1 μm microporous membrane separating a red solution that was dialyzed against pure water through a dialysis membrane for 2 days. The aqueous solution was then lyophilized giving a red solid (16.5 mg).

5.7.6 Synthesis of BODIPY-COOH

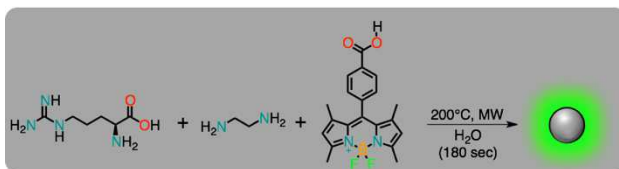


8-(4-Carboxyphenyl)-1,3,7,9-tetramethyl-BODIPY (BODIPY-COOH) was synthesized according to a modified literature procedure.¹²² A suspension of 2,4-dimethylpyrrole (1.1 mL, 12.3 mmol) and 4-carboxybenzaldehyde (0.9 g, 6.0 mmol) in CH_2Cl_2 (0.6 L) was purged with Ar for 2 h. One drop of TFA was added and the solution was stirred overnight at room temperature, in dark under Ar. At this point, a solution of DDQ (1.4 g, 6.0 mmol) in CH_2Cl_2 (0.1 L) was added and the reaction mixture was stirred for 30 min. Then, Et_3N (5.0 mL, 35.9 mmol) and $\text{BF}_3 \cdot \text{OEt}_2$ (5.0 mL, 40.5 mmol) were added and the mixture was stirred 30 min. more. The organic solution was then washed with H_2O (3×0.1 L) and then aqueous phase was extracted with CHCl_3 (3×0.1 L). The organic phases were collected, dried (Na_2SO_4) and then eliminated under reduced pressure. The mixture was purified by successive column chromatographies (SiO_2 , $\text{CHCl}_3 \rightarrow \text{CHCl}_3/\text{CH}_3\text{OH}$ 98:2) to obtain the product as dark red solid (0.7 g, 30% yield).

$^1\text{H-NMR}$ (500 MHz, Dimethylsulfoxide- d_6): δ 8.09 (*d*, $J = 8.0$ Hz, 2H), 7.52 (*d*, $J = 8.0$ Hz, 2H), 6.18 (*s*, 2H), 2.44 (*s*, 6H), 1.31 (*s*, 6H); $^{13}\text{C-NMR}$ (125 MHz, Dimethylsulfoxide- d_6): δ 167.37, 155.91, 143.31, 141.39, 138.45, 131.99, 130.70, 128.97, 127.36, 121.96, 14.69, 14.47.

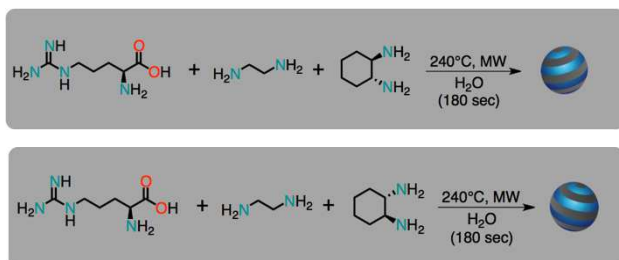
MS (MALDI, DHB): found 368.6 $[\text{M}+\text{H}]^+$. $\text{C}_{20}\text{H}_{19}\text{BF}_2\text{N}_2\text{O}_2$ requires 368.2.

5.7.7 Synthesis of BCNDs



BCNDs were obtained via microwave irradiation of an aqueous solution of L-Arginine (Arg), ethylenediamine (EDA), 8-(4-carboxyphenyl)-1,3,7,9-tetramethyl-BODIPY (BODIPY-COOH) (1:0.5:0.25 mol). Typically, Arg (40.0 mg), EDA (8.0 μ L), BODIPY (22.0 mg), and Milli-Q water (70.0 μ L) were heated at 200 °C, 5 psi and 200 W for 180 seconds. In the process of microwave heating, the color changed from yellow to red as a result of formation of CNDs. The reaction mixture was then diluted with a few milliliters of water and the solution was filtered through a 0.1 μ m microporous membrane. The pH of the solution was adjusted to pH 7.2 and then filtered through a 0.1 μ m microporous membrane separating a deep orange solution that was dialyzed against pure water through a dialysis membrane for 2 days. The aqueous solution was then lyophilized giving a red solid (20.0 mg).

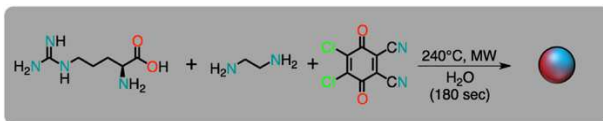
5.7.8 Synthesis of (—)- and (+)-CNDs



Chiral CNDs were obtained via microwave irradiation of an aqueous solution of L-Arginine (Arg) and (*RR*)-(—)-cyclohexanediamine or

(*SS*)-(+)-cyclohexanediamine (1:1 mol). Typically, Arg (87.0 mg), (*RR*)-(—)-cyclohexanediamine or (*SS*)-(+)-cyclohexanediamine (57.0 mg) and Milli-Q water (100.0 μL) were heated at 240 $^{\circ}\text{C}$, 60 psi and 200 W for 180 seconds. In the process of microwave heating, the color changed from yellow to dark brown as a result of formation of CNDs. The reaction mixture was then diluted with a few milliliters of water and the solution was filtered through a 0.1 μm microporous membrane separating a deep yellow solution that was dialyzed against pure water through a dialysis membrane for 2 days. The aqueous solution was then lyophilized giving a brownish solid ((—)-CNDs: 20.5 mg; (+)-CNDs: 22.0 mg).

5.7.9 Synthesis of qCNDs



qCNDs were obtained via microwave irradiation of an aqueous solution of L-Arginine (Arg), ethylenediamine (EDA), 2,3-dichloro-5,6-dicyano-1,4-benzoquinone (DDQ) (1:1:0.5 mol). Typically, Arg (87.0 mg), EDA (33.0 μL), DDQ (56.7 mg) and Milli-Q water (100.0 μL) were heated at 240 $^{\circ}\text{C}$, 26 bar and 200 W for 180 seconds. In the process of microwave heating, the solution changed color from transparent to brown as a result of formation of CNDs. The solution was diluted with water and was filtered through a 0.1 μm microporous membrane separating a deep yellow solution that was dialyzed against pure water through a dialysis membrane for 2 days. The aqueous solution of NCNDs was lyophilized giving a brownish solid (qCNDs: 19.0 mg).

5.7.10 Chiral supramolecular assembly

Chiral CNDS stock solutions were prepared by dissolving 1.9 mg in 2.5 mL of ultrapure water (obtained from Elga Purelab Flex system by Veolia). The stock solution of *meso*-tetrakis(4-sulfonatophenyl)porphyrin (H_2TPPS^4) was prepared by dissolving a small amount of solid in ultrapure water at pH 7 in order to obtain concentration about $2 \cdot 10^{-4}$ M, checked by the UV-Vis spectrophotometer using $\epsilon = 4.8 \cdot 10^{-5} M^{-1} cm^{-1}$ at $\lambda = 413$ nm.

The sample solution was prepared mixing CNDS and H_2TPPS^4 solutions at pH = 6.5. After 30 minutes, the pH was decrease at 2.5 in order to induce the formation of J-aggregates.

5.7.11 Supporting figures

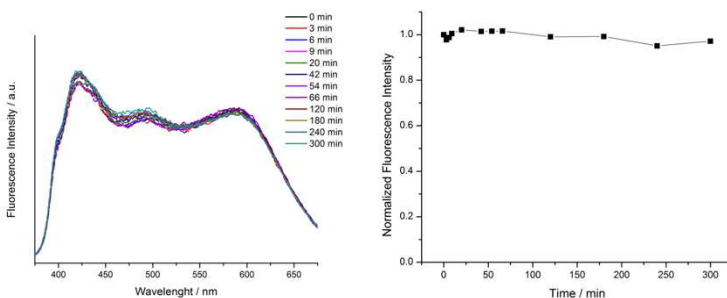


Figure S5.2 Dependence of FL intensity on UV excitation time for WCNDs. Emission spectra recorded upon excitation at 350 nm over 5 hours of UV irradiation (left) and normalized fluorescence intensity over time (right).

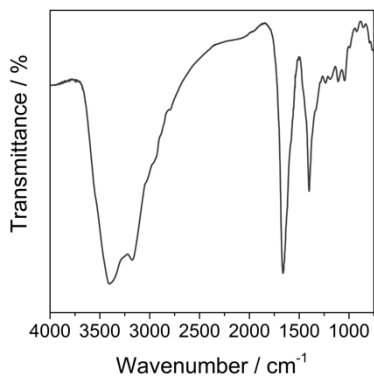


Figure S5.3 FT-IR spectrum of cNDI•CNDs.

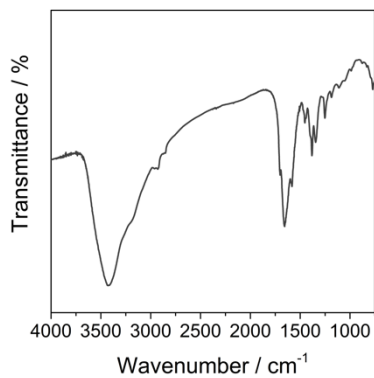


Figure S5.4 FT-IR spectrum of NDI•CNDs.

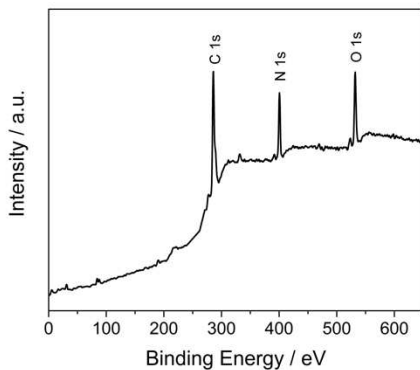


Figure S5.5 XPS survey of NDI•CNDs.

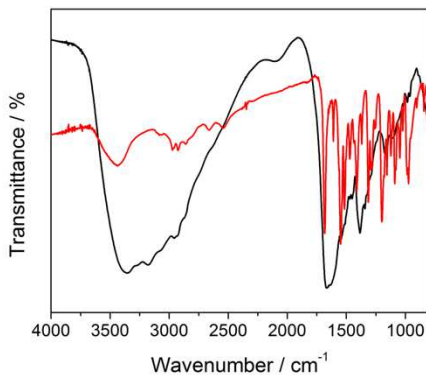


Figure S5.6 FT-IR spectra of BCNDs (black line) and BODIPY-COOH (red line).

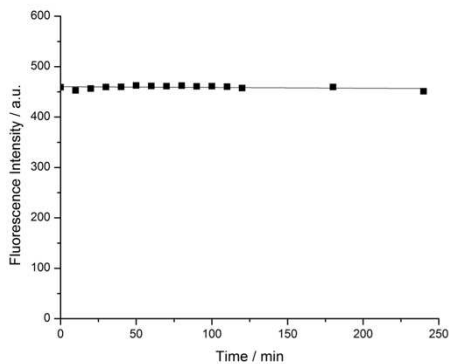


Figure S5.7 Dependence of FL intensity on UV excitation time for BCNDs.

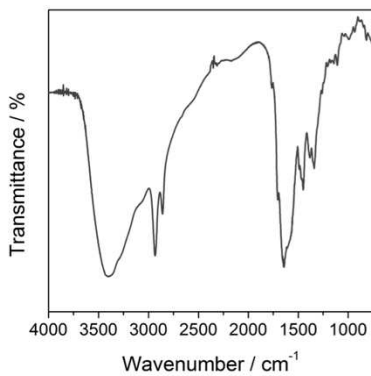


Figure S5.8 FT-IR spectrum of (—)-CNDs.

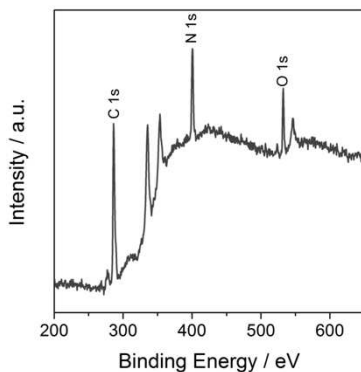


Figure S5.9 XPS survey of (—)-CNDs.

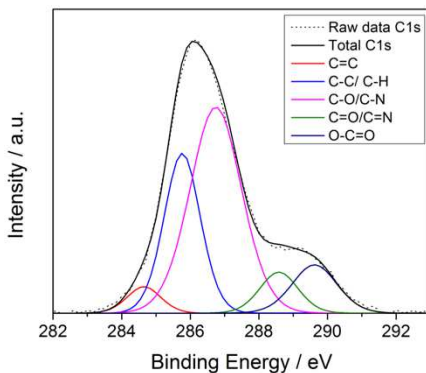


Figure S5.10 Deconvoluted C1s spectrum of (—)-CNDs.

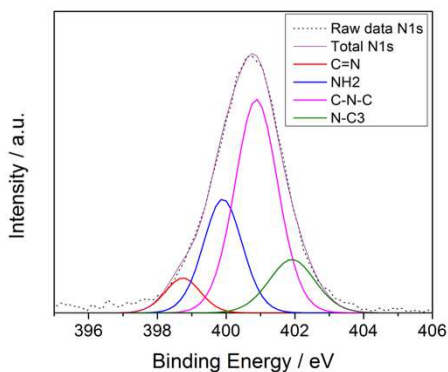


Figure S5.11 Deconvoluted N1s spectrum of (—)-CNDs.

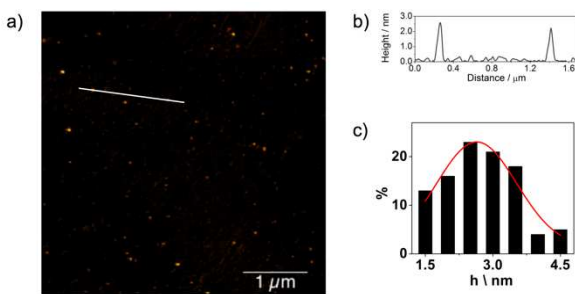


Figure S5.12 a) Tapping mode AFM image of (—)-CNDs ($4.4 \times 4.4 \mu\text{m}$) drop-casted on a mica substrate; b) height profile of (—)-CNDs; c) size histogram of (—)-CNDs with curve fit to the data using a Gaussian model ($2.64 \pm 0.89 \text{ nm}$. FWHM: 2.090).

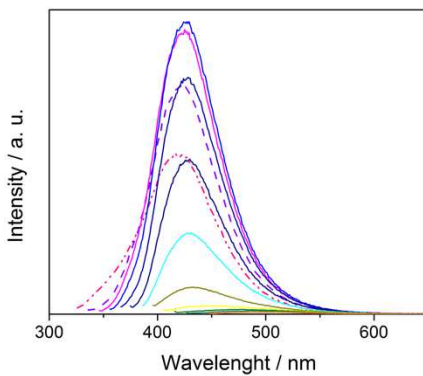


Figure S5.13 FL emission spectra of (—)-CNDs in water (298 K) at different excitation wavelengths (320-440 nm).

5.8 References

- (1) Reineck, P.; Francis, A.; Orth, A.; Lau, D. W. M.; Nixon-Luke, R. D. V.; Rastogi, I. Das; Razali, W. A. W.; Cordina, N. M.; Parker, L. M.; Sreenivasan, V. K. A.; *et al.* Brightness and Photostability of Emerging Red and Near-IR Fluorescent Nanomaterials for Bioimaging. *Adv. Opt. Mater.* **2016**, *4*, 1549–1557.
- (2) Tao, H.; Yang, K.; Ma, Z.; Wan, J.; Zhang, Y.; Kang, Z.; Liu, Z. In Vivo NIR Fluorescence Imaging, Biodistribution, and Toxicology of Photoluminescent Carbon Dots Produced from Carbon Nanotubes and Graphite. *Small* **2012**, *8*, 281–290.
- (3) Wei, W.; Xu, C.; Wu, L.; Wang, J.; Ren, J.; Qu, X. Non-Enzymatic-Browning-Reaction: A Versatile Route for Production of Nitrogen-Doped Carbon Dots with Tunable Multicolor Luminescent Display. *Sci. Rep.* **2014**, *4*, 3564–3570.
- (4) Zhu, S.; Meng, Q.; Wang, L.; Zhang, J.; Song, Y.; Jin, H.; Zhang, K.; Sun, H.; Wang, H.; Yang, B. Highly Photoluminescent Carbon Dots for Multicolor Patterning, Sensors, and Bioimaging. *Angew. Chem. Int. Ed.* **2013**, *52*, 3953–3957.
- (5) Cong, L.; Takeda, M.; Hamanaka, Y.; Gonda, K.; Watanabe, M.; Kumasaka, M.; Kobayashi, Y.; Kobayashi, M.; Ohuchi, N. Uniform Silica Coated Fluorescent Nanoparticles: Synthetic Method, Improved Light Stability and Application to Visualize Lymph Network Tracer. *PLoS One* **2010**, *5*, e13167.
- (6) Ow, H.; Larson, D. R.; Srivastava, M.; Baird, B. A.; Webb, W. W.; Wiesner, U. Bright and Stable Core–Shell Fluorescent Silica Nanoparticles. *Nano Lett.* **2005**, *5*, 113–117.
- (7) Song, S.; Qin, Y.; He, Y.; Huang, Q.; Fan, C.; Chen, H.-Y. Functional Nanoprobes for Ultrasensitive Detection of

-
- Biomolecules. *Chem. Soc. Rev.* **2010**, *39*, 4234–4243.
- (8) Yuan, F.; Li, S.; Fan, Z.; Meng, X.; Fan, L.; Yang, S. Shining Carbon Dots: Synthesis and Biomedical and Optoelectronic Applications. *Nano Today* **2016**, *11*, 565–586.
- (9) Ge, J.; Jia, Q.; Liu, W.; Guo, L.; Liu, Q.; Lan, M.; Zhang, H.; Meng, X.; Wang, P. Red-Emissive Carbon Dots for Fluorescent, Photoacoustic, and Thermal Theranostics in Living Mice. *Adv. Mater.* **2015**, *27*, 4169–4177.
- (10) Jiang, K.; Sun, S.; Zhang, L.; Lu, Y.; Wu, A.; Cai, C.; Lin, H. Red, Green, and Blue Luminescence by Carbon Dots: Full-Color Emission Tuning and Multicolor Cellular Imaging. *Angew. Chem. Int. Ed.* **2015**, *54*, 5360–5363.
- (11) Ding, H.; Yu, S.-B.; Wei, J.-S.; Xiong, H.-M. Full-Color Light-Emitting Carbon Dots with a Surface-State-Controlled Luminescence Mechanism. *ACS Nano* **2016**, *10*, 484–491.
- (12) Bao, L.; Zhang, Z. L.; Tian, Z. Q.; Zhang, L.; Liu, C.; Lin, Y.; Qi, B.; Pang, D. W. Electrochemical Tuning of Luminescent Carbon Nanodots: From Preparation to Luminescence Mechanism. *Adv. Mater.* **2011**, *23*, 5801–5806.
- (13) Hu, S.; Trinchì, A.; Atkin, P.; Cole, I. Tunable Photoluminescence across the Entire Visible Spectrum from Carbon Dots Excited by White Light. *Angew. Chem. Int. Ed.* **2015**, *54*, 2970–2974.
- (14) *CIE. Commission Internationale de l'Éclairage Proceedings*; Cambridge University Press 1931; Cambridge, 1932.
- (15) Chang, Y.-L.; Song, Y.; Wang, Z.; Helander, M. G.; Qiu, J.; Chai, L.; Liu, Z.; Scholes, G. D.; Lu, Z. Highly Efficient Warm White Organic Light-Emitting Diodes by Triplet Exciton Conversion. *Adv. Funct. Mater.* **2013**, *23*, 705–712.
- (16) Gaynor, W.; Hofmann, S.; Christoforo, M. G.; Sachse, C.; Mehra, S.; Salleo, A.; McGehee, M. D.; Gather, M. C.; Lüssem, B.; Müller-Meskamp, L.; *et al.* Color in the Corners: ITO-Free White OLEDs with Angular Color Stability. *Adv.*
-

- Mater.* **2013**, *25*, 4006–4013.
- (17) Gather, M. C.; Köhnen, A.; Meerholz, K. White Organic Light-Emitting Diodes. *Adv. Mater.* **2011**, *23*, 233–248.
- (18) *Can Be Found under* [Http://trinirobotics.com/wp-content/uploads/2014/07/rgb-Led-350x350.jpg](http://trinirobotics.com/wp-content/uploads/2014/07/rgb-Led-350x350.jpg).
- (19) Kasha, M. Characterization of Electronic Transitions in Complex Molecules. *Discuss. Faraday Soc.* **1950**, *9*, 14–19.
- (20) Lakowicz, J. R. *Principles of Fluorescence Spectroscopy*; Lakowicz, J. R., Ed.; Springer US: Boston, MA, 2006.
- (21) Valeur, B.; Mario, B. *Molecular Fluorescence: Principles and Applications. 2nd Ed.*; Weinheim: Wiley-VCH; 2012, 2012.
- (22) Bandichhor, R.; Petrescu, A. D.; Vespa, A.; Kier, A. B.; Schroeder, F.; Burgess, K. Water-Soluble Through-Bond Energy Transfer Cassettes for Intracellular Imaging. *J. Am. Chem. Soc.* **2006**, *128*, 10688–10689.
- (23) Nandhikonda, P.; Heagy, M. D. An Organic White Light-Emitting Dye: Very Small Molecular Architecture Displays Panchromatic Emission. *Chem. Commun.* **2010**, *46*, 8002–8004.
- (24) Cao, H.; Chang, V.; Hernandez, R.; Heagy, M. D. Matrix Screening of Substituted N-Aryl-1,8-Naphthalimides Reveals New Dual Fluorescent Dyes and Unusually Bright Pyridine Derivatives. *J. Org. Chem.* **2005**, *70*, 4929–4934.
- (25) Jiao, G.-S.; Thoresen, L. H.; Burgess, K. Fluorescent, Through-Bond Energy Transfer Cassettes for Labeling Multiple Biological Molecules in One Experiment. *J. Am. Chem. Soc.* **2003**, *125*, 14668–14669.
- (26) Mukherjee, S.; Thilagar, P. Organic White-Light Emitting Materials. *Dye. Pigment.* **2014**, *110*, 2–27.
- (27) Nandhikonda, P.; Heagy, M. D. Dual Fluorescent N-Aryl-2,3-Naphthalimides: Applications in Ratiometric DNA
-

-
- Detection and White Organic Light-Emitting Devices. *Org. Lett.* **2010**, *12*, 4796–4799.
- (28) Yang, Y.; Lowry, M.; Schowalter, C. M.; Fakayode, S. O.; Escobedo, J. O.; Xu, X.; Zhang, H.; Jensen, T. J.; Fronczek, F. R.; Warner, I. M.; *et al.* An Organic White Light-Emitting Fluorophore. *J. Am. Chem. Soc.* **2006**, *128*, 14081–14092.
- (29) Täuscher, E.; Weiß, D.; Beckert, R.; Fabian, J.; Assumpção, A.; Görls, H. Classical Heterocycles with Surprising Properties: The 4-Hydroxy-1,3-Thiazoles. *Tetrahedron Lett.* **2011**, *52*, 2292–2294.
- (30) Huynh, H. V.; He, X.; Baumgartner, T. Halochromic Generation of White Light Emission Using a Single Dithienophosphole Luminophore. *Chem. Commun.* **2013**, *49*, 4899–4901.
- (31) Liu, D.; Zhang, Z.; Zhang, H.; Wang, Y. A Novel Approach towards White Photoluminescence and Electroluminescence by Controlled Protonation of a Blue Fluorophore. *Chem. Commun.* **2013**, *49*, 10001–11003.
- (32) Tang, K.-C.; Chang, M.-J.; Lin, T.-Y.; Pan, H.-A.; Fang, T.-C.; Chen, K.-Y.; Hung, W.-Y.; Hsu, Y.-H.; Chou, P.-T. Fine Tuning the Energetics of Excited-State Intramolecular Proton Transfer (ESIPT): White Light Generation in A Single ESIPT System. *J. Am. Chem. Soc.* **2011**, *133*, 17738–17745.
- (33) Kwon, J. E.; Park, S.; Park, S. Y. Realizing Molecular Pixel System for Full-Color Fluorescence Reproduction: RGB-Emitting Molecular Mixture Free from Energy Transfer Crosstalk. *J. Am. Chem. Soc.* **2013**, *135*, 11239–11246.
- (34) Sakai, A.; Tanaka, M.; Ohta, E.; Yoshimoto, Y.; Mizuno, K.; Ikeda, H. White Light Emission from a Single Component System: Remarkable Concentration Effects on the Fluorescence of 1,3-Diaroylmethanoboron Difluoride. *Tetrahedron Lett.* **2012**, *53*, 4138–4141.
- (35) Karpiuk, J.; Karolak, E.; Nowacki, J. Tuneable White
-

-
- Fluorescence from Intramolecular Exciplexes. *Phys. Chem. Chem. Phys.* **2010**, *12*, 8804–8809.
- (36) Yagai, S.; Kitamura, A. Recent Advances in Photoresponsive Supramolecular Self-Assemblies. *Chem. Soc. Rev.* **2008**, *37*, 1520–1529.
- (37) Maiti, D. K.; Banerjee, A. A Peptide Based Two Component White Light Emitting System. *Chem. Commun.* **2013**, *49*, 6909–6911.
- (38) Giansante, C.; Raffy, G.; Schäfer, C.; Rahma, H.; Kao, M.; Olive, A. G. L.; Del Guerzo, A. White-Light-Emitting Self-Assembled NanoFibers and Their Evidence by Microspectroscopy of Individual Objects. *J. Am. Chem. Soc.* **2011**, *133*, 316–325.
- (39) Maiti, D. K.; Bhattacharjee, R.; Datta, A.; Banerjee, A. Modulation of Fluorescence Resonance Energy Transfer Efficiency for White Light Emission from a Series of Stilbene-Perylene Based Donor–Acceptor Pair. *J. Phys. Chem. C* **2013**, *117*, 23178–23189.
- (40) Molla, M. R.; Ghosh, S. Hydrogen-Bonding-Mediated J-Aggregation and White-Light Emission from a Remarkably Simple, Single-Component, Naphthalenediimide Chromophore. *Chem. - A Eur. J.* **2012**, *18*, 1290–1294.
- (41) Abbel, R.; van der Weegen, R.; Pisula, W.; Surin, M.; Leclère, P.; Lazzaroni, R.; Meijer, E. W.; Schenning, A. P. H. J. Multicolour Self-Assembled Fluorene Co-Oligomers: From Molecules to the Solid State via White-Light-Emitting Organogels. *Chem. - A Eur. J.* **2009**, *15*, 9737–9746.
- (42) Watanabe, K.; Sakamoto, T.; Taguchi, M.; Fujiki, M.; Nakano, T. A Chiral π -Stacked Vinyl Polymer Emitting White Circularly Polarized Light. *Chem. Commun.* **2011**, *47*, 10996–10998.
- (43) Sanju, K. S.; Ramaiah, D. White Photoluminescence and Electroluminescence from a Ternary System in Solution and
-

-
- a Polymer Matrix. *Chem. Commun.* **2013**, *49*, 11626–11628.
- (44) Takamizu, K.; Inagaki, A.; Nomura, K. Precise Synthesis of Poly(fluorene Vinylene)s Capped with Chromophores: Efficient Fluorescent Polymers Modified by Conjugation Length and End-Groups. *ACS Macro Lett.* **2013**, *2*, 980–984.
- (45) Kim, E.; Kyhm, J.; Kim, J. H.; Lee, G. Y.; Ko, D.-H.; Han, I. K.; Ko, H. White Light Emission from Polystyrene under Pulsed Ultra Violet Laser Irradiation. *Sci. Rep.* **2013**, *3*, 3253–3256.
- (46) Vijayakumar, C.; Praveen, V. K.; Ajayaghosh, A. RGB Emission through Controlled Donor Self-Assembly and Modulation of Excitation Energy Transfer: A Novel Strategy to White-Light-Emitting Organogels. *Adv. Mater.* **2009**, *21*, 2059–2063.
- (47) Ajayaghosh, A.; Praveen, V. K.; Vijayakumar, C.; George, S. J. Molecular Wire Encapsulated into π Organogels: Efficient Supramolecular Light-Harvesting Antennae with Color-Tunable Emission. *Angew. Chem. Int. Ed.* **2007**, *46*, 6260–6265.
- (48) Santhosh Babu, S.; Aimi, J.; Ozawa, H.; Shirahata, N.; Saeki, A.; Seki, S.; Ajayaghosh, A.; Möhwald, H.; Nakanishi, T. Solvent-Free Luminescent Organic Liquids. *Angew. Chem. Int. Ed.* **2012**, *51*, 3391–3395.
- (49) Rao, K. V.; Datta, K. K. R.; Eswaramoorthy, M.; George, S. J. Highly Pure Solid-State White-Light Emission from Solution-Processable Soft-Hybrids. *Adv. Mater.* **2013**, *25*, 1713–1718.
- (50) Malinge, J.; Allain, C.; Brosseau, A.; Audebert, P. White Fluorescence from Core-Shell Silica Nanoparticles. *Angew. Chem. Int. Ed.* **2012**, *51*, 8534–8537.
- (51) Melucci, M.; Zambianchi, M.; Barbarella, G.; Manet, I.; Montalti, M.; Bonacchi, S.; Rampazzo, E.; Rambaldi, D. C.; Zattoni, A.; Reschiglian, P. Facile Tuning from Blue to White
-

-
- Emission in Silica Nanoparticles Doped with Oligothiophene Fluorophores. *J. Mater. Chem.* **2010**, *20*, 9903–9909.
- (52) Zhang, X.; Rehm, S.; Safont-Sempere, M. M.; Würthner, F. Vesicular Perylene Dye Nanocapsules as Supramolecular Fluorescent pH Sensor Systems. *Nat. Chem.* **2009**, *1*, 623–629.
- (53) Wang, R.; Peng, J.; Qiu, F.; Yang, Y.; Xie, Z. Simultaneous Blue, Green, and Red Emission from Diblock Copolymer Micellar Films: A New Approach to White-Light Emission. *Chem. Commun.* **2009**, 6723–6725.
- (54) Wang, R.; Peng, J.; Qiu, F.; Yang, Y. Enhanced White-Light Emission from Multiple Fluorophores Encapsulated in a Single Layer of Diblock Copolymer Micelles. *Chem. Commun.* **2011**, *47*, 2787–2789.
- (55) Vijayakumar, C.; Sugiyasu, K.; Takeuchi, M. Oligofluorene-Based Electrophoretic Nanoparticles in Aqueous Medium as a Donor Scaffold for Fluorescence Resonance Energy Transfer and White-Light Emission. *Chem. Sci.* **2011**, *2*, 291–294.
- (56) Nishiyabu, R.; Sugino, Y.; Kubo, Y. White-Light Emitting Boronate Microparticles for Potential Use as Reusable Bright Chemosensors in Water. *Chem. Commun.* **2013**, *49*, 9869–9871.
- (57) Takamizu, K.; Nomura, K. Synthesis of Oligo(thiophene)-Coated Star-Shaped ROMP Polymers: Unique Emission Properties by the Precise Integration of Functionality. *J. Am. Chem. Soc.* **2012**, *134*, 7892–7895.
- (58) Tseng, K.-P.; Fang, F.-C.; Shyue, J.-J.; Wong, K.-T.; Raffy, G.; Del Guerso, A.; Bassani, D. M. Spontaneous Generation of Highly Emissive RGB Organic Nanospheres. *Angew. Chem. Int. Ed.* **2011**, *50*, 7032–7036.
- (59) Luo, Z.; Qi, G.; Chen, K.; Zou, M.; Yuwen, L.; Zhang, X.; Huang, W.; Wang, L. Microwave-Assisted Preparation of
-

- White Fluorescent Graphene Quantum Dots as a Novel Phosphor for Enhanced White-Light-Emitting Diodes. *Adv. Funct. Mater.* **2016**, 2739–2744.
- (60) Guo, X.; Wang, C.-F.; Yu, Z.-Y.; Chen, L.; Chen, S. Facile Access to Versatile Fluorescent Carbon Dots toward Light-Emitting Diodes. *Chem. Commun.* **2012**, 48, 2692–2694.
- (61) Wang, F.; Kreiter, M.; He, B.; Pang, S.; Liu, C. Synthesis of Direct White-Light Emitting Carbogenic Quantum Dots. *Chem. Commun.* **2010**, 46, 3309–3311.
- (62) Kwon, W.; Do, S.; Lee, J.; Hwang, S.; Kim, J. K.; Rhee, S.-W. Freestanding Luminescent Films of Nitrogen-Rich Carbon Nanodots toward Large-Scale Phosphor-Based White-Light-Emitting Devices. *Chem. Mater.* **2013**, 25, 1893–1899.
- (63) Chen, B.; Feng, J. White-Light-Emitting Polymer Composite Film Based on Carbon Dots and Lanthanide Complexes. *J. Phys. Chem. C* **2015**, 119, 7865–7872.
- (64) Mandani, S.; Sharma, B.; Dey, D.; Sarma, T. K. White Light Emission by Controlled Mixing of Carbon Dots and Rhodamine B for Applications in Optical Thermometry and Selective Fe³⁺ Detection. *RSC Adv.* **2016**, 6, 84599–84603.
- (65) Wang, Y.; Kalytchuk, S.; Wang, L.; Zhovtiuk, O.; Cepe, K.; Zboril, R.; Rogach, A. L. Carbon Dot Hybrids with Oligomeric Silsesquioxane: Solid-State Luminophores with High Photoluminescence Quantum Yield and Applicability in White Light Emitting Devices. *Chem. Commun.* **2015**, 51, 2950–2953.
- (66) Yuan, F.; Wang, Z.; Li, X.; Li, Y.; Tan, Z.; Fan, L.; Yang, S. Bright Multicolor Bandgap Fluorescent Carbon Quantum Dots for Electroluminescent Light-Emitting Diodes. *Adv. Mater.* **2017**, 29, 1604436.
- (67) Martindale, B. C. M.; Joliat, E.; Bachmann, C.; Alberto, R.; Reisner, E. Clean Donor Oxidation Enhances the H2
-

- Evolution Activity of a Carbon Quantum Dot-Molecular Catalyst Photosystem. *Angew. Chem. Int. Ed.* **2016**, *55*, 9402–9406.
- (68) Martindale, B. C. M.; Hutton, G. A. M.; Caputo, C. A.; Reisner, E. Solar Hydrogen Production Using Carbon Quantum Dots and a Molecular Nickel Catalyst. *J. Am. Chem. Soc.* **2015**, *137*, 6018–6025.
- (69) Harris, R. D.; Bettis Homan, S.; Kodaimati, M.; He, C.; Nepomnyashchii, A. B.; Swenson, N. K.; Lian, S.; Calzada, R.; Weiss, E. A. Electronic Processes within Quantum Dot-Molecule Complexes. *Chem. Rev.* **2016**, *116*, 12865–12919.
- (70) Tetsuka, H.; Nagoya, A.; Fukusumi, T.; Matsui, T. Molecularly Designed, Nitrogen-Functionalized Graphene Quantum Dots for Optoelectronic Devices. *Adv. Mater.* **2016**, 4632–4638.
- (71) Barron, L. D. *Molecular Light Scattering and Optical Activity*; Cambridge University Press: Cambridge, 2004.
- (72) Noguez, C.; Garzón, I. L. Optically Active Metal Nanoparticles. *Chem. Soc. Rev.* **2009**, *38*, 757–771.
- (73) Urbanova, M.; Malon, P. *Analytical Methods in Supramolecular Chemistry*; Schalley, C. A., Ed.; WILEY-VCH: Weinheim, 2007.
- (74) Pasteur, L. Recherches Sur Les Relations Qui Peuvent Exister Entre La Forme Crystalline, La Composition Chimique et Le Sens de La Polarisation Rotatoire. *Ann. Chim. Phys.* **1848**, *24*, 442–459.
- (75) Rayment, T.; McKendry, R.; Theoclitou, M.; Abell, C. Chiral Discrimination by Chemical Force Microscopy. *Nature* **1998**, *391*, 566–568.
- (76) Kühnle, A.; Linderoth, T. R.; Hammer, B.; Besenbacher, F. Chiral Recognition in Dimerization of Adsorbed Cysteine Observed by Scanning Tunnelling Microscopy. *Nature* **2002**, *415*, 891–893.
-

- (77) Kitaev, V. Chiral Nanoscale Building Blocks-from Understanding to Applications. *J. Mater. Chem.* **2008**, *18*, 4745–4749.
- (78) Wang, Y.; Xu, J.; Wang, Y.; Chen, H. Emerging Chirality in Nanoscience. *Chem. Soc. Rev.* **2013**, *42*, 2930–2962.
- (79) Gautier, C.; Bürgi, T. Chiral Gold Nanoparticles. *ChemPhysChem* **2009**, *10*, 483–492.
- (80) Chen, Z.; Wang, Q.; Wu, X.; Li, Z.; Jiang, Y.-B. Optical Chirality Sensing Using Macrocycles, Synthetic and Supramolecular Oligomers/ Polymers, and Nanoparticle Based Sensors. *Chem. Soc. Rev.* **2015**, *44*, 4249–4263.
- (81) Ben-Moshe, A.; Maoz, B. M.; Govorov, A. O.; Markovich, G. Chirality and Chiroptical Effects in Inorganic Nanocrystal Systems with Plasmon and Exciton Resonances. *Chem. Soc. Rev.* **2013**, *42*, 7028–7041.
- (82) Xia, Y.; Zhou, Y.; Tang, Z. Chiral Inorganic Nanoparticles: Origin, Optical Properties and Bioapplications. *Nanoscale* **2011**, *3*, 1374–1382.
- (83) Guerrero-Martínez, A.; Alonso-Gómez, J. L.; Auguie, B.; Cid, M. M.; Liz-Marzán, L. M. From Individual to Collective Chirality in Metal Nanoparticles. *Nano Today* **2011**, *6*, 381–400.
- (84) Ma, W.; Kuang, H.; Xu, L.; Ding, L.; Xu, C.; Wang, L.; Kotov, N. A. Attomolar DNA Detection with Chiral Nanorod Assemblies. *Nat. Commun.* **2013**, *4*, 2689; 1-8.
- (85) Milton, F. P.; Govan, J.; Mukhina, M. V.; Gun'ko, Y. K. The Chiral Nano-World: Chiroptically Active Quantum Nanostructures. *Nanoscale Horiz.* **2016**, *1*, 14–26.
- (86) Liu, Y.; Zhang, X. Metamaterials: A New Frontier of Science and Technology. *Chem. Soc. Rev.* **2011**, *40*, 2494–2507.
- (87) Zhao, Y.; Askarpour, A. N.; Sun, L.; Shi, J.; Li, X.; Alù, A. Chirality Detection of Enantiomers Using Twisted Optical
-

- Metamaterials. *Nat. Commun.* **2017**, *8*, 14180–1486.
- (88) Ben-Moshe, A.; Wolf, S. G.; Sadan, M. B.; Houben, L.; Fan, Z.; Govorov, A. O.; Markovich, G. Enantioselective Control of Lattice and Shape Chirality in Inorganic Nanostructures Using Chiral Biomolecules. *Nat. Commun.* **2014**, *5*, 4302–4310.
- (89) Ben-Moshe, A.; Govorov, A. O.; Markovich, G. Enantioselective Synthesis of Intrinsically Chiral Mercury Sulfide Nanocrystals. *Angew. Chem. Int. Ed.* **2013**, *52*, 1275–1279.
- (90) Mukhina, M. V.; Maslov, V. G.; Baranov, A. V.; Fedorov, A. V.; Orlova, A. O.; Purcell-Milton, F.; Govan, J.; Gun'ko, Y. K. Intrinsic Chirality of CdSe/ZnS Quantum Dots and Quantum Rods. *Nano Lett.* **2015**, *15*, 2844–2851.
- (91) Choi, J. K.; Haynie, B. E.; Tohgha, U.; Pap, L.; Elliott, K. W.; Leonard, B. M.; Dzyuba, S. V.; Varga, K.; Kubelka, J.; Balaz, M. Chirality Inversion of CdSe and CdS Quantum Dots without Changing the Stereochemistry of the Capping Ligand. *ACS Nano* **2016**, *10*, 3809–3815.
- (92) Baimuratov, A. S.; Rukhlenko, I. D.; Noskov, R. E.; Ginzburg, P.; Gun'ko, Y. K.; Baranov, A. V.; Fedorov, A. V. Giant Optical Activity of Quantum Dots, Rods, and Disks with Screw Dislocations. *Sci. Rep.* **2015**, *5*, 14712–1422.
- (93) Moloney, M. P.; Govan, J.; Loudon, A.; Mukhina, M.; Gun'ko, Y. K. Preparation of Chiral Quantum Dots. *Nat. Protoc.* **2015**, *10*, 558–573.
- (94) Evans, C. M.; Cass, L. C.; Knowles, K. E.; Tice, D. B.; Chang, R. P. H.; Weiss, E. A. Review of the Synthesis and Properties of Colloidal Quantum Dots: The Evolving Role of Coordinating Surface Ligands. *J. Coord. Chem.* **2012**, *65*, 2391–2414.
- (95) Hines, D. a; Kamat, P. V. Recent Advances in Quantum Dot Surface Chemistry. *ACS Appl. Mater. Interfaces* **2014**, *6*,
-

3041–3057.

- (96) Tohgha, U.; Varga, K.; Balaz, M. Achiral CdSe Quantum Dots Exhibit Optical Activity in the Visible Region upon Post-Synthetic Ligand Exchange with D- or L-Cysteine. *Chem. Commun.* **2013**, *49*, 1844–1846.
- (97) Tohgha, U.; Deol, K. K.; Porter, A. G.; Bartko, S. G.; Choi, J. K.; Leonard, B. M.; Varga, K.; Kubelka, J.; Muller, G.; Balaz, M. Ligand Induced Circular Dichroism and Circularly Polarized Luminescence in CdSe Quantum Dots. *ACS Nano* **2013**, *7*, 11094–11102.
- (98) Vázquez-Nakagawa, M.; Rodríguez-Pérez, L.; Herranz, M. A.; Martín, N. Chirality Transfer from Graphene Quantum Dots. *Chem. Commun.* **2016**, *52*, 665–668.
- (99) Suzuki, N.; Wang, Y.; Elvati, P.; Qu, Z.-B.; Kim, K.; Jiang, S.; Baumeister, E.; Lee, J.; Yeom, B.; Bahng, J. H.; *et al.* Chiral Graphene Quantum Dots. *ACS Nano* **2016**, *10*, 1744–1755.
- (100) Baumgartner, B.; Svirikova, A.; Binting, J.; Hametner, C.; Marchetti-Deschmann, M.; Unterlass, M. M. Green and Highly Efficient Synthesis of Perylene and Naphthalene Bisimides in Nothing but Water. *Chem. Commun.* **2017**, *53*, 1229–1232.
- (101) Sakai, N.; Mareda, J.; Vauthey, E.; Matile, S. Core-Substituted Naphthalenediimides. *Chem. Commun.* **2010**, *46*, 4225–4237.
- (102) Suraru, S.-L.; Würthner, F. Strategies for the Synthesis of Functional Naphthalene Diimides. *Angew. Chem. Int. Ed.* **2014**, *53*, 7428–7448.
- (103) Bhosale, S. V.; Jani, C. H.; Langford, S. J. Chemistry of Naphthalene Diimides. *Chem. Soc. Rev.* **2008**, *37*, 331–342.
- (104) Bhosale, S. Photoproduction of Proton Gradients with π -Stacked Fluorophore Scaffolds in Lipid Bilayers. *Science* **2006**, *313*, 84–86.
-

-
- (105) Guo, S.; Sun, J.; Ma, L.; You, W.; Yang, P.; Zhao, J. Visible Light-Harvesting Naphthalenediimide (NDI)-C60 Dyads as Heavy-Atom-Free Organic Triplet Photosensitizers for Triplet-triplet Annihilation Based Upconversion. *Dye. Pigment.* **2013**, *96*, 449–458.
- (106) Papirer, E.; Lacroix, R.; Donnet, J.; Nanse, G.; Fioux, P. XPS Study of the Halogenation of Carbon Black-Part 1. Bromination. *Carbon N. Y.* **1994**, *32*, 1341–1358.
- (107) Šimek, P.; Klímová, K.; Sedmidubský, D.; Jankovský, O.; Pumera, M.; Sofer, Z. Towards Graphene Iodide: Iodination of Graphite Oxide. *Nanoscale* **2015**, *7*, 261–270.
- (108) Zheng, J.; Liu, H.-T.; Wu, B.; Di, C.-A.; Guo, Y.-L.; Wu, T.; Yu, G.; Liu, Y.-Q.; Zhu, D.-B. Production of Graphite Chloride and Bromide Using Microwave Sparks. *Sci. Rep.* **2012**, *2*, 662–667.
- (109) Li, Y.; Chen, H.; Voo, L. Y.; Ji, J.; Zhang, G.; Zhang, G.; Zhang, F.; Fan, X. Synthesis of Partially Hydrogenated Graphene and Brominated Graphene. *J. Mater. Chem.* **2012**, *22*, 15021–15024.
- (110) Arcudi, F.; Đorđević, L.; Prato, M. Synthesis, Separation, and Characterization of Small and Highly Fluorescent Nitrogen-Doped Carbon NanoDots. *Angew. Chem. Int. Ed.* **2016**, *55*, 2107–2112.
- (111) Loudet, A.; Burgess, K. BODIPY Dyes and Their Derivatives: Syntheses and Spectroscopic Properties. *Chem. Rev.* **2007**, *107*, 4891–4932.
- (112) Ulrich, G.; Ziessel, R.; Harriman, A. The Chemistry of Fluorescent Bodipy Dyes: Versatility Unsurpassed. *Angew. Chem. Int. Ed.* **2008**, *47*, 1184–1201.
- (113) Vo-Hoang, Y.; Micouin, L.; Ronet, C.; Gachelin, G.; Bonin, M. Total Enantioselective Synthesis and In Vivo Biological Evaluation of a Novel Fluorescent BODIPY α -Galactosylceramide. *ChemBioChem* **2003**, *4*, 27–33.
-

-
- (114) Gießler, K.; Griesser, H.; Göhringer, D.; Sabirov, T.; Richert, C. Synthesis of 3'-BODIPY-Labeled Active Esters of Nucleotides and a Chemical Primer Extension Assay on Beads. *European J. Org. Chem.* **2010**, *2010*, 3611–3620.
- (115) Dilek, Ö.; Bane, S. L. Synthesis, Spectroscopic Properties and Protein Labeling of Water Soluble 3,5-Disubstituted Boron Dipyrromethenes. *Bioorg. Med. Chem. Lett.* **2009**, *19*, 6911–6913.
- (116) Dodani, S. C.; He, Q.; Chang, C. J. A Turn-On Fluorescent Sensor for Detecting Nickel in Living Cells. *J. Am. Chem. Soc.* **2009**, *131*, 18020–18021.
- (117) Niu, S.-L.; Ulrich, G.; Retailleau, P.; Harrowfield, J.; Ziessel, R. New Insights into the Solubilization of Bodipy Dyes. *Tetrahedron Lett.* **2009**, *50*, 3840–3844.
- (118) Niu, S. L.; Ulrich, G.; Ziessel, R.; Kiss, A.; Renard, P.-Y.; Romieu, A. Water-Soluble BODIPY Derivatives. *Org. Lett.* **2009**, *11*, 2049–2052.
- (119) Li, L.; Han, J.; Nguyen, B.; Burgess, K. Syntheses and Spectral Properties of Functionalized, Water-Soluble BODIPY Derivatives. *J. Org. Chem.* **2008**, *73*, 1963–1970.
- (120) Atilgan, S.; Ozdemir, T.; Akkaya, E. U. A Sensitive and Selective Ratiometric near IR Fluorescent Probe for Zinc Ions Based on the Distyryl-Bodipy Fluorophore. *Org. Lett.* **2008**, *10*, 4065–4067.
- (121) Jiao, L.; Li, J.; Zhang, S.; Wei, C.; Hao, E.; Vicente, M. G. H. A Selective Fluorescent Sensor for Imaging Cu²⁺ in Living Cells. *New J. Chem.* **2009**, *33*, 1888–1893.
- (122) Zhu, S.; Zhang, J.; Vegesna, G.; Luo, F.-T.; Green, S. A.; Liu, H. Highly Water-Soluble Neutral BODIPY Dyes with Controllable Fluorescence Quantum Yields. *Org. Lett.* **2011**, *13*, 438–441.
- (123) Lai, R. Y.; Bard, A. J. Electrogenerated Chemiluminescent Properties of Selected Dipyrromethene - BF₂ Dyes. *J. Phys.*
-

- Chem.* **2003**, *107*, 5036–5042.
- (124) Nepomnyashchii, A. B.; Cho, S.; Rossky, P. J.; Bard, A. J. Dependence of Electrochemical and Electrogenenerated Chemiluminescence Properties on the Structure of BODIPY Dyes. Unusually Large Separation between Sequential Electron Transfers. *J. Am. Chem. Soc.* **2010**, *132*, 17550–17559.
- (125) Nepomnyashchii, A. B.; Pistner, A. J.; Bard, A. J.; Rosenthal, J. Synthesis, Photophysics, Electrochemistry and Electrogenenerated Chemiluminescence of PEG-Modified BODIPY Dyes in Organic and Aqueous Solutions. *J. Phys. Chem. C* **2013**, *117*, 5599–5609.
- (126) Kiessling, R.; Klein, E.; Pross, H.; Wigzell, H. “Natural” killer Cells in the Mouse. II. Cytotoxic Cells with Specificity for Mouse Moloney Leukemia Cells. Characteristics of the Killer Cell. *Eur. J. Immunol.* **1975**, *5*, 117–121.
- (127) Moretta, A.; Bottino, C.; Vitale, M.; Pende, D.; Biassoni, R.; Mingari, M. C.; Moretta, L. Receptors for HLA Class-I-Molecules in Human Natural Killer Cells. *Annu. Rev. Immunol.* **1996**, *14*, 619–648.
- (128) Moretta, A.; Bottino, C.; Vitale, M.; Pende, D.; Cantoni, C.; Mingari, M. C.; Biassoni, R.; Moretta, L. Activating Receptors and Coreceptors Involved in Human Natural Killer Cell-Mediated Cytolysis. *Annu. Rev. Immunol.* **2001**, *19*, 197–223.
- (129) Ritz, J.; Schmidt, R. E.; Michon, J.; Hercend, T.; Schlossman, S. F. Characterization of Functional Surface Structures on Human Natural Killer Cells. *Adv. Immunol.* **1988**, *42*, 181–211.
- (130) Della Chiesa, M.; Pesce, S.; Muccio, L.; Carlomagno, S.; Sivori, S.; Moretta, A.; Marcenaro, E. Features of Memory-Like and PD-1+ Human NK Cell Subsets. *Front. Immunol.* **2016**, *7*, 351.

- (131) Vitale, M.; Bottino, C.; Sivori, S.; Sanseverino, L.; Castriconi, R.; Marcenaro, E.; Augugliaro, R.; Moretta, L.; Moretta, A. NKp44, a Novel Triggering Surface Molecule Specifically Expressed by Activated Natural Killer Cells, Is Involved in Non-Major Histocompatibility Complex-Restricted Tumor Cell Lysis. *J. Exp. Med.* **1998**, *187*, 2065–2072.
- (132) Gulino, A.; Mineo, P.; Scamporrino, E.; Vitalini, D.; Fragalà, I. Molecularly Engineered Silica Surfaces with an Assembled Porphyrin Monolayer as Optical NO₂ Molecular Recognizers. *Chem. Mater.* **2004**, *16*, 1838–1840.
- (133) Medforth, C. J.; Wang, Z.; Martin, K. E.; Song, Y.; Jacobsen, J. L.; Shelnut, J. A. Self-Assembled Porphyrin Nanostructures. *Chem. Commun.* **2009**, 7261–7277.
- (134) Romeo, A.; Castriciano, M. A.; Occhiuto, I.; Zagami, R.; Pasternack, R. F.; Scolaro, L. M. Kinetic Control of Chirality in Porphyrin J-Aggregates. *J. Am. Chem. Soc.* **2014**, *136*, 40–43.
- (135) van der Boom, T.; Hayes, R. T.; Zhao, Y.; Bushard, P. J.; Weiss, E. A.; Wasielewski, M. R. Charge Transport in Photofunctional Nanoparticles Self-Assembled from Zinc 5,10,15,20-Tetrakis(perylene-diimide)porphyrin Building Blocks. *J. Am. Chem. Soc.* **2002**, *124*, 9582–9590.
- (136) Anderson, H. L. Building Molecular Wires from the Colours of Life: Conjugated Porphyrin Oligomers. *Chem. Commun.* **1999**, 2323–2330.
- (137) Schick, G. A.; Schreiman, I. C.; Wagner, R. W.; Lindsey, J. S.; Bocian, D. F. Spectroscopic Characterization of Porphyrin Monolayer Assemblies. *J. Am. Chem. Soc.* **1989**, *111*, 1344–1350.
- (138) Fleischer, E. B.; Palmer, J. M.; Srivastava, T. S.; Chatterjee, A. Thermodynamic and Kinetic Properties of an Iron-Porphyrin System. *J. Am. Chem. Soc.* **1971**, *93*, 3162–3167.

-
- (139) Akins, D. L.; Zhu, H.-R.; Guo, C. Aggregation of Tetraaryl-Substituted Porphyrins in Homogeneous Solution. *J. Phys. Chem.* **1996**, *100*, 5420–5425.
- (140) Collings, P. J.; Gibbs, E. J.; Starr, T. E.; Vafek, O.; Yee, C.; Pomerance, L. A.; Pasternack, R. F. Resonance Light Scattering and Its Application in Determining the Size, Shape, and Aggregation Number for Supramolecular Assemblies of Chromophores. *J. Phys. Chem. B* **1999**, *103*, 8474–8481.
- (141) Pasternack, R.; Collings, P. Resonance Light Scattering: A New Technique for Studying Chromophore Aggregation. *Science* **1995**, *269*, 935–939.
- (142) Micali, N.; Romeo, A.; Lauceri, R.; Purrello, R.; Mallamace, F.; Scolaro, L. M. Fractal Structures in Homo- and Heteroaggregated Water Soluble Porphyrins. *J. Phys. Chem. B* **2000**, *104*, 9416–9420.
- (143) Koti, A. S. .; Taneja, J.; Periasamy, N. Control of Coherence Length and Aggregate Size in the J-Aggregate of Porphyrin. *Chem. Phys. Lett.* **2003**, *375*, 171–176.
- (144) Maiti, N. C.; Ravikanth, M.; Mazumdar, S.; Periasamy, N. Fluorescence Dynamics of Noncovalently Linked Porphyrin Dimers, and Aggregates. *J. Phys. Chem.* **1995**, *99*, 17192–17197.
- (145) Koti, A. S. R.; Periasamy, N. Self-Assembly of Template-Directed J-Aggregates of Porphyrin. *Chem. Mater.* **2003**, *15*, 369–371.
- (146) Ribó, J. M.; Crusats, J.; Farrera, J.-A.; Valero, M. L. Aggregation in Water Solutions of Tetrasodium Diprotonated Meso-tetrakis(4-Sulfonatophenyl)porphyrin. *J. Chem. Soc., Chem. Commun.* **1994**, 681–682.
- (147) Castriciano, M. A.; Romeo, A.; Zagami, R.; Micali, N.; Scolaro, L. M. Kinetic Effects of Tartaric Acid on the Growth of Chiral J-Aggregates of tetrakis(4-
-

-
- Sulfonatophenyl)porphyrin. *Chem. Commun.* **2012**, 48, 4872–4874.
- (148) Micali, N.; Villari, V.; Castriciano, M. A.; Romeo, A.; Monsù Scolaro, L. From Fractal to Nanorod Porphyrin J-Aggregates. Concentration-Induced Tuning of the Aggregate Size. *J. Phys. Chem. B* **2006**, 110, 8289–8295.
- (149) Castriciano, M. A.; Romeo, A.; Villari, V.; Micali, N.; Scolaro, L. M. Structural Rearrangements in 5,10,15,20-Tetrakis(4-Sulfonatophenyl)porphyrin J-Aggregates under Strongly Acidic Conditions. *J. Phys. Chem. B* **2003**, 107, 8765–8771.
- (150) Besenius, P.; Portale, G.; Bomans, P. H. H.; Janssen, H. M.; Palmans, A. R. A.; Meijer, E. W. Controlling the Growth and Shape of Chiral Supramolecular Polymers in Water. *Proc. Natl. Acad. Sci.* **2010**, 107, 17888–17893.
- (151) Escudero, C.; Crusats, J.; Díez-Pérez, I.; El-Hachemi, Z.; Ribó, J. M. Folding and Hydrodynamic Forces in J-Aggregates of 5-Phenyl-10,15,20-tris(4-Sulfophenyl)porphyrin. *Angew. Chem. Int. Ed.* **2006**, 45, 8032–8035.
- (152) D’Urso, A.; Randazzo, R.; Lo Faro, L.; Purrello, R. Vortexes and Nanoscale Chirality. *Angew. Chem. Int. Ed.* **2010**, 49, 108–112.
- (153) Randazzo, R.; Mammana, A.; D’Urso, A.; Lauceri, R.; Purrello, R. Reversible “Chiral Memory” in Ruthenium Tris(phenanthroline)-Anionic Porphyrin Complexes. *Angew. Chem. Int. Ed.* **2008**, 47, 9879–9882.
- (154) Hosamani, B.; Ribeiro, M. F.; da Silva Júnior, E. N.; Namboothiri, I. N. N. Catalytic Asymmetric Reactions and Synthesis of Quinones. *Org. Biomol. Chem.* **2016**, 14, 6913–6931.
- (155) Song, Y.; Buettner, G. R. Thermodynamic and Kinetic Considerations for the Reaction of Semiquinone Radicals to
-

- Form Superoxide and Hydrogen Peroxide. *Free Radic. Biol. Med.* **2010**, *49*, 919–962.
- (156) Prier, C. K.; Rankic, D. A.; MacMillan, D. W. C. Visible Light Photoredox Catalysis with Transition Metal Complexes: Applications in Organic Synthesis. *Chem. Rev.* **2013**, *113*, 5322–5363.
- (157) Kärkäs, M. D.; Johnston, E. V.; Verho, O.; Åkermark, B. Artificial Photosynthesis: From Nanosecond Electron Transfer to Catalytic Water Oxidation. *Acc. Chem. Res.* **2014**, *47*, 100–111.
- (158) Lasser, L.; Ronca, E.; Pastore, M.; De Angelis, F.; Cornil, J.; Lazzaroni, R.; Beljonne, D. Energy Level Alignment at Titanium Oxide–Dye Interfaces: Implications for Electron Injection and Light Harvesting. *J. Phys. Chem. C* **2015**, *119*, 9899–9909.
- (159) Kudo, A.; Miseki, Y. Heterogeneous Photocatalyst Materials for Water Splitting. *Chem. Soc. Rev.* **2009**, *38*, 253–278.

6 Experimental techniques

This chapter briefly describes the major instrumental methods employed in this doctoral thesis. The conditions used for all the experimental techniques are reported in the experimental sections of each chapters.

6.1 Absorption spectroscopy

In order to avoid influences exerted by other phenomena (mainly related to short-term changes in source intensity), a double-beam UV-Vis spectrophotometer is usually used.¹ A schematic diagram of a double-beam UV-Vis spectrophotometer is shown in **Figure 6.1**. The monochromator selects a particular wavelength from the light source, which is split into two separate beams. These two beams are guided through the sample and through the pure solvent (reference) using optically transparent cells (generally quartz cuvettes). The intensity of the two beams is compared to give the respective absorbances.

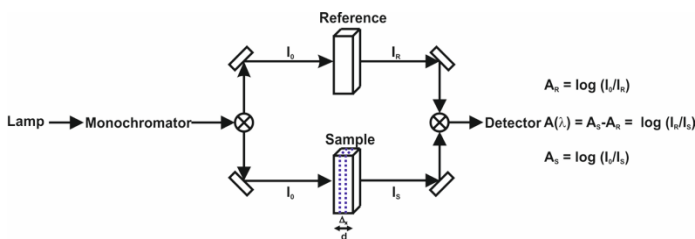


Figure 6.1 Schematic illustration of a double beam spectrophotometer.

Considering a thin slab of solution of thickness dx , that contains n light-absorbing molecules/cm³ (**Figure 6.1**): if σ is the effective cross-section for absorption in cm², the light intensity dI absorbed per

thickness dx is proportional to the intensity of the incident light I , σ and the number of molecules per cm^3 :

$$\frac{dI}{dx} = I\sigma n$$

Rearrangements and integrations, subject to the boundary condition $I = I_0$ at $x = 0$, yields the Beer-Lambert equation, which is generally used in the following alternative form:

$$\log \frac{I_0}{I} = \varepsilon cd$$

where ε is the molar extinction coefficient (in $\text{M}^{-1} \text{cm}^{-1}$) and c is the concentration in moles/liter. Also the transmittance (T) is frequently used and it is defined as the ratio between the intensity of light that passes through a medium (transmitted light, I) and the intensity of the incident light (I_0), *i.e.* as the negative logarithm of the absorbance. Beer's Law predicts that the optical density is directly proportional to the concentration of the absorbing species. However, deviations from Beer's law (positive or negative) can result from both instrumental and intrinsic causes. For instance, biological and/or supramolecular systems that contain macromolecules or other large aggregates, can lead to turbid samples that scatter light. The optical density resulting from scatter will be proportional to $1/\lambda^4$ (Rayleigh scattering), and may thus be easily recognized as a background absorption that increases rapidly with decreasing wavelength.

6.2 Fluorescence spectroscopy

Fluorescence is one of the possible process following light absorption and generally results from the lowest energy vibrational state.² While an emission spectrum is the wavelength distribution of an emission measured at a single constant excitation wavelength, an excitation spectrum is the dependence of emission intensity, measured at a

single emission wavelength, upon scanning the excitation wavelength. Such spectra can be presented on either a wavelength scale or a wavenumber scale. Light of a given energy can be described in terms of its wavelength or wavenumber.

A simple and schematic representation of a spectrofluorometer is reported in **Figure 6.2**. It basically consists on a light source, excitation/emission monochromators and photomultiplier tubes that collect the emission of the sample at 90° .

Different detectors need to be used depending on the considered region of the light spectrum. The excitation spectra have to be corrected for source intensity (lamp and excitation grating), for detector spectral response and emission grating by standard correction curves. Optical filters are used to remove unwanted wavelengths in the excitation beam, or to remove scattered light from the emission channel. Polarizers (that can be present in both the excitation and emission light paths) require an accurate angular positioning for the measurement of fluorescence anisotropies.

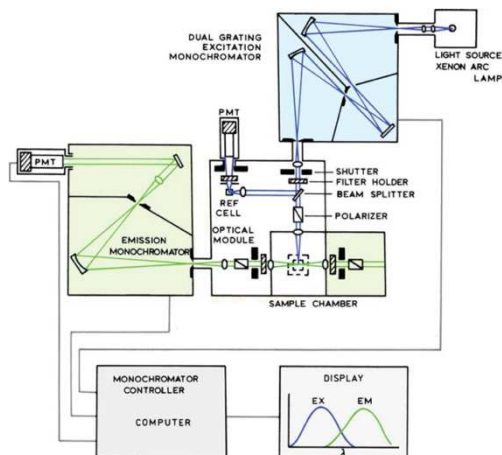


Figure 6.2 Schematic diagram of a spectrofluorometer.

Contrary to absorption spectroscopy in which a double-beam configuration can avoid many artefacts, there is no an ideal spectrofluorometer. The available instruments do not yield true excitation or emission spectra. This is because of the spectral output of the light sources and the wavelength-dependent efficiency of the monochromators and detector tubes are not uniform. The polarization or anisotropy of the emitted light can also affect the measured fluorescence intensities because the efficiency of gratings depends on polarization. Therefore, emission spectra recorded on different instruments can be different because of the wavelength-dependent sensitivities of the instruments.

6.3 Luminescence quantum yield

The photoluminescence quantum yield (PLQY) of a molecule in solution varies depending on the experimental conditions, including the type of solvent, the concentrations of the sample, dissolved oxygen in the solution, temperature, and excitation wavelength.²⁻⁴ When the physical conditions are fully specified, the quantum yield can, in principle, be precisely determined. However, a number of pitfalls exist and must be considered to determine reliable quantum yields. These include polarization effects, refractive index effects, re-absorption/ re-emission effects, internal reflection effects, and the spectral sensitivity of the detection system.

Luminescence quantum yields methods can be classified into absolute (or primary) methods and relative (or secondary) methods.

In secondary methods, the quantum yield of a sample solution is determined by comparing the integrated fluorescence intensity with a standard solution under identical conditions of incident irradiance. Thus, it is necessary to correct for the spectral sensitivity of the instrument and the measured quantum yield is as accurate as the certainty of the quantum yield of the fluorescence standard.

The absorption factors f of the standard and the sample are calculated from the measured absorbance values (A) at the excitation wavelength using the following equation:

$$f = 1 - 10^{-A\lambda_{exc}}$$

The fluorescence quantum yields are calculated according to the equation:

$$\Phi_x = \Phi_{st} \cdot \frac{I_x}{I_{st}} \cdot \frac{f_{st}}{f_x} \cdot \frac{\eta_x^2}{\eta_{st}^2}$$

where I is the measured integrated fluorescence emission intensity, f is the absorption factor, η is the refractive index of the solvent, Φ is the quantum yield and the index x denotes the sample, while the index st denotes the standard. In this expression it is assumed that sample and reference are excited at the same wavelength.

The absolute methods require performing various complex corrections to obtain accurate quantum yields. Many different absolute (or primary) methods for determining PLQY have been developed such as the Weber and Teale methods (using scattering solutions as standard).⁵ Another approach consists in the use of an integrating sphere (**Figure 6.3**), which collects all the emitted photons with a calibrated photodiode and sets them into relation with the number of absorbed photons. In this way the effects of polarization, scattering and refractive index are eliminated from the measurements. Light from a xenon lamp is monochromatized at the selected wavelength and guided by an optical fiber into the integrating sphere. The emitted light from the sample is collected by a detector, after passing through another optical fiber and a second monochromator.

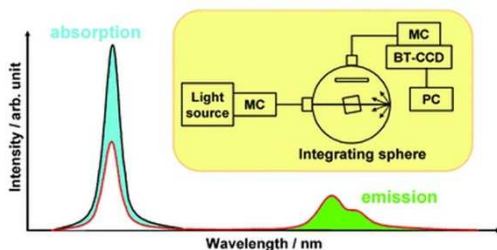


Figure 6.3 Schematic representation of an integrating sphere for measuring absolute luminescence quantum yields. MC stands for monochromator, and BT-CCD is a back thinned CCD. The number of photons absorbed is proportional to the difference of the integrated excitation light profiles, while the number of photons emitted is proportional to the area under the fluorescence spectrum.

The PLQY is then calculated from the number of photons absorbed (difference of the integrated excitation light profiles) and the number of photons emitted (integrated fluorescence spectrum), according to the equation:

$$\Phi = \frac{PN(Em)}{PN(Abs)} = \frac{\int \frac{\lambda}{hc} [I_{em}^{sample}(\lambda) - I_{em}^{reference}(\lambda)] d\lambda}{\int \frac{\lambda}{hc} [I_{exc}^{reference}(\lambda) - I_{exc}^{sample}(\lambda)] d\lambda}$$

where $PN(Abs)$ is the number of photons absorbed by the sample and $PN(Em)$ is the number of photons emitted from the sample, λ is the wavelength, h is Planck constant, c is the velocity of light, I_{exc}^{sample} and $I_{exc}^{reference}$ are the integrated intensities of the excitation light with and without the sample respectively; I_{em}^{sample} and $I_{em}^{reference}$ are the photoluminescence intensities with and without the sample, respectively. In this thesis, it was used a Hamamatsu Photonics absolute PL quantum yield measurement system (C9920-02) equipped with a L9799-01 CW Xenon light source (150 W), monochromator, C7473 photonic multichannel analyzer, integrating

sphere and employing U6039-05 PLQY measurement software (Hamamatsu Photonics, Ltd., Shizuoka, Japan).

6.4 Lifetime measurement

Time-resolved experiments, such as the excited state lifetime determination, can be carried out by time-correlated single-photon counting (TCSPC).² The schematic diagram of the setup is shown in **Figure 6.4**. The experiment starts with the excitation pulse (either a flash lamp or a laser), which excites the sample and sends a signal to the electronics. This signal is passed through a constant function discriminator (CFD), which accurately measures the arrival time of the pulse.

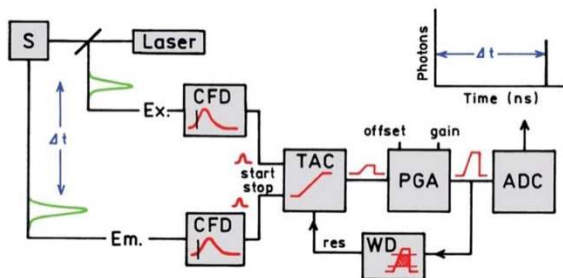


Figure 6.4 Electronic schematic for TCSPC.

The signal (START) is passed to a time-to-amplitude converter (TAC), which starts the charging of the capacitor by generating a voltage ramp. The voltage increases linearly with the time on the nanosecond timescale. A second channel detects the pulse from the single detected photon (STOP). The arrival time of the signal is also accurately determined using a CFD, which sends a signal to stop the voltage ramp. TAC now contains a voltage proportional to the time delay and it is stored in a histogram in which the x-axis in the histogram is the time difference between START and STOP signal

and the y-axis is the number of photons detected for this time difference. The voltage is amplified by a programmable gain amplifier (PGA) and converted to a numerical value by the analog-to-digital converter (ADC). To minimize false readings the signal is restricted to given range of voltages. If the signal is not within this range the event is suppressed by a window discriminator (WD). The voltage is converted to a digital value that is stored as a single event with the measured time delay. By repetitive measurements, a statistical time distribution of the emitted photons is obtained.

The multichannel analyzer consists of a multichannel card. The light input is discriminated for its intensity and if the input pulse amplitude falls within the threshold of the lower level and the upper level discriminators, the control and logic circuit are enabled and the peak amplitude is stored. Generally, the signal intensities are collected in different channels and the collected total light intensities are counted and correlated to the time frame of each channel giving an intensity-time profile.

In this thesis, time-resolved measurements up to $\sim 10 \mu\text{s}$ were performed using the TCSPC option (PicoHarp) of a FluoTime 300 “EasyTau” apparatus (PicoQuant) equipped with subnanosecond LDH sources (375, 405, 440, 510 and 640 nm, with 50-100 ps pulse-width) powered by a PicoQuant PDL 820 variable (0.2-80 MHz) pulsed power supply. A PMA-C was employed for the detection in the UV-visible (200-900 nm). For excited state lifetimes $> 10 \mu\text{s}$, NanoHarp 250 MCS (Multi Channel scaler Card) histogram accumulating real-time processor was employed. The decays were analyzed by means of PicoQuant FluoFit Global Fluorescence Decay Analysis Software (PicoQuant GmbH, Germany). The quality of the fit was assessed by minimizing the reduced χ^2 function and by visual inspection of the weighted residuals. For multi-exponential decays, the intensity, namely $I(t)$, has been assumed to decay as the sum of

the individual single exponential decays: $I(t) = \sum_{i=1}^n a_i e^{-\frac{t}{\tau_i}}$ where τ_i are the decay times and a_i are the amplitudes of the component at $t = 0$. The percentages to the pre-exponential factors, a_i , are listed upon normalization.

6.5 X-ray photoelectron spectroscopy

X-ray photoelectron spectroscopy is a powerful surface analysis technique.⁶ It provides qualitative and quantitative information on the elements present on the surface of the sample, as well as on their electronic structure and chemical state/bonding. When a sample is irradiated by low energy X-rays (200~2000 eV) mono-energetic photons knock out surface atom core electrons. These electrons have a certain kinetic energy and are referred to as photoelectrons (**Figure 6.5**). The energy spectrum of the emitted photoelectrons is determined by means of a high-resolution electron spectrometer, which sees the surface in the area of a circle with 40 μm of diameter. A typical XPS spectrum is a plot of the number of electrons detected versus their kinetic energy. All elements with order number 3 and above can be measured. Counting and measuring kinetic energy of the emitted photoelectrons enables determination of their binding energy, since the energy of X-rays photons is known. Each element has a unique set of binding energies, therefore it is possible to clearly identify the elements at the surface and their chemical composition. Semi-quantitative analysis of the element concentration can also be performed, since it is correlated to the intensity of the peak weighted by the sensitivity factor. Therefore, the atomic concentrations of the elements can be calculated from the peak areas of elemental peaks.

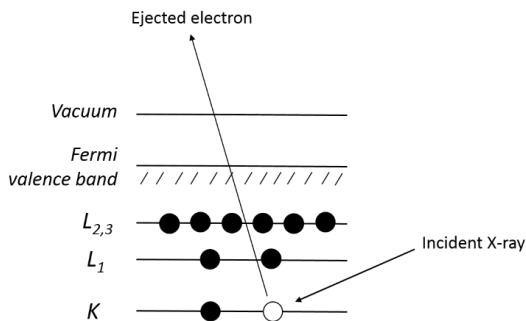


Figure 6.5 Schematic diagram of the XPS process.

6.6 Atomic force microscopy

Atomic Force Microscopy (AFM) is a scanning probe microscopy (SPM).^{7,8} It is a state-of-the-art instrument to image, measure and manipulate matter at the nano-level. It provides a 3D profile of the surface by measuring forces between a sharp probe (<10 nm) and the surface at very short distance (0.2-10 nm probe-sample separation). The probe is supported on a flexible cantilever. The AFM tip “gently” touches the surface and records the small force between the probe and the surface. The amount of force between the probe and the sample is dependent on the spring constant (stiffness) of the cantilever and the distance between the probe and the sample surface. This force can be described by using Hooke’s Law. If the spring constant of cantilever (typically ~ 0.1 -1 N/m) is less than surface, the cantilever bends and the deflection is monitored. The resulting forces range from nN to μ N in open air. The motion of the probe across the surface is controlled by using a feedback loop and a piezoelectric scanner. The deflection of the probe is typically measured by a “beam bounce” method. A photodiode detector measures the bending of the cantilever during the scan of the tip over the sample. The measured cantilever deflections are used to generate a map of the surface topography.

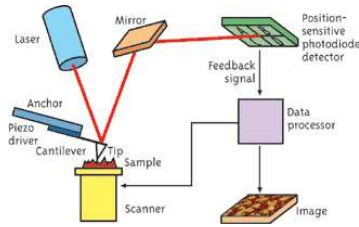


Figure 6.6 Schematic representation of an AFM instrument.

The dominant interactions at short probe-sample distances are Van der Waals (VdW) interactions. During the contact with the sample, the probe predominately experiences repulsive VdW forces (contact mode) leading to the tip deflection. As the tip moves further away from the surface, attractive VdW forces are dominant (non-contact mode).

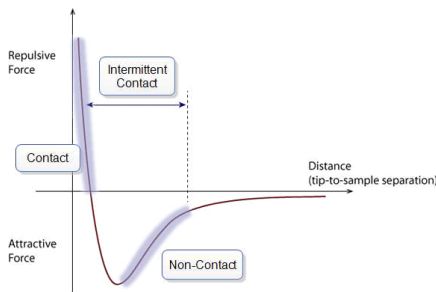


Figure 6.7 Plot of the force as a function of probe-sample separation.

There are three primary imaging modes in AFM: contact (<0.5 nm probe-surface separation), intermittent contact (or tapping mode) ($0.5-2$ nm probe-surface separation) and non-contact ($0.1-10$ nm probe-surface separation). The principle of contact AFM is detecting the force exerted between the tip and the sample surface. When the spring constant of the cantilever is less than surface, the cantilever

bends. The force on the tip is repulsive and, maintaining a constant cantilever deflection (using the feedback loops), the force between the probe and the sample remains constant and an image of the surface is obtained. It can be used for fast scanning and for rough samples, but soft samples could be damaged.

In tapping mode, the imaging is similar to contact, but the cantilever is oscillated at its resonant frequency. The probe lightly “taps” on the sample surface during scanning, contacting the surface at the bottom of its swing. By maintaining a constant oscillation amplitude, a constant tip-sample interaction is maintained and an image of the surface is obtained. It allows high resolution of samples without any damages, but need slow scan speeds.

In non-contact mode the probe does not contact the sample surface, but is forced to oscillate near its resonant frequency. Using a feedback loop to monitor changes in the amplitude due to the attractive VdW forces, the surface topography can be measured. The main advantage is that a low force is exerted on the sample (10^{-12} N), but compared to other imaging modes, generally, provides lower resolution and needs ultra-high vacuum condition to provide the best imaging.

6.7 Electrochemistry

6.7.1 Cyclic voltammetry

Cyclic voltammetry is the most used electroanalytical technique. It is performed by connecting a potentiostat to an electrochemical cell.⁹ The cell contains the sample solution and three electrodes: working electrode (WE), reference electrode (RE) and counter electrode (CE). A cyclic voltammogram is obtained by applying the working electrode potential swept linearly between two voltages at a fixed rate. **Figure 6.8** shows an example of a cyclic voltammogram. As the potential is swept back and forth, it crosses the formal potential, E_0 ,

of an analyte and a current flows through the electrode, that either oxidizes or reduces the analyte.

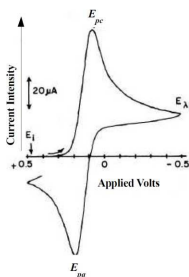


Figure 6.8 Example of a cyclic voltammogram.

As shown in **Figure 6.8**, when the potential sweep back and forth two peaks are obtained: the peak potential for the anodic sweep, E_{pa} , and the peak potential for the cathodic peak, E_{pc} . The difference between the two, ΔE , if the redox couple is reversible, satisfy the relationship $n \Delta E = 59 \text{ mV}$, where n is the number of electrons involved in the redox couple. Moreover, the anodic peak current, i_{pa} , is equal to the cathodic peak current, i_{pc} , so that the relationship $(i_{pa}/i_{pc}) = 1$ also holds true for the reversible redox couple. Besides, if $59 \text{ mV} < \Delta E < 100 \text{ mV}$ the redox couple is described as quasi-reversible, and if $\Delta E > 100 \text{ mV}$ the redox couple is described as irreversible. The formal potential E_0 for a reversible redox couple is determined as the average of the two peak potentials as follows:

$$E_0 = \frac{(E_{pa} + E_{pc})}{2}$$

6.7.2 Potentiostatic techniques

In a potential step experiment, two responses can be recorded, whereby the potential of a working electrode is changed

instantaneously and the current time (galvanostatic) or the charge time (potentiostatic) is found.⁹ In chronoamperometry, the potential is stepped so as to drive a Faradaic reaction. This potential is held while the current with time is monitored at the electrode (**Figure 6.9**). At the initial potential, no significant current flows. At the final potential, the analyte is consumed at the electrode surface. There is a depletion of the concentration of the analyte near the electrode. The current response is shown by a rapid increase followed by decay as the analyte is exhausted and equilibrium is reached. In this case, the charge for reduction is calculated by integrating the area under the current versus time curve, within the limits of the initial to final deposition time.

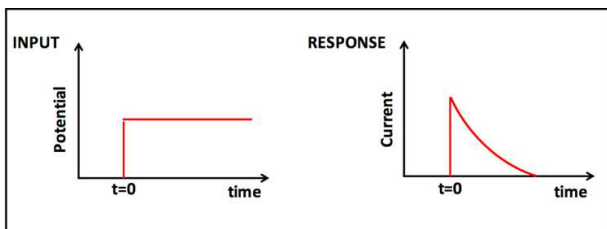


Figure 6.9 Variation of the current in potentiostatic method.

6.8 References

- (1) Tissue, B. M. Ultraviolet and Visible Absorption Spectroscopy. In *Characterization of Materials*; John Wiley & Sons, Inc.: Hoboken, NJ, USA, 2002.
- (2) Lakowicz, J. R. *Principles of Fluorescence Spectroscopy*; Lakowicz, J. R., Ed.; Springer US: Boston, MA, 2006.
- (3) Crosby, G. A.; Demas, J. N. Measurement of Photoluminescence Quantum Yields. A Review. *J. Phys. Chem.* **1971**, *75*, 991–1024.
- (4) Würth, C.; Grabolle, M.; Pauli, J.; Spieles, M.; Resch-Genger, U. Relative and Absolute Determination of Fluorescence Quantum Yields of Transparent Samples. *Nat. Protoc.* **2013**, *8*, 1535–1550.
- (5) Hercules, D. M.; Frankel, H. Colloidal Silica as a Standard for Measuring Absolute Fluorescence Yield. *Science* **1960**, *131*, 1611–1612.
- (6) Watts, J. F.; Wolstenholme, J. *An Introduction to Surface Analysis by XPS and AES*; Wiley-VCH, Ed.; John Wiley & Sons, Ltd: Chichester, UK, 2003.
- (7) Lang, H. P.; Gerber, C.; Samori, P. *STM and AFM Studies on (Bio)molecular Systems: Unravelling the Nanoworld*; Samori, P., Ed.; Topics in Current Chemistry; Springer Berlin Heidelberg: Berlin, Heidelberg, 2008; Vol. 285.
- (8) Haugstad, G. *Atomic Force Microscopy*; John Wiley & Sons, Inc.: Hoboken, NJ, USA, 2012.
- (9) Bard, A. J.; Faulkner, L. R. *Electrochemical Methods. Fundamentals and Applications.*; John Wiley & Sons, Inc., 2000.

Curriculum Vitae

- 1988** Born on August 8th in Palermo (Italy)
- 2001-2006** High School Diploma, Liceo Classico Giovanni Meli, Palermo (Italy)
- 2001-2013** Master Degree in Chemistry, thesis under the supervision of *Dr. Serena Riela* and *Prof. Renato Noto*, University of Palermo (Italy)
- 2013-2016** Ph.D. in Chemical Science under the supervision of *Prof. Maurizio Prato*, University of Trieste (Italy)
- 2015** Visiting Ph.D.-Erasmus Traineeship Program-under the supervision of *Prof. Luisa De Cola*, Institut de Science et d'Ingénierie Supramoléculaires, Université de Strasbourg (France)

Publications

- (1) Arcudi F.; Cavallaro G.; Lazzara G.; Massaro M.; Milioto S.; Noto R.; Riela S. Selective Functionalization of Halloysite Cavity by Click Reaction: Structured Filler for Enhancing Mechanical Properties of Bionanocomposite Films *J. Phys. Chem. C*, **2014**, *118* (27), 15095-15101.
- (2) Riela S.; Arcudi F.; Lazzara G.; Lo Meo P.; Guernelli S.; D'Anna F.; Milioto S.; Noto R. Binding abilities of new cyclodextrin-cucurbituril supramolecular hosts *Supramol. Chem.*, **2015**, *27*, 233.
- (3) Arcudi, F.; Đorđević, L.; Prato, M. Synthesis, Separation, and Characterization of Small and Highly Fluorescent Nitrogen-Doped Carbon NanoDots. *Angew. Chem. Int. Ed.* **2016**, *55*, 2107–2112.
- (4) Arcudi, F.; Đorđević, L.; Prato, M. Rationally Designed Carbon Nanodots towards Pure White-Light Emission *Angew. Chem. Int. Ed.* **2017**, *56*, 4170-4173.

- (5) Carrara, S.; Arcudi, F.; Prato, M., De Cola, L. Amine-Rich Nitrogen-Doped Carbon NanoDots as Platform for Self-Enhancing Electrochemiluminescence *Angew. Chem. Int. Ed.* **2017**, *56*, 4757-4761. Featured as cover picture.
 - (6) Arcudi, F.; D'Urso, A.; Đorđević, L.; Purrello, R.; Prato, M. Synthesis of inherently chiral carbon nanodots and their use as template for chiral porphyrin aggregates, *manuscript in preparation*
 - (7) Arcudi, F.; Carlomagno, S.; Đorđević, L.; Rigodanza, F.; Sivori, S.; Moretta, A.; Prato, M. BODIPY-based carbon nanodots promote natural killer cells activation and maturation, *manuscript in preparation*.
 - (8) Arcudi F., Strauss V., Đorđević L., Cadranel A.; Guldi D. M.; Prato M. Porphyrin Antennas on Carbon Nanodots: Excited State Energy and Electron Transduction, *manuscript in preparation*.
 - (9) Arcudi F.; Rizzo C.; Dintcheva N.T.; Noto, R.; D'Anna F.; Prato M. Nitrogen-doped carbon nanodots/ionogels with powerful radical scavenging activity, *manuscript in preparation*.
 - (10) Arcudi, F.; Đorđević, L.; Rigodanza, F.; Cacioppo M.; Prato M. Carbon Dots: shining light on their synthesis and applications, *manuscript in preparation*
 - (11) Arcudi, F.; Prato M. Towards tailored carbon nanodots, *manuscript in preparation*
 - (12) Rigodanza, F.; Arcudi, F.; Đorđević, L.; Prato, M. Customizing energy levels in carbon nanodots through bottom-up quinone-doped synthesis, *manuscript in preparation*
 - (13) Dimos, K.; Arcudi, F.; Kouloumpis A.; Koutselas I.B.; Rudolf P.; Gournis D.; Prato M. Top-Down and Bottom-Up Approaches to Transparent, Flexible and Luminescent Nitrogen-Doped Carbon NanoDots-Clay Hybrid Film, *manuscript in preparation*
 - (14) Gomez, I.J.; Arnaiz B.; Arcudi F.; Prato M. Carbon NanoDots as New Nanocarriers for the Imaging-Guided-Delivery of Poorly Water-Soluble Antineoplastic Drugs, *manuscript in preparation*
-

